THIN FILM

COPLANAR TRANSMISSION LINES

THIN FILM
COPLANAR TRANSMISSION LINES

by

P. A. J. Dupuis, B. Eng.

A Thesis

Submitted to the Faculty of Graduate Studies

in Partial Fulfilment of the Requirements

for the Degree

Master of Engineering

McMaster University

April, 1973.

MASTER OF ENGINEERING (1973) McMASTER UNIVERSITY

(Electrical Engineering) Hamilton, Ontario.

TITLE: THIN FILM COPLANAR TRANSMISSION LINES

AUTHOR: P. A. J. DUPUIS, B. ENG., McMASTER UNIVERSITY

SUPERVISOR: PROFESSOR C. K. CAMPBELL

NUMBER OF PAGES: (xxii), 323.

SCOPE AND CONTENTS:

A theoretical and experimental study was performed in the 1-2 GHz frequency range on evaporated aluminum thin film coplanar waveguides. The major aspect of the study included an investigation of characteristic impedance and its associated geometric tolerances, plus attenuation, and contact loss. As a result of measurements made on a large number of samples, simple and reliable design guidelines were presented.

ABSTRACT

The theoretical aspects of coplanar waveguides were studied with special emphasis on the attainment of precise characteristic impedances and low losses in the 1-2 GHz frequency range. To this end, a literature survey was performed, and characteristic impedance design curves were reproduced exactly by means of a digital computer. An exact tolerance analysis method was then performed in order to determine geometrical tolerances which would enable a characteristic impedance of 50 Ω ± 10% to be attained for a given relative dielectric constant of 9.2 ± 10%. A loss theory which neglected dielectric losses and assumed thin films of conducting metal less than 1 skin depth thick was also presented. Two similar fabrication techniques were then studied and 43 coplanar waveguide samples were fabricated. Of these 43 samples, 32 were tested by swept frequency techniques and time domain reflectometer techniques.

The theory for characteristic impedance was found to be accurate to within ±2 Ω providing a few simple design guidelines were followed. The transmission loss theory corresponded very well with experimental measurements, which were estimated to be accurate to within 22%. Furthermore, fixtures for mounting the samples quickly and repetitively were designed and fabricated.

ACKNOWLEDGEMENTS

I am very much indebted to my supervisor Dr. C.K. Campbell for his interest, patience, moral support, and judicious advice throughout the course of this work. I also wish to express a very warm thankyou to the other members of my M. Eng. supervisory committee, Dr. S.S. Haykin, and Dr. E.G. Cristal, for their interest in this thesis.

Many others also contributed to this work by providing stimulating discussions and criticisms at various occasions. In appreciation of this help, I thank Dr. Alan Davis, Mr. John Kostynyk, Mr. Emerson Johnston, Mr. Paul Nolan, Mr. Vance Crowe, and Mr. V.K. Jha.

In addition, I wish to express my gratitude to Mr. Steve Kocsis and Mr. Jeff Hine for their suggestions and their fine work of machining the small "Coplanar Waveguide Launchers"; designed herein for mounting coplanar waveguide samples in experimental tests.

During the later stages of the experimental work, the program for fabricating the coplanar waveguide samples was accelerated with the employment of Mr. Brian diCenzo, whose laboratory assistance was invaluable. A very sincere thankyou is forwarded to Mr. diCenzo for his efficient and precise work.

Another thankyou must also be expressed to Dr. J. Shewchun for the use of his M-100 Angstrometer, which was extremely useful for calibrating our thin film thickness gauge.

The financial assistance provided by McMaster University in the form of a teaching assistantship and university scholarship is gratefully acknowledged.

Finally, I would like to thank my fiancée, Miss Donna DelVecchio, for her competent and meticulous typing, not to mention her love, patience, and understanding throughout this endeavour.

TABLE OF CONTENTS

LIST OF FIGURES

FIGURE		Page
E.11	Theoretical Frequency Response of the Input Reflection Coefficient ρ_1 in the 1-2 GHz Band with Z_{LC} as Parameter where R=20.6 Ω/m and α'=.00523 Np/in	313

LIST OF TABLES

LIST OF TABLES CONTINUED

CHAPTER I

INTRODUCTION

1.0 Background Information

A great deal of research has gone on recently in the microwave integrated circuits (MIC) area from which systems engineers have extracted small, lightweight, batch processed modules for radar and communications systems. These modules have been extremely useful in space satellites, modern aircraft and other mobile units where it is essential that bulk and weight be kept to a minimum. The major component of such modules is the microwave integrated circuit transmission line. Researchers such as Cristal, Podell and Parker [1] have surveyed the various types of lines available, outlining the advantages and disadvantages of each. Of particular interest to this thesis, the coplanar waveguide (CPW) described by C.P. Wen [5] as being extremely important for nonreciprocal gyromagnetic device applications, is shown by Cristal, Podell and Parker [1] to have approximately the same desirable properties for MIC applications as the well known veteran of 10 years; the microstrip transmission line. It appears that the only possible drawback one might encounter with the CPW is a slightly worse radiation problem. This radiation begins at frequencies slightly less in the CPW than in microstrip lines.

Though these microstrip lines have been used extensively in

the frequency range from 1-10 GHz for the past 10 years, and though in [1] they are rated as the best available transmission lines for a wide variety of applications, the CPW appears to hold a close secondary position in a list of nine available structures [1]. It is then certainly worthy of a detailed investigation. One obvious definite advantage of a CPW over a microstrip line is that a built-in circularly polarized magnetic field vector which is easily accessible at the surface of the CPW substrate is not provided by the microstrip line or strip line [5]. As a result, the CPW lends itself to nonreciprocal magnetic devices and the other two do not. This fact alone makes the transmission line properties of the CPW worth exploring.

1.1 Scope of this Thesis

The effectiveness of thin film CPW's as quasi-TEM mode transmission lines operating in the 1-2 GHz frequency band will be studied herein. The thesis will survey Wen's theory [5] and clarify or correct it wherever it is deemed necessary. A tolerance study will be undertaken and a simple theory for calculating propagation loss in thin film coplanar structures will be presented. Fabrication techniques and the electrical contact problems obtained when mounting the coplanar structures will also be discussed. Both straight and meandered lines will be fabricated and compared. Finally, experimental measurements will be used to verify or even modify the theory where this is required in order to describe the performance of a CPW more accurately.

As for theoretical aspects, Wen's characteristic impedance curves will be reproduced with precision. The concept of inductance per unit length will be introduced and Wen's pictorial representation of magnetic field lines in CPW's will be modified slightly. Finally, an attempt will be made to account for dispersion at higher frequencies, though the thesis will not verify this dispersion phenomena experimentally. The reason for this is that only the 1-2 GHz frequency band is of interest here. Dispersion is a problem at and above 4 GHz when a relative dielectric constant of 100 is used. For smaller relative dielectric constants dispersion only begins to occur at higher frequencies.

In order to account for observed experimental deviations in characteristic impedance, one must have a feeling for the tolerances involved when overall tolerances of ±10% are specified for the characteristic impedance. An exact tolerance analysis developed by the author is used to analyse the CPW with the result that exact tolerance specifications are placed on the pertinent geometrical parameters. The idea is to note all measured deviations from the theoretical characteristic impedance curves that are larger than the predicted deviations one would expect from geometrical tolerances. These deviations indicate how to utilize the theory in a practical way for a more exact design.

The calculation of propagation loss for a matched line is also simplified herein. Since thin conductor films are used to fabricate the coplanar structures in this thesis, a d.c. resistance approximation becomes valid for calculating ohmic losses in the structures.

Good experimental agreement with this method was obtained.

The fabrication and mounting of CPW's receives a great deal of attention herein. Wen [5] discusses permanent encapsulation of CPW's for industrial use, but for experimental purposes a clean, cheap, and easy method of mounting and unmounting the sample structures without destroying them is a must; especially when 20 to 30 samples have to be tested and retested on 3 or 4 different types of apparatus. In this respect, it is also desirable to have thin films that adhere well to a substrate. The choice of materials that serve this function and at the same time are easy to work with is very important. Finally, certain geometrical tolerances must be met in order to ensure a satisfactory performance, and to this end the choice of a suitable fabrication technique must be made.

Electrical measurements reported in this thesis over the 1-2 GHz frequency range were obtained with the aid of two network analysers as well as two time domain reflectometers. The characteristic impedance as a function of coplanar geometry, the propagation loss as a function of thin film thickness, and the phase velocity were some of the important properties measured. These measurements led to a few practical design guidelines for using Wen's coplanar waveguide theory.

CHAPTER II

COPLANAR WAVEGUIDE DESIGN

2.0 Introduction

The goal of this thesis was to design and fabricate with 96% Coors alumina substrates a 50 Ω ± 10% thin film coplanar waveguide (CPW), to be operated in the 1-2 GHz frequency range, and mounted by means of standard 3 mm coaxial connectors. A detailed study of C.P. Wen's theory [5] was first accomplished, and a few theoretical modifications were introduced to account for distributed inductance and circularly polarized magnetic fields accessible at the surface of the CPW. C.P. Wen's design curves were also reproduced exactly by means of an HP 9100A digital computer. The characteristic impedance, phase velocity, dispersion and radiation were discussed from a design viewpoint. An exact tolerance analysis developed by the author was also used to calculate tolerances required to achieve the above goal. Finally, a simple loss theory was presented for predicting transmission loss in thin film CPW's on a d.c. resistance basis.

2.1 Coplanar Waveguide Analysis

In Figure 2.1-1, a thin film coplanar waveguide (CPW) is shown with its RF magnetic field configuration. A center strip of thin metallic film with two adjacent ground planes on the same surface of a dielectric slab, forms a surface strip transmission line with a quasi-TEM mode of propagation. There is no low frequency cutoff in the CPW because of the quasi-TEM mode of propagation. Experimental investigations by Wen indicate that the CPW promises to be useful up to frequencies within the X band region.

Notice that the RF magnetic field H, of the CPW has both transverse and longitudinal components which are symmetrically located about the center strip at the surface of the guide [5]. The transverse RF magnetic field component is due to the longitudinal current in the center strip and the longitudinal RF magnetic field component is due to a transverse displacement current density between the center strip and ground planes. If the relative dielectric constant ϵ_r, of the substrate is much larger than unity, this RF magnetic field at the air-dielectric interface is nearly circularly polarized in a plane of polarization perpendicular to the surface of the substrate. This means that the longitudinal and transverse components of H are equal in magnitude and 90° out of phase. Since this built-in circularly polarized magnetic vector is easily accessible at the surface of the substrate, the CPW is suitable for non-reciprocal gyromagnetic device applications. Wen has successfully fabricated and

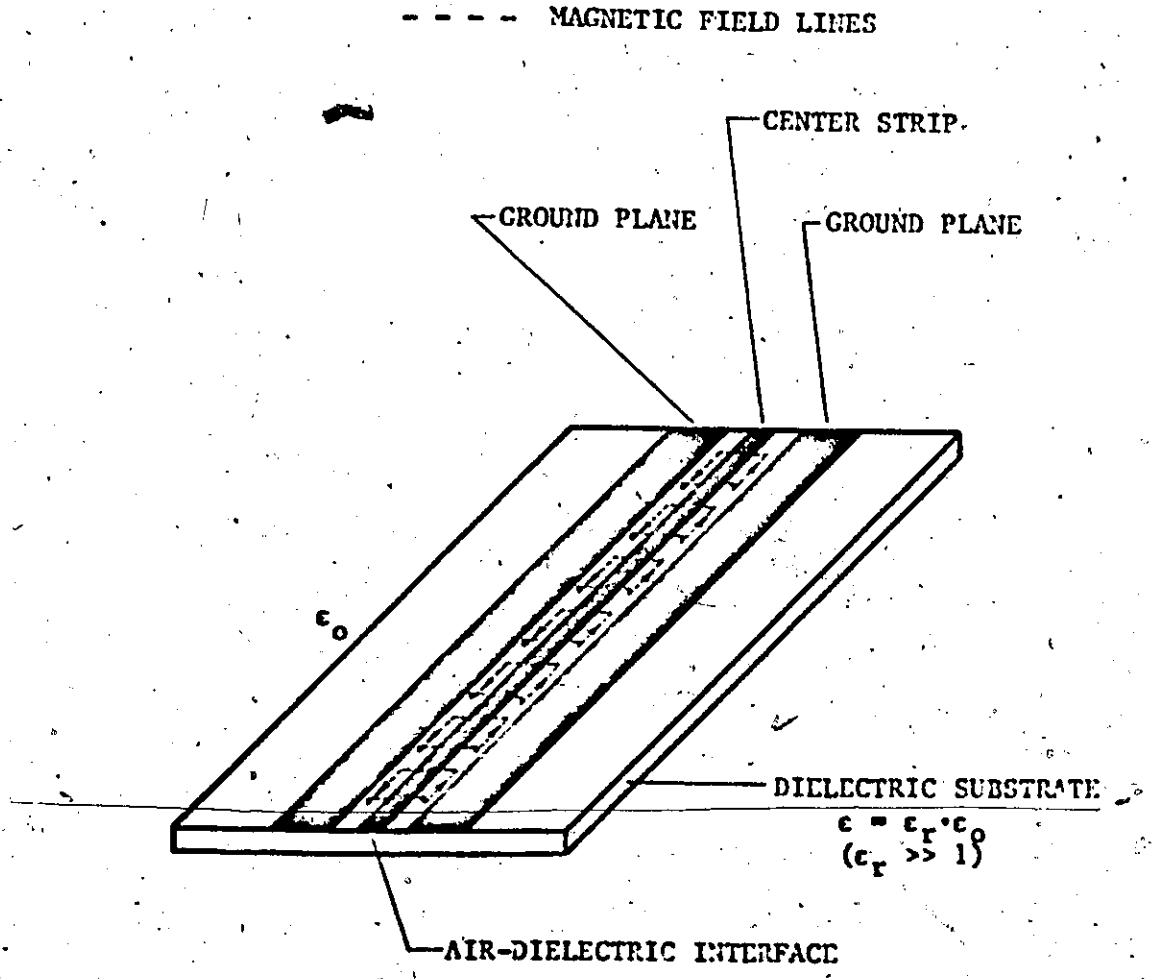

Figure 2.1-1: Coplanar Waveguide (CPW) with RF Magnetic Field Configuration.

tested such devices [5].

The CPW lends itself to monolithic microwave integrated circuit fabrication techniques. The connection of shunt elements and the fabrication of series and shunt capacitances is easy, with all three conducting planes on the same side of the dielectric substrate. Also, ferrimagnetic and YIG rods or slabs are easily mounted.

A relatively simple theory based on a conformal mapping approach makes CPW design easy to achieve. Figure 2.1-2 illustrates the conformal mapping approach. An end view of the CPW is shown centralized in the complex plane Z_1 with the dielectric region shaded and assumed infinite. The width of the ground planes is also assumed to be infinite. The right and left edges of the center strip are labelled $+a_1$ and $-a_1$ respectively, and the corresponding inside edges of the ground planes are labelled $+b_1$ and $-b_1$. Each of these edges represent material discontinuities at a metallic-air interface, and correspondingly, the electric field lines, which must enter and end on the metallic strips in a perpendicular fashion, are also discontinuous at the metallic-air interface. Each of these four discontinuities also lie along the real axis of the Z_1 plane, and when transformed by conformal mapping into another complex plane, Z, they each contribute a 90° bend to the map. Four right angle bends form a rectangle with the boundaries representing stream function values, $+a$ and $-a$, and a total potential difference b. These boundaries also contain the dielectric.

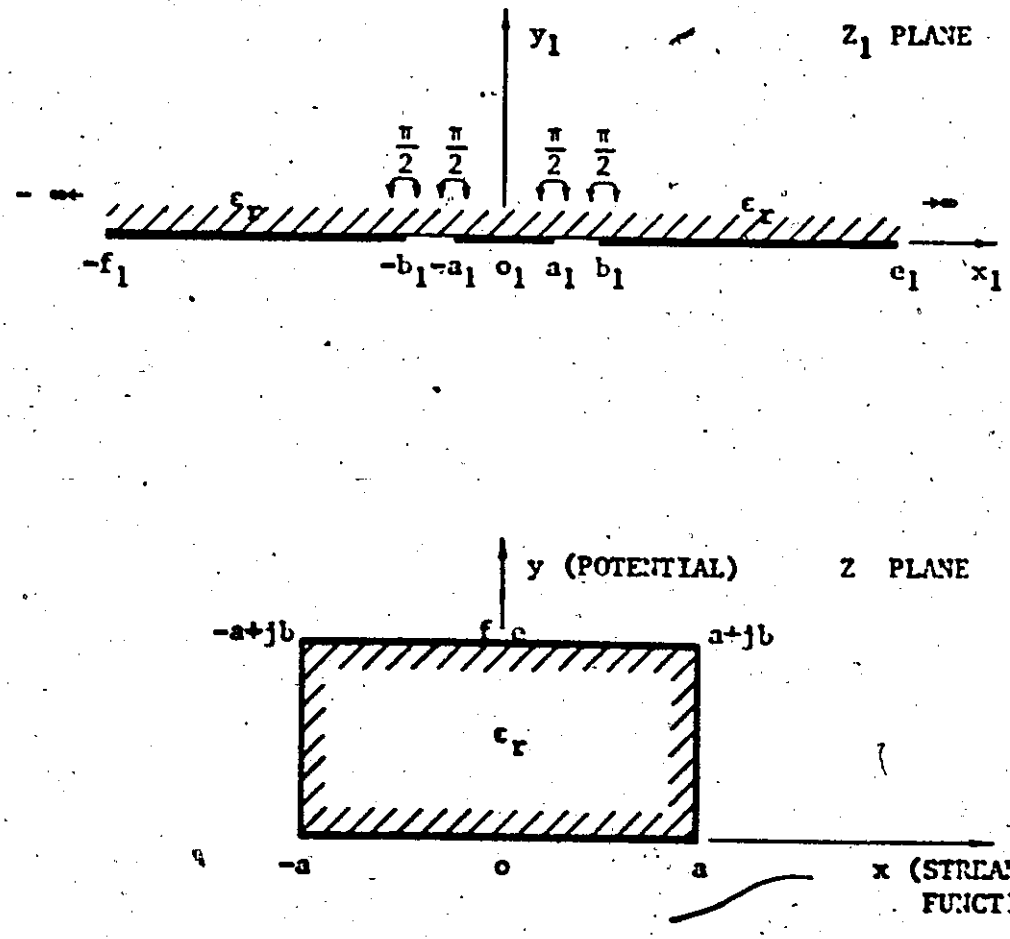

Figure 2.1-2: Conformal Mapping Transformation of the Upper Half Plane of a CPW into the Interior of a Rectangle.

For simplicity, the subscripted letters in the Z_1 plane correspond to the same unsubscripted letters in the Z plane. For example $+a_1$ in the Z_1 plane corresponds to $+a$ in the Z plane.

The above zeroth order, quasi static approximation [5] may be obtained mathematically by the Schwarz-Christoffel transformation

$$\frac{dZ}{dZ_1} = \frac{A}{(Z_1^2 - a_1^2)^{\frac{1}{2}} (Z_1^2 - b_1^2)^{\frac{1}{2}}} \qquad (2.1\text{-}1)$$

where A is a constant. Integration of (2.1-1) along the real axis of the complex Z_1 plane from 0_1 through a_1 to b_1 yields

$$a + jb = \int_{0_1}^{b_1} \frac{A dZ_1}{(Z_1^2 - a_1^2)^{\frac{1}{2}} (Z_1^2 - b_1^2)^{\frac{1}{2}}}$$

$$= -\int_{0_1}^{a_1} \frac{A dx_1}{(a_1^2 - x_1^2)^{\frac{1}{2}} (b_1^2 - x_1^2)^{\frac{1}{2}}}$$

$$+ j \int_{a_1}^{b_1} \frac{A dx_1}{(x_1^2 - a_1^2)^{\frac{1}{2}} (b_1^2 - x_1^2)^{\frac{1}{2}}}$$

$$= A [K(k) + j K(k')] \qquad (2.1\text{-}2)$$

where

$$k = a_1 / b_1$$

K (k) = complete elliptical integral of the first kind

K'(k) = K (k')

$$k' = (1-k^2)^{\frac{1}{2}}.$$

As a result

$$\frac{2a}{b} = \frac{2k(k)}{K(k')}, \qquad (2.1\text{-}3)$$

where 2a represents a stream function increment and b represents a potential difference. Since elliptic integrals can be easily calculated by means of a digital computer, 2a/b is also easily calculated. The rectangle in Figure 2.1-2 represents a dielectric filled capacitor with a relative dielectric constant of ϵ_r. In parallel with this capacitor is another similar air filled capacitor as shown in Figure 2.1-3. Both capacitances are assumed to be ideal. That is, a uniform electric field is assumed in each capacitor with known stream function increments and known potential difference between the plates of the capacitors.

By definition, the capacitance per unit length in a 2-dimensional electric field is given by

$$C = \frac{Q}{| V_2 - V_1 |} \quad \text{(farads / m)}, \qquad (2.1\text{-}4)$$

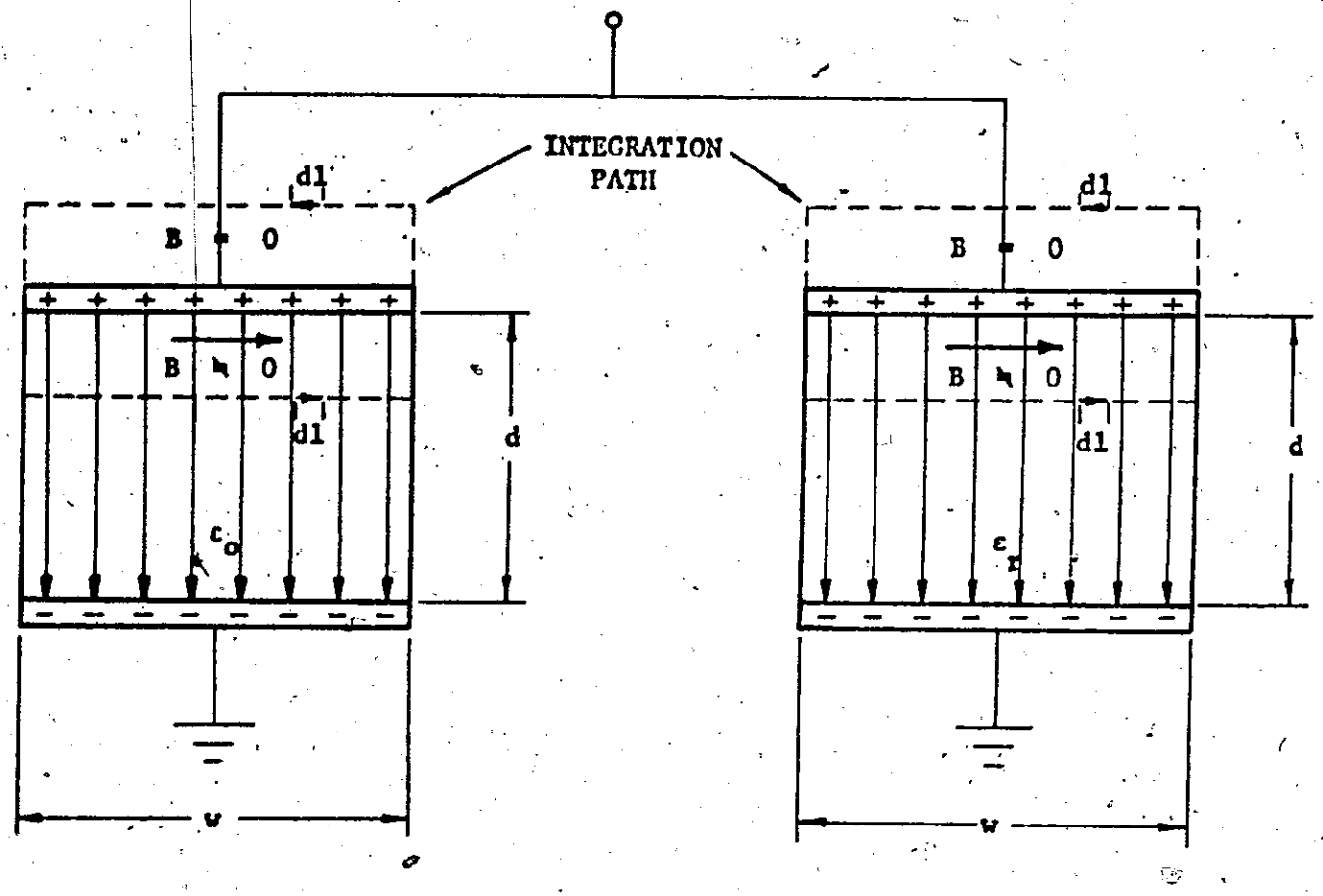

Figure 2.1-3: Parallel Combination of the CPW's Air Filled and Dielectric Filled Capacitors, Showing their uniform Electric Flux Distribution and the Strength of the Magnetic Induction Field, B, Inside and Outside the Capacitors.

which can be shown to be equivalent to

$$C = \frac{\epsilon\ (U_2 - U_1)}{|\ V_2 - V_1\ |} \quad \text{(farads / m)}, \qquad (2.1\text{-}5)$$

where Q is the total charge on the capacitor per unit length, $|\ V_2 - V_1\ |$ is the potential difference applied across the plates, and $(U_2 - U_1)$ is the difference in the stream function values defining two boundaries in the field for the region of interest [10]. The total flux per unit length is also given by

$$Q = \epsilon\ (U_2 - U_1) \quad \text{(coulombs / m)}. \qquad (2.1\text{-}6)$$

For an ideal parallel plate capacitor it is known that

$$C = \frac{\epsilon \cdot W}{d} \quad \text{(farads / m)} \qquad (2.1\text{-}7)$$

where W is the plate width and d the plate separation. Combining equations (2.1-7) and (2.1-5) then gives

$$\frac{W}{d} = \frac{(U_2 - U_1)}{|\ V_2 - V_1\ |}$$

$$= \frac{2a}{b} \qquad (2.1\text{-}8)$$

This equation then states the basic relation relating the geometry of an ideal parallel plate capacitor to its flux and potential distribution. From Figure 2.1-3, the total effective capacitance per unit length for a CPW is given by

$$C = (\varepsilon_r + 1) \cdot \varepsilon_o \cdot \frac{2a}{b} \quad \text{(farads / m)} \qquad (2.1\text{-}9)$$

The inductance per unit length should also be taken into account. Since the above capacitors have been assumed to have uniform electric fields, the plates act like infinite plates. This means that the magnetic field strength inside each capacitor must be uniform and non zero whereas it must be zero outside each capacitor. Figure 2.1-3 also shows this situation. Ampere's circuital law may now be applied by integration around the closed, rectangular, dashed lines to yield

$$B = \frac{\mu_o i}{W} \quad \text{(webers / m}^2\text{)} \qquad (2.1\text{-}10)$$

for both capacitors, where i is the total current flowing into the capacitor and μ_o is the magnetic permeability for both the dielectric and air. The resulting inductance per unit length for two identical inductors in parallel is then

$$L = \frac{1}{2}\left|\frac{B\,d}{1}\right|$$

$$= \frac{1}{2}\left|\frac{\mu_{od}}{W}\right|$$

$$= \frac{1}{2}\left|\frac{\mu_{ob}}{2a}\right| \qquad (H / m) \qquad (2.1\text{-}11)$$

This result along with the capacitance equation, (2.1-9), leads to the following simple result for a lossless coplanar transmission line.

$$V_{ph} = \frac{1}{\sqrt{L\,C}}$$

$$= \left[\frac{2}{1 + \epsilon_r}\right]^{\frac{1}{2}} \cdot c \qquad (m / sec.) \qquad (2.1\text{-}12)$$

where V_{ph} is the phase velocity of the quasi-TEM wave propagating down the line, and c is the velocity of light. The equation implies V_{ph} is constant for a given uniform substrate, and any frequency range. That is, no functional dependence of the phase velocity on frequency or geometry is implied by equation (2.1-12), unless ϵ_r is itself a function of frequency and space.

Figure 2.1-4 displays the functional dependence of the phase velocity on ϵ_r.

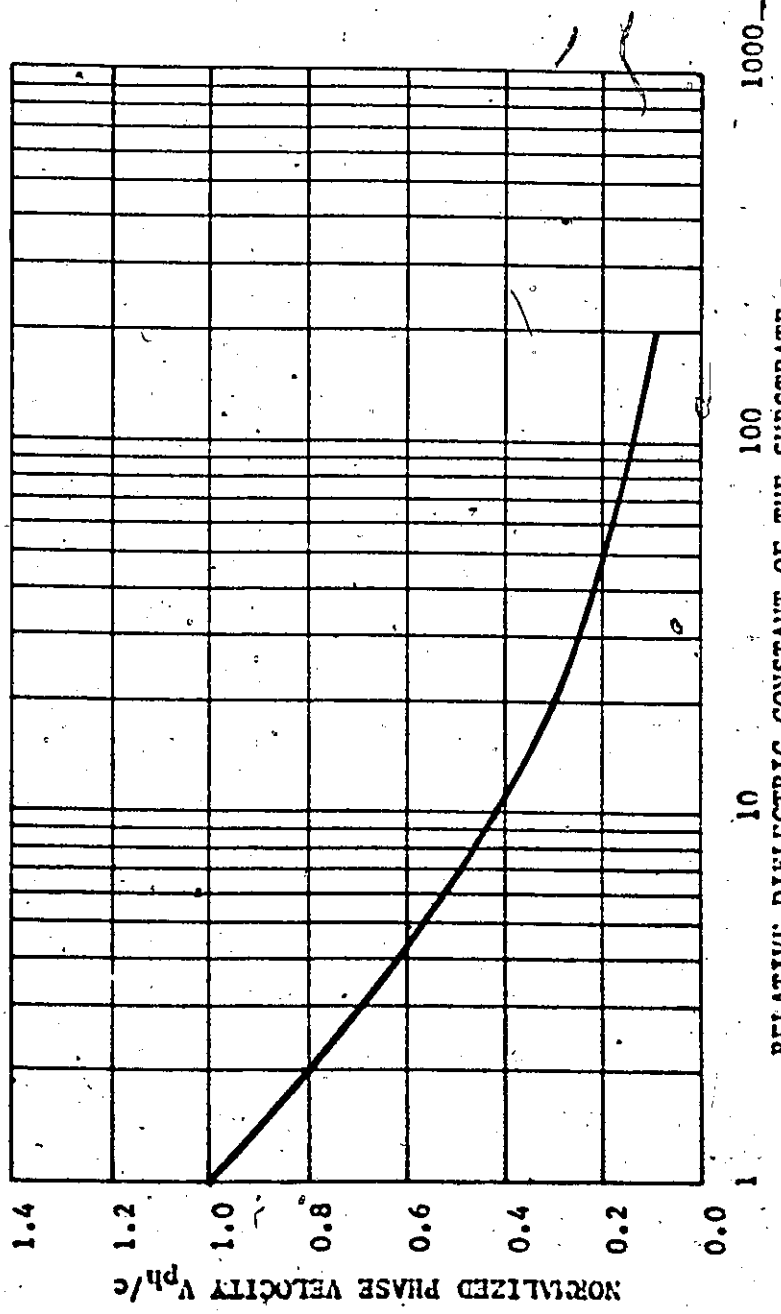

Figure 2.1-4: Normalized Phase Velocity V_{ph}/c in a CPW vs. the Relative Dielectric Constant of the Substrate.

For CPW substrate materials with relative dielectric constants larger than 100, a free space wave can be slowed down to a value less than 0.1407 times the free space velocity of light, c. Rutile has a value of ϵ_r equal to 100 and so a CPW with a rutile substrate will propagate a quasi-TEM wave at 0.1407 • c. Alumina (96%, ϵ_r = 9.2) on the other hand, will slow the free space wave to a value of 0.4428 • c.

The "dispersion characteristic" for the CPW can now be plotted. Since it is known that

$$V_{ph} = \frac{\omega}{\beta} \tag{2.1-13}$$

and

$$V_{group} = \frac{d\omega}{d\beta} \tag{2.1-14}$$

a constant value of V_{ph} over a specified frequency range yields

$$V_{ph} = V_{group} = \text{a constant}, \tag{2.1-15}$$

and thus

$$\beta = \frac{2\pi f}{V_{ph}} \tag{2.1-16}$$

is a linear function of frequency f.

Since, for a fixed length of Transmission line L; (m) a plot of f vs. $\beta L'$ (radians) constitutes a "dispersion characteristic", one would expect this characteristic for a CPW to be a straight line. Figure 2.1-5 illustrated this ideal dispersion characteristic for alumina and rutile substrates in dashed lines. C.P. Wen [5] has made experimental measurements for single-crystal, rutile substrates and these are compared with the ideal dispersion characteristic for rutile in the same figure. Slight experimental deviation from the ideal straight line occurs above a frequency of 3 GHz. It is clear that at frequencies above 3 GHz, larger β values and consequently lower phase velocities are obtained than would be predicted by the foregoing theory. This could be due to a frequency dependent ϵ_r value, as well as approximations made in the theory. The reader should be reminded that conductor thickness was ignored, and infinitely wide ground planes along with an infinitely thick dielectric substrate were assumed.

It is expected that the finite dielectric would simply reduce the effective relative dielectric constant of the substrate and not introduce a frequency dependent term other than ϵ_r itself. The conductor thickness contribution to theoretical deviations is assumed to be slight for thin films, since this is the case for microstrip lines. Figure 2.1-6 illustrates that for microstrip lines with films less than 27,000 Angstroms (27 kÅ) thick the necessary per cent width correction in the center strip is less than -1%.

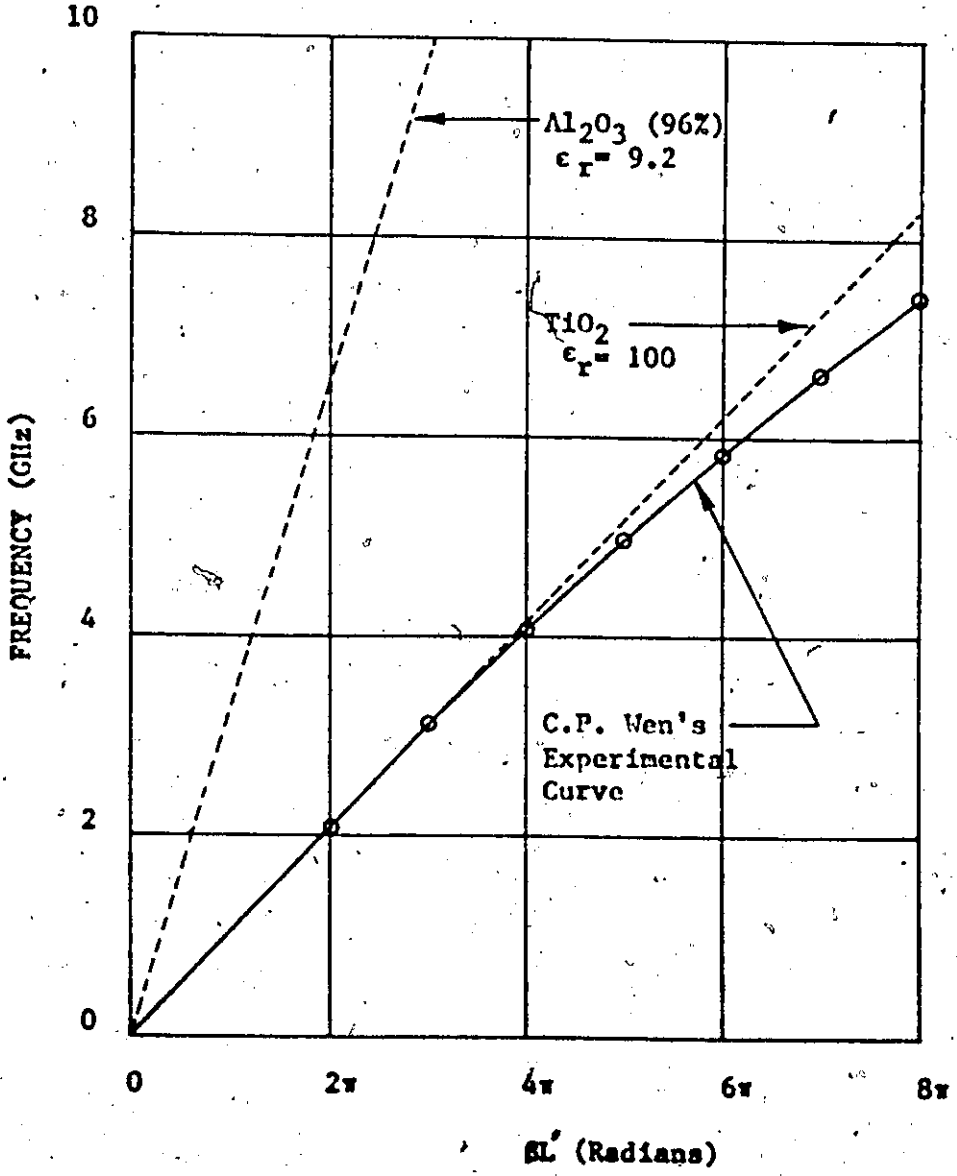

Figure 2.1-5: Dispersion Characteristic of a .8 Inch Long CPW for a Rutile Substrate (C.P. Wen), and a 96% Alumina Substrate.

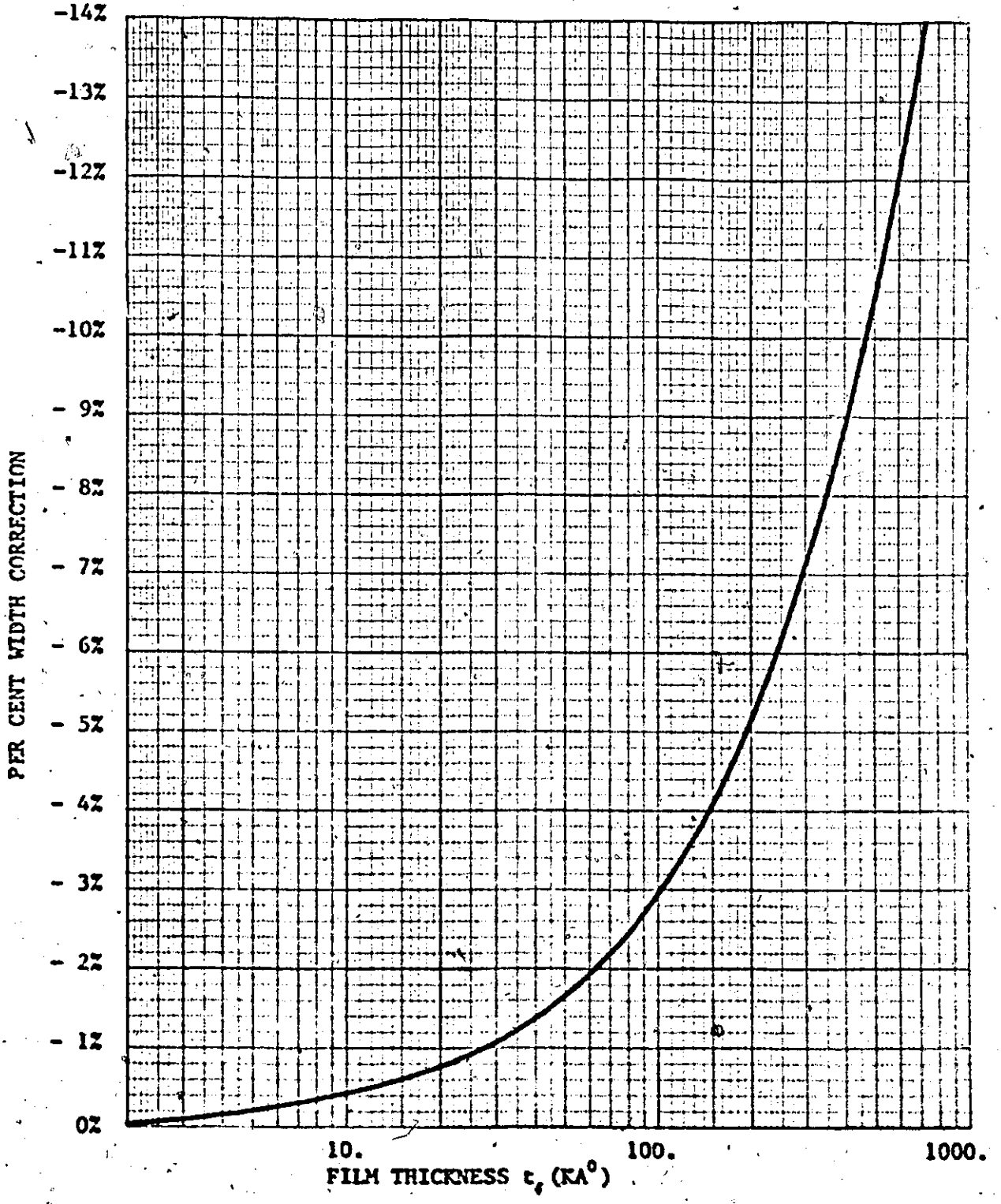

Figure 2.1-6: Per Cent Width Correction for a 50 Ω Microstrip Line on a 25 Mil Thick Alumina Substrate of 96% Purity vs. the Thickness t_f (kÅ) of the Conducting Strip.

This data was calculated by Dr. Alan Davis at McMaster University and was based on the work of S.B. Cohn [8].

Time domain reflectometry measurements in Chapter V will show that even the width of the ground planes does not seem as important as the dielectric substrate thickness. It then seems reasonable to assume that a frequency dependent ε_r and perhaps an anisotropic dielectric substrate are major factors affecting the deviation of the measured dispersion characteristic from the ideal. The quasi-TEM zeroth order approximation in the theory might also be relevant. However, Wen states that "it is not known what portion of the dispersion characteristic is caused by the crystal anisotropy of the substrate and what portion is attributed to the inherent characteristics of the CPW mode of propagation on a dielectric half-space".

A check of the wavelengths for the quasi-TEM mode of propagation above 1.5 GHz might give a clue as to what contribution various higher order modes would have to the non-linearity in the dispersion characteristic for rutile. Table 2.1-1 illustrates the theoretical frequency dependence of the guide half-wavelength for the quasi-TEM mode of propagation in a CPW for alumina and rutile substrates. The values shown are based on the phase velocity equation (2.1-12) and on the well known fact that

$$V_{ph} = f \cdot \lambda . \qquad (2.1\text{-}17)$$

Frequency (GHz)	Values of λ/2 (inches)	
	Alumina (96%) $\varepsilon_r = 9.2$	Rutile ε_r=100
1.5	1.7433	0.5540
3.0	0.8717	0.2770
6.0	0.4358	0.1385
9.0	0.2906	0.0726
12.0	0.2179	0.0545

Table 2.1-1: Values of λ/2 in a CPW for Alumina and Rutile Substrates as a Function of Frequency above 1.5GHz.

It seems reasonable to expect that if the guide half-wavelength for the quasi-TEM mode of propagation approaches the ground plane separation $2b_1$, modes other than the quasi-TEM mode will begin to propagate. The table shows that alumina substrates of 96% purity produce half-wavelengths that are 3.15 times larger than the half-wavelengths associated with rutile substrates at the same frequency. Also, at 3 GHz the half wavelength for rutile is slightly larger than a quarter of an inch, and at 6 GHz it is slightly larger than an eighth of an inch, and so on. If a center strip width of .050" is used in a particular CPW design along with a k of approximately 1/3, the ground plane separation is roughly .150", which lies between 1/4" and 1/8". Hence it might be reasonable to expect moding problems to begin to appear between 3 and 6 GHz for rutile substrates, as shown in figure 2.1-5. On the other hand, alumina substrates used with the same coplanar geometry would not produce such moding problems until frequencies 3.15 times higher were used, because of the larger wavelengths obtained with a smaller relative dielectric constant.

2.2 Characteristic Impedance as a Function of Coplanar Geometry

The characteristic Impedance of the CPW follows directly from section 2.1 where the inductance and capacitance per unit length of the coplanar line was derived as well as a corresponding phase velocity expression. Since the characteristic impedance Z_o of a lossless transmission line is given by

$$Z_o = \sqrt{\frac{L}{C}} = \frac{1}{v_{ph} \cdot C}, \qquad (2.2\text{-}1)$$

the characteristic impedance for a lossless CPW may be written as

$$Z_o = \frac{1}{\sqrt{2(\epsilon_r + 1)} \cdot \epsilon_o \cdot \frac{2a}{b} \cdot c} \qquad (2.2\text{-}2)$$

where ϵ_r is the relative dielectric constant of the dielectric substrate, ϵ_o is the permittivity of vacuum, c is the velocity of light in free space, and a/b is the ratio of two complete elliptic integrals K(k) and K(k') as defined by (2.1-3). It is clear that the value of Z_o depends on two distinct variables; ϵ_r and the ratio a/b. An increase in both these variables decreases Z_o, but a/b in not a true physical variable as is ϵ_r. The ratio a/b increases with the physical geometrical variable a_1/b_1, but only through the rather complicated elliptical

integral transformation described in section 2.1. A graphical representation of the impedance Z_o as a function of coplanar geometry with ϵ_r as parameter is then of great practical interest.

Figure 2.2-1 depicts the functional dependence of the characteristic impedance Z_o on geometry and the relative dielectric constant ϵ_r. An increase in ϵ_r decreases Z_o as expected, but it is now clear that as the center strip width, $2a_1$, increases, the impedance Z_o decreases. An increase in the ground plane separation, $2b_1$, has the reverse effect on Z_o, causing Z_o to increase.

The characteristic curves were plotted on a Hewlett Packard 9105A calculator plotter interfaced with a 9100A H.P. calculator and 9101A H.P. extended memory unit. With this equipment it was an easy matter to magnify certain regions of interest for tolerance studies and accurate selection of design points. At this stage of the work the foregoing theory was assumed to be precise.

2.3 Tolerance Studies

An exact method of tolerance analysis, which bypasses first and second order approximations to Taylor series expansions, was developed by the author, and the details of this work appear in Appendix A. In general an upper and lower bound is placed upon a given nominal design performance curve which is a function of n parameters. The application of such bounds then creates an acceptable region of design R_A in an n-dimensional multiparameter space.

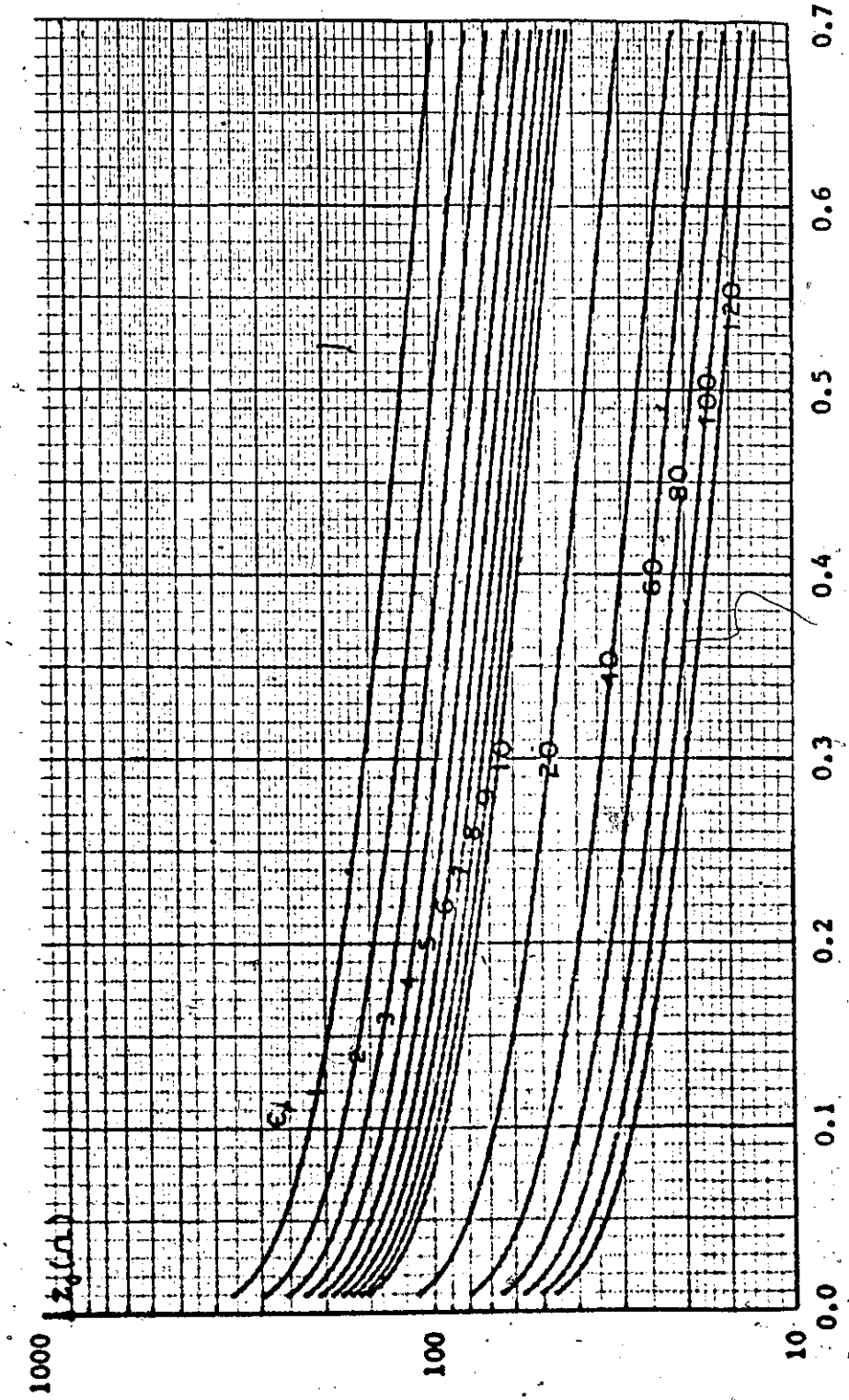

Figure 2.2-1: Characteristic Impedance Z_0 of CPW as a Function of the Ratio a_1/b_1 with the Relative Dielectric Constant ϵ_r as Parameter.

Within this design region R_A, all points are acceptable nominal designs in the sense that they theoretically give an acceptable design performance. However, this does not take tolerances into account.

It is reasonable to expect that the central point of R_A would be the best nominal design point tolerance-wise, since then all deviations from nominal component values which create performance violations would be equalized. The chance of obtaining a reject on a production line basis would then be minimized. This new numerical process automatically centralizes the nominal design in R_A.

An n-dimensional box called a "tolerance box" is grown inside the region R_A by a new numerical technique. The sides of the box are each parallel to two parameter axes. Initially these sides are weighted such that one parameter is favoured 100:1 with respect to all other parameters. The box is then long and narrow such that it looks like a meter stick. It is then used to measure the maximum length of R_A in the direction of the favoured parameter. Each parameter is then favoured in turn, and finally the ratios of the maximum lengths of these meters to each other are taken to comprise an "optimum tolerance set". In this way the size of the region R_A is accurately measured.

The above optimum tolerance set is used once more to weight the tolerance box sides for one final tolerance box growth. When the box has reached its maximum size, the individual tolerances related to the given overall performance specification

are known precisely. These are then rounded off to the next lowest realistic obtainable tolerances such as is the case for 2% resistors, for example, or 10% capacitors. The center of the tolerance box represents the best nominal design values obtainable. Of course in a practical situation, they too must be rounded off to realistic, obtainable values. However the degree of rounding used on a specific parameter must be much less than its specific tolerance by at least a factor of 10 if accuracy is to be maintained. Tunable components allow for mechanical rounding, thus ensuring accuracy.

In the case of the CPW, the geometric quantities $2a_1$ and $2b_1$ are the relevant parameters. The quantity ϵ_r is known to have a fixed value as specified by the manufacturer of the substrate used. The tolerance on ϵ_r may also be given, but if this information is not known, statistical treatment of laboratory measurements of ϵ_r over a specified frequency range will lead to the necessary tolerance information.

Herein the tolerance on ϵ_r was not known beforehand and was simply assumed to be ±10%. This was used in a trial analysis of the CPW in order to give a feeling for the necessary tolerances on $2a_1$ and $2b_1$ when a ±1% deviation on Z_o was specified along with a nominal value of 50 Ω.

Figure 2.3-1 shows this upper and lower bound specification for a CPW in an expanded region of the characteristic impedance

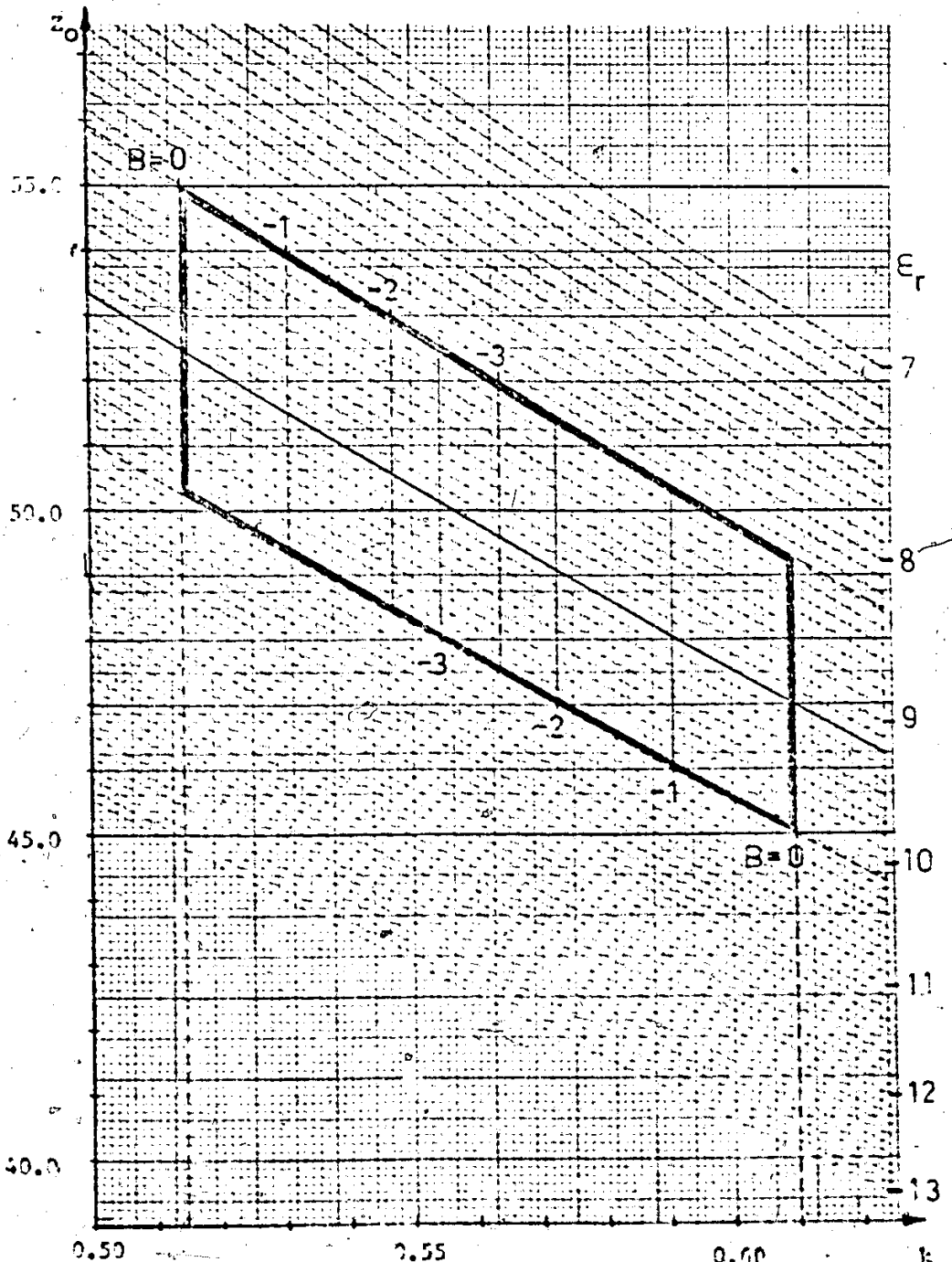

Figure 2.3-1: Range of k for a 10% Tolerance on ε_r and a 10% Specification on the Characteristic Impedance Z_o.

vs k plot, with ε_r as parameter. The quantity ε_r takes on values ranging from 8.28 through 9.20 to 10.12, and the value of Z_o is allowed to lie between 45.00 Ω and 55.00 Ω. This describes a region approximately shaped like a rhombus whose vertical sides designate the minimum and maximum values of k allowed for the above design specifications. The B values on the graph denote the various degrees by which these specifications can be tightened. B=0 means that 50.0 ± 5.0 Ω is specified as a desired tolerance on Z_o. B=-1 means that the specification has been tightened to 50.0 ± 4.0 Ω; and so on.

The minimum and maximum values of k obtained from Figure 2.3-1 above are then translated to Figure 2.3-2; a 2-dimensional parameter space with $2a_1$ and $2b_1$ as parameters. Remember that k is simply the ratio of $2a_1$ to $2b_1$, and so the minimum and maximum values of k obtained from Figure 2.3-1 represent the minimum and maximum slope values respectively for straight lines through the origin in Figure 2.3-2. These straight lines are the two boundaries of an open ended region R_A with B constant. The figure shows that as B is reduced from 0.0 in increments of -0.5, the region R_A is correspondingly reduced in size, as would be expected. For each value of B larger that -2.50, there exists a single finite region R_A containing an infinite number of acceptable design points including the exact solution for a 50 Ω line. Since R_A is open ended, an upper bound must be placed on both $2a_1$ and $2b_1$ so that the CPW will not become cumbersomely large. R_A must be a closed region.

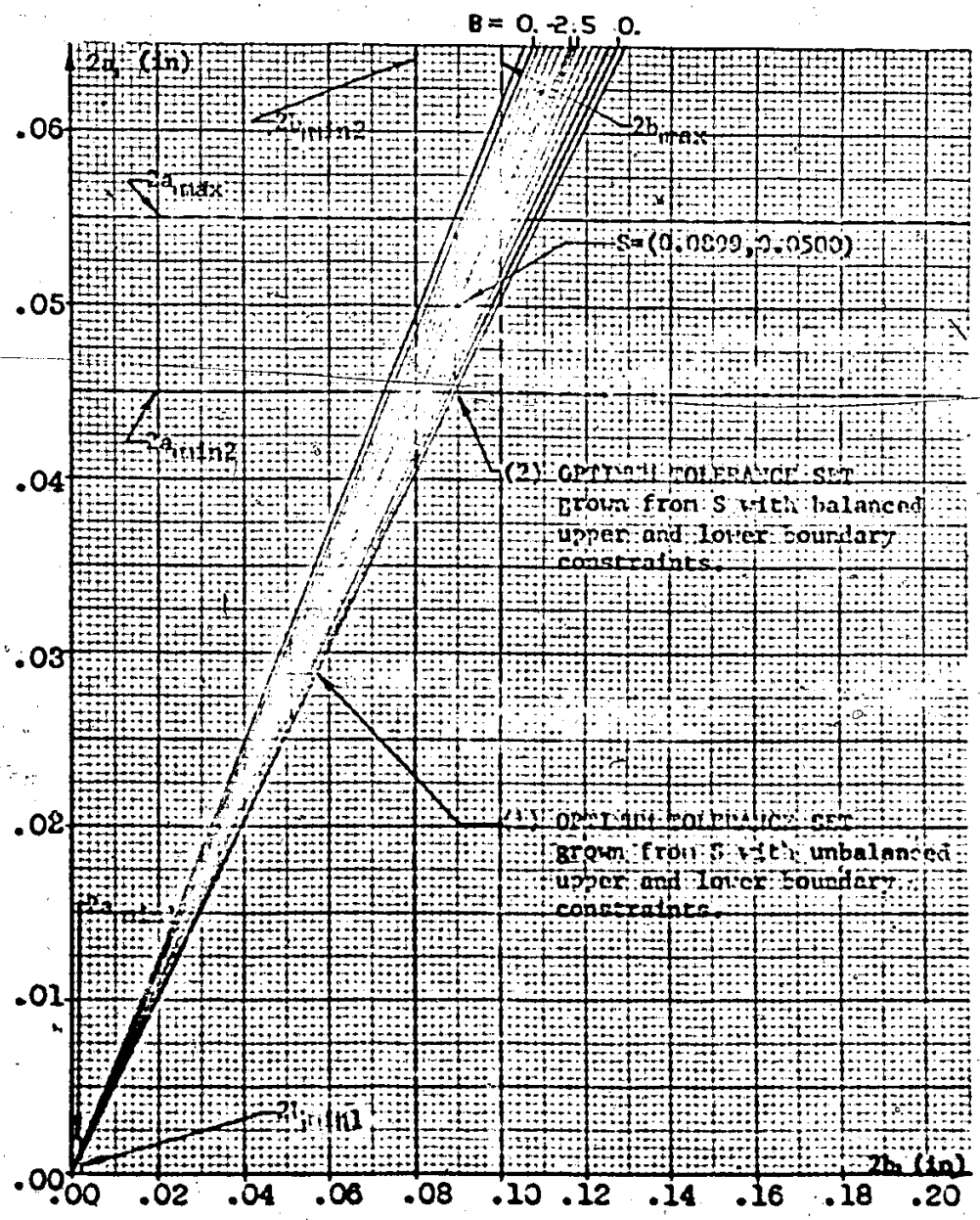

Figure 2.3-2: Optimum Tolerance Sets Obtained with Balanced and Unbalanced Upper and Lower Boundary Constraints for the Acceptable Region of Design, R_A, in a 2 Dimensional Parameter Space Containing $2a_1$ and $2b_1$ as Parameters.

Also, a good geometrical match with 3 mm coaxial connectors having 50 mil center pins is required. That is, the center strip of the CPW should be approximately 50 mils.

Lower bounds on $2a_1$ and $2b_1$ are also important. It should be remembered that the new method of "tolerance box growth" allows the nominal design to centralize itself in R_A. If the lower bounds placed on $2a_1$ and $2b_1$ are given larger and larger values, R_A shrinks in size and its central point moves upwards. The central nominal design can then be shifted upwards by raising the values of the lower bounds.

This effect was tested numerically by the growth of two optimum tolerance sets about a starting point S, denoting a center strip 50 mils wide plus the corresponding exact solution for $2b_1$. In both cases the upper bounds had values 10% greater than the exact solution values of point S. However the lower bounds were different in each case. In the first case $2a_{1\ min\ 1}$ and $2b_{1\ min\ 1}$ were both 2 mils. In the second case, $2a_{1\ min\ 2}$ and $2b_{1\ min\ 2}$ were both -10% of the parameter values at point S. In summary, the first case had unbalanced upper and lower boundary constraints of ±10% about S.

The optimum tolerance sets grown from S for both cases with B=0 are shown in Figure 2.3-2. Case 2 proved to be more desirable since the balanced upper and lower boundary constraints allowed the center strip width to remain at 50 mils. The optimum tolerance set of case 2 was then used to grow tolerance boxes

inside R_A for different consecutive values of B from -2.0 to +0.5 in increments of +0.5.

These numerically grown boxes are shown in Figure 2.3-3 in an expanded view of R_A for the balanced upper and lower boundary constraints of case (2). The tolerance meters are also shown. The boxes, like the meters, were grown from starting point S. Points C_1 and C_2 are the centers of the vertical and horizontal meters respectively. A slight drift of the box centers of less than ±0.1 mils in 50 mils was noticed from box to box.

For B equal to zero, a tolerance design of

$$2a_1 = 0.05009" \pm 4.223\%$$
$$2b_1 = 0.08941" \pm 4.238\% \quad (2.3\text{-}1)$$

resulted from the above analysis. This should be compared with the exact analysis of point S being

$$2a_1 = 0.05000" \pm 0.00\%$$
$$2b_1 = 0.0899" \pm 0.00\% . \quad (2.3\text{-}2)$$

Since in Figure 2.3-3 the discrepancy between the various box centers is 0.2%, the tolerances used on $2a_1$ and $2b_1$ should be reduced to 4.0% in order to ensure that all specifications are met. It should also be noted that the discrepancy between point S and the new nominal values of 2.3-1 is no more than 0.58 mils in 89.9 mils, which is 0.645%. Hence the exact solution of point S may be

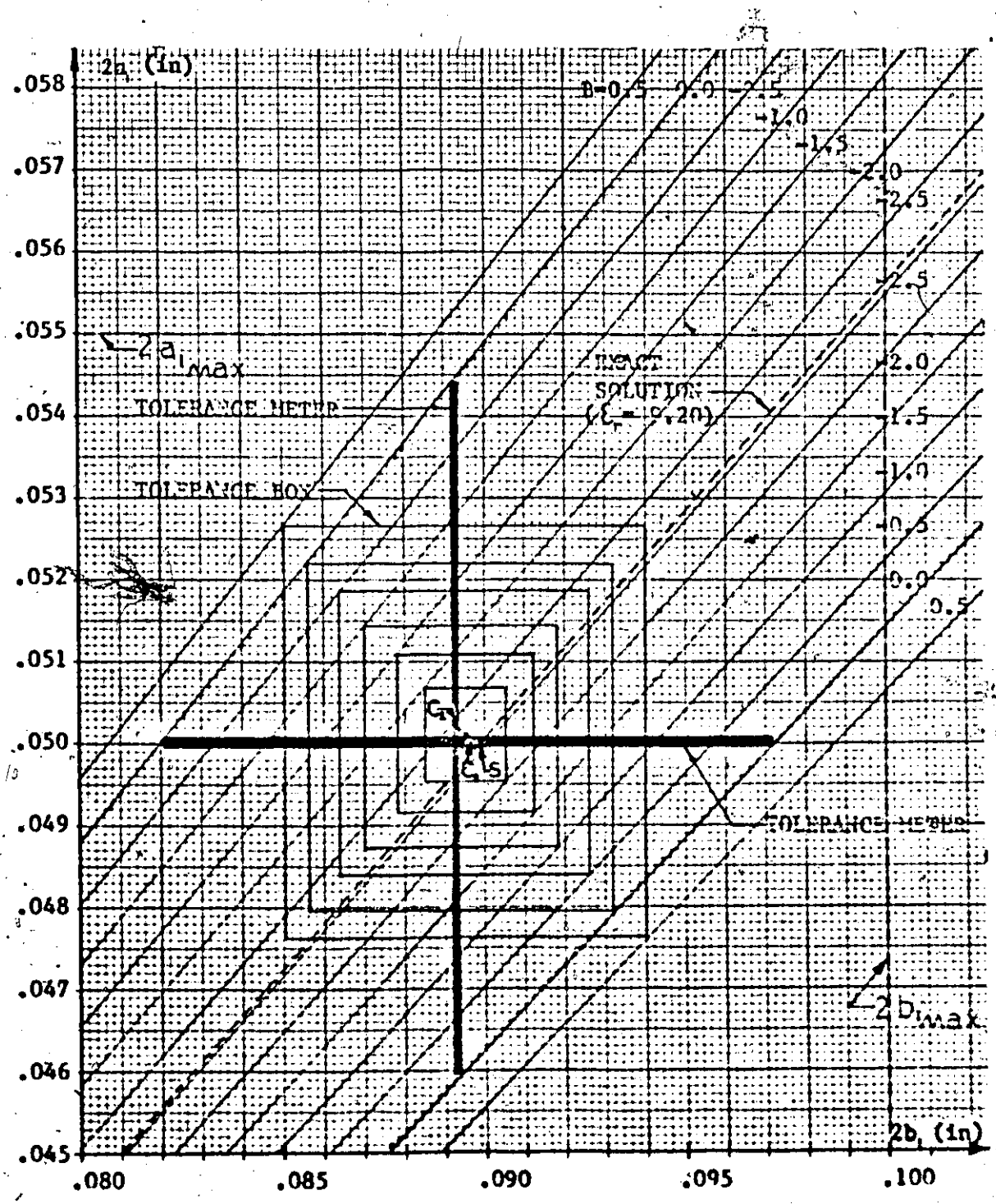

Figure 2.3-3: Optimum Tolerance Set and Corresponding Tolerance Boxes shown inside an Expanded View of R_A, with Balanced Upper and Lower Boundary Constraints on $2a_1$ and $2b_1$.

used with tolerances of 3.35% instead of 4.00%. That is, $2a_1$ should be manufactured to within ± 1.67 mils and $2b_1$ should lie within ± 3.01 mils if the characteristic impedance of all manufactured CPW's is to lie between 45 Ω and 50 Ω.

As a final comment, it should be remembered that the CPW theory of section 2.1 was assumed to be exact. The approximations in the theory suggest that significant experimental discrepencies from the theory may arise in surplus of the random fabrication errors and the random performance measurement errors. This was in fact the case, as will be seen in Chapter V. However, a means of compensation for this problem will also be discussed in the same chapter.

2.4 Losses in Thin Film Coplanar Structures

The theoretical calculation of losses at high frequencies is usually complicated [9], but for thin films of one skin depth or less, a simplifying approximation can be made. The theory presented here provides an easy method for calculating losses, for which experimental measurements give good correlation.

Only nonmagnetic dielectric materials will be considered. Therefore, only two types of losses in the dominant quasi-TEM mode need to be investigated. These are the ohmic losses in the thin metallic film of the CPW, and the dielectric losses in the substrate. Both of these losses are associated with the attenuation factor α; assuming small losses.

2.4.1 General Transmission Loss Considerations

For a general transmission line with distributed parameters R, L, C, and G, the propagation constant, γ, is given by

$$\gamma = \alpha + j\beta$$

$$= [\ (R + j\omega L) \cdot (G + j\omega C)\ ]^{\frac{1}{2}}\ (m^{-1}). \qquad (2.4\text{-}1)$$

The dielectric loss is associated with G and metallic loss with R. When the real and imaginary parts are separated, the attenuation constant and phase constant are found to be

$$\alpha = \left[\frac{1}{2} \{ [\ (R^2 + \omega^2 L^2\ )(\ G^2 + \omega^2 C^2\ )\ ]^{\frac{1}{2}} + RG - \omega^2 LC\ \} \right]^{\frac{1}{2}} \quad (Np/m) \qquad (2.4\text{-}2)$$

and

$$\beta = \left[\frac{1}{2} \{ [\ (R^2 + \omega^2 L^2\ )(\ G^2 + \omega^2 C^2\ )\ ]^{\frac{1}{2}} - RG + \omega^2 LC\ \} \right]^{\frac{1}{2}} \quad (rad/m) \qquad (2.4\text{-}3)$$

respectively, where ω represents frequency in radians per second. The normal or matched-line attenuation in decibels of a length of line x metres long is given by

$$A_o = 8.686\ \alpha\ x\ (dB) \qquad (2.4\text{-}4)$$

2.4.2 Skin Depth

The theoretical losses in thin film CPW's are found by an approximation based on knowledge of the skin depth within the frequency range of interest. The skin depth is given by

$$\delta_{sd} \triangleq \sqrt{\frac{2}{\omega \mu_o \sigma}} \qquad (2.4\text{-}5)$$

where ω represents frequency in radians per second, μ_o is the free space permeability ($4\pi \times 10^{-7}$ henry/metre), and σ represents conductivity in the metallic medium. Figure 2.4-1 shows a plot of the skin depth for aluminum, gold and copper from 100 MHz to 100 GHz. For aluminum at 100 MHz the skin depth is 81.15 kÅ, and at 10 GHz it is 8.115 kÅ, where 1 kÅ represents a thousand angstroms.

At d.c. the skin depth is infinitely thick, and at high frequencies it is usually smaller than the thickness of the conducting metal. However, when thin metallic films of 100 Å to 18,000 Å thickness are used at microwave frequencies, the skin depth can be larger than the thickness of the conducting metal.

2.4.3 Practical Loss Calculations for Thin Film Transmission Lines Operating in the 1-2 GHz Frequency Range

In this thesis aluminum conductors will be used in the investigation of CPW performance in the 1-2 GHz range of frequencies. The corresponding range of skin depth for aluminum for this frequency range is 25.8 kÅ to 18.2 kÅ. In the middle of this range the skin depth is

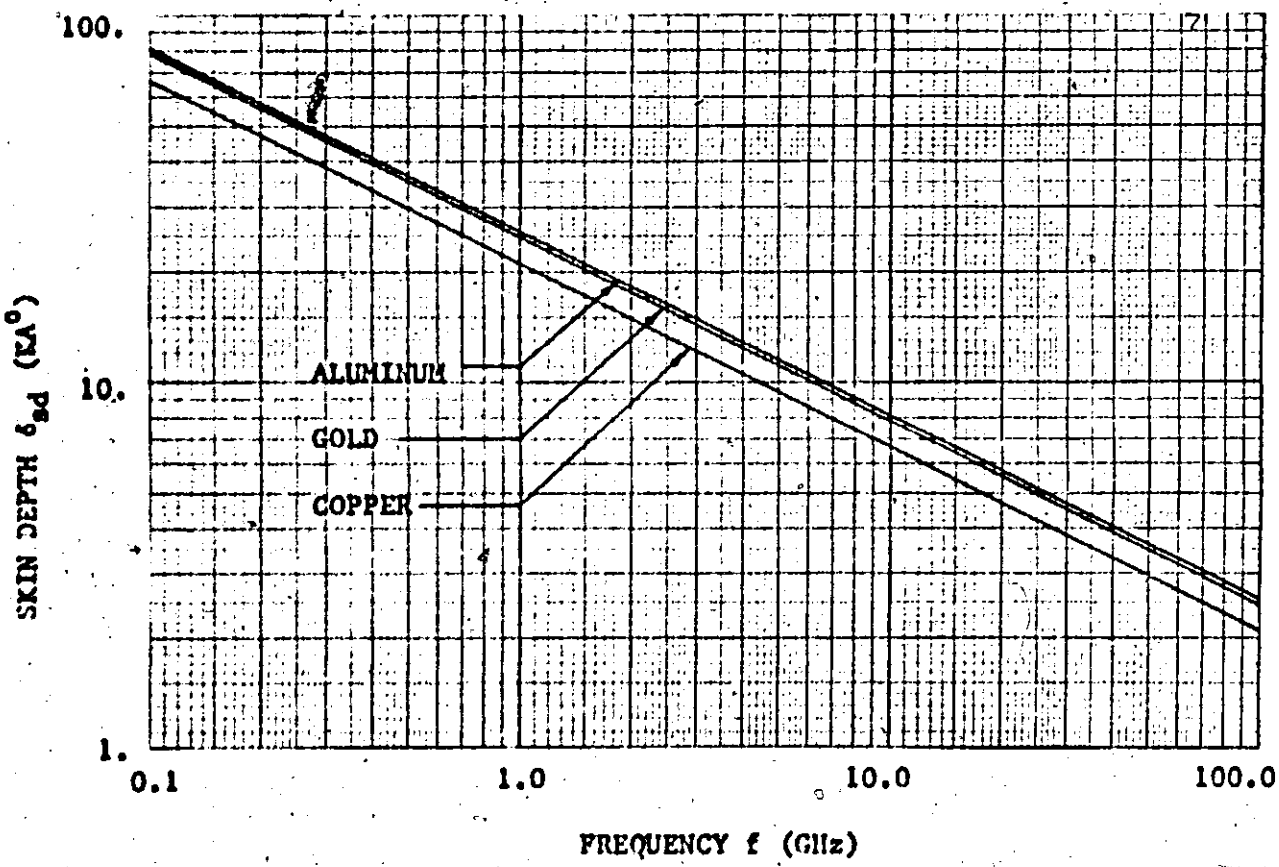

Figure 2.4-1: Plot of Skin Depth from .1 GHz to 100 GHz for Aluminum, Gold, and Copper.

21.0 kÅ. Herein, thin films of 18 kÅ or less will be used due to limitations in evaporation techniques, and therefore the thickness of the CPW's metallic conductors will always be less than the skin depth. As a result it is reasonable to assume that the d.c. resistance per unit length of transmission line is a valid simplifying approximation to R for use in the calculation of losses in thin film CPW's at frequencies less than 2 GHz. R is calculated from knowledge of the width and thickness of metallic film used.

For the above given conditions R is greater than the skin depth resistance per unit length, R_{sd}. For thin film thicknesses larger than one skin depth the value of R_{sd} should be used instead of the d.c. resistance per unit length for calculating transmission line loss. A plot of R_{sd} in ohms per metre vs frequency, from 100 MHz to 100 GHz, is shown in Figure 2.4-2 for aluminum, gold, and copper strips with widths of 50 mils and 100 mils. This information is redrawn in Figure 2.4-3 with more general units of ohms per square, which removes any dependence on strip width. These latter two graphs were intended for use in designing CPW's with thicker metallic conductors, but with regards to this thesis they have been used to determine a lower bound for measured losses when film thickness approaches and exceeds 1 skin depth.

The attenuation constant α was calculated from (2.4-2) as a function of R at 1.5 GHz, and then converted to A_o dB by (2.4-4). The conductance G was assumed to be zero here since alumina substrates with resistivity greater than 10^{14} were used, making G negligibly small. The resulting values of A_o were then normalized to the CPW wavelength λ, at

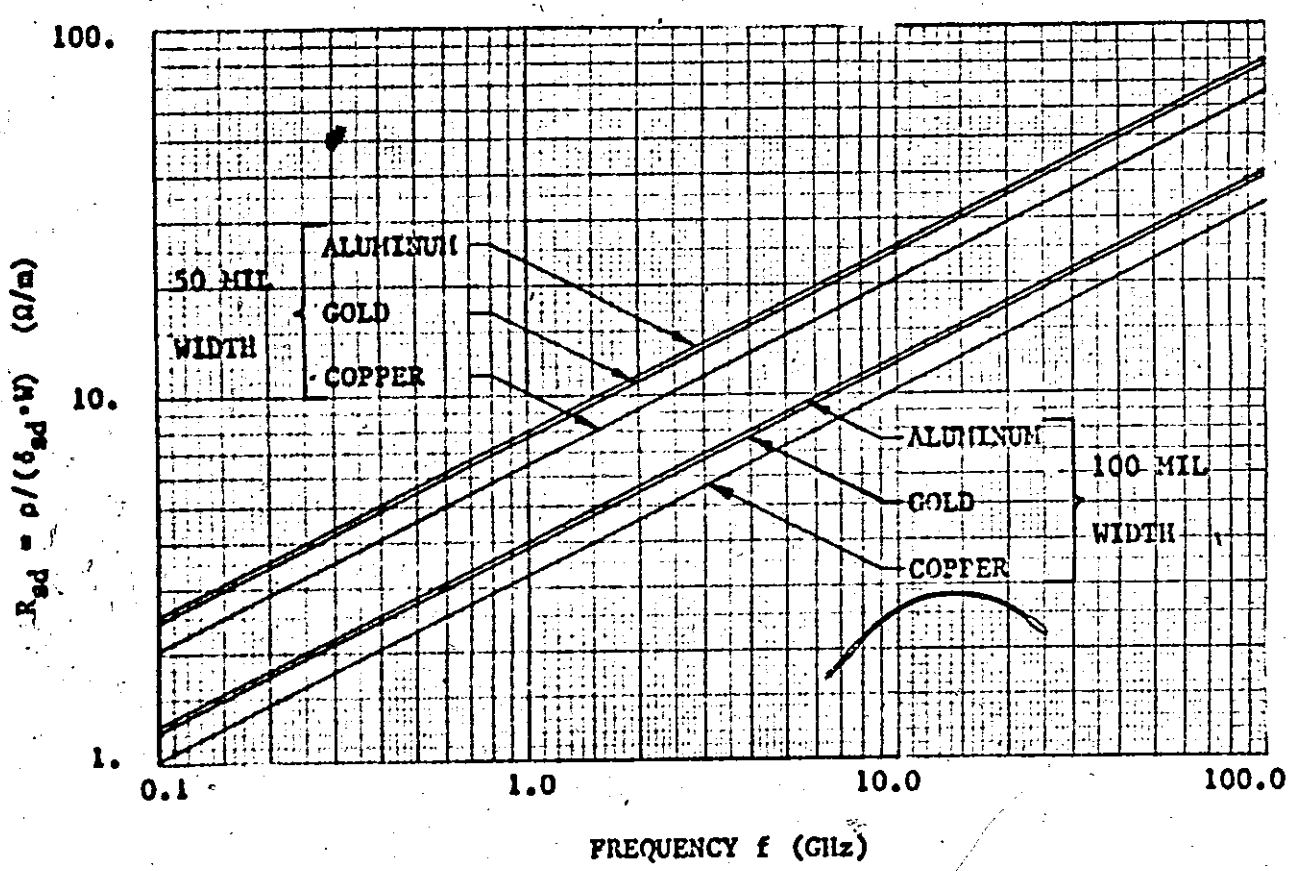

Figure 2.4-2: Skin Depth Resistance in Ω/□ vs Frequency.

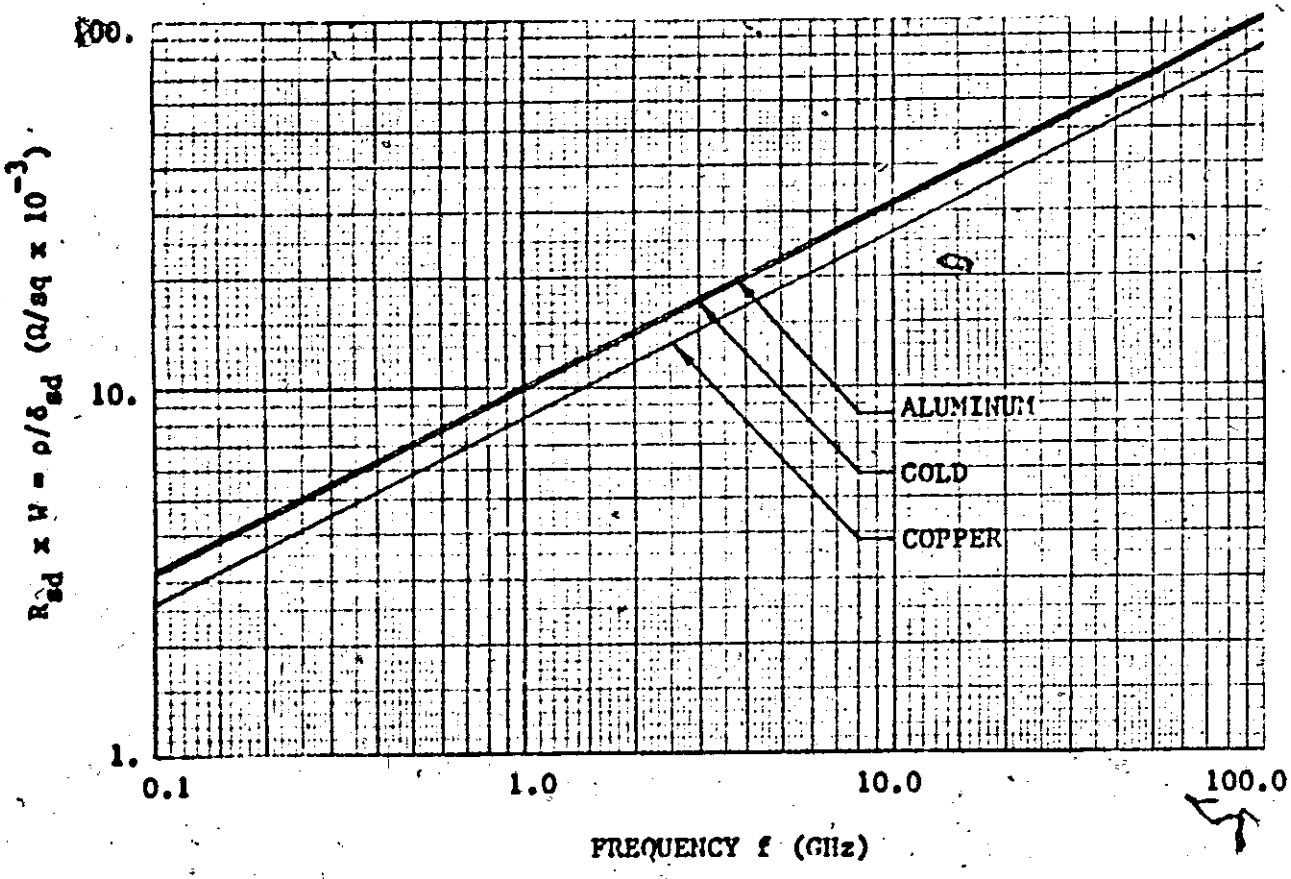

Figure 2.4-3: Skin Depth Resistance in Ω/sq vs Frequency.

1.5 GHz and plotted against R as shown in Figure 2.4-4. This data was then used to plot the loss A_0' in decibels per wavelength at 1.5 GHz against film thickness as in Figure 2.4-5. This was to serve as a simple check of experimental loss, measured as a function of thin film thickness.

The curves labelled "INFINITE GROUND PLANES" for aluminum, gold, and copper in Figure 2.4-5, represent the case where the loss in the ground planes is negligible compared to the loss in the center strip. The curves labelled "FINITE GROUND PLANES", and applied to aluminum only, are for real designs which will be presented in Chapter III. Series A and A- have 100 mil center strip widths, and series C and PCD- have center strips that are 50 mils wide. The figure then illustrates the effect of finite ground planes on the losses in a CPW. The total losses in the real designs were calculated by adding the ground plane distributed resistance to the center strip distributed resistance and then calculating α and A_0'. Note that for both designs, the losses are approximately the same.

2.4.4 Conclusions

In summary, a simple loss theory was applied to thin film coplanar structures with assumed d.c. resistance in the metallic film and with dielectric losses neglected for alumina substrates. All relevant curves were simple straight line functions plotted on a "log-log" basis which allowed a wide range of information to be displayed on each graph. The effect of the losses in the ground planes was also predicted by adding the ground plane resistance per metre to the center strip resistance per

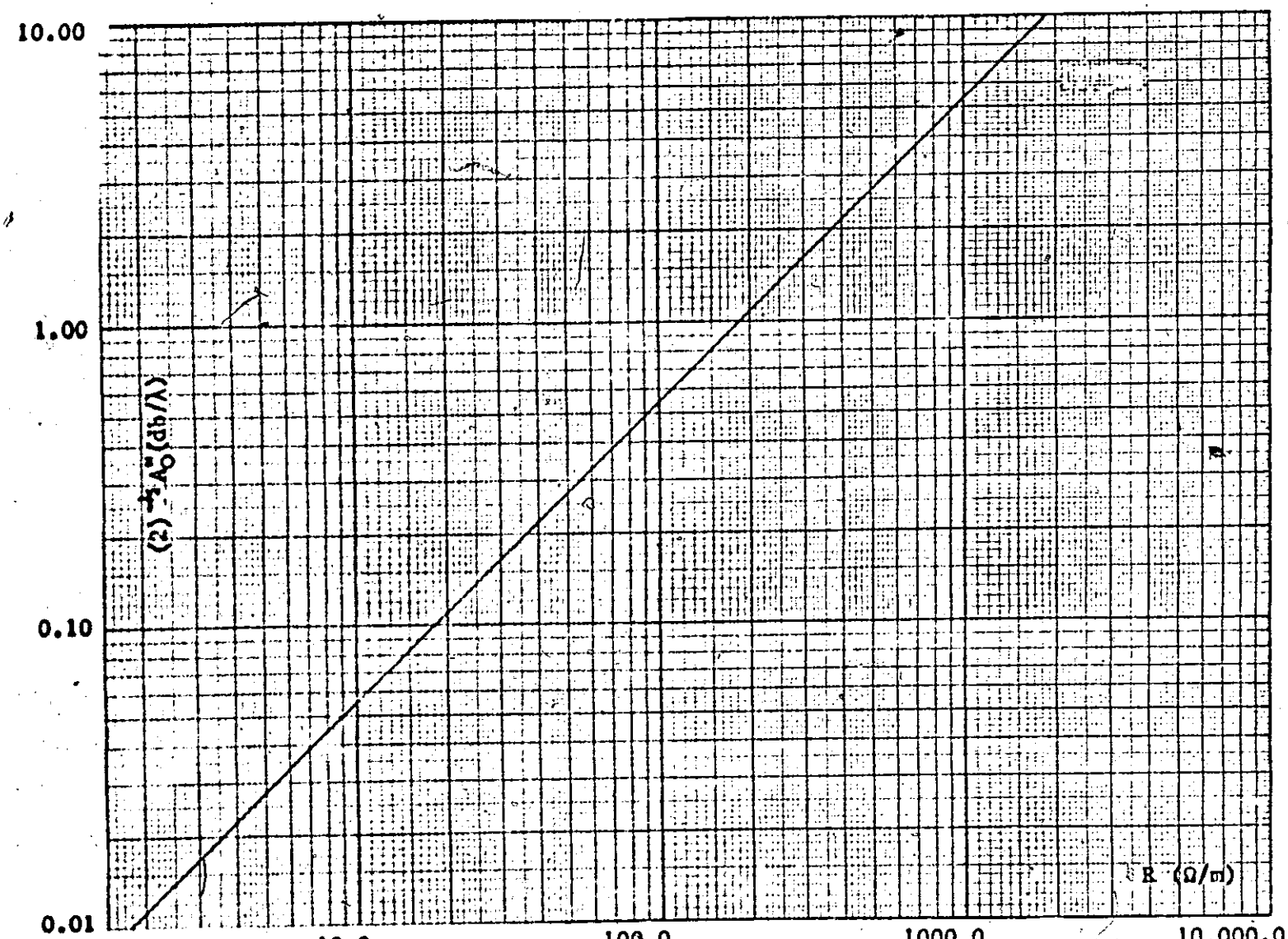

Figure 2.4-4: Loss in db/λ at 1.5 GHz vs Resistance per Unit length (Ω/m).

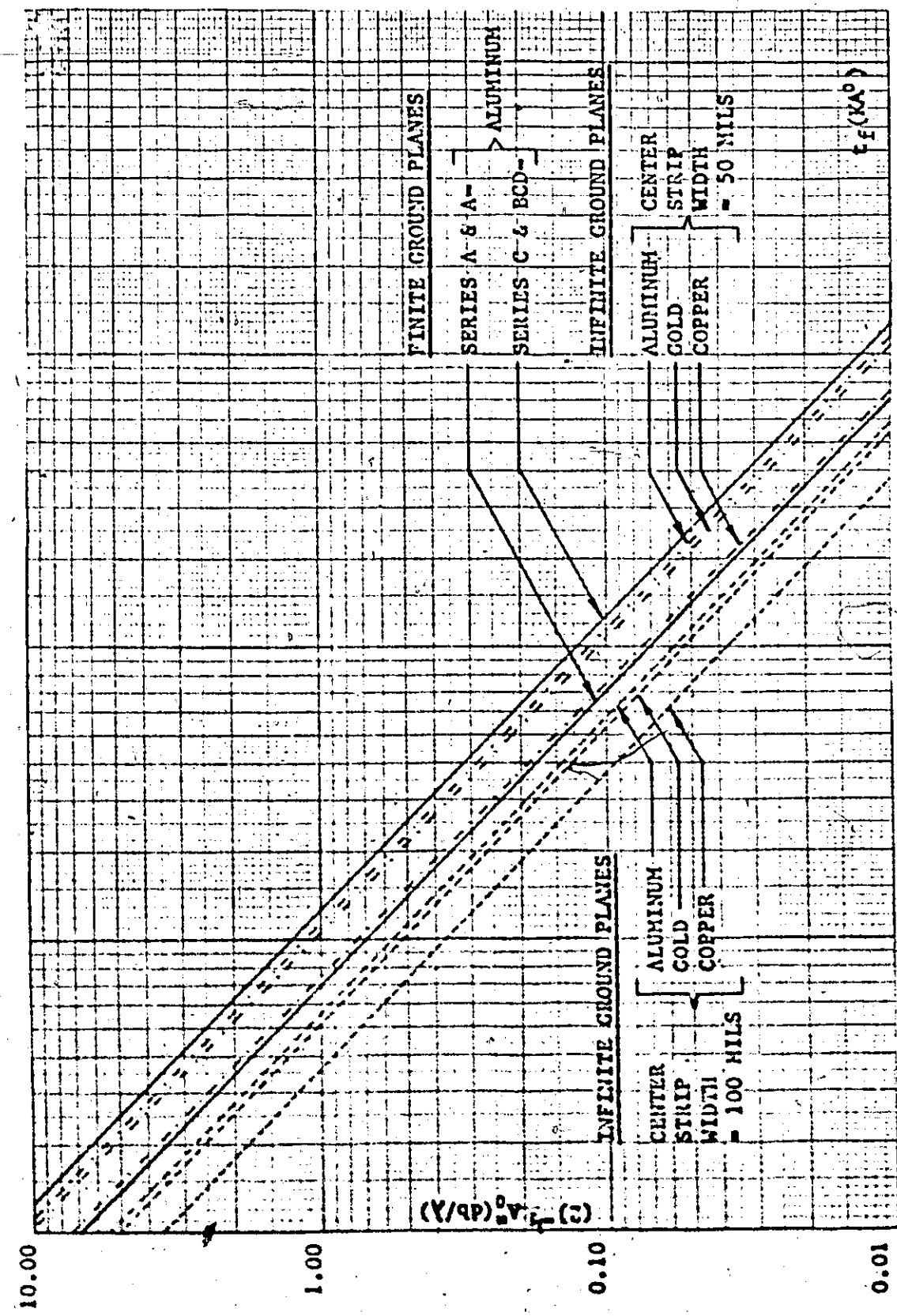

Figure 2.4-5: Theoretical Thin Film CPW Losses at 1.5 GHz vs. Film Thickness (KA^o).

metre. As will be seen in Chapter V, "good experimental agreement" with this theory was obtained within a 22% range of uncertainty.

CHAPTER III

FABRICATION AND MOUNTING OF THIN FILM COPLANAR TRANSMISSION LINES

3.0 Introduction

The study of the fabrication of microwave integrated circuits (MIC) is an involved subject. Initially, this chapter briefly surveys this field to indicate where the fabrication of thin film coplanar waveguides and the related materials fit in with respect to other widely accepted techniques and materials used in MIC fabrication. As it turns out, the chosen techniques for this thesis form a subset of a more general technique in current use.

Photographic techniques are discussed next in section 3.2 where the merits of a "masking" technique applied in a vacuum evaporation unit are compared with "direct photographic etching", which is better for thick film techniques. Methods used for vacuum evaporation are discussed in section 3.3, and the various designs for verifying and expanding the theory of chapter II are presented in section 3.4. Last, but not least, the techniques for achieving effective electrical contacts in the mounting of coplanar waveguides are given in section 3.5, both for permanent industrial use and repeated experimental applications. This includes a new and effective experimental mount designed by the author.

3.1 Choice of Conductor Materials and Substrates

The choice of materials for microwave integrated circuits is an extremely important area of study. Some pertinent information on these materials is presented in surveys on microwave integrated circuits conducted by M. Caulton and H. Sobel: references [2] and [3]. Another excellent evaluation is found in reference [4], where F. Z. Keister concentrates mainly on available materials. Keister evaluates substrate materials of varying purities and surface finishes, including aluminas, beryllias, quartz, and glass. He also appraises conductor materials which include silver, copper, gold, and aluminum. Herein important aspects such as power loss, adherence of metallic films to substrates, attainment of design specifications, durability, and ease of fabrication will be discussed in relation to the aforementioned references.

3.1.1 Substrate Materials

According to Keister, substrates for microwave integrated circuits should have the following ideal properties:

1) high relative dielectric constant,
2) low dissipation factor or loss tangent and a corresponding high resistivity,
3) the dielectric constant should remain constant over the frequency range of interest as well as over the temperature range of interest,
4) high purity,
5) high surface smoothness and constant thickness,

6) high dielectric strength,

7) High thermal conductivity.

The least important of these items are 1) and 4). First of all, too high a dielectric constant will produce a very slow wave and a very small wavelength. This can excite higher order surface waves causing dispersion to appear at lower frequencies, as discussed in section 2.1 of Chapter II. Large relative dielectric constants are also more temperature sensitive. One might therefore have to select a moderately small relative dielectric constant not only as a compromise between an acceptable dispersion characteristic and a low phase velocity, but also for temperature stability [3]. Also a substrate of extremely high purity is often not as essential as a homogeneous substrate. For example, 96% alumina is just as useful as 99.5% alumina providing both are homogeneous and have smooth surfaces. On the other hand, a low loss tangent and a stable relative dielectric constant are obvious necessities. Obtaining a uniform thickness in combination with a high surface smoothness helps to ensure precise device geometry. This same planar smoothness simultaneously contributes to the adherence of metallic films onto the substrate and reduces RF conductor loss [3]. Finally, a high thermal conductivity leads to temperature stability in high power devices by preventing the microwave integrated circuitry from heating up to high temperatures at which circuit performance no longer lies within design specifications.

Table 3.1-1 shows a list of the five substrate materials assessed by Keister taking into account a wide selection of vendors, purities, and surface finishes. A quick study reveals that

Substrate Material	Purity (%)	Substrate Thickness (cm)	(mils)	Surface Finishes (μ m)		(μ in)	
Alumina (Al_2O_3)	96.0	0.064	25	0.62		24.4	
Alumina (Al_2O_3)	99.5	0.064	25	0.20	0.25	7.88,	9.84
(from 3 vendors)				0.40	0.50	15.75,	19.69
Alumina (Al_2O_3)	99.6	0.064	25	0.05	0.25	1.97,	9.84
Alumina (Al_2O_3)	99.7	0.064	25	0.40		15.75	
Alumina (Al_2O_3)	99.9	0.064	25	0.05	2.87	1.97,	113.
Glazed Alumina	96.0	0.076	30	0.025		0.99	
Sapphire (from 2 vendors)	100.0	0.051	20	0.005		.20	
Pervllia (BeO) (from 2 vendors)	99.5	0.064	25	0.45		17.72	
Glazed Pervllia	99.5	0.074	29	0.025		0.99	
Quartz (S_1O_2)	99.9	0.102	40	<0.006		<0.24	
Borosilicate Glass	alkali-free	0.076	30	<0.006		<0.24	

Table 3.1-1: Keister's Listing of Substrate Materials Including a Wide Selection of Vendors, Purities, and Surface Finishes.

the top five entries in the table give unglazed alumina with five different purities ranging from 96% to 99.9%. All of these five examples are 25 mils thick but their surface finishes differ from nominal values as low as 2 microinches to as high as 113 microinches. However the next entry, 96% glazed alumina, has a one microinch finish. This is a typical example of how a high resistivity glaze can be used

to improve the surface finish of a substrate. Notice that the high purity alumina substrates generally have a good surface finish in comparison to the 96% alumina substrates. Caulton states that "the less pure aluminas are rougher due to the impurities" [3]. Yet, the application of a glaze to the 96% alumina substrates improves the surface finish by a ratio of approximately 25 :1.

The other entries in the table include sapphire, glazed and unglazed beryllia, quartz and borosilicate glass. All are of extremely high purity and all have a surface finish as low as 0.2 microinches, except for beryllia which compares closely to alumina as far as surface smoothness is concerned. A surface finish of 17.72 microinches is shown for unglazed beryllia and a 1 microinch finish is shown for glazed beryllia. Again, the glaze makes a significant improvement; this time by a ratio of 18 :1. It is quite apparent then that the surfaces of alumina and beryllia substrates can be made almost as smooth as the surfaces of sapphire, quartz, and borosilicate glass if a glaze is used.

Since the surface smoothness does not necessarily determine the choice of the best of the above substrate materials, how then do these materials compare in terms of the relative dielectric constant of the material, and losses in it? Table 3.1-2 illustrates limited data for these two properties for materials surveyed by Keister [4]. The values of relative dielectric constant shown in parentheses were not taken from data sheets, but were measured at Hughes Aircraft at 9.28 Ghz by the resonant

Substrate Material	Relative Dielectric Constant at 25°C		Dissipation Factor Tan δ at 25°C	
	10 GHz	25 GHz	10 GHz	25 GHz
96% Alumina	8.9 (9.2)	8.7	0.0006	0.0007
99% Alumina	9.0 (9.7)	8.9	0.0001	0.0003
99.5% Alumina	9.5	9.0	0.0002	0.0001
99.9% Alumina	9.9		0.000025	
99% Beryllia	6.1	6.0	0.0001	0.004
99.5% Beryllia	6.1 (6.8)	6.0	0.0001	0.004
Quartz	3.78	3.78	0.0015	
Borosilicate Glass	5.74		0.0036	
Sapphire	11.0		0.0002	

Table 3.1-2 : Keister's Tabulation of the High Frequency Properties of Substrate Materials Taken from Vendor's Data Sheets or the Technical Literature.

cavity dielectrometer technique. They proved to be slightly higher than the corresponding values taken from data sheets. Table 3.1-2 also illustrates a decrease in the value of relative dielectric constant with an increase in frequency from 10 GHz to 25 GHz for alumina, beryllia and quartz. Data was not available for borosilicate glass and sapphire at 25 GHz. The table indicated that a decrease in the relative dielectric constant ϵ_r, of at least 5% could occur with increasing frequency over a 15 GHz bandwidth. By linear interpolation, one would expect an increment in ϵ_r of -1/3% or less over a one GHz bandwidth in the frequency range from 10 GHz to 25 GHz.

In this thesis, experimental measurements, were made within the 1-2 GHz range. Though data for ϵ_r was not available for this frequency range it was expected that a decrease in ϵ_r over this bandwidth of less than 2/3% would be reasonable for these lower frequencies. This idea was supported with data for alumina substrates from Coors Porcelain Co., which indicated that from 1 KHz to 0.1 GHz the value of ϵ_r was constant. Since ϵ_r decreased approximately by 1/3% per 1 GHz increase in bandwidth above 10 GHz, some frequency dependence of ϵ_r might be expected between .1 GHz to 10 GHz, but it probably would be less than the variation found above 10 GHz.

What is considered a good value for ϵ_r? Caulton [3] states that "the dielectric constant ϵ_r should be in the 8-16 range for normal integrated circuit size reduction" for the same reasons discussed at the beginning of this section. All values of ϵ_r in Table 3.1-2 fall within this category. In this table, sapphire gives a slightly better circuit size reduction than alumina.

Losses are also important in the selection of a substrate. According to Caulton [3] "glass is the most lossy and has the poorest thermal conductivity, while beryllia, with one of the highest thermal conductivities, is difficult to handle. Table 3.1-2 shows glass to be the most lossy too. Quartz is about half as lossy, and alumina, sapphire and beryllia are even less lossy by a factor of 10.

It then appears from the foregoing discussion that sapphire and alumina are some of the best choices in substrate materials for microwave integrated circuits. Rutile, used by Wen, is not shown in Table 3.1-2, but is listed in [2] and [3] as having a tan δ of 0.0004 and a relative dielectric constant of 100 at 10 GHz. These references also show it to have a surface 5 times rougher than 96% unglazed alumina. However, in some applications such as Wen's nonreciprocal gyromagnetic devices, the high ϵ_r value is an asset. In any case, a glaze could perhaps improve the surface of rutile as well.

Herein glazed 96% alumina substrates from Coors Porcelain Co. were selected for the fabrication of coplanar waveguides because of the aforementioned attributes. The substrate dimensions were 1" x 1" x .025". Tables 3.1-3 and 3.1-4 contain the mechanical, thermal, and electrical properties of unglazed Coors alumina in detail. The properties of the glaze which furnishes a 1 μin finish are given in Table 3.1-5. The glaze has a high electrical resistivity which is comparable to that of alumina, and a high softening point of 775° C. The maximum temperature quoted for alumina is 1700° C. In surplus, alumina substrates have the advantage of being compatable with aluminum films. One must then ask if any other conductor materials are better than aluminum for use with alumina substrates.

PROPERTY		UNITS	ADS-96F NOMINALLY 96% Al_2O_3 For Use in Thick-Film Circuits. Surface <25μin CLA. (As-Fired)
SPECIFIC GRAVITY			3.75
WATER ABSORPTION			None
PERMEABILITY			Gas-Tight
FLEXURAL STRENGTH	Typical, 70°C	psi	51,000
COMPRESSIVE STRENGTH	Typical, 70°C	psi	>300,000
HARDNESS	Typical	Rockwell 45N	79
COLOR			White
SURFACE FINISH	As-Fired	Microinches (CLA)	<25
MAXIMUM TEMPERATURE	For No-Load	°C(°F)	1700(3100)
THERMAL CONDUCTIVITY	20°C 100°C 400°C	g-cal/cm²/cm/s/°C	0.063 0.048 0.029
THERMAL COEFFICIENT OF EXPANSION	25-200°C 25-500°C 25-800°C 25-1000°C	PER °C	5.9×10^{-6} 7.1×10^{-6} 7.8×10^{-6} 8.1×10^{-6}
VOLUME RESISTIVITY	25°C 300°C 700°C	Ω/cm/cm²	$>10^{14}$ 2.0×10^{12} 1.6×10^{7}
TE VALUE	Temp. when Resistivity = 1 MΩ-cm	°C	925
DIELECTRIC STRENGTH	0.250" Thick 0.025" Thick	Volts/Mil (60 c/s ac, avg rms)	225 500
DIELECTRIC CONSTANT (Relative Permittivity)	1 kHz, 25°C 1 MHz, 25°C 100 MHz, 25°C		9.2 9.2 9.2
LOSS TANGENT (Dissipation Factor)	1 kHz 1 MHz 100 MHz		0.0010 0.0004 0.0004
LOSS FACTOR	1 kHz 1 MHz 100 MHz		0.009 0.004 0.004

Table 3.1-3: Mechanical, Thermal, and Electrical Properties of COORS 96%, Unglazed Alumina Substrates.

PROPERTY		UNITS	ADS-995 NOMINALLY 99.5% Al_2O_3 For Use in Thick-Film Circuits. Surface ≤25μin CLA. (As-Fired)
SPECIFIC GRAVITY			
WATER ABSORPTION			
PERMEABILITY			
FLEXURAL STRENGTH	Typical, 70°C	psi	68,000
COMPRESSIVE STRENGTH	Typical, 70°C	psi	>400,000
HARDNESS	Typical,	Rockwell 45T	84
COLOR			White
SURFACE FINISH	As-Fired	Microinches (CLA)	<10
MAXIMUM TEMPERATURE	For No-Load	°C(°F)	1750(3182°F)
THERMAL CONDUCTIVITY	20°C 100°C 400°C	g-cal/cm²/cm/s/°C	0.075 0.065 0.028
THERMAL COEFFICIENT OF EXPANSION	25-200°C 25-500°C 25-800°C 25-1000°C	PER °C	6.0×10^{-6} 7.3×10^{-6} 7.9×10^{-6} -
VOLUME RESISTIVITY	25°C 300°C 700°C	Ω/cm/cm²	$>10^{14}$ 10^{13} 1.0×10^{9}
TE VALUE	Temp. when Resistivity = 1 MΩ-cm	°C	1100
DIELECTRIC STRENGTH	0.250" Thick 0.025" Thick	Volts/Mil (60 c/s ac, avg rms)	225 550
DIELECTRIC CONSTANT (Relative Permittivity)	1 kHz, 25°C 1 MHz, 25°C 100 MHz, 25°C		9.8 9.8 9.8
LOSS TANGENT (Dissipation Factor)	1 kHz 1 MHz 100 MHz		0.0002 0.0001 0.0001
LOSS FACTOR	1 kHz 1 MHz 100 MHz		0.002 0.001 0.001

Table 3.1-4: Mechanical, Thermal, and Electrical Properties of CERAMS 99.5%, Unglazed Alumina Substrates.

PROPERTY		UNITS	G-232 GLAZE
COMPOSITION: Lead Aluminum Silicate (Alkali Content = 3%)			
SOFTENING POINT		°C(°F)	775(1427)
SURFACE FINISH	As Fired	Microinches CLA	1
THERMAL COEFFICIENT OF EXPANSION	25-500°C	PER °C	6.3×10^{-6}
SURFACE RESISTIVITY	25°C	Ω/Square	$>10^{15}$
	200°C		1.8×10^{13}
	300°C		2.0×10^{11}
	400°C		4.0×10^{9}

Table 3.1-5: Properties of COORS G-232 Glaze.

3.1.2 Conductor Materials

According to Keister [4], the conductor materials used for microwave intergated Circuit (MIC) applications should have the following properties:

1) high conductivity,
2) small temperature coefficient of resistance,
3) good adhesion to the substrate,
4) good etchability and solderability,
5) easily deposited or electroplated.

Caulton [3] adds that a small linear thermal expansion coefficient is necessary for MIC's in order to maintain pattern definition during temperature fluctuations that occur in the fabrication of such devices. He also states that only several skin depths of conductor material are required, whereas Keister claims that at least 4 skin depths are necessary to include 98% of the current that would be obtained for an infinitely thick conductor. In this thesis, film thicknesses of one skin depth or less will be used to investigate the effect of film thickness on losses and characteristic impedance of a coplanar waveguide.

Table 3.1-6 is a compilation of information on conductor materials for MIC applications [2], [3], [36]. The table is divided into four groups of metals. Group I contains excellent conductors which can be deposited by a number of methods as well as photoetched.

GROUP NO.	CONDUCTOR MATERIAL		BASIC PROPERTY	RESISTIVITY @ 20°C (μΩ-cm)	TEMPERATURE COEFFICIENT (μΩ-cm/°C)	SKIN DEPTH AT 10 GHz (kÅ)	THERMAL CONDUCTIVITY @ 20°C (W/cm-°C)	LINEAR THERMAL EXPANSION @ 20°C (/°Cx10⁶)	ADHESION TO DIELECTRIC
I	SILVER	Ag	GOOD CONDUCTORS	1.62		6.41	4.08	18.9	POOR
	COPPER	Cu		1.72	0.0039	6.61	3.94	16.5	POOR
	GOLD	Au		2.44	0.0034	7.86	2.96	14.2	POOR
	ALUMINUM	Al		2.62	0.0039	8.11	2.18	22.9	FAIR
II	CHROMIUM	Cr	REDUCING AGENTS (GLUES)	(12.9)		18.08	0.69	6.2	GOOD
	TANTALUM	Ta		13.1	0.003	18.22	0.54	6.6	GOOD
	TITANIUM	Ti		(81.5)		45.44		8.5	GOOD
III	MOLYBDENUM	Mo	REFRACTIVE METALS	4.77	0.0033	10.99	1.46	4.9	FAIR
	TUNGSTEN	W		5.48	0.0045	11.78	1.99	4.3	FAIR
IV	PLATINUM	Pt	BARRIER METALS	10.5	0.003	16.31	0.69	8.9	
	PALLADIUM	Pd		10.8	0.0033	16.54	0.70	11.8	

Table 3.1-6: Properties of Conductor Materials for Microwave Integrated Circuits.

All but aluminum have poor adhesion to dielectric. Group II shows three poorer conductor metals that are commonly used as a type of "glue" which binds the good conductors of group I to a dielectric. The "glue- metal" films are really reducing agents which are oxidized in a vacuum deposition unit at the metal-dielectric interface when the substrate is hot. The top surface of the "glue-metal" does not oxidize, providing the vacuum is not broken, and can form a good chemical bond with the metals of group I. Chemical bonds are necessary in this type of work [3] since mechanical bonds require a rough surface and this defeats the purpose of creating metallic planes with precisions as high as 1 μin. Group II metals all have good adhesion to dielectrics. The group III metals in the same table are simply refactive metals which are fair conductors. They also have fair adhesion to dielectrics. Finally, thin films of the barrier metals of group IV are used inbetween the group I and II metals to prevent them from diffusing into each other to form alloys.

All of these materials can be deposited by sputtering, though this technique is especially important for group III metals. Groups I, II, and III metals can also be vacuum evaporated from a source heated by an electron beam. Vacuum evaporation from a resistive boat source applies to groups I and II only.

In general, the layers of material involved in the fabrication of a microwave integrated circuit are statified in the following order:

1) substrate,

2) group II oxide bond with substrate,

3) remaining non-oxidized group II metal,

4) thin layer of barrier metal,

5) a thin vacuum deposited layer of group I metal, used here to seed an electroplating process,

6) an electroplated layer of the same group I metal of desired thickness, applied before or after photo resist is used.

Of course, variations on this pattern can be used. One may wish to eliminate the electroplating process altogether and simply deposit the conductor to the desired thickness without breaking the vacuum However, this does limit the thickness to be deposited in small vacuum coating units. For some experimental purposes the thin layer of barrier metal can be left out as well. Also, aluminum adheres quite well to alumina substrates. The glue metal can then be eliminated for these two materials, which simplifies the fabrication process further.

3.1.3 Conclusion

The foregoing discussion on substrate and conductor materials was by no means exhaustive and was only introduced briefly to show the relationship of the materials used in this thesis to some other widely accepted materials and techniques. Aluminum was selected in conjunction with alumina substrates because of the compatability of these two excellent materials. This led to a fairly simple procedure for fabricating CPW's as will be discussed in section 3.2.

3.2 Masking and Etching Photographic Techniques

The techniques for fabricating MIC's are numerous and complicated and so only the two techniques attempted for this thesis will be discussed herein. These will be labelled "Masking" and "Direct Photographic Etching". A comparison will be made between them to show that direct photographic etching is not only cleaner and simpler to use, but gives the best results as well.

3.2.1 Preliminaries

Before either technique was employed four preliminary steps were considered:

1) design phase,
2) cutting the design pattern accurately out of a sheet of rubilith material on a scale of 20x,
3) photoreduction of this rubilith pattern by a ratio of 20:1,
4) developing the picture and making a positive from the negative if necessary.

The design phase will be treated in section 3.4, so let us look at the rubilith problem.

A sheet of rubilith is made up of 2 layers of material pressed together. One of these layers is a thin red film of sticky elastic material which is opaque to yellow light and which adheres to a second layer of transparent plastic. The plastic gives body to the rubilith and allows light to be transmitted through it where the red elastic coating has been peeled off. In step two the desired

design pattern was cut on the side of this thin red coating with a fine blade. In this case, use of a 1200 x 1200 mm Haag Street Coordinatograph enabled dimensional accuracies of 0.05 mil to be obtained. The red coat was then peeled off the plastic sheet in regions where light transmission to a camera was desired. Yellow light was used to illuminate the rubilith pattern so that its red areas actually appeared black to the camera.

The camera that was used to make negatives of the rubilith pattern was an HLC Mikrokon 1700 camera. A calibration procedure enabled it to be positioned accurately for a 20:1 picture reduction. From the accuracy of the plotting table it was estimated that the resulting photograph of the design pattern had dimensions containing only a 0.1 mils of error. These errors were checked experimentally and will be discussed in section 3.4.

Kodak high resolution 2" x 2" photographic plates (No. KP 58-751 A) with a development time of 5 min. were used to make the above negatives. The exposure time was set on the Mikrokon 1700 at 10 seconds. Positives were made from the negatives with Kodak high resolution 4" x 5" film (No. 50-343), when required.

With these preliminaries completed, we could proceed to one of two relatively simple fabrication techniques; masking and direct photographic etching. Our aim was to fabricate 1" x 1" x .025" CPW samples with high precision, ease, and reproducibility. In this respect, direct photographic etching was definitely the best method to use.

3.2.2 Masking

This technique simply involves placing a negative metallic replica of a given design pattern in close contact with a given substrate and evaporating a desired material through this mask inside a vacuum chamber. The masks are easily etched out of thin metallic copper sheets 5 mils thick but undercutting and perferential etching in sharp corners of the mask are quite apparent problems. Geometrical deviations of 7 or 8 mils in such corners are not uncommon. Rough edges with deviations of 3 or 4 mils can also be a problem if the etchant is not strong enough to eat through the copper within 5 minutes or less. The direction and degree of agitation also affects geometrical precision, and so the creation of an acceptable mask tolerance wise is dependent upon trial and error procedures.

Another significant problen that occurs with masking techniques is a phenomena called"specular Migration". A hot metal vapor source in a vacuum coating unit directs energetic particles of metal in a fairly steady stream towards the mask and substrate target. The mask is positioned as close to the surface of the substrate as possible in order to reduce specular migration but it cannot be eliminated completely when very hot vapor sources are used. The reason for this is that the molecules of metal for such a source contain a great deal of energy when they strike the substrate

surface or any other surface in the vacuum chamber, and either migrate about on these surfaces in order to expend their surplus energy or are vaporized once more. The very fine separation between the substrate and mask allows some of these hot molecules of metal to find their way under the mask in a random fashion. Also, in such an active bombardment of metal molecules, secondary sources of vapor, including the substrate surface, which are not as directional as the primary vapor source, actually compound the problem. Exact delineation of mask patterns by vacuum deposition is then only possible with moderately hot vapor sources. This in turn limits the thickness of material which is deposited on the substrate since then the primary stream of vapor is less directional and sees a wider target area. A great deal of the metal vapor from the source is then wasted on the internal surfaces of the vacuum chamber at low evaporation rates.

It was found that accurate films of 1 kÅ to 2 kÅ could easily be obtained by using masking techniques. At 1.5 Ghz this was at best 1/10 of a skin depth of metal, and so it was fine as a seed material for electroplating, but for a finished sample with low losses it was not acceptable. With much experimentation and some luck in placing the mask in closer contact with the substrate, thicker films with little specular migration were deposited, but this short technique should not be recommended for any industrial purpose other than producing a seed layer for electroplating.

The masking procedure is as follows:

1) prepare a clean dry copper sheet 5 mils thick,

2) apply Shipley's AZ-1350 positive photo resist in a puddle covering the copper sheet,

3) spin the copper sheet slowly at first to obtain a uniform layer of photo resist,

4) spin quickly to help dry the photo resist,

5) pre-bake this copper sheet at 80° C for 15 minutes to complete the drying process,

6) apply the positive or negative photograph discussed in the preliminaries in close contact with the dry photo resist,

7) expose at a distance of one foot from an ultraviolet light source for 5 minutes and develop the photo resist pattern,

8) post-bake at 100° C for at least one hour,

9) to protect the back of the copper sheet coat it with a carbon tetrachloride-Apeizon wax solution and a let dry 1/2 hour,

10) etch away unwanted copper with a warm saturated solution of $FeCl_3$, (if the solution has a temperature $\geq$ 85° C the wax will melt)

11) remove unwanted photo resist with acetone,

12) apply the mask to the alumina substrate with a mask holder and place in a vacuum coating unit,

13) evaporate aluminum metal through the mask.

This evaporation was performed in an Edwards High Vacuum Coating unit (Model 12E3) containing four resistance boat vapor sources. As for the wax used in step 9), Apiezon Wax Sticks (No. 14-638-25c) which dissolve easily in carbon tetrachloride were used. The softening point of the dry wax was 85° C and its vapor point was 180° C. With carbon tetrachloride as a solvent, the solution dried quickly.

The Shipley AZ-1350 positive-working photo resist mentioned in step 2) is sensitive to ultraviolet light in the 3.0 to 4.5 kÅ range and must be used under yellow light. It has a resolution capability of 6 kÅ or .02362 mils. This is better than the photographic error of .1 mil in the preliminaries. Though the surface to which the photo resist is applied must be very clean to avoid pin holes, some of its advantages are as follows:

a) dust particles on the photograph do not result in pin holes on the photo resist pattern,

b) developing is clean with no remaining residues,

c) exposure and development time limits are not critical,

d) during the development process the photo resist is unaffected by humidity and temperature,

e) it has aqueous developer and remover solutions,

f) during the development process the photo resist is removed within seconds,

g) the photo resist has a high solids content,

h) the undeveloped photo resist is insensitive to gold fluorescent light for hours,

i) the photo resist image does not swell or soften during development,

j) it can be applied to virtually all metals, glass, ceramics, etc.,

k) multiple exposures are practical because of its positive working characteristics and so multiple depth etching can be performed without the application of multiple photo resist coats,

l) the photo resist is resistant to most common etchants used for semiconductor manufacture, and this resistance is increased by post-baking,

m) though exposure to white light causes problems, coated substrates can be stored in the dark for indefinite periods of time.

The coplanar waveguides fabricated via masking techniques were not satisfactory with respect to square corners and straight lines, specular migration behind the mask, and the thickness of films which could accurately be deposited. It was also found that dust on the copper sheet or in the photo resist before or during the application of the photo resist led to occasional pin holes in the resulting mask. Hence a dust free environment was an asset for the fabrication of the masks. Also, spotless substrates were required since moisture or dust could destroy the adhesion capability of aluminum to alumina.

3.2.3 Direct Photographic Etching

The direct photographic etching process is clean, easy to use, and gives excellent results. The basic steps are as follows:

1) evaporate the desired aluminum film thickness onto dry alumina substrates 1"x1"x.025" inside a vacuum coating unit,
2) apply Shipley's AZ-1350 positive photo resist in a puddle which covers the aluminum film,
3) spin the sample slowly at first to obtain a uniform layer of photo resist,
4) spin quickly to help dry the photo resist,
5) pre-bake the sample at 80° C for 15 minutes to complete the drying process,
6) apply the positive or negative photograph discussed in the preliminaries in close contact with the dry photo resist.
7) expose at a distance of one foot from an ultraviolet light source for 5 minutes and develop the photo resist pattern,
8) post-bake at 100° C for at least 1 hour,
9) etch away the unwanted aluminum with a warm solution of phosphoric, acetic, and nitric acids mixed volumetrically in the ratio 25:5:1,
10) remove the unwanted photo resist with acetone.

The resulting coplanar waveguides had a sharply defined geometry and the aluminum films adhered well to the alumina substrates providing absolutely dry substrates were used in step 1). A type 12E3 Edwards vacuum coating unit was more useful with this technique than with the masking technique since specular migration was no longer important. High evaporation rates could then be used with the result that 4 resistive boats yielded film thicknesses as large as 20 kÅ (2 microns). This was close to one skin depth at 1.5 GHz which for aluminum is actually 21 kÅ (2.1 microns). With masking the previous section showed that useful films were usually 2 kÅ or less, because of the predomination of specular migration in the evaporation of thicker films. As in the masking technique, dust was a problem. In regions where the aluminum films were not absolutely clean and moisture free, the photo resist did not protect the underlying aluminum from the etching solution, and pin holes resulted.

3.2.4 Conclusions

In this work, the direct photographic etching process was found to be superior to masking. Also, less steps were involved as shown in Figure 3.2-1 where a quick summary and comparison of the processes is given. The direct photographic etching method was not only cleaner, but was much more precise than masking. Thicker aluminum films could also be obtained by the former. However, both procedures required a dust free environment to eliminate pin holes.

*Design Phase

↓

*Cut Rubilith Pattern (20x)

↓

*Photoreduction (20:1)

↓

*Make a Positive from Negative if Required

↓

(a) MASKING	(b) DIRECT PHOTOGRAPHIC ETCHING
*Prepare Clean, Dry, Copper Sheet 5 Mils Thick	*Evaporate Desired Aluminum Film Thickness onto Alumina Substrate (Edwards Type Vacuum Coating Unit)
*Apply AZ-1350 Positive Photo Resist Evenly on Clean Side (Spin to Make Uniform)	*Apply AZ-1350 Positive Photo Resist Evenly on Metal Film (Spin to Make Uniform)

↓

*Pre-bake 15 Minutes @ 80°C

↓

*Apply +ve or -ve Photograph

↓

*Expose to Ultraviolet Light for 5 Minutes and Develop

↓

*Post-bake @ 100°C, 1 Hour

*Coat Back Of Copper Sheet with Apeizon Wax Solution (Let Dry)	
*Etch Away Unwanted Copper with Warm (<85°C) Saturated $FeCl_3$ Solution (Wax Melts if Hot) and Remove Photo Resist	*Etch Away Unwanted Aluminum (Phosphoric-Acetic-Nitric Acid Mixed Volumetrically 25:5:1) and Remove Photo Resist
*Evaporate with Mask (Edwards Type Vacuum Coating Unit)	
*Coplanar Waveguide 1 Inaccurate corners and lines. 2 Specular migration. 3 Dusty copper causes pin holes.	*Coplanar Waveguide 1 Accurate corners and lines. 2 Sharp definition. 3 Dusty aluminum film causes pin holes.

Figure 3.2-1: Comparison of Masking and Direct Photographic Etching Techniques.

3.3 Evaporation Systems and Techniques

Herein a description of the model 12E3 Edwards High Vacuum coating unit and its operation will be given. Some of the problems encountered in using this apparatus for the fabrication of aluminum-alumina CPW's will be discussed, including the mounting of samples, masks, and resistive boats with their charges.

3.3.1 Edwards High Vacuum Coating Unit Model 12E3

The Edwards High Vacuum Coating Unit 12E3 is a small but quite versatile coating unit which can be used for both resistive boat evaportation or sputtering. It is the resistive boat technique that concerns us here, but only a slight modification to the apparatus will allow sputtering to be performed as well. Four boats can be loaded for each vacuum run, since a rotatable turret allows each boat to be positioned under a fixed target. The problems of charging the boats efficiently and the problems of regulating the evaporation rate are solved partially by trial and error. Substrates and masks must be mounted securely with the mask in close contact with the substrate. The apparatus and all materials must be kept clean for best relults. Most important of all, the substrate must be moisture free.

Figure 3.3-1 shows a schematic diagram of the apparatus with major parts labeled from (1) to (34). A list of these parts is given in Table 3.3-1. The unit has a glass enclosed vacuum chamber (10) mounted over a "Speedvac" high vacuum baffle valve (9). The vacuum

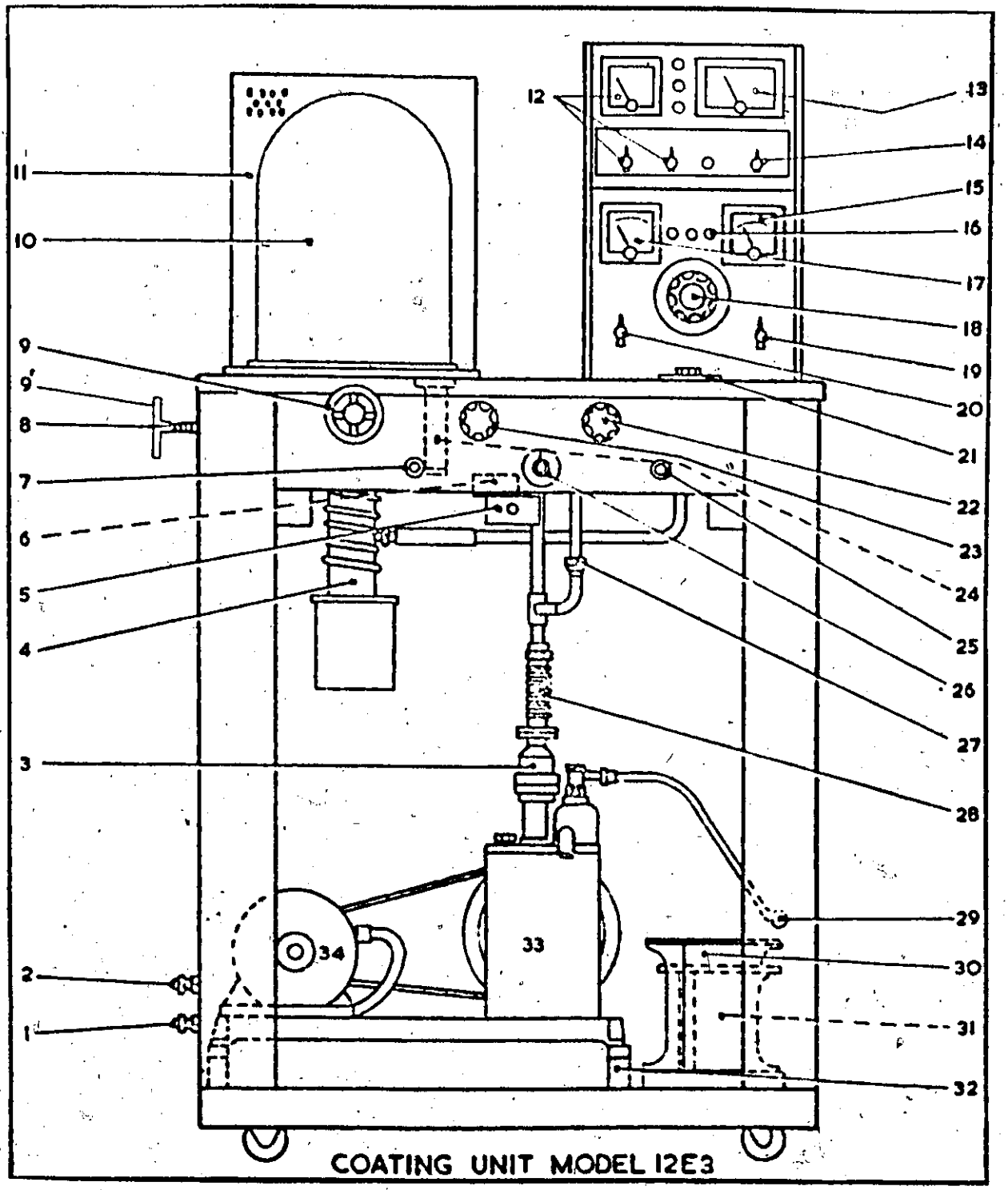

Figure 3.3-1: Schematic Diagram of Coating Unit 12E3 with Important Parts Labled from 1 to 34.

1. Water Outlet
2. Water Inlet
3. Non-Return Valve
4. 403A Vapour Diffusion Pump
5. Door Safety Switch
6. VSK1 Switch
7. Chamber Air Admittance Valve
8. Gas Inlet Nozzle
9. Rotary Hand Wheel
9. 5L2 Baffle Valve
10. Glass Work Chamber
11. Work Chamber Metal Cover
12. Pirrani Gauge and Switches
13. Penning Gauge ($1x10^{-5}$ torr)
14. Penning Gauge Switch
15. H.T. Meter, 2 Amp. F.S.D.
16. Circuit Fuses
17. L.T. Meter Switch, 60 Amp. F.S.D.
18. L.T. and H.T. Control
19. Electrical Service Switch
20. Pump Selector Switch
21. Filament Selector Switch
22. Backing Valve
23. Roughing Valve
24. Penning Head 5MF
25. Rotary Pump Air Admittance Valve
26. Gas Inlet Valve
27. Pirani Head M6A
28. Flexible Connection
29. Exhaust Connection
30. L.T. Transformer
31. H.T. Transformer
32. Anti-Vibration Mountings
33. ES150 Rotary Pump
34. Motor

Table 3.3-1: List of Numbered Parts for Figure 3.3-1.

chamber is evacuated by a "Speedivac" oil vapour diffusion pump (4), backed by a "Speedivac" Model ES150, single stage, gas ballasted rotary pump (33). The operation of the pumping system is controlled by a rotary switch (20) on the instrument panel.

The pumping system is provided with the following valves:

(a) a "Speedivac" high vacuum baffle valve for isolating the vacuum chamber,

(b) a 1/2" "Speedivalve" (22) for backing purposes,

(c) a 1/2" "Speedivalve" (23) to permit the vacuum chamber to be rough pumped to a pressure below 0.2 torr (mm Hg) before pumping with the diffusion pump,

(d) a "Speedivac" type RS1A air admittance valve (7) to admit air to the vacuum chamber at the end of each coating cycle,

(e) a "Speedivac" type RS1A air admittance valve (25) to admit air to the rotary pump when it is switched off,

(f) a "Speedivac" type GS1 gas inlet valve (26) to admit a controlled flow of gas into the vacuum chamber during high tension cleaning or sputtering operations,

(g) a "Speedivac" non-return valve (3) to prevent oil from being forced back into the system should the rotary pump stop when unattended. This is a short term device only; the plant should not be left for long periods of time.

The unit is supplied with a "Speedivac" model 2A combined Piranni-Penning type vacuum gauge with a separate meter for each

separate gauge. The Pirani gauge meter allows high vacuum pressures from 1000 microns to .1 micron to be read. The Penning gauge meter allows lower pressures to be read in two ranges; 10^{-2} - 10^{-4} torr, and 10^{-4} - 10^{-5} torr. The Pirani type gauge head (27) indicates the backing line pressure between the backing line valve (23) and the rotary pump. The Penning gauge head (24) indicates the vacuum chamber pressure.

A "Speedivac" model VSK1 pressure switch (6) is used to automatically isolate the "Regavolt" electricity supply from the vacuum chamber terminals when the chamber is at atmospheric pressure. The pressure switch acts as a safety device to protect the user when the vacuum is broken.

A low tension filament heating circuit contains a low tension transformer (30) capable of continuously supplying 40 amperes of current at 12 volts, and 60 amperes intermittently at the same voltage. This current is regulated by a "Regavolt" variable auto-transformer (18) which also controls the high tension and radiant heater services; this is permissible since the services are never required simultaneously. The high tension (H.T.) and low tension (L.T.) services are selected by means of a rotary switch (19) on the control panel. The low tension current is measured by an ammeter (17) of 60 amperes full scale deflection (F.S.D.). The "Regavolt" transformer is protected by a circuit fuse (16) rated at 5 amperes. A filament selector switch (21) enables any one of the four source electrodes to be selected at will.

The high-tension transformer (31) incorporated in the unit provides high-tension ionization cleaning. The transformer is a high reactance type with a normal rating of 50 milliamperes at 3000 volts (o/c, 5000 volts), and can withstand intermittent short circuits on the secondary winding. The meter which registers the H.T. current (15) has a 2 ampere full scale deflection. The electrode system for ionic bombardment cleaning consists of two aluminum rings suitably shielded and mounted so that they do not obstruct the vapour stream from the evaporation source. Both high tension leads from the transformer are taken into the workchamber via insulated baseplate electrodes, thus neither side is earthed and no gas discharge appears in the vapour diffusion pump body. This prevents any decomposition of the working fluid and also prevents any sputtering back onto the work from metal deposited on the work table during previous coating cycles. The aluminium ring electrodes are shielded from the evaporation source to prevent contamination of the electrodes with evaporated metal or non-conducting films. Where a number of vapour sources are used additional masks must be provided to shield the high tension electrodes.

Figure 3.3-2 displays the rotary jig handwheel assembly with a multi-filament turret head attached. In the model 12S3 Edwards high vacuum coating unit the turret assembly enables four materials to be evaporated in any order from the same location in the centre of the chamber. Hence a four stage sequential evaporation can be performed in one vacuum run.

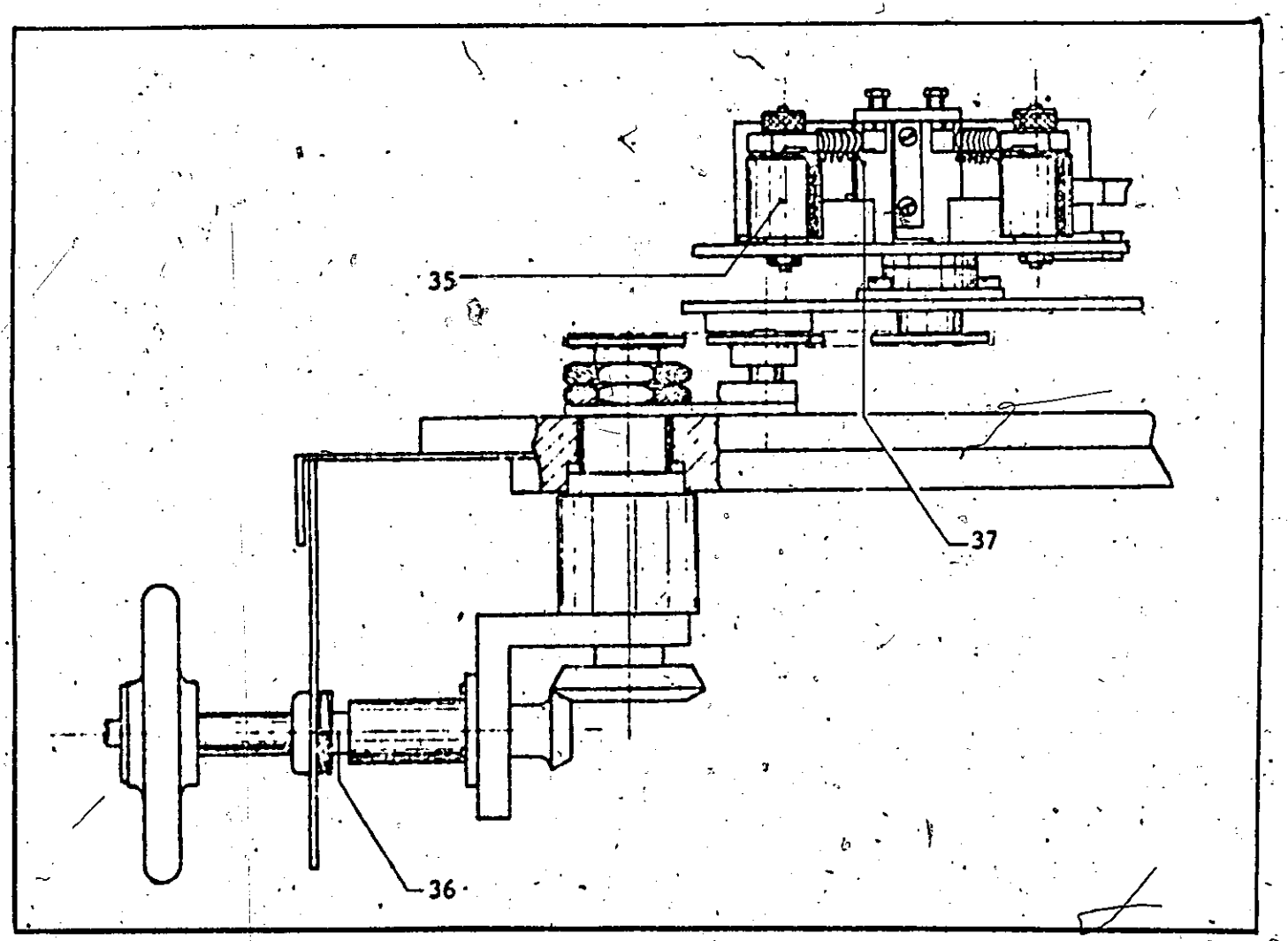

Figure 3.3-2 : Rotary Jig Handwheel Assembly and Multi-filament Turret Head.

The handwheel and its shaft (36) drive a table supporting four pairs of binding posts. A helical tungsten filament or molybdenum boat may be located between the outer binding post (35) and an inner one (37). Figure 3.3-2 shows two tungsten helixes mounted between two sets of binding posts with 12 to 14 aluminum hooks suspended along the bottom of each helix. The aluminum hooks are made simply by bending 1/2" lengths of pure aluminum wire at their mid points to form a V 1/4" long. They are then carefully and uniformly placed on each helix in an inverted position with a fine pair of clean, stainless steel tweezers. A simpler method of loading involves placing a straight length of aluminum wire inside each helix along its axis. However, the former method is preferred because it gives a higher evaporation yield; as much as 5 kÅ per helix. Perhaps the combination of both methods could raise the yield even further but this has not been attempted.

The diameter of the tungsten filament wire depends on the temperature to which the source must be raised to evaporate a given material. Aluminum melts at 660° C and boils at 2,467° C for one atmosphere of pressure. At low pressures such as 10^{-5} torr (mm Hg), the boiling point is considerably less. At 10^{-3} torr the boiling point of aluminum ranges from 1,080° C to 1,360° C because of an energy state transition in the metal. At 10^{-4} torr another energy state transition occurs and aluminum boils in a similar range of 974° C to 1,200° C. At 10^{-5} torr the boiling point range is approximately 875° C to 1,080° C. Again the jump in temperature is

due to an energy state transition. Between these distinct pressures, the boiling point rises linearly on a semilog plot, where boiling point temperature (Vapour pressure temperature) is plotted on the linear scale. This data was obtained from the following equation:

$$\log_{10} P = \frac{-16,450}{T} + 12.36 - 1.023 \log T \qquad (3.3\text{-}1)$$

where the vapour pressure is in torr and the temperature is in degrees Kelvin [37]. In any case, the tungsten wire helix must at least be able to withstand a temperature of 2,467° C.

Such a tungsten single wire helix may be constructed by winding a 0.5 mm diameter wire of maximum length 220 mm to give 10 turns on a 3.5 mm diameter former. The heater current required for most purposes is about 20 amperes. After the aluminum melts, the coils of the helix are joined by molten aluminum which decreases the total resistance in the heater circuit considerably. If the applied voltage control is not changed from the initially applied value of 20 amperes (about 21% of total L.T. voltage), the current will suddenly double to about 40 amperes when the aluminum charge melts. Since the rating of the L.T. transformer is 40 amperes continuously at 12 volts, there is no danger of burning out the transformer with the above process, providing more voltage is not applied to increase the current flow over 40 amperes.

A tungsten triple wire helix may also be formed by first winding 3 lengths of 0.5 mm diameter tungsten wire together in a twisted strand. The wires are first clamped between two chucks one of which is free to rotate. Then the wires are heated by a gas flame and twisted together by rotating the free chuck. A vice and a hand brace can serve as a fixed and free chuck respectively. The resultant triple strand is then wound on a former to produce a helical filament.

This filament can take up to 45 amperes of current, which also is a good reason for limiting the heater current to 40 amperes. One may then wonder how much of an aluminum charge may be used. A straight 1" length of 20 gauge aluminum wire is recommended as a suitable charge by Edwards High Vacuum Ltd. It is also recommended that the coils of the helix should be far enough apart in order that they do not become bridged when the aluminum melts. However, 12 to 14 aluminum hooks have been evaporated from a single helix quite successfully as described previously in the discussion of Figure 3.3-2. It was observed that the molten aluminum did on occasion bridge the coils of the tungsten helix, but the heater current was always under 40 amperes. This allowed 5 kÅ of aluminum film to be deposited from a single source.

For heating gold, silver, copper, etc., and powders such as magnesium fluoride, and silicon monoxide, a molybdenum boat may be used. This refractory metal is obtainable as a foil which can then be bent into a narrow trough, or indented at its center to form

a small circular bowl in order to hold the metal or salt to be vaporized. The previously mentioned current limitation of 40 amperes again applies.

3.3.2 The Mask and Substrate Holder

The mask and substrate should be positioned securely and in close contact with each other if the masking technique is used. A small rectangular jig mounted on a circular disc has been designed with two tracks separated by a distance of approximately 5 mils. The alumina substrate slides along the top track and at the end of this top track falls towards the bottom track where a spring loaded tab applies vertical pressure onto the substrate. The mask and mask holder then are inserted into the top track until the mask is positioned directly over the substrate and in close contact with it due to the spring loaded tab under the substrate.

A picture of the two mask holders and their masks (A and C) used for this thesis is shown in figure 3.3-3. The 5 mil thick masks are simply spot welded onto the substrate holders in a recess 5 mils deep. The meaning of A and C will be discussed in section 3.3.

In order to dismantle the above arrangement after a film of aluminum has been deposited, the spring loaded tab must be pulled out first. The substrate then drops away from the mask onto the second track. It then slides out easily without any damage occurring to the aluminum film. Finally the mask and mask holder are pulled out of the top track.

If no mask is used as in the direct photographic etching

MASK A

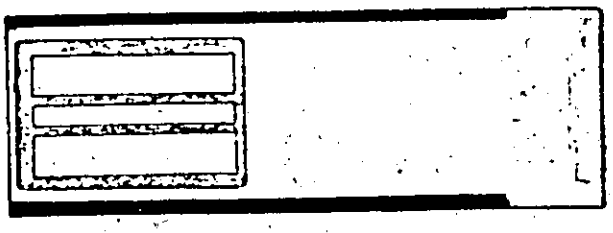

MASK C

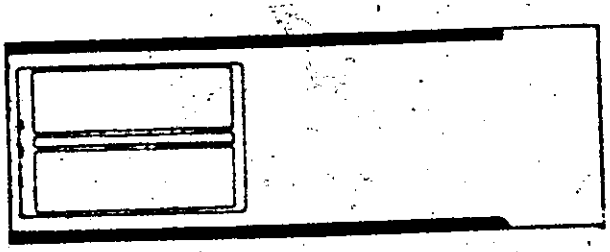

Figure 3.3-3: Pictures of Masks from Two Different Designs Shown Attached to Mask Holders.

process, is simplified. A track for the alumina substrates must be provided and then it is just a simple matter of sliding the substrates into this track before evaporation. After a film has been deposited the substrates slide out of their track just as easily. The films are then ready for etching.

3.3.3 Thin Film Thickness Gauge

The measurement of thin film thickness was performed by means of a type 5216A Hewlett Packard 12.5 MHz electronic counter and a crystal controlled oscillator circuit operating just below 6 MHz. A 6 MHz crystal is placed inside the vacuum chamber beside the substrate target. The film thickness obtained varies directly with the mass of the aluminum deposited onto a fixed cross section of the crystal. The mass of the crystal in turn varies linearly with the natural frequency of the crystal, over a specified frequency range. Hence the film thickness deposited can be read directly as a change of frequency on the above counter from the time the evaporation has started to its termination.

The above thickness gauge must however be calibrated for each type of material deposited. For this thesis, calibration of aluminum thin films was performed on a Sloan M-100 Angstrometer which is useful for measuring thin shiny films against a glossy substrate. This instrument uses yellow monochromatic light with a wavelength of 5.890 kÅ and aims this light in a small beam to the edge of the film to be measured. Half of the beam sees the shiny glaze of the substrate and half sees the film. This discontinuity causes interference fringes with a corresponding discontinuity. The fringes

can be photographed by a camera mounted on the Sloan M-100 Angstrometer. The length of the dip measured in half wavelengths multiplied by 2.945 kÅ per half wavelength gives the desired film thickness.

The resulting average figure of merit for two measured aluminum films was found to be .724 ± .0891 kÅ / kHz. This figure was applied as a scaling factor for the change of frequency measured by the above thickness gauge to yield the thickness of the deposited thin film in kÅ.

3.3.4 Operation of the 12E3 Edwards Vacuum Coating Unit

The vacuum chamber is loaded as described above. The bell jar and its protective cover are then placed over the multi-filament turret head. The pump selector switch is set at the "Rotary and Diffusion" position. An initial rough pump down to at least 20 microns pressure is performed with the high vacuum valve and backing line valve closed. All air admittance valves are closed and the roughing line valve is open. This valve is closed when the desired pressure of 20 microns is reached and the backing line valve is opened slowly. The high pressure on the Pirani-gauge may rise slightly but only momentarily while the backing line air is being removed. Finally the high vacuum valve is opened very slowly, and again the Pirani pressure will rise. The valve is opened slowly to ensure that this pressure on the Pirani gauge does not exceed 150 microns. The Penning gauge can be turned on to its first range when the Pirani gauge reading falls again to 20 microns. When the Penning gauge reads 10^{-4} torr, the second range may be used. Finally, when this range indicates 2 or 3 x 10^{-5} torr the system is ready for evaporation.

Evaporation involves first selecting the desired charged filament with the filament head selector, selecting L.T. on the electrical services switch and then increasing the L.T. and H.T. control slowly towards 20% of the total L.T. voltage until 20 amperes heater current is obtained. If the helix is eyed simultaneously through the bell jar, the sudden increase in heater current to 40 amperes at the melting point can be observed. A slight adjustment of the L.T. and H.T. control may then be necessary to control the evaporation rate.

When the aluminum has evaporated completely the heater current will have again been reduced to 20 amperes. If the filament has burned out during the evaporation process, the resulting open circuit will cause the heater current meter to read zero amperes. Filaments are not too durable and usually last for at most two evaporations. A single evaporation is then quite costly.

The vacuum may be broken by first setting the electrical services switch to off, closing all valves, and then opening the chamber air admittance valve slowly. When the chamber pressure has been equalized with respect to the surrounding atmosphere, the protective hood and bell jar may be removed. It is sometimes necessary to lean into the bell jar gently to dislodge it.

3.4 Various Coplanar Line Designs and Tolerance Checks During Processing

From the beginning of this study it was hoped that Wen's

theory could be verified and that meandered lines based on this theory could be fabricated. Hence straight lines and meandered lines were designed and fabricated in accordance with the aforementioned fabrication techniques in order to achieve the above goal. A detailed record of the actual measured tolerances was kept throughout the project in order to ensure that any noted experimental deviations from Wen's characteristic curves was not due to unknown fabrication errors.

3.4.1 The Straight Coplanar Lines

Figure 3.4-1 and Figure 3.4-2 show two straight line designs with their respective rubilith photographs at the top of each figure. The design conditions are given as well along with optical comparitor measurements of the shown photograph. These measurements were accurate to ± 0.2 mils. Design A, a trial design, has a nominal center strip width of 50.0 mils. The latter value of 50.0 mils was chosen in order to create a good match with the end contacts available. More will be said about this in the next section. The values of k for each design also differ. The value of k for design A was only chosen in an approximate manner from Wen's large scale characteristic impedance curves [5] in order to create a trial design. The aim here was not design accuracy, but familarization with fabrication of CPW's and the related equipment. The value of k for design FCD was chosen as an exact solution from Figure 2.3-3. In this case mathematical and experimental precision were of utmost importance.

Section 2.3 showed that if an exact solution was chosen with a center strip width of 50.0 mils, a theoretical tolerance

Photograph of Rubilith Pattern

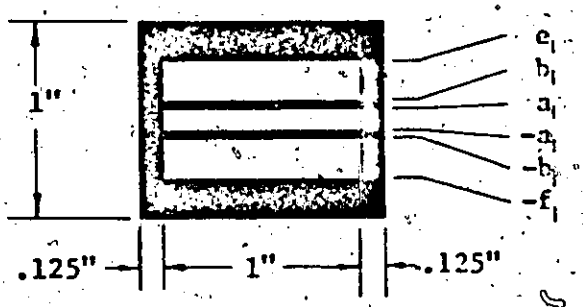

Design Conditions

* $a_1/b_1 = .52335$
* Substrate Properties
  - $\varepsilon_r = 9.2$ (96% alumina)
  - Dimensions 1" x 1" x 0.025"
  - Surface Finish: 1 µin Glaze
* Center Strip = 100 mils
* Frequency Range: 1-2 GHz
* Wavelength: 11.811" - 5.905" in Vacuum
  5.230" - 2.615" in CPW
* To Minimize Radiation $2b_1 << \lambda_{min}/2$
  ie $2b_1 << 1.307"$

Nominal Design Values		Measured Photograph	
$2a_1 = .1031"$	$a_1 = .05155"$	$2a_1 = .1047$	(Error + 1.55%)
$2b_1 = .1970"$	$b_1 = .0985"$	$2b_1 = .1946$	(Error - 1.22%)
$2e_1 = .591" = 2f_1$	$e_1 = .2955" = f_1$		
$k = .52335$		$k = .53803$	(Error + 2.73%)

Figure 3.4-1: Design of Mask A plus Optical Comparator Measurements on the Photograph of the Rubilith Pattern.

Photograph of Rubilith Pattern

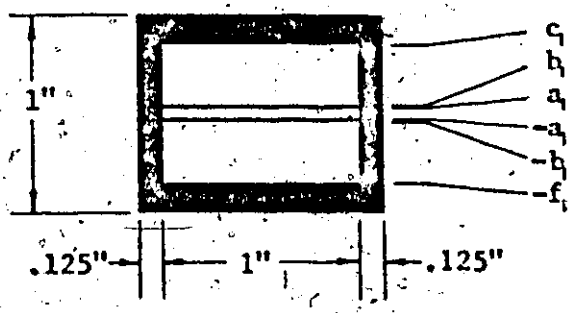

Design Conditions

* $a_1/b_1 = .556174$
* Substrate Properties
  - $\varepsilon_r = 9.2$ (96% alumina)
  - Dimensions 1" x 1" x 0.025"
  - Surface Finish: 1 µin Glaze
* Center Strip = 50 mils
* Frequency Range: 1-2 GHz
* Wavelength: 11.811" - 5.905" in Vacuum
  6.230" - 2.615" in CPW
* To Minimize Radiation $2b_1 \ll \lambda_{min}/2$
  ie $2b_1 \ll 1.307"$

Nominal Design Values		Measured Photograph
$2a_1 = .0500"$	$a_1 = .0250"$	$2a_1 = .04925"$ (Error -1.50%)
$2b_1 = .0899"$	$b_1 = .04495"$	$2b_1 = .09040"$ (Error +0.56%)
$2c_1 = .7000" = 2f_1$	$c_1 = .3500"$	
$k = .556174$		$k = .5446$ (Error -2.04%)

Figure 3.4-2: Design of Mask BCD plus Optical Comparator Measurements on the Photograph of the Rubilith Pattern.

of 3.35% should be applied to $2a_1$ and $2b_1$ in order that the characteristic impedance of the CPW lie between 45.0 Ω and 55.0 Ω. In absolute values this turned out to be ± 1.67 mils on $2a_1$ and ± 3.01 mils on $2b_1$. Both Figure 3.4-1 and Figure 3.4-2 show that such tolerances were obtained for the measured photograph. However, as will be seen shortly, this was not the case for copper masks.

The design goals should first of all be clarified. Initially a value of k, a choice of materials, and knowledge of the properties of these materials must be known. However, the center strip width cannot necessarily be chosen arbitrarily. Its choice depends indirectly on the frequency range one wishes to work in. This frequency range in turn determines the wavelength of the quasi-TEM wave in the CPW. Then the ground plane separation $2b_1$ must be chosen to be much less than half this wavelength in order to minimize radiation problems [5]. The width of the center strip $2b_1 \cdot k$, must then be chosen less than a finite calculated amount in order to keep radiation to a negligibly small magnitude. For a frequency range of 1-2 GHz, and a maximum value of $2b_1$ equal to 0.1307, the maximum value of the center strip width turned out to be 68.50 mils for design A and 72.69 mils for design BCD. Hence, the radiation limitation was very nearly met for design A where 103.1 mils was used for the center strip width. The radiation condition was certainly met for design BCD since 50.0 mils was employed for $2a_1$.

The obtainable tolerances on the copper masks caused some concerns in the fabrication area. One copper mask was fabricated for design A and was labeled "Mask A". Three masks were made for design BCD and were labeled "Mask A", "Mask B", and "Mask C". Significant

preferential etching in the supposed square corners of the masks as well as small ridges and linearity deviations along the mask were observed. Optical comparator measurements of ± 0.2 mils accuracy were made on all four masks at the center and both ends causing mask B and D to be rejected. Rejection was based on measured values of k which fell outside the acceptable range for k shown in Figure 2.3-1.

The small ridges appearing on one side of the mask as a result of etching were negligible providing this side faced the aluminum vapour source during evaporation. However, the preferential etching and linearity deviations were quite significant as shown in Table 3.4-1. The table compares the results of optical comparator measurements on the rubilith photographs which have sharp corners, with the four corresponding masks. At the ends of the masks the deviations are mostly as large as 3 and 4 mils. At the center of the mask they are smaller in magnitude but opposite in sign. It is the values of k at the ends of masks B and D where preferential etching occurred that caused these masks to be rejected. These measurements agree with observations made during the etching process when it was observed that the corners were etched through first, followed by the straight edges of the mask.

Direct photographic etching did not cause the same problem at the corners of the CPW since the aluminum was being etched from around the outside of the corners. Any horizontal etching was considered minimal since it normally is twice the film thickness [2] and the film thickness employed was only 20 kÅ or less (.0786 mils or less). This was negligible compared to the 50 mil

Mask	Parameter	Rubilith Photograph Measurements (mils±0.2)	Mask Deviations from Photograph		
			LEFT (mils±0.4)	CENTER (mils±0.4)	RIGHT (mils±0.4)
A	$2a_1$	104.7	+3.50	-0.80	+2.60
	$2b_1$	104.6	-1.21	+1.60	-2.30
	k	0.53803	0.50284	0.52031	0.55772
B (Reject)	$2a_1$	40.25	+4.34	-2.57	+1.08
	$2b_1$	90.40	-4.30	+1.30	-0.93
	k	0.54480	0.62307	0.51563	0.56285
C	$2a_1$	40.25	+0.75	-0.75	+3.05
	$2b_1$	90.40	-3.00	+1.00	-2.90
	k	0.54480	0.57104	0.52551	0.59739
D (Reject)	$2a_1$	40.25	+0.75	-0.50	+5.40
	$2b_1$	90.40	-4.95	+1.30	-5.30
	k	0.54480	0.63195	0.53163	0.64219

Table 3.4-1: Optical Comparator Measurements of Masks A, B, C, and D Compared to the Same Measurements on the Corresponding Rubilith Patterns.

center strip width. As a result, the CPW's fabricated via the direct photographic etching technique were effectively as accurate as the rubilith photograph itself. These CPW's then had suitable geometries in accordance with the tolerance goals outlined in section 2.3 of Chapter two.

3.4.2 The Meandered Coplanar Line

Once the properties of straight 1" long coplanar lines had been investigated, attention was focused on simple meandered lines with one or two bends. Three designs were attempted; M_1, M_2, M_3, with M_3 being longer than M_2, and M_2 longer than M_1. Lines M_1, M_2, and M_3 are shown in Figures 3.4-3, 3.4-4, and 3.4-5 respectively. M_1 consists of two 1/4" lengths of straight coplanar lines spaced 1/2" apart and joined by a single semi-circular coplanar bend. M_2 consists of two straight .55" long coplanar lines joined to a straight .6" transverse coplanar line by two rectangular bends. M_3 ressembles M_1 in shape except that the ground planes are much wider and the center line length is about 1.74 times larger. Design M_3 was meant for the full use of a 2" x 2" x .025" alumina substrate surface. It was initially thought that the wider ground planes would be an asset, but as will be seen shortly, they are more likely to cause radiation at a bend.

Semi-circular arcs, were employed in M_1 and M_3 in an attempt to maintain the value of a_1 / b_1 around the bend. M_2 was designed with square bends for comparison purposes. The rectangular bends in M_2 were shorter in length though k varied in value along the bend. Experiments discussed in Chapter V showed M_2 had a very similar performance to M_1. This seems to indicate that a rectangular band is as good as a long semi-circular bend for which k is kept constant throughout the bend.

DESIGN M1

(Center Line Length = 2.05493")

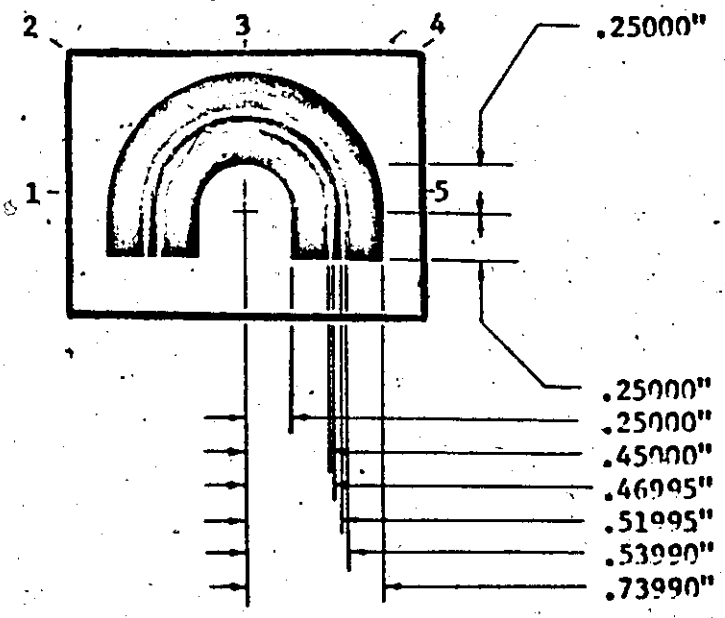

Point Measured	e_1-b_1 inches	b_1-a_1 inches	$2a_1$ inches	b_1-a_1 inches	e_1-b_1 inches	k	% Error in k
Nominal Values	.20000	.01995	.05000	.01995	.20000	.55617	+0.00%
1 Left Side	.20067	.01905	.05075	.01910	.19928	.57087	+2.64%
2 45° Left	.20041	.01880	.05099	.01869	.20091	.57629	+3.62%
3 Center	.20005	.01889	.05186	.01885	.20039	.57879	+4.07%
4 45° Right	.19935	.01920	.05109	.01886	.20105	.57308	+3.04%
5 Right Side	.19952	.01880	.05028	.01947	.19980	.56782	+2.09%

$\bar{k}$ = .57337 +3.09%

Figure 3.4-3: Design of Meandered Line M1 below which the Optical Comparator Measurements on the Rubilith Pattern Photograph are Tabulated for Comparison to Nominal Design Values.

DESIGN M2

(Center Line Length = 2.67980")

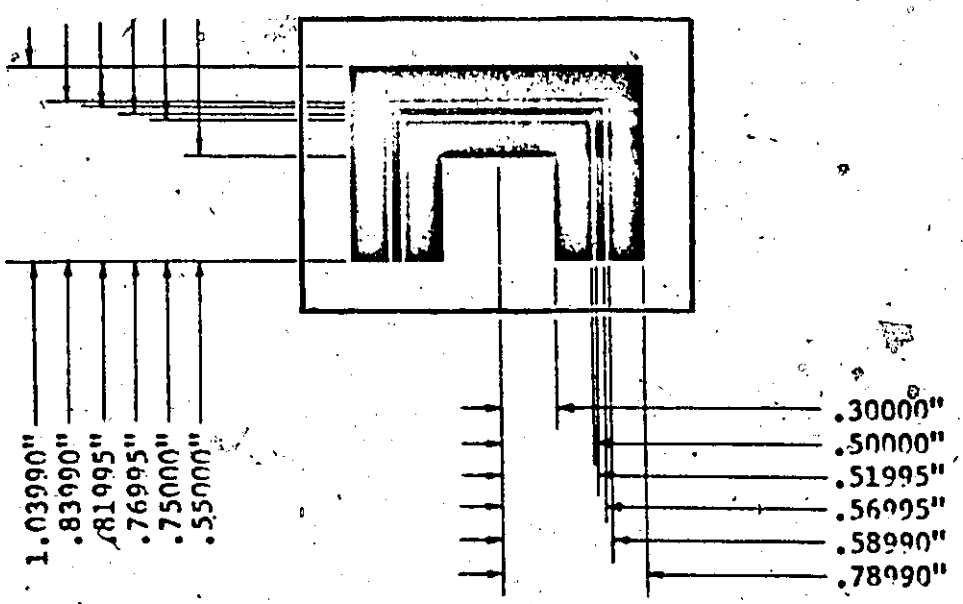

Region Measured	$2a_1$ (mils ± .2)	$2b_1$ (mils ± .2)	k	% Increase in k
Nominal Values	50.00	89.90	.55617	+0.00%
Left Side	50.73	89.39	.56751	+2.04%
Top Side	50.80	89.06	.57040	+2.56%
Right Side	50.61	88.97	.56884	+2.28%
			$\bar{k}$ = .56892	+2.29%

Figure 3.4-4: Design of Meandered Line M2 Below Which the Optical Comparator Measurements on the Rubilith Pattern Photograph are Tabulated for Comparison to Nominal Design Values.

DESIGN M3

(CENTER LINE LENGTH = 3.56503")

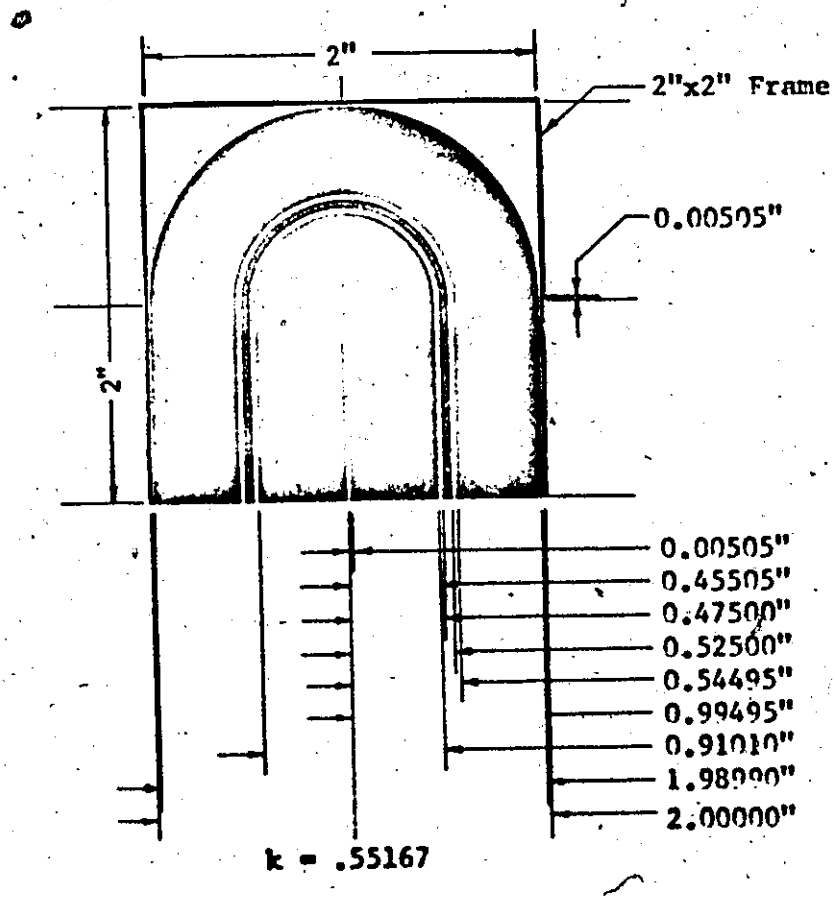

Figure 3.4-5: Design of Meandered Line M3 for Use on a 2"x2"x.025" Alumina (96%) Substrate.

Of the three meandered lines described above, only the first two were tested since minor technical problems arose in photographing the rubilith pattern for M_3. The larger size of M_3 prevented a direct picture from being taken by the Mikrokon 1700 camera described in section 3.2. It was necessary to reduce the pattern into a 1" x 1" frame with the Mikrokon 1700, and then enlarge it by a factor of 2x. Due to the lack of proper enlarging equipment the desired accuracy for the final photograph could not be obtained. As was the case with the straight lines M_1 and M_2 were both fabricated by direct photographic etching. The reasons for this choice of fabrication technique are described in detail in section 3.2.

Optical comparator measurements of ± .2 mils accuracy on the rubilith pattern photographs have been displayed below designs M_1 and M_2 in Figures 3.4-3 and 3.4-4 respectively. It is obvious from these results that in cutting the rubilith pattern the circular bend was more difficult to cut accurately than the rectangular bend. A maximum percentage error in k of 4.07% was obtained at the center of M_1 compared to a maximum value of 2.56% at the center of M_2.

As discussed for the straight coplanar lines, the ground plane separation had to be much less than half a wavelength in order to minimize radiation effects. This involved selecting a 50 mil center strip in design PCD for the selected value of k. For the three meandered lines, M_1, M_2, and M_3, the value of k and the center strip width were kept at the same values as in design PCD. It could then be assumed that at least the straight line sections of the

meandered designs would not radiate energy to any significant amount.

The bends required closer investigation however. Just as a uniform flow of fluid undergoes a spatial redistribution of streamlines at a bend in a pipe, it might be expected that a similar phenomena might occur at a bend in a coplanar transmission line. In a pipe bend the flow is compressed towards the outside surface of the bend due to the large inherent momentum of the flow and the need to satisfy Newton's laws of momentum and acceleration. It is true that the fluid would travel through a shorter distance and hence a lower potential difference by travelling along the inside surface of the pipe bend. However, the momentum of the large mass of moving fluid would cause the fluid to travel along the longer pipe surface where action reaction forces would be at work.

In a CPW one might expect the reverse to be true. The momentum of flow of the low mass electrons would be insignificant in comparison to the gain to be made by allowing the electrons to take the shorter, lower potential path around the inside edge of the bend. The inside path would then be favoured over the external path.

Another important phenomena directly related to capacitance would also be at work in the CPW bend. The center strip in a straight coplanar line tends to draw the ground plane currents towards itself. The outside edge of the ground planes for this transmission line carries little current. This capacitance effect is supported experimentally in Chapter V by measurements made on the K series of straight lines to be described shortly. The results showed that the

characteristic impedance of a CPW was not noticeably sensitive to variations in the ground plane width. The ground plane current tries to pass as close as possible to the center strip without at the same time causing excessive heating in the ground planes.

The losses in the ground planes are therefore concentrated in a very narrow width nearest the center strip. The magnitude of this width, Δb_1, is as of this writing undetermined though it is known from the symmetry of the CPW that almost half of the electric field lines leaving the center strip must reach each ground plane at $\pm [b_1 + \Delta b_1]$. The loss theory of section 2.4 does not take this effect into account, and a uniform ground plane current distribution is assumed instead. The measured losses of Chapter V are approximately 2.5 times larger than the theoretical losses, and though experimental error is quite significant, it is possible that some of this increase is due to the above capacitance effect. A similar situation has been noted in microstrip lines [9] where the ground plane current concentrates itself in a fairly narrow region beneath the top conducting strip. Another more obvious example of this is the case of a simple parallel plate capacitor for which charge resides on the inside surfaces of the parallel plates.

How then does this "capacitance effect" combine with the "shorter conduction path effect" at a bend in a CPW? By superposition one would expect that the inside ground plane of a bend would have its high current density within Δb_1 decreased by the "shorter conduction path effect". Conversely, one would expect the

outside ground plane at the bend to have its current density increased by the "shorter conduction path effect". Such a difference in current densities in each ground plane could then create a small dipole antenna at the bend such that radiation would be increased in this locality. How significant this increase would be has not been determined in this work. The measured impedance at the bends of the meandered coplanar line in Chapter V did not appear to be different, from the characteristic impedance in the straight CPW sections. This did not however negate the possibility of a significant increase in radiation at the bends since special equipment would be necessary to detect this radiation.

Researchers at RCA Laboratories, Montreal, have detected increased radiation at coplanar line bends and have attempted to equalize the ground plane current densities at a coplanar bend by bridging the edges of the ground planes nearest the center strip with a short conduction path. This however, appears physically cumbersome and an easier solution comes to mind. Why not deliberately design the inside ground plane of the bend to be as narrow as Δb_1? Then the current density in this ground plane could not possibly be lowered by electrons taking a shorter conduction path around the bend. In fact, the capacitance effect would probably allow narrow ground planes to be used in all CPW designs.

Very narrow ground planes in coplanar lines have not been tested experimentally by the author, but are proposed herein as a follow up to the work achieved in this thesis. It would certainly be useful to know how narrow a ground plane could be tolerated before affecting the characteristic impedance value of the CPW. In this thesis, ground planes 200 mils wide have been used successfully with 50 mil wide center strips.

3.4.3 Coplanar Geometry Varied in K Series of CPW's

The K series of coplanar lines was created in order to verify Wen's characteristic impedance curves for various values of k, and also test the effect of varying the width of the ground planes. Table 3.4-2 lists the K series design values along with the optical comparator measurements of each rubilith pattern photograph. The list consists of six designs with values of k ranging from 0.1 to 0.6 in increments of 0.1. The errors in geometry range from zero mils to 2 mils.

In order to study the finite ground plane effect, Table 3.4-3 was drawn up. The idea was to extend the ground planes with the use of aluminum foil and Eccobond solder. The small and varied initial design ratios of e_1 / b_1 were increased to a new value $e_1' / b_1' = 10$. Table 3.4-3 contains the lengths of aluminum foil required for the above extensions allowing a .1" overlap section for soldering purposes. The foil was cut to length and then applied to the initial samples. The performance of these samples was then remeasured in order to check for any noticeable improvement. Chapter 5 will discuss these experimental results in detail, but in general no noticeable improvement was found. This gave further support to the theory presented in the previous section on meandered lines, that the ground plane currents in a CPW reside in a very narrow band, Δb_1, at the ground plane edges nearest the center strip.

3.5 Techniques for Achieving Effective Electrical Contacts

C.P. Wen [5] discusses the ease with which CPW's can be mounted for effective electrical contacts. Figure 3.5-1 is an illustration of

k (K SERIES)	Ground Plane e_1-b_1 (inches)	Slot Width b_1-a_1 (inches)	Center Strip $2a_1$ (inches)	Slot Width b_1-a_1 (inches)	Ground Plane e_1-b_1 (inches)
.1000 (.1023)	.1000 (.1008)	.2250 (.2231)	.0500 (.0509)	.2250 (.2236)	.1000 (.1007)
.2000 (.2040)	.2250 (.2258)	.1000 (.0988)	.0500 (.0506)	.1000 (.0987)	.2250 (.2256)
.3000 (.3039)	.2666* (.2565)	.0580 (.0575)	.0500 (.0502)	.0580 (.0575)	.2666* (.2565)
.4000 (.4050)	.2875 (.2874)	.0375 (.0368)	.0500 (.0504)	.0375 (.0372)	.2875 (.2875)
.5000 (.4950)	.3000 (.3000)	.0250 (.0255)	.0500 (.0495)	.0250 (.0250)	.3000 (.2993)
.6000 (.5935)	.3083* (.3088)	.0166* (.0160)	.0500 (.0502)	.0166* (.0185)	.3083* (.3062)

Table 3.4-2: Nominal Design Values for Six Different Values of k Ranging from .1 to .6, Below which the Bracketed Quantities Indicate the Corresponding Optical Comparator Measurements on the Rubilith Pattern Photographs for these Designs.

Wen's method of encapsulating two adjacent CPW's with a metallic capsule for proper ground plane connections. The ceiling of the capsule must be at least two slot widths away from the surface of the CPW in order to minimize loading effects. Also the side and inner ground plane contacts must be made far enough away from the CPW center strips in order that interference with normal electric field patterns will not occur. Since the ground plane currents reside in a narrow band, Δb_1, at the ground plane edges nearest the

k	a_1 (inches)	b_1 (inches)	$e_1=f_1$ (inches)	e_1/b_1	$e_1'=f_1'$ (inches)	Aluminum Extension ($e_1'/b_1'=10.$) (inches)
.1	.0250	.2500	.3500	1.40	2.500	2.150 + .1
.2	.0250	.1250	.3500	2.80	1.250	0.900 + .1
.3	.0250	.0833	.3500	4.20	0.833	0.480 + .1
.4	.0250	.0625	.3500	5.60	0.625	0.275 + .1
.5	.0250	.0500	.3500	7.00	0.500	0.150 + .1
.6	.0250	.0416	.3500	8.40	0.416	0.066 + .1

Table 3.4-3: Ratio of e_1/b_1 for Series K Designs, Including the Aluminum Foil Extensions Required to Increase e_1/b_1 to $e_1'/b_1'=10.$, Allowing a .1" Overlap for Soldering Purposes.

center strips, the necessary air space over the ground planes is not much greater than Δb_1. The magnitude of Δb_1 is however still a nebulous quantity. It is expected that Δb_1, is most likely less than a_1; ie less than half the center strip width. The loss measurements of chapter five will shed more light on this problem.

Wen's metallic encapsulation of CPW's is fine as a permanent mount but not for experimentation purposes. It was desirable to be able to mount and unmount CPW samples easily without destroying them. To this end a Wave Tek experimental mount designed for microstrip line samples was used for CPW samples as well. This arrangement is shown in Figure 3.5-2. The ground plane contacts caused problems however. The thumb screws on the mount were intended for a single

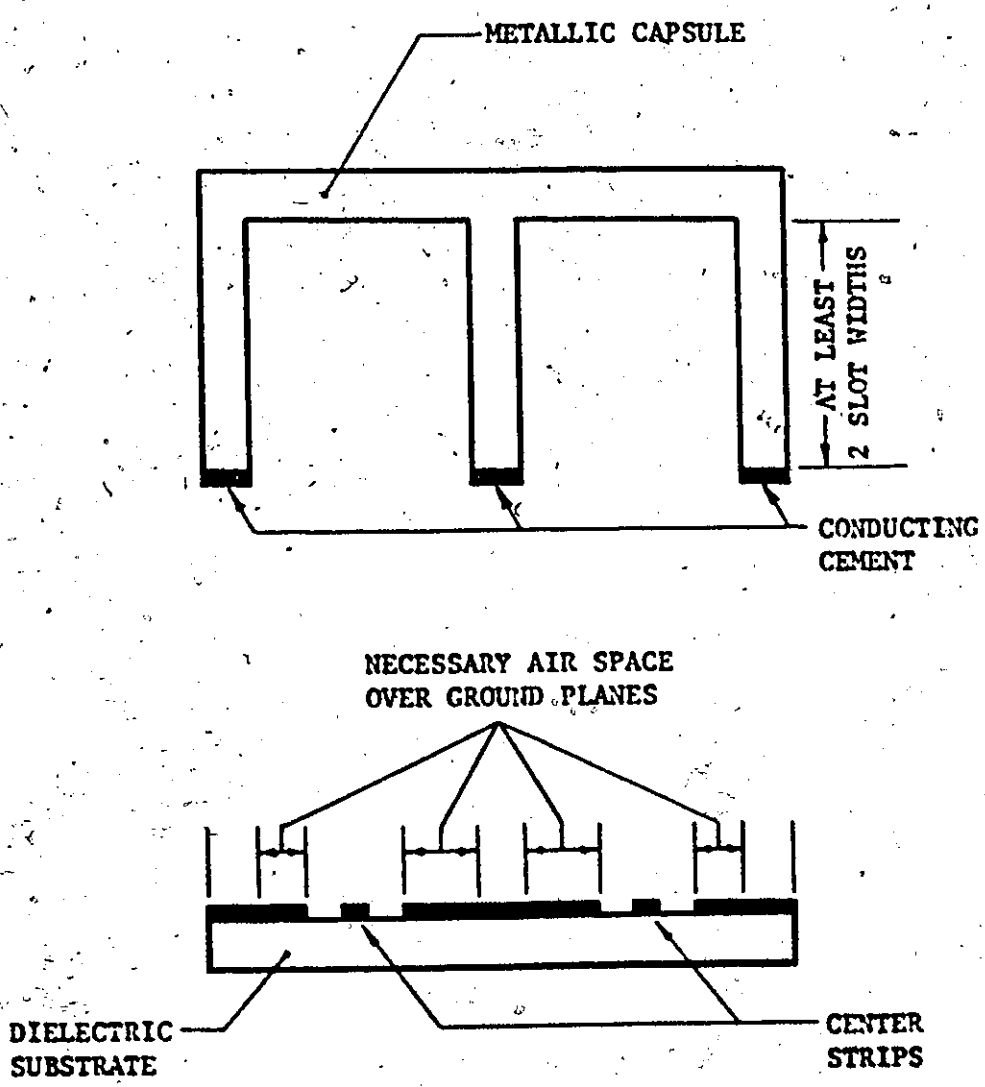

Figure 3.5-1: Metallic Encapsulation of Two Adjacent Coplanar Waveguides for Proper Ground Plane Connections.

Figure 3.5-2: The Wave Tek Experimental Mount for Microstrip Lines Used for Mounting Coplanar Waveguide Samples.

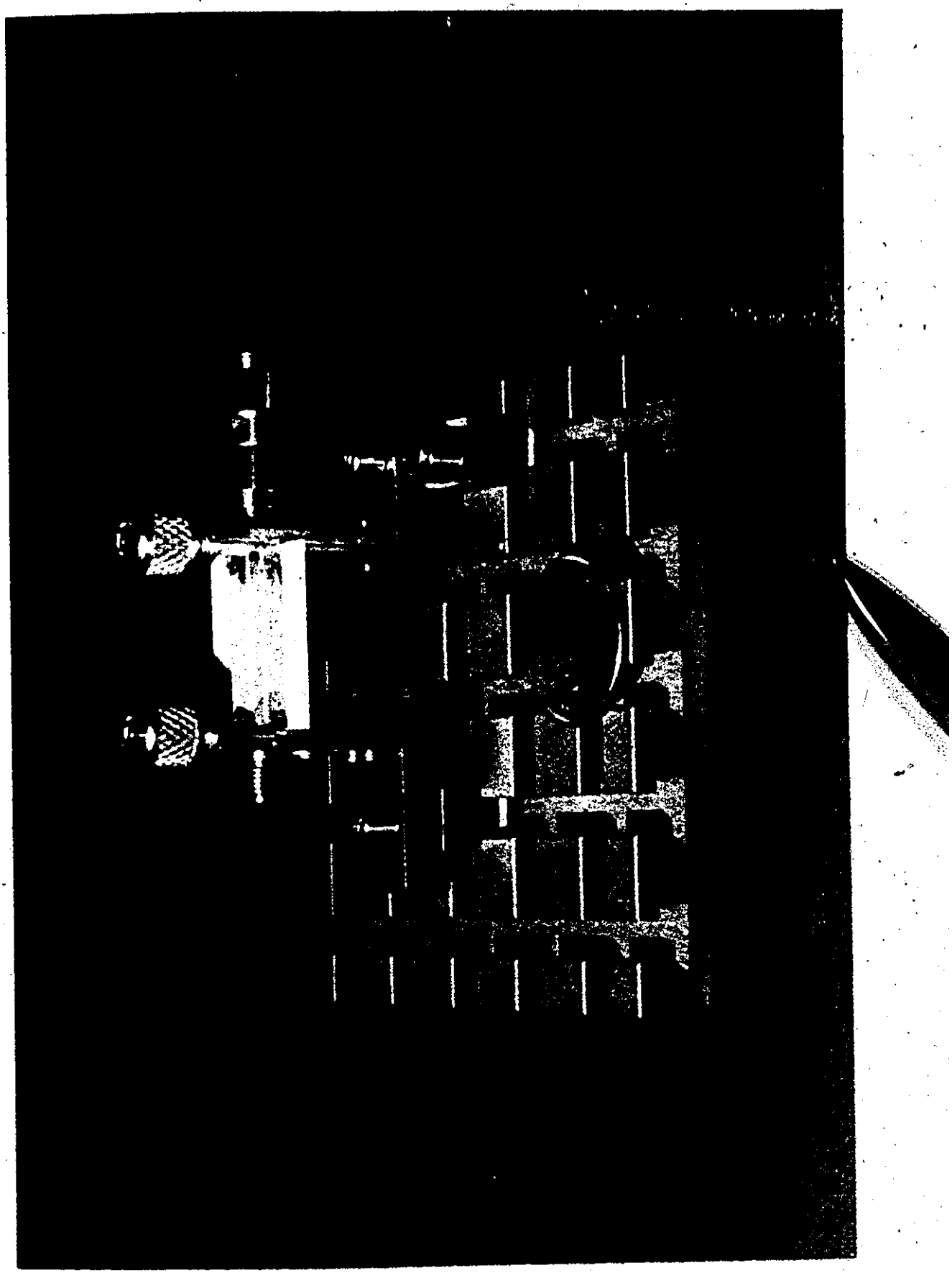

center strip, and the ground plane contacts had to be made by applying inward longitudinal pressure by hand to the two posts supporting the CPW, and then screwing them down tightly. The posts then touched metallic extensions that had been soldered to the ground plane ends. The electrical contacts were quite good but small variations in performance were noted from day to day on samples which were mounted and unmounted many times. One could never be sure that the ground plane contacts were the best possible ones since the hand pressure applied to the supporting posts during mounting varied each time. A more reliable mount had to be developed.

In the meantime the Wave Tek mount had to be used. Initially, phosphor bronze spring contacts were cut and shaped from 5 mil thick sheets of this metal and soldered to the ground planes in order to extend them longitudinally. Epoxy glue was used sparingly underneath the contacts for mechanical strength. However these contacts had a tendency to tear the aluminum films from the CPW substrate surface.

A small roll of aluminum foil attached to the ground planes by Eccobond solder 56C was tried next. This proved more successful but was messy to prepare. The two types of contacts have been compared in Figure 3.5-3.

As a result, the author designed his own special brass mounts, called "3 mm Coplanar Waveguide Launchers". Such a mount is shown in Figure 3.5-4. The insert is a standard 3 mm connector assembly of type OSM 204 CC. The launchers were very effective, easy to use and elliminated the previous need for Eccobond solder, except for repair purposes. A great deal of time was saved by

Figure 3.5-3: Spring Type Phosphor Bronze Contacts Compared to Flat Aluminum Foil Contacts.

Figure 3.5-4: The New 3 mm Coplanar Waveguide Launcher Shown Alongside the 3 mm Coaxial Insert.

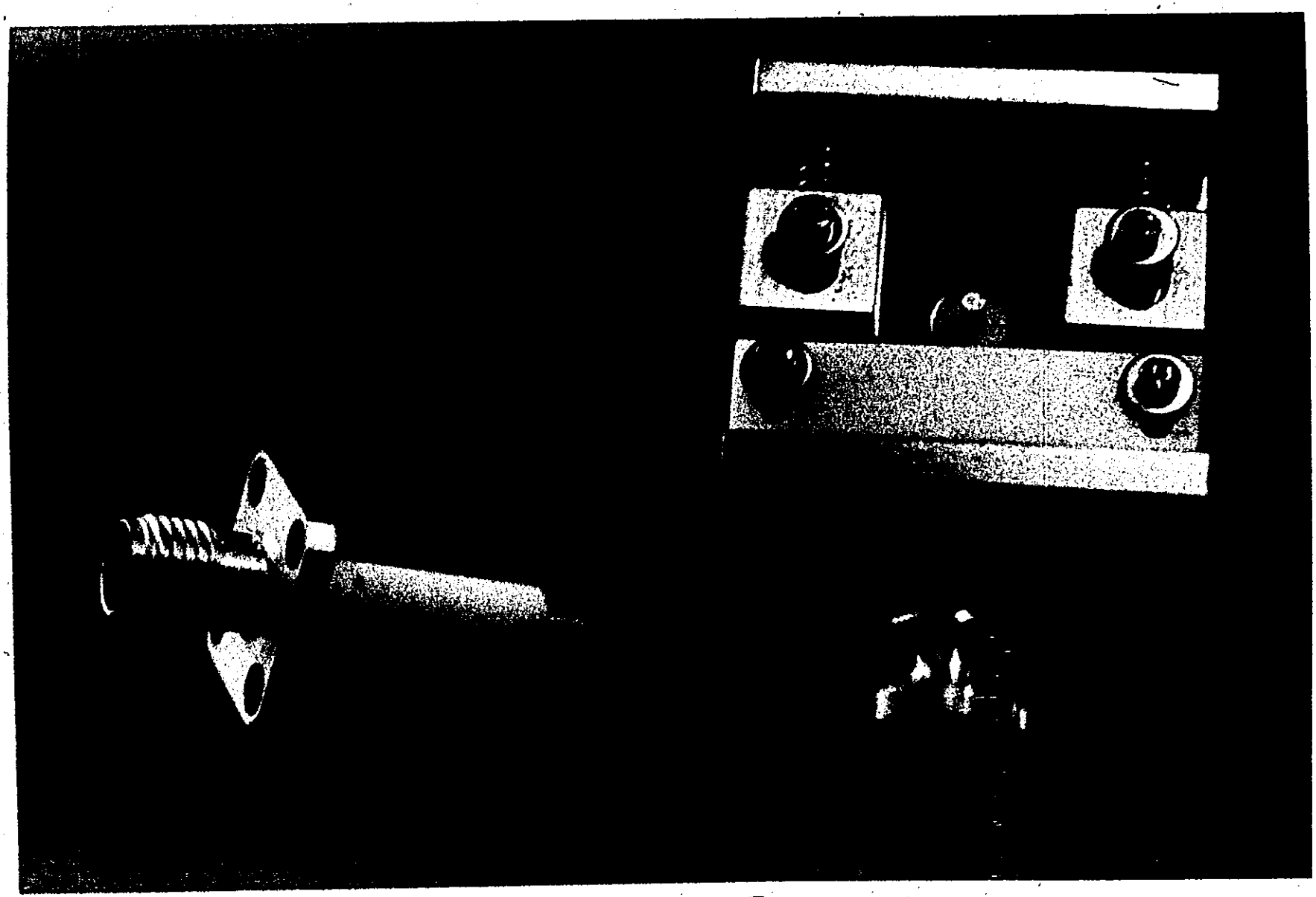

using these clean dry launchers. A CPW sample could be mounted within a minute by turning one thumb screw on each of two launchers. A mounted sample is shown in Figure 3.5-5.

During unmounting, the aluminum thin films on the CPW substrates did not often tear away, and if they did it was only in very small flakes which could easily be repaired with a touch of Eccobond solder. Hence, it was possible to maintain accurate coplanar geometries through a wide range of experimental tests. The launchers also made it easy for experimental results to be rechecked after samples had been unmounted and stored away.

Figure 3.5-5: A Coplanar Waveguide Mounted on Two CPW Launchers.

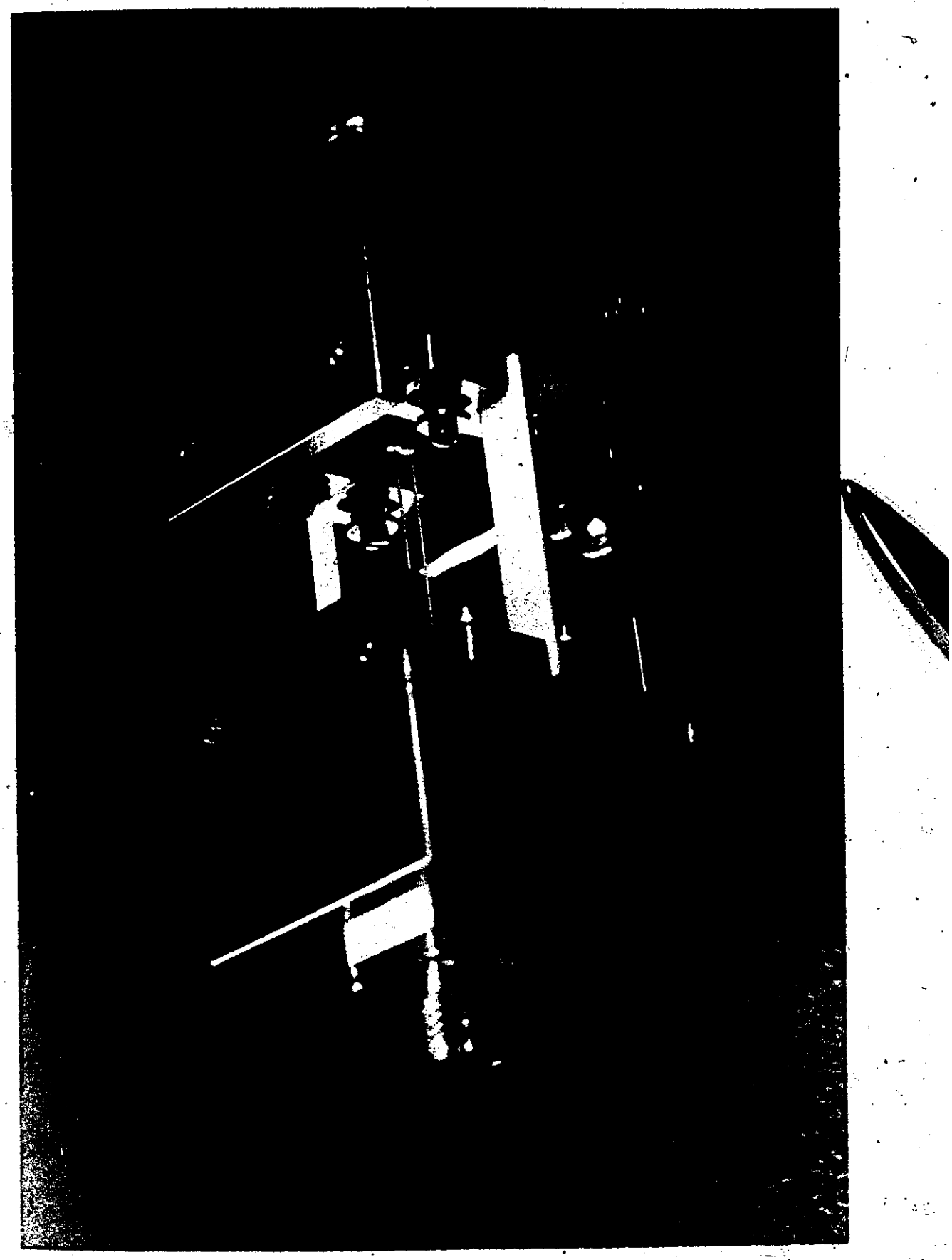

CHAPTER IV

EXPERIMENTAL INSTRUMENTATION AND MEASUREMENT TECHNIQUES

4.0 Introduction

Knowledge of the capabilities of each measuring instrument in any experiment is of vital importance. Error magnitudes indicate whether or not the theory and the measurements correspond within experimental error. Also, one measuring instrument may measure additional unwanted effects which have to be extracted before the correlation of experimental data with theory can take place.

Such unwanted effects existed in the reflection and transmission loss measurements of section 4.1. The net measured reflection coefficient for each CPW sample did not directly indicate the characteristic impedance of the sample. Consequently, a theory of small reflections involving attenuation in the sample had to be derived in order to extract meaningful reflection coefficient values from the experimental data. Moreover, the transmission loss measurements of this same section contained large experimental errors, and a statistical treatment of this transmission data had to be performed. Similar measurements in section 4.2 required an equal amount of care in the interpretation of the experimental results. On the other hand, the instrumentation of section 4.3 measured the true reflection coefficients with reasonable accuracy. Phase velocities and net relative dielectric constants were also measured by this technique.

4.1 Swept Frequency Techniques and Singer Instrumentation Used To Measure Characteristic Impedance and Power Loss in CPW Samples

4.1.1 System Description

In order to fascilitate the investigation of wave propagation in the 1-2 GHz frequency range for a large number of CPW samples, it was necessary to have a simple and reasonably accurate measuring system on hand for the measurement of return loss and transmission loss in these samples. Figure 4.1-1 shows a photograph of one such system.

An Alfred nomograph was used in conjunction with this equipment in order to fascillitate the conversion of return loss measurements to the corresponding mismatch loss, VSWR, and reflection coefficient values. The characteristic impedance of each measured CPW sample followed directly from the VSWR value. The measured transmission losses, on the other hand, were first corrected for mismatch loss at the central 1.5 GHz frequency. The resulting loss values contained large measurement errors and were statistically treated by means of a least squares fit. This led to the determination of a total average contact loss which was subsequently subtracted from the statistical result to yield the net power loss associated with quasi-TEM mode propagation of power at 1.5 GHz down the length of the CPW structures. This net power loss was then plotted as a function of thin film

Figure 4.1-1: Photograph of the Singer 8000/7051 Steep Network Analyzer System Shown Wired for a Transmission Calibration.

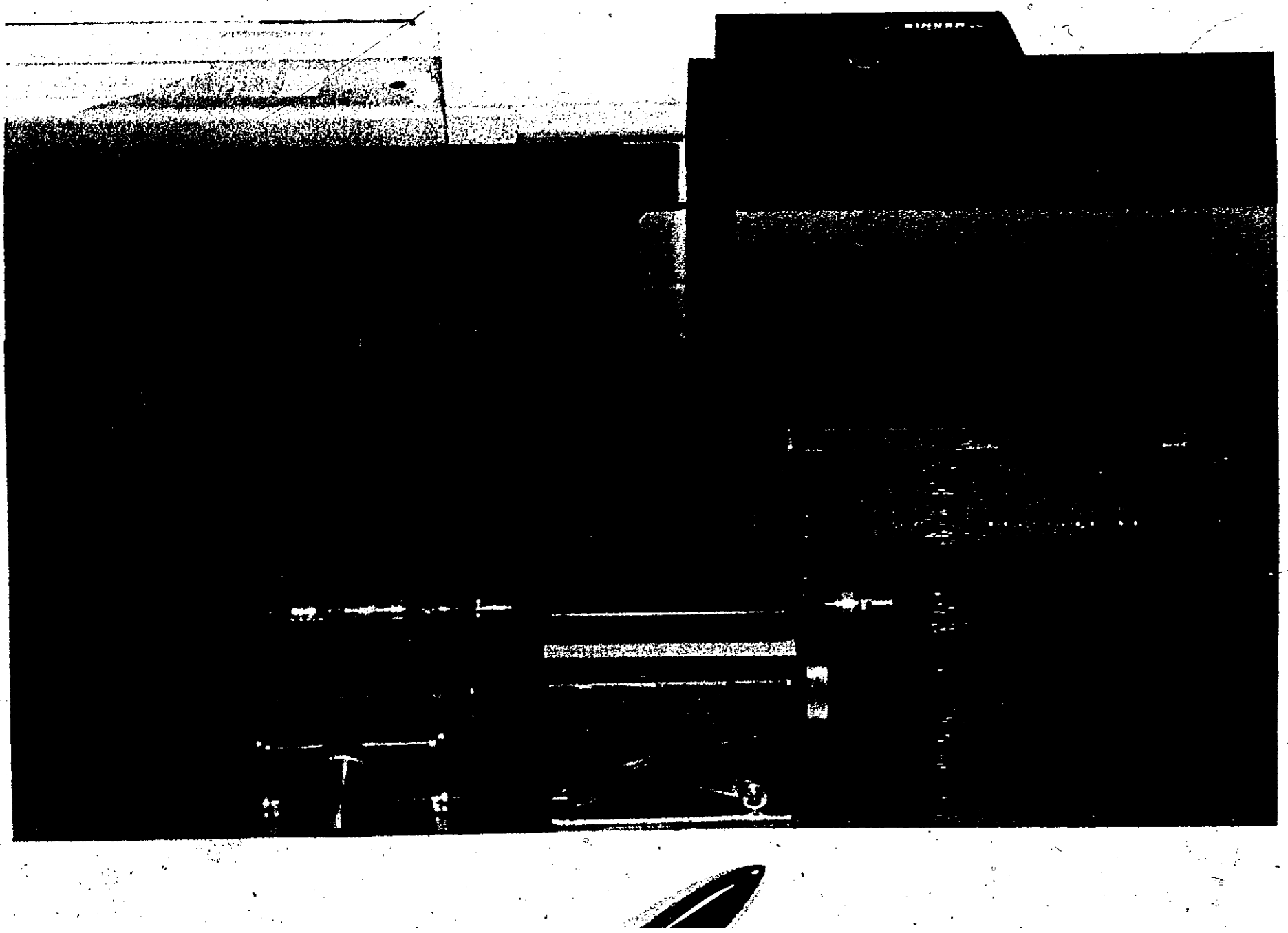

thickness to enable a comparison with the loss theory of section 2.4 of Chapter II.

The photograph of the instrumentation in Figure 4.1-1 is an illustration of a Singer Alfred 3000/7051 sweep network analyzer and an Alfred 6600/6608D sweep oscillator wired for a transmission loss calibration check on channel B of the network analyzer. The sweeper shown can produce continuous RF power over two separate frequency bands in the HF, VHF and UHF regions. The lower band ranges from 10 MHz to 1 GHz and the upper band ranges from 1 GHz to 12 GHz. The RF power from the sweeper enters directly into the input of a Model 3022 Narda Microline 20dB bi-directional coaxial coupler. Three frequency markers are fed directly from the sweeper to the marker input of the network analyzer, and the frequency sweep from the frequency sweep oscillator is wired directly to the horizontal input of the network analyzer.

In the foreground, three model 1001 Alfred crystal detectors are shown connected to the aforementioned bi-directional coaxial coupler. The right-hand crystal detector in the photograph is mounted over the input of the coupler and measures the magnitude of the incident RF power taken directly from the sweeper. This first crystal detector has a direct coaxial line to the reference channel of the network analyzer. The central crystal detector mounted on the directional coupler measures reflected RF power from the load at the output of the coupler and is wired directly to channel A of the network analyzer. The third crystal detector at the far left measures transmitted RF power from the output of the test sample and is fed directly to channel

B of the network analyzer.

In measuring an active or passive device, the 3 mm coaxial connectors between the left most crystal detector and the output of the directional coupler are disconnected and the device to be measured is inserted. A short circuit (s/c) and/ or open circuit (o/c) placed at this point in the test set-up is used for the calibration of channel A in return loss measurements. A s/c load is preferred over an o/c load since a true o/c is usually very difficult to obtain.

Figure 4.1-2 shows a block diagram of the above system for greater clarity. An attenuator is usually placed between the device under test and the third crystal detector carrying the transmitted RF power. This protects the crystal detector and the network analyzer against destructive power levels; especially when active devices are being measured.

The network analyser provides several convenient mathematical functions which permit the measurement of absolute or relative power levels. The reference channel (REF) and channels A and B may be selected individually or A and B may be selected simultaneously. Also, A/REF and B/REF may be selected individually or simultaneously. Absolute power levels are measured in dBm, and relative power levels are measured in dB. For this work only relative power levels were measured since interest was focused on the relative transmission loss in dB and the return loss also in dB.

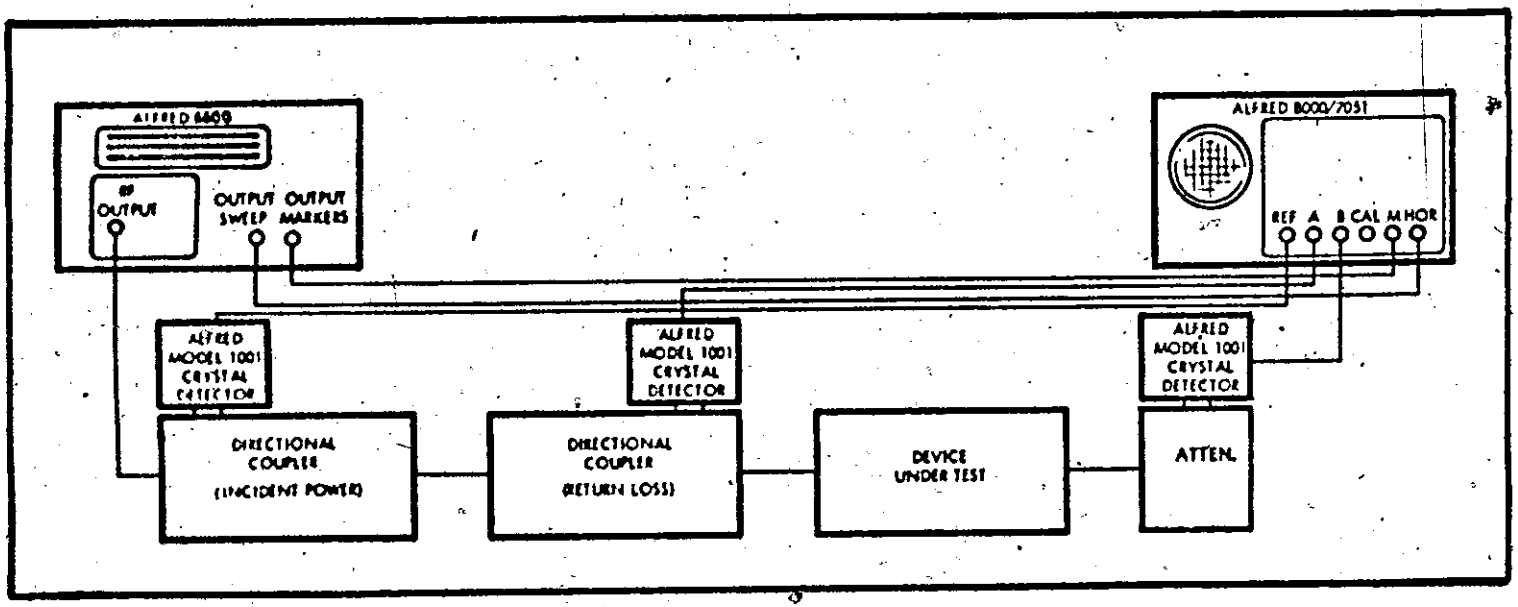

22₂ Figure 4.1-2: Typical Test Connections for Simultaneous Measurement of Return (VSWR) and Transmission Gain or Loss Performance of Active or Passive Devices.

4.1.2 Mismatch Loss Corrections

The previously described Singer instrumentation was used to measure return loss R_L(dB), mismatch loss M_L(dB), transmission loss T_L(dB), and contact loss C_L(dB) for straight, one inch long CPW samples and longer meandered CPW samples. The designs for these coplanar structures were discussed in section 3.4. Both return loss and transmission loss for these samples were obtained directly from the Singer equipment over the 1-2 GHz bandwidth. Return loss at 1.5 GHz was used to calculate mismatch loss, which was then used to correct transmission loss for reflected power at the same frequency in order to obtain the total ohmic loss in each CPW sample. This corrected loss was treated in a least squares sense for several series of CPW samples and for thin films of various thicknesses. A resulting linear plot of loss vs the inverse of film thickness (t_f^{-1}) was extrapolated to the infinite film thickness condition to yield an average contact loss value. This contact loss was then subtracted from the least squares fit values to give the attenuation in each sample in dB per wavelength, A_o". In this thesis the symbol A_o represents a general attenuation in dB, A_o' represents attenuation in dB/in and A_o" represents attenuation at a specific frequency in dB/λ; dB per wavelength.

Return loss and mismatch loss were closely related to each other by the modulus $|\rho|$ of the net reflection coefficient ρ at the input end of each test sample. Return loss was defined as

$$R_L \triangleq -10 \log_{10} [|\rho|^2] \quad \text{(dB)} \qquad (4.1\text{-}1)$$

where $|\rho|^2$ represented the reflected power ratio at each CPW input. The reflected power (channel A) was compared to the incident power (reference channel) via the A ÷ REF function which was available on the Alfred 8000/7051 network analyzer. Mismatch loss was then easily obtained from

$$M_L \triangleq -10 \log_{10} [1-|\rho|^2] \quad (dB) \qquad (4.1\text{-}2)$$

or by means of an Alfred nomograph which gave mismatch loss values to within slide rule accuracy.

Transmission loss, on the other hand, represented the available power at each CPW output (channel B), in comparison to incident power at the input end (reference channel). The selection of the B ÷ REF function on the Alfred 8000/7051 network analyzer enabled transmission loss to be displayed directly in accordance with

$$T_L \triangleq -10 \log_{10} \left[\frac{P_T}{P}\right] \quad (dB) \qquad (4.1\text{-}3)$$

where P_T represented transmitted output power and P represented incident power.

It was important to realize that for a lossless or nearly lossless mismatched line ρ depended solely on power reflections from two reflecting discontinuities due to characteristic impedance mismatches at the input and output of each CPW sample. However, as losses increased significantly, corrections to the lossless theory had to be considered. The simpler theory for a mismatched lossless line was used initially to

account for the frequency dependency of ρ due to reflections at the output discontinuity. This frequency variation was also related to the electrical length of the line

$$\theta = \beta L' \qquad (4.1\text{-}4)$$

where β was the phase constant in radians per unit length and L' was the length of coplanar line. The net complex reflection coefficient ρ at the input end varied with trigonometric expressions of θ.

Collin [38] derived the theory of small reflections for two reflecting junctions and a lossless propagation medium. This theory was modified slightly by introducing a small attenuation αL' which gave

$$\begin{aligned} \rho &= |\rho| e^{j\phi} \\ &= \rho e^{j\phi} \\ &= \rho_1 + \rho_o e^{-2\alpha L' - j2\theta} \end{aligned} \qquad (4.1\text{-}5)$$

where ρ_1 and ρ_o were in general complex reflection coefficients at the input and output of the two junction device respectively. The relationship between the modulus $|\rho|$ and phase ϕ to ρ_1 and ρ_o was then easily established. The quantities ρ_1 and ρ_o were very nearly real constants if αL' was small. The above expression had better than 4% accuracy if ρ_1 and ρ_o were less than 0.2.

Figure 4.1-3 was used to derive (4.1-5). The Figure is a schematic representation of signal flow in a mismatched CPW sample which is nominally 50 Ω and is placed between two calibrated 50 Ω

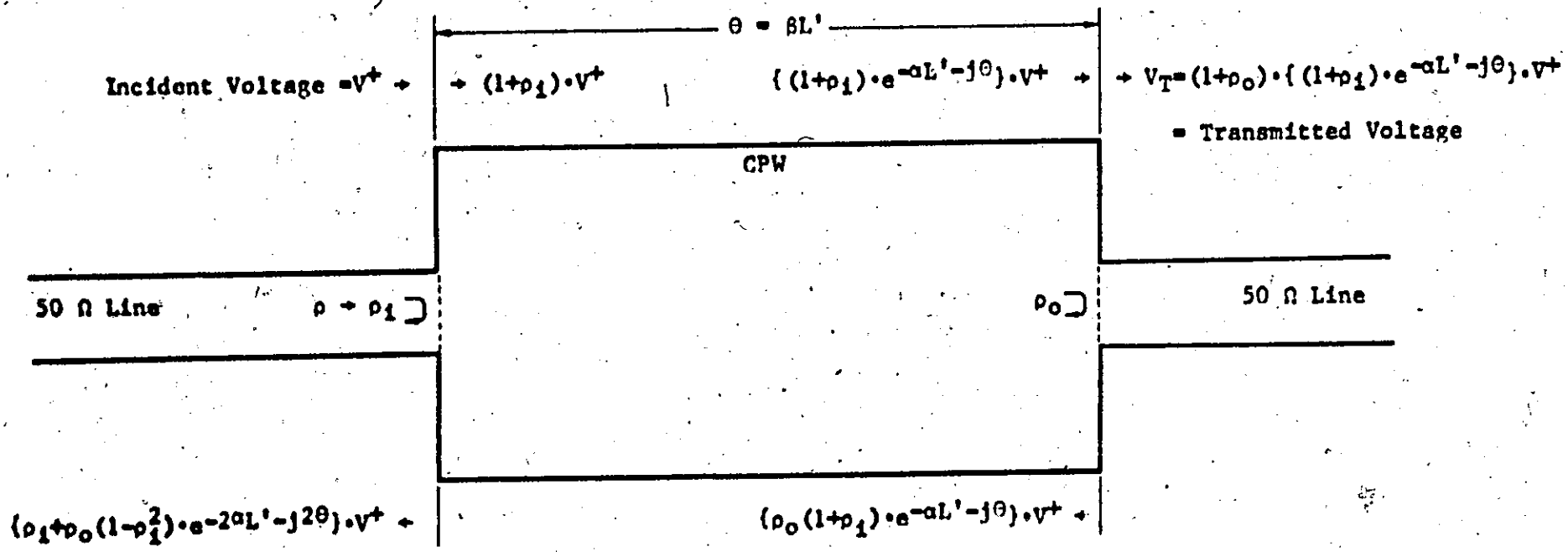

Figure 4.1-3: Effect of Reflection Coefficient Magnitudes on Signal Flow Through a CPW Sample from One 50 Ω Line to Another, where an Impedance Mismatch Exists at Both Ends of the Sample, where Only Primary Reflections are Considered, and where 2α Represents One Way Power Loss in Nepers per Metre.

transmission lines. The symbol α simply represents a small attenuation per unit length in the sample. It was reasonable to write

$$\rho_o = -\rho_i \qquad (4.1\text{-}6)$$

since the coplanar transmission line was a symmetrical device and had the same inherent characteristic impedance at both the input and output ends. Also, ρ_i could be expressed as

$$\rho_i = |\rho_i| e^{j\delta_i} \qquad (4.1\text{-}7)$$

This allowed (4.1-5) to be separated into

$$|\rho| / |\rho_i| = \sqrt{1 - 2e^{-2\alpha L'} \cdot \cos(2\theta) + e^{-4\alpha L'}} \qquad (4.1\text{-}8)$$

$$\phi - \delta_i = \tan^{-1}\left[\frac{e^{-2\alpha L'} \sin(2\theta)}{1 - e^{-2\alpha L'} \cos(2\theta)}\right] \qquad (4.1\text{-}9)$$

where ϕ was the total phase of ρ and δ_i was the phase of ρ_i. When $\alpha L'$ was allowed to approach zero δ_i approached zero and ρ_i became a real constant. When $\alpha L'$ was small and finite a slight attenuation of $|\rho| / |\rho_i|$ existed along with a slight phase distortion of $\phi - \delta_i$ from linearity. The total problem was compounded by δ_i which was very sensitive to the value of $\alpha L'$. This added further nonlinearities in the phase characteristic ϕ vs frequency over a given frequency bandwidth. Equation (4.1-8) accounted for the general shape of the $|\rho|$ versus frequency plot found experimentally since it gave the resonance conditions for a given frequency bandwidth, but

equation (4.1-7) had to be analyzed more closely when thin film thickness varied since $\alpha L'$ was quite significant. Then $|\rho_i|$ and especially ϕ_i changed in magnitude drastically.

In order to account for such drastic changes in $|\rho_i|$ and ϕ_i, the characteristic impedance of the coplanar transmission line had to be written as

$$Z = \sqrt{\frac{R + j\omega L}{j\omega C}}$$

$$= |Z| e^{-j \cdot \phi_z} \qquad (4.1\text{-}10)$$

where

$$|Z| = \left[\left[\frac{L}{C} \right]^2 + \left[\frac{R}{\omega C} \right]^2 \right]^{\frac{1}{4}} \qquad (4.1\text{-}11)$$

$$\phi_z = \frac{1}{2} \tan^{-1} \left[\frac{R/\omega C}{L/C} \right] \qquad (4.1\text{-}12)$$

and

$$Z_{LC} = \sqrt{L/C} \qquad (4.1\text{-}13)$$

was the characteristic impedance of the line due to ϵ_r and geometry only. Then with Z_o representing the characteristic impedance of the main line, the input reflection coefficient was

expressed as

$$\rho_i = \frac{\frac{|z|e^{-j\phi_z}}{z_o} - 1}{\frac{|z|e^{-j\phi_z}}{z_o} + 1} \qquad (4.1\text{-}14)$$

which gave

$$|\rho_i| = \frac{\left[\left[\frac{|z|}{z_o}\right]^2 - 2\cdot\frac{|z|}{z_o}\cdot\cos\phi_z + 1\right]^{\frac{1}{2}}}{\left[\left[\frac{|z|}{z_o}\right]^2 + 2\cdot\frac{|z|}{z_o}\cdot\cos\phi_z + 1\right]^{\frac{1}{2}}} \qquad (4.1\text{-}15)$$

and

$$\phi_i = \tan^{-1}\frac{\left[\frac{|z|}{z_o}\cdot\sin\phi_z\right]}{\left[\frac{|z|}{z_o}\cdot\cos\phi_z + 1\right]} - \tan^{-1}\frac{\left[\frac{|z|}{z_o}\cdot\sin\phi_z\right]}{\left[\frac{|z|}{z_o}\cdot\cos\phi_z - 1\right]} \qquad (4.1\text{-}16)$$

Plots of (4.1-8), (4.1-9), (4.1-15) and (4.1-16) over the

1-2 GHz frequency band for various values of α are contained in appendix C for reference purposes. These plots appeared to be quite useful for interpreting the Singer instrumentation measurements of the modulus $|\rho|$. They were equally useful for interpreting the results obtained by the instrumentation of section 4.2 and 4.3 as well.

Moreover, transmission loss measurements required knowledge of $|\rho|$ in order that corrections be made for mismatch loss. Transmission loss and mismatch loss had to first of all be approximated by use of a Taylor series expansion of $\log_{10}(x + \Delta x)$, truncated to the first order approximation

$$\log_{10}(x + \Delta x) \approx \frac{1}{\ln 10}\left[\ln x + \frac{\Delta x}{x}\right] \qquad (4.1\text{-}17)$$

where

$$\frac{\Delta x}{x} << 1.$$

Consequently (4.1-2) became

$$T_L \approx \frac{10 \cdot \rho^2}{\ln 10} \qquad (4.1\text{-}18)$$

where

$$\rho^2 << 1$$

and (4.1-3) became

$$T_L \approx \frac{10}{\ln 10}\left[1 - \frac{PT}{P}\right] \qquad (4.1\text{-}19)$$

where

$$\left[1 - \frac{P_T}{P}\right] << 1,$$

P was incident power, and P_T was total transmitted power. This transmission loss expression was then expanded by the insertion of the total transmitted power at the input minus the power loss P_L due to the attenuation α to yield

$$T_L = \frac{10}{\ln 10}\left[1 - \frac{\{(1-\rho^2)\cdot P - P_L\}}{P}\right] . \quad (4.1\text{-}19)$$

This reduced to

$$T_L = \frac{10}{\ln 10}\left[\rho^2 + \frac{P_L}{P}\right] . \quad (4.1\text{-}20)$$

For reflection coefficients of 0.2 or less these approximations were quite valid considering the large experimental errors in the original loss measurements. Equation (4.1-18) was used in conjunction with (4.1-20) to yield

$$T_L - T'_L = \frac{10}{\ln 10}\left[\frac{P_L}{P}\right] \quad (4.1\text{-}21)$$

Use of (4.1-17) finally gave the desired mismatch loss correction expression

$$T_L - M_L = 10 \log_{10}\left[1 - \frac{P_L}{P}\right]$$

$$= A_o' \cdot L'' \text{ (dB)} \qquad (4.1\text{-}22)$$

where A_o' represented attenuation per inch of coplanar line, L" was the length of line in inches, and where

$$\frac{P_L}{P} << 1. \qquad (4.1\text{-}23)$$

In other words, this assumed ohmic losses to be small. For 54% of the measured samples P_L/P was less than .1, for 79% of the measured samples P_L/P was less than .2, and for 88% of the measured samples P_L/P was less than .3. For the remaining samples P_L/P was less than .4. Hence for most of the samples (4.1-22) was valid to a first order approximation.

In Chapter V the symbol A_o'' will be used to represent attenuation per unit wavelength for each specific frequency at which this measurement was made. The use of attenuation per unit wavelength is quite common in the literature and applies to a specific chosen frequency. The author prefers to normalize attenuation values to standard unit lengths such as in the previously defined A_o', but has used A_o'' to enable comparison with attenuation values found in the

literature. Permanent loss measurement records for the 26 CPW samples, will be found in appendix D and their implications will be discussed in chapter V.

4.1.3 Measurement Errors

Four major sources of error were considered and of these four, three were subtracted out by the measurement technique used. The first error considered was the model 8000/7051 instrumentation error of 2% or .4dB, whichever was the greatest. Next was the error due to the imperfect directivity of the directional couplers used in the external test loop. Thirdly was the error due to some amount of mainline VSWR in the directional couplers used in the external test loop. Finally there was the error due to the imperfect frequency response and/or frequency response tracking of the directional couplers and other components in the external test loop. These last three types of error could fortunately be subtracted out during the measurement process so that the only error of any significance was the instrumentation error mentioned above. In order to give an appreciation of the magnitudes of these other three measurement errors a brief description and analysis of them will be given.

A small value of coupler directivity would have led to very large measurement errors if corrections over the frequency band of interest had not been made. The effect of directivity is derived and illustrated graphically as a function of return loss for return loss

measurements in Figure 4.1-4. For this case both incident and reflected power were involved. For transmission loss measurements only incident power was measured by means of a directional coupler, and the directivity errors became insignificant in comparison to instrument errors and frequency tracking errors. From Figure 4.1-4 it is clear that for a return loss measurement of 10 dB with a 20 dB directional coupler, errors in the measurement of + 3.5 dB and -2.7 dB are possible.

In comparison the coupler mainline VSWR effects are derived and illustrated graphically in Figure 4.1-5 for return loss measurements as a function of the reflected power coupler mainline VSWR. Since the measurement of transmission loss does not involve the reflected power coupler, the mainline VSWR effect was not relevant to transmission loss measurement error. The crystal detectors had a VSWR specification of 1.4 or less for frequencies up to 10 GHz, and if this value is taken for the mainline VSWR an error of + 1.6 dB and - 1.3 dB in the return loss measurements should be expected.

Frequency tracking error in ratiometric level measurements for the determination of transmission gain and loss or for return loss can be quite significant if the two directional couplers used in the external test loop are not matched. If the imperfect frequency response characteristic of the couplers are matched exactly, the coupler frequency tracking errors for incident, reflected, and transmitted power sampling will cancel. In practice, closely matched couplers will yield a frequency tracking error of a few tenths of a dB or less. This error can also be subtracted out in the measurement procedure.

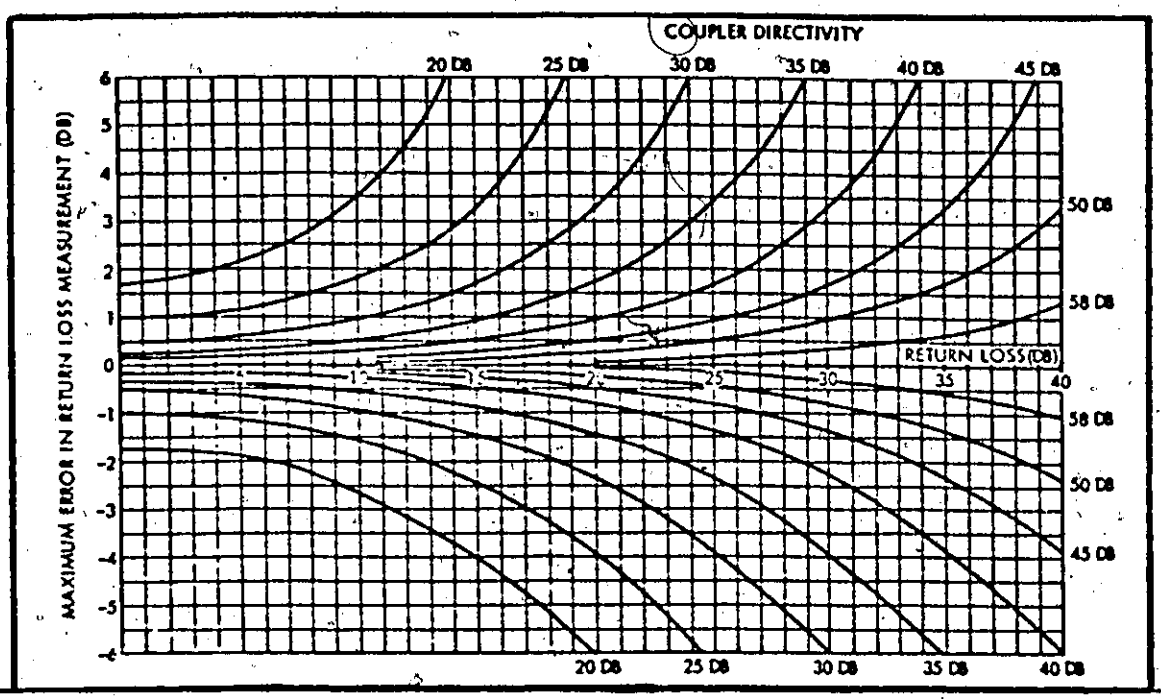

E_{REV} = Voltage output from reverse (reflected) power coupler = $[\rho_L E_{in} \pm D E_{in}]K$ (1)

where ρ_L = load reflection coefficient; E_{in} = input voltage; D = coupler directivity; K = coupling factor

E_{INC} = Voltage output from incident power coupler = $[E_{in} \pm \rho_L E_{in} D]\ K$ (2)

$$\rho_{measured} = \rho_M = \frac{E_{REV}}{E_{INC}} = \frac{\rho_L \pm D}{1 \pm \rho_L D}$$ (assuming both couplers have same K and D) (3)

$$= \frac{\rho_L \pm D}{1 - \rho_L D}$$ (for maximum deviation of either polarity) (4)

$\rho_{measured\ (max.)} = \rho_L + \rho_{error}$ (5)

$$\rho_{error\ (+)} = \rho_{max.} - \rho_L = \frac{\rho_L + D}{1 - \rho_L D} - \rho_L$$ (6)

and

db readout $_{(max.)} = -20 \log (\rho_L + \rho_{error})$ (7)

$$= -20 \log \rho_L \left(1 + \frac{\rho_{error}}{\rho_L}\right)$$ (8)

since log (AB) = log A + log B, and true return loss = $-20 \log \rho_L$,

db error readout $_{(-)} = -20 \log \left(1 + \frac{\rho_{error}}{\rho_L}\right)$ (9)

substituting from (6),

db error (-) = $-20 \log \left[1 + \frac{1}{\rho_L}\left(\frac{\rho_L + D}{1 - \rho_L D} - \rho_L\right)\right]$ (10)

simplify,

max. db error (-) = $-20 \log \left[\frac{\rho_L + D}{\rho_L - \rho_L^2 D}\right]$ (11)

$\rho_{measured\ (min.)} = \rho_L - \rho_{error}$ (5)

$$\rho_{error} = \rho_L - \rho_{min.} = \rho_L - \frac{\rho_L - D}{1 + \rho_L D}$$ (6)

and

db readout $_{(min.)} = -20 \log (\rho_L - \rho_{error})$ (7)

$$= -20 \log \rho_L \left(1 - \frac{\rho_{error}}{\rho_L}\right)$$ (8)

db error readout (+) = $-20 \log \left(1 - \frac{\rho_{error}}{\rho_L}\right)$ (9)

db error (+) = $-20 \log \left[1 - \frac{1}{\rho_L}\left(\rho_L - \frac{\rho_L - D}{1 + \rho_L D}\right)\right]$ (10)

max. db error (+) = $-20 \log \left[\frac{\rho_L - D}{\rho_L + \rho_L^2 D}\right]$ (11)

Figure 4.1-4: Maximum + and - dB Error in Return Loss Measurements Due to Coupler Directivity vs Return Loss.

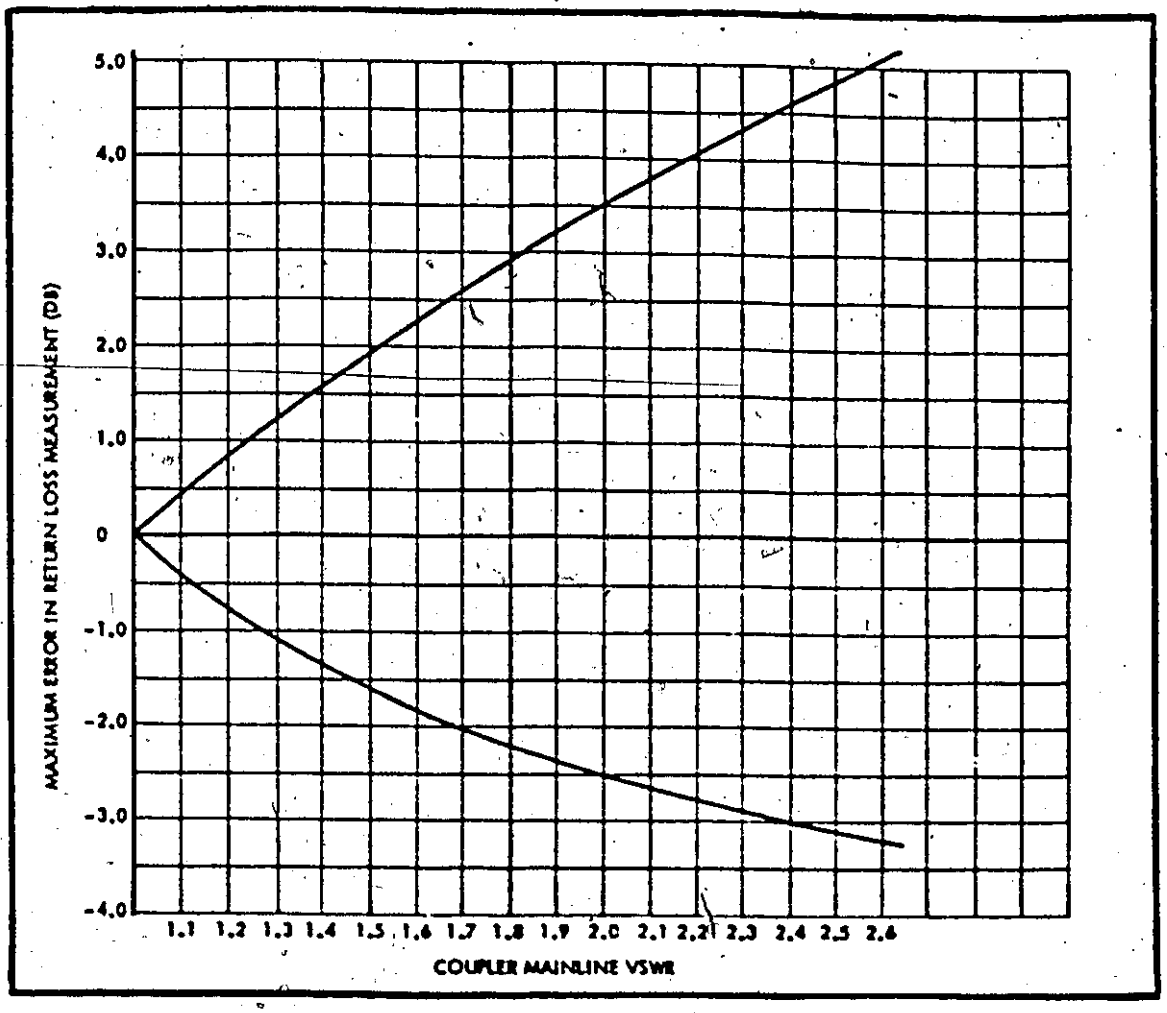

The portion of the reflected signal "robbed" from the reflected power coupler because of reflection at the coupler primary output port, due to mainline VSWR, is given by $(E_{in}\ \rho_L\ \rho_{ML})$; where ρ_{ML} = reflection coefficient of reflected power coupler. Therefore: (12)

$$\rho_{measured} = \rho_L \pm \rho_L\ \rho_{ML} = \rho_L\ (1 \pm \rho_{ML}) \quad (13)$$

$$\text{Indicated Return Loss} = -20 \log \rho_L - 20 \log (1 \pm \rho_{ML}) \quad (14)$$

$$\text{db error} = -20 \log (1 \pm \rho_{ML}) \quad (15)$$

This is the equation used to plot Figure

A convenient expression of mainline VSWR error in terms of the reflection coefficient is as follows:

$$\rho_{\substack{error \\ increment}} = \pm \rho_L\ \rho_{ML} \quad (16)$$

Figure 4.1-5: Maximum + and - dB Error in Return Loss Measurements Due to Mainline VSWR Effects.

An initial calibration procedure with S/C and O/C loads allowed all measurement errors to be subtracted out except for the Singer 8000/7051 ratiometer instrumentation error. This amounted to .4 dB or 2% errors—whichever was the greatest. For return loss measurements, this led to about 2% or 3% errors in the reflection coefficient values obtained from the Alfred nomograph. However, for transmission loss measurements of 0.4 dB to 3.0 dB, 100% to 13% errors were involved. This made the interpretation of attenuation measurements in each coplanar sample rather difficult. The transmission loss was first corrected for mismatch loss as outlined in section 4.1.2. A linear regression analysis was then performed in order to obtain the best possible fit of a straight line through these corrected transmission loss data points.

4.2 Hewlett Packard Automatic Network Analyzer

4.2.1 General Description

The Hewlett Packard (HP) Automatic Network Analyzer combines the control and computational ability of a small computer with the amplitude and phase measurement capability of a network analyzer to form a very accurate and sophisticated measurement center for push button ease analysis, optimization, and design at microwave frequencies. The initial cost of computer hardware may be minimized by attaching the system to a local timeshare terminal, which then also yields a larger computing capability. This computational facility greatly enhances measurement accuracy.

Such a versatile system can automatically take measurement errors into account before the final measured values are displayed to the user. An array of complex error coefficients can be measured and stored during an initial calibration procedure. These coefficients represent the measurement errors of the system in accordance with a pre-selected HP error model. During the analysis of a particular device, the stored errors are automatically subtracted from the corresponding measured values, thus increasing the final accuracy, which depends mainly on the error model contained in the selected HP software programme. This software is conveniently written in a modified version of the BASIC computer language to allow for user-computer interaction.

The network analyzer section of the above system provides

amplitude and phase information which can be converted by the computer to VSWR, return loss, impedance, gain or attenuation, group delay, and h, y, z, or s parameters. Measured data can be fed directly into statistical or computer aided design programs. The results of such analyses can then be displayed automatically on a teletype terminal at the measurement site. Less accurate measurements may be made without the computational aids either from the network analyzer's CRT displays or by means of permanent traces takes via xy recorder equipment connected at the back of the network analyzer.

4.2.2 Basic Components of the HP Automatic Network Analyzer

Figure 4.2-1 shows a picture of the HP 8545A Automatic Network Analyzer facility, which was used on a timeshare basis with a CDC 6400 digital computer. The figure also shows an alpha-numeric Beehive-Keyboard-CRT terminal at the left of the network analyzer plus an extra sweeper at the top of the network analyzer. The various levels are to be described herein in six parts from top to bottom.

The top level of the system consists of an HP 8620A sweep oscillator mainframe into which an HP 8621A RF drawer is inserted at the right. The sweep oscillator is a completely programmable high frequency source. Wide or narrow bandwidths of continuous wave (CW) power can be investigated manually or automatically. A CW vernier allows precise settings of CW center frequencies in the bandwidths to be investigated. The RF drawer has at present a multiband capability with a total range from 0.1 to 4.2 GHz, which is actually subdivided into two overlapping bands of 0.1 to 2.0 GHz and 1.8 to 4.2 GHz.

Figure 4.2-1: Photograph of the Hewlett Packard 8545A Automatic Network Analyzer System.

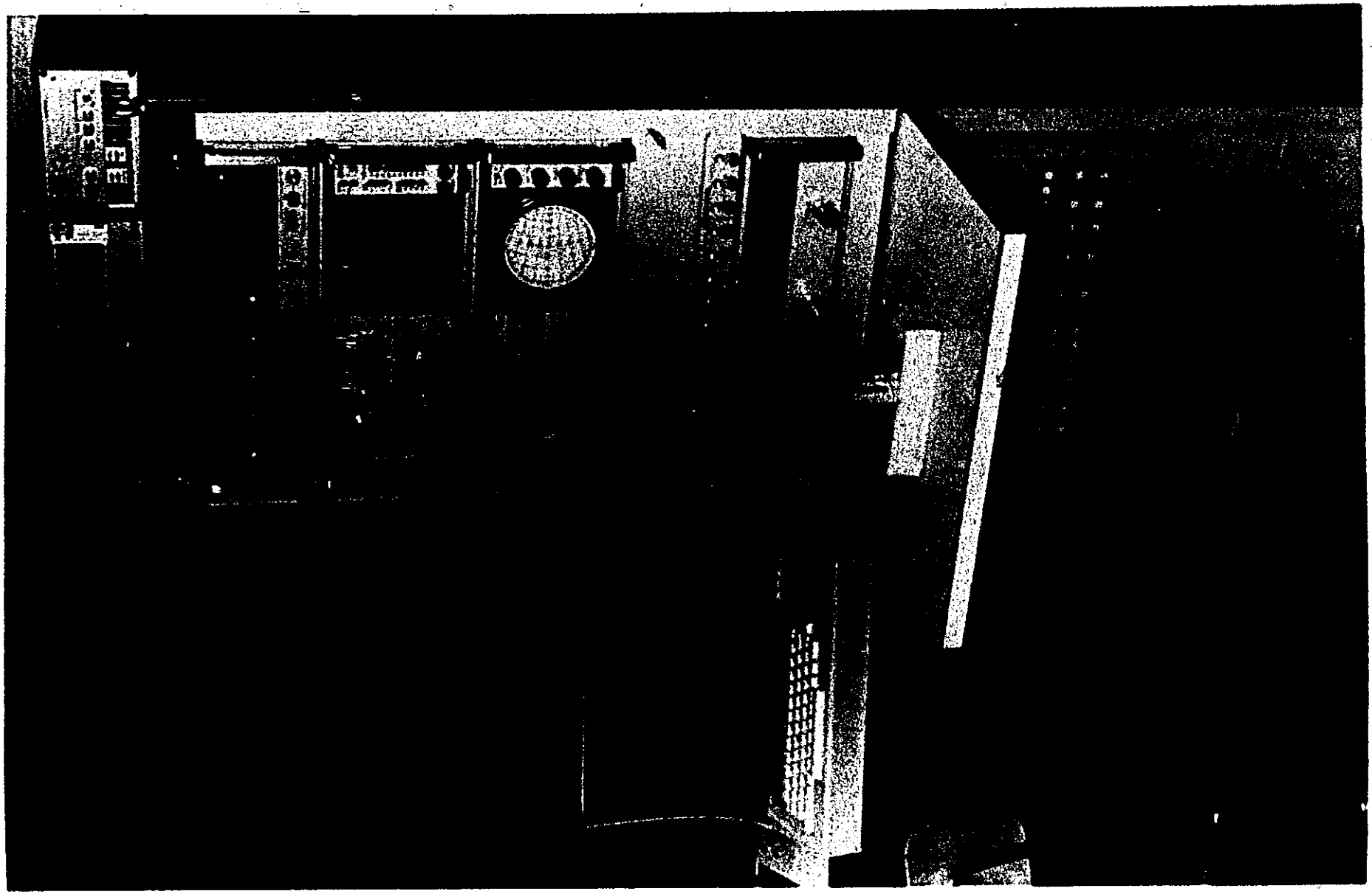

These two bandwidths are derived from two corresponding plug-in modules within the RF drawer. Plug-in modules which extend the upper frequency limit to 12.4 GHz are available and are soon to be acquired for the McMaster installation. For investigation of CPW performance, measurements herein have been limited to the 1-2 GHz range.

Level II of the HP 8545A Automatic Network Analyzer consist of the HP 8410A network analyzer mainframe, and the HP 8412A phase-magnitude display at the right of the mainframe. The network analyzer converts RF signals to lower frequency IF signals for processing. Tuning circuits, IF amplifiers and precision IF attenuators in the mainframe yield processed phase-magnitude information of high accuracy. This information is then presented on the HP 8412A phase-magnitude in dB and degrees where the phase is referenced to an imaginary variable plane positioned accurately between the test channel inputs. This data is plotted against frequency on the screen of this display. A polar plot of the same data is available on level three of the system. Permanent records of each plot are obtainable on compatable X-Y recorder equipment.

Level III consists of the HP 8410B network analyzer interface mainframe with the HP 8414A polar display drawer. The interface unit allows interaction between computer facilities and the network analyzer subsystem. The polar display presents amplitude and phase data in polar coordinates on a 5" CRT. Clear plastic overlays placed on the tube face enable the display to be used as a normal full sized Smith chart or as an expanded Smith chart for the determination of

reflection coefficients, VSWR, impedance or admittance.

Level IV contains the HP 85433A system control unit. From this unit the automatic or manual system mode can be selected. Also, two sweeper oscillators are used for a greater frequency range capability, the system control unit has provision for the selection of either of these two sweepers. A timeshare control section is also provided for monitoring and routing the flow of information between a timeshare terminal and the computer hardware of the HP 3545A Automatic Network Analyzer terminal.

Level V consists of an 8746B opt 002 S-Parameter Test Set (.5-12.4 GHz). This is actually a wideband RF power divider and reflectometer with a calibrated line stretcher and a selectable 0-70 dB attenuator. Two ports are accessible from the unit above a convenient work table for mounting the devices to be measured. The calibrated line stretcher allows a calibrated imaginary reference plane to be extended and positioned between ports 1 and 2 to a high degree of accuracy. The phase and magnitude information processed in level II of the system is referenced to this imaginary plane. The attenuator allows RF power to be scaled down in 10 dB increments from 0 dB to 70 dB with push-button ease. Each of the four S-Parameters between ports 1 and 2 can be selected for measurement by also depressing a push-button . Figure 4.2-1 shows the rectangular meandered line sample of design #2 mounted on the work table by means of the 3 mm coplanar waveguide launchers described in section 3.5. The sample is terminated with a 50 Ω load.

Level VI consists of the HP 2100A digital computer which can be used as a communication link between a timeshare terminal and the network analyzer in the automatic mode, or used for computations as well. It contains 4096 16 bit words of core memory, a self contained power supply and 14 input / output channels. Other features built into the 2100A include extended arithmetic instructions, power fail interrupt with automatic restart, memory parity chech with interrupt, and memory protect. It also has a direct memory access (DMA).

4.2.3 Measurement Errors

The measurement errors involved in measuring reflection coefficient and VSWR via the 8545A Network Analyzer in the manual mode are similar in nature to the corresponding errors obtained with the Singer instrumentation of section 4.1. However the directivities of the directional couplers in the 8545A are 25 dB or better over various frequency bands. A glance at Figure 4.1-4 will show that the error in return loss measurements due to coupler directivity would be approximately one half of the coupler directivity error on the Singer instrumentation of section 4.1, where 20 dB couplers were used. If the automatic mode is used these errors are automatically subtracted from the measured values and the resulting data is very accurate. For this thesis, the automatic mode was not available and so possible errors of 25% or better were expected from the manual mode due to coupler directivity. As a result

the 8545A network analyser was used in the manual mode mainly as a check on the Singer instrumentation measurements of section 4.1. The measured reflection coefficients were reasonably close in magnitude to the more accurate Singer instrumentation measurements of section 4.1.

4.3 Techniques

4.3.1 Introduction

With the advent of extremely fast rise time sampler plug in modules, Time Domain Reflectometry (TDR) has recently become a very useful analytical tool for designing and testing microwave circuits, microwave circuit components and transmission lines at frequencies as high as 12.4 GHz. The R, L, and C values of microwave components can be readily measured by observing reflection coefficient magnitudes and rise and fall times as small as 35 ps on a CRT display. The input and output impedance of circuits, connectors and transmission lines can also be readily observed. Any discontinuities due to line faults and bad contacts are easily discovered via TDR techniques so that maintenance checks are simplified. In the design area TDR techniques are a valuable asset since phase velocity, characteristic impedance, relative dielectric constants and large losses can be determined with ease. However, if moderate and small losses are to be measured, other measurements techniques must be used.

In this thesis, TDR techniques are used to measure characteristic

impedance, propagation time, phase velocity, and the effective relative dielectric constant in straight and meandered thin film CPW samples. The straight samples are only 1" long and the meandered samples are 2"-3" long. This makes the total losses in each sample quite small, even though thin films of metallic conductors are used. Transmission losses of 0.1 dB/in to 3.0 dB/in were typical magnitudes observed by means of the Singer instrumentation of section 4.1. TDR techniques were not useful for measuring such small losses reliably, though the total dc resistance of each sample, including contact resistance, could be estimated by a short circuited output test. Typical values of 5 to 10 Ω resistance per inch were obtained.

4.3.2 System Description

Figure 4.3-1 shows an HP 1415A TDR in an HP 140A oscilloscope mainframe. Connected to the output of the 1415A plug is a coplanar waveguide sample secured in a Wavetek mount, and terminated in a 50 Ω load. The 1415A TDR has a time resolution capability of 0.1 ns/cm though the system rise time is .15 ns. Differential time measurements can be made to within ±5% accuracy unless the rise time error of .15 ns is larger. The vertical scale, calibrated in terms of reflection coefficient values has a maximum resolution of .005/cm. Overshoot in the system is guaranteed to be less than 5% and the ringing in the system due to spurious inductance and capacitance is guaranteed to be less than 1/2 % over a period of time equal to 2 ns. The step generator output impedance is guaranteed to be 50 ± 1 Ω. The major drawback with this

Figure 4.3-1: The HP 1415A Time Domain Reflectometer Shown with a CPW Sample Secured in a Wavetek Mount Which is Terminated with a 50 Ω Calibrated Load.

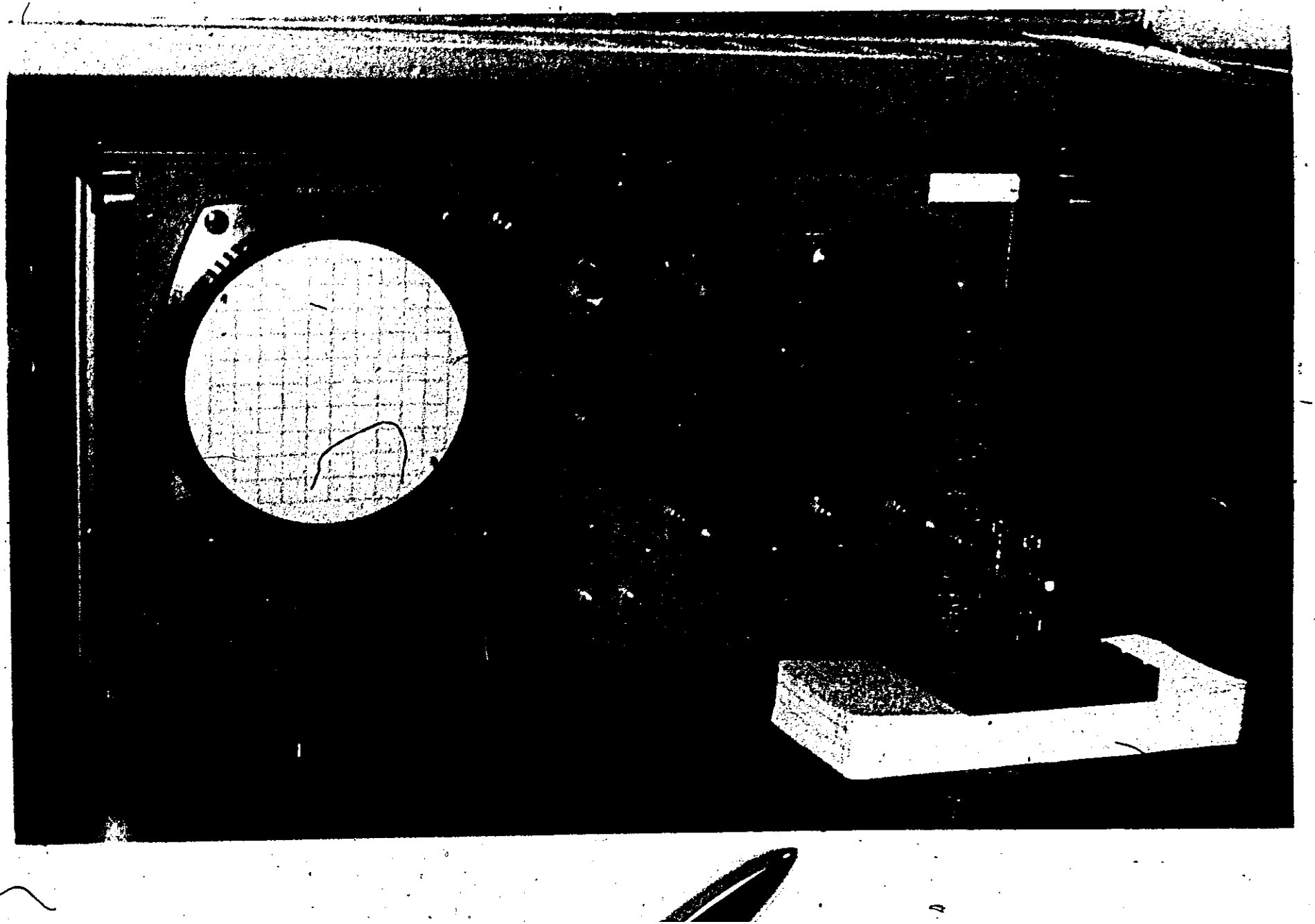

system for return propagation time measurements of 0.4 ns or less lies in the system rise time of .15 ns. This involves a measurement error of 37.5% or more. However, there is little noise or jitter in the 1415A system which allows discontinuities to be resolved clearly over periods of time larger than .15 ns.

Figure 4.3-2 shows an HP 1815B TDR/SAMPLER in an HP 181A storage oscilloscope mainframe and connected through a tunnel diode to an HP 1817A sampler. The 1817A sampler is shown in the foreground attached to a CPW sample which is mounted between two CPW launchers and terminated in a 50 Ω load. The 1815B TDR system has a total rise time of 35 ns though the 1817A sampler has a rise time of 28 ns. The horizontal time axis has a resolution of 0.01 ns/cm ± 3% but the 0.035 ns rise time determines the final accuracy. For this thesis it was assumed that the return propagation time measurements of 0.4 ns or less contained absolute errors of ± 35 ps. This TDR system was more accurate than the 1415A TDR system and was used to measure propagation times for the series A- and BCD- samples. As a result phase velocities and net relative dielectric constants were calculated for these samples with reasonable accuracy. The effect of substrate thickness was also studied by means of these measurements which led to a means of correcting the theory of Chapter II for practical design purposes.

Noise and jitter in the 1815B TDR/SAMPLER system was more apparent than in the 1415A TDR. Reflection coefficient traces also exhibited ringing effects and these had to be averaged. This was due to the higher time scale sensitivity of the 1815B system which tracked

Figure 4.3-2 : The HP 1815B Time Domain Reflectometer Shown with a CPW Mounted in the Foreground between Two CPW Launchers and Terminated with a 50 Ω Calibrated Load.

small capacitive and inductive effects quite well. A signal average switch was provided on the 1815B plug-in to make this problem easier to deal with, but then useful information could have been averaged out with the noise if care wasn't taken. As a result any XY recorder traces for this thesis were taken without the use of the signal averaging switch.

4.3.3 Measurement Techniques

The TDR techniques for this thesis supply involved the propagation of a very fast rise time voltage step through a test sample and its mount to a known termenation. The TDR CRT display was calibrated to read reflection coefficients directly. Three different terminations were used; a calibrated 50 Ω load, an open circuit, and a short circuit. The 50 Ω load could only be placed at the end of the test mount whereas the O/C could be placed at the actual input and output of each CPW sample and at the output of the mount. The S/C which was a piece of aluminum foil or a manufactured OSM 3 mm load could only be placed accurately at the input of the sample and the output of the mount respectively, due to size limitations. Whenever these loads are to be referred to in this thesis they will be designated by the following symbols; 50 Ω_{oo}, O/C_I, O/C_o, O/C_{oo}, S/C_I, S/C_{oo}. The double subscripts "oo" designate the output of the mount. The subscript "I" designates the input of the CPW sample and the subscript "o" designates the output of the sample.

TDR traces for the above six load conditions were recorded via an HP-Moseley 7030A XY recorder for various CPW samples. Expanded

recordings in the region of interest for a 50 Ω_{oo} termination were also taken. Care had to be excercized in order to ensure that the inherent overshoot of the XY recorder was not added to these permanent traces. From these records characteristic impedance could be measured quite accurately by averaging out any ringing effects. The dc resistance-plus contact resistance could be determined from the residual reflection obtained with the S/C_{oo} termination. The S/C_I termination was used for comparison purposes. The O/C terminations were used to measure return propagation times directly off the TDR oscilloscope screen since the XY recorder traces were considered less accurate for these small time measurements.

Since 26 samples were measured a large amount of experimental data was accumulated. Chapter V will simply summarize the important aspects of this data and the permanent records of the TDR measurements will be found in appendixes B, C, and D for reference purposes.

CHAPTER V

MEASUREMENTS AND IMPLICATIONS

5.0 General

The four different groups of instrumentation presented in the Chapter IV have led to simple guidelines for CPW design. Herein it will be shown that CPW's designed for the 1-2 GHz frequency band and fabricated with 96% Coors alumina, exhibit moderately low losses for thin aluminum films thicker than 10 kÅ. For these thin aluminum films contact loss is a more serious problem when the CPW's are only 1" or 2" long. Moreover, the propagation losses can be accurately predicted on a d.c. resistance basis. The measurements contained herein also lead to a reliable design approach for which C.P. Wen's theory [5] applies.

5.1 Singer Instrumentation Measurements

The Singer instrumentation described in section 4.1 of Chapter IV was especially useful for determining attenuation in CPW's as a function of thin film thickness at 1.5 GHz. Singer reflection measurements were also useful for determining the characteristic impedance of each CPW, but as will be seen in sections 5.2 and 5.4, TDR measurements were better suited to this purpose.

5.1.1 Approach to Singer Instrumentation Measurements

The Singer instrumentation described in Chapter IV could not be used to measure the attenuation and characteristic impedance of each CPW sample directly. Instead, a total frequency dependent transmission loss T_L and a net frequency dependent reflection coefficient magnitude $|\rho|$ were measured. It was therefore necessary to derive a suitable theory in section 4.1 which would extract the pertinent information from the Singer measurements in order to obtain attenuation and characteristic impedance for each CPW sample. Various theoretical curves were plotted and described in Appendix E for comparison with measured values. These values have been summarized graphically in Appendix D.

The theoretical curves of Appendix E first of all showed that the reflection and attenuation theory of section 4.1 was quite accurate in determining the shape of the $|\rho|$ vs frequency plots for the straight 1" CPW samples. It was found that a plot of $|\rho|/|\rho_i|$ against frequency from equation (4.1-8) determined the basic shape of a plot of $|\rho|$ vs frequency in the frequency band of interest. In Appendix E conditions for resonance and reinforcement between input and output reflections were derived. For low losses the peak value of $|\rho|/|\rho_i|$ in a wide frequency band had a value of approximately 2. This peak value was due to complete reinforcement of the input reflection with the output reflection. If α' was less than .05 Np/in $[|\rho|/|\rho_i|]_{max}$ ranged from 1.9 to 2.0 in 1" long samples. For α' less than .01 Np/in $[|\rho|/|\rho_i|]_{max}$ ranged from 1.99 to 2.0. For this latter range of α', $|\rho_i|$ was essentially frequency independent.

The best method to determine $|\rho_1|$ from the Singer instrumentation measurements on 1" long CPW samples was to take the peak value of $|\rho|$ in a wide frequency band and divide by 2 if the attenuation was less than .01 Np/in. This applied to film thicknesses larger than approximately 13.4 kÅ for 50 mil center strips, and 6.7 kÅ for 100 mil center strips. For thinner films of aluminum the theory showed that a slight correction of the $[|\rho|/|\rho_1|]_{max}$ values was necessary in order to account for the attenuation of the $|\rho|/|\rho_1|$ characteristic and the slight frequency dependence of $|\rho_1|$ in the frequency band of interest.

For the longer meandered samples, a comparison of the experimental results in Figure D.5 of Appendix D to the theory of Appendix E, for corresponding line lengths, showed that the shape of the measured $|\rho|$ curves corresponded only approximately to the theoretical curves. It should be remembered that the theory considered only input and output reflections. Any slight experimental discrepancies were thought to originate from small reflections in the detectors, connectors, bi-directional couplers of the measuring system and possibly the bends of the meandered lines. However, TDR measurements did not indicate reflections in the meandered line bends, and so small reflections internal to the Singer instrumentation were thought to be the cause of the above small discrepancies between theory and practice.

Contact resistance was not considered in the theory and this was thought to increase $|\rho_1|$. Loss measurements and TDR measurements showed significant contact resistance existed. A total d.c. resistance of as much as 3.8 Ω was measured by TDR techniques from Figure B.C5-F in Appendix B for a film thickness of 11.50 kÅ. A contact resistance of 1 Ω was expected.

A plot of $\frac{1}{2}|\rho|_{max}$ vs the inverse of thin film thickness t_f (kÅ)

is of interest since it indicates the amount of contact resistance and CPW mismatch as $1/t_f$ approaches zero. In interpreting such a graph it should be remembered that the graph essentially represents a plot of $|\rho_1|$ against $1/t_f$, if $t_f > 13.4$ kÅ for 50 mil wide center strips, and $t_f > 6.7$ kÅ for 100 mil wide center strips. For thinner films down to .7 kÅ, $\frac{1}{2}|\rho|_{max}$ underestimates $|\rho_1|$ slightly. For even thinner films the output reflected wave is attenuated significantly and when such attenuation is applied $|\rho'|/|\rho_1|$ approaches unity. At the same time $|\rho_1|$ becomes very large. A plot of $\frac{1}{2}|\rho|_{max}$ against $1/t_f$ is shown in Figure 5.1-1 for various series of samples. The data for this graph was taken from Appendix D. Deviations from a smooth curve likely came from varied contact resistance.

5.1.2 Extraction of Attenuation from Transmission Loss Measurements at 1.5 GHz

The data for transmission loss measurements summarized in Appendix D showed the necessity for mismatch loss corrections as defined by equation (4.1-22). This data clearly indicated that as $|\rho|$ increased, T_L also increased in magnitude. However, (4.1-22) neglects contact loss and this had to be subtracted out graphically after mismatch loss corrections were made. Figure 5.1-2 shows a least squares fit of the transmission loss data as a function of $1/t_f$ (kÅ)$^{-1}$ at 1.5 GHz for two CPW designs after mismatch loss corrections have been made. These two curves are then shifted to the origin to eliminate contact loss. For design BCD the average contact loss was measured to be .321 dB in 1" long CPW samples. For design A the average contact loss was measured to be .424 dB in 1" long samples. Notice that the widely employed practice of

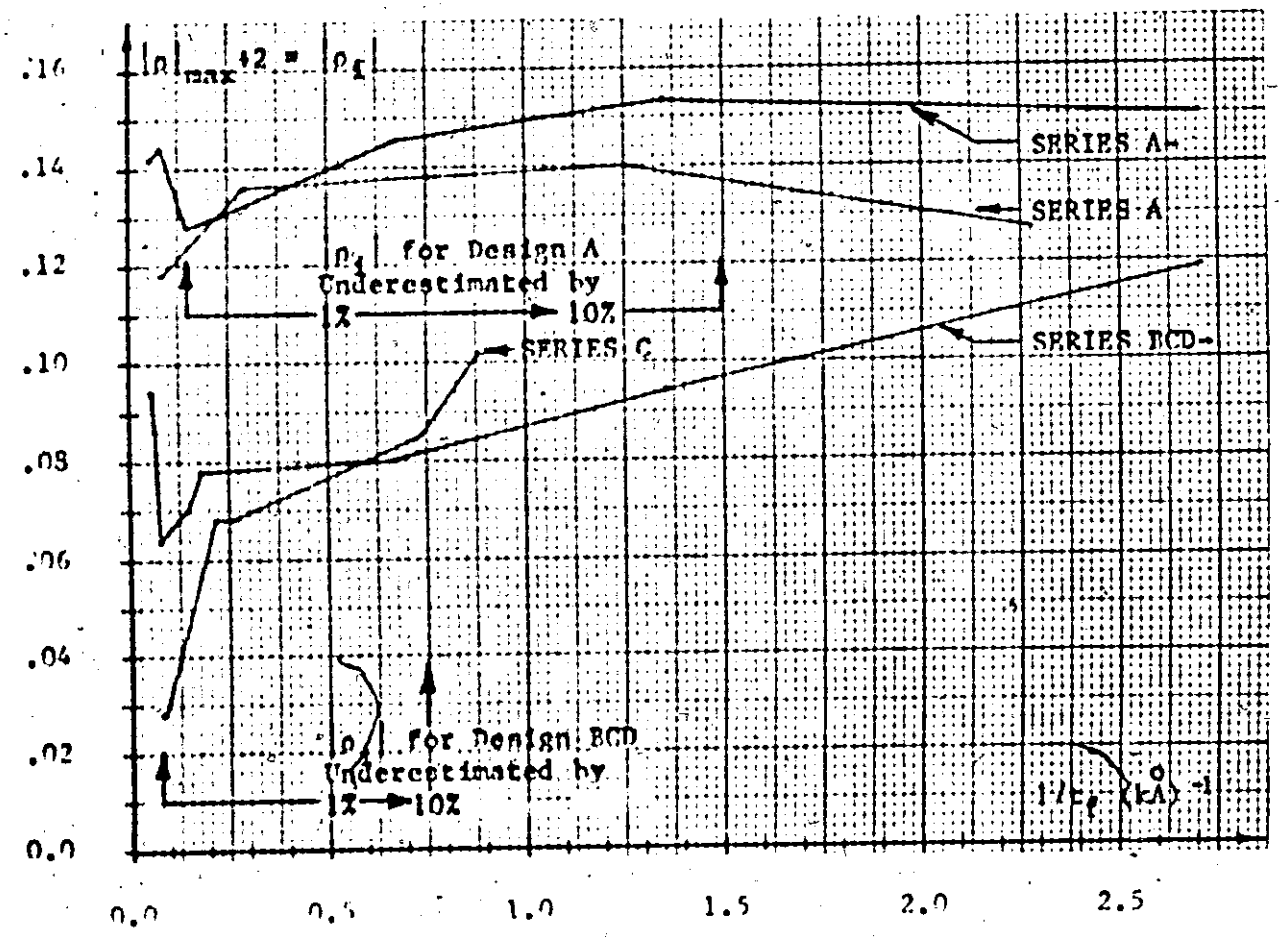

Figure 5.1-1: Estimation of $|\alpha_f|$ as a function of $1/t_f\ (k\delta)^{-1}$ from Singer Instrumentation Measurements.

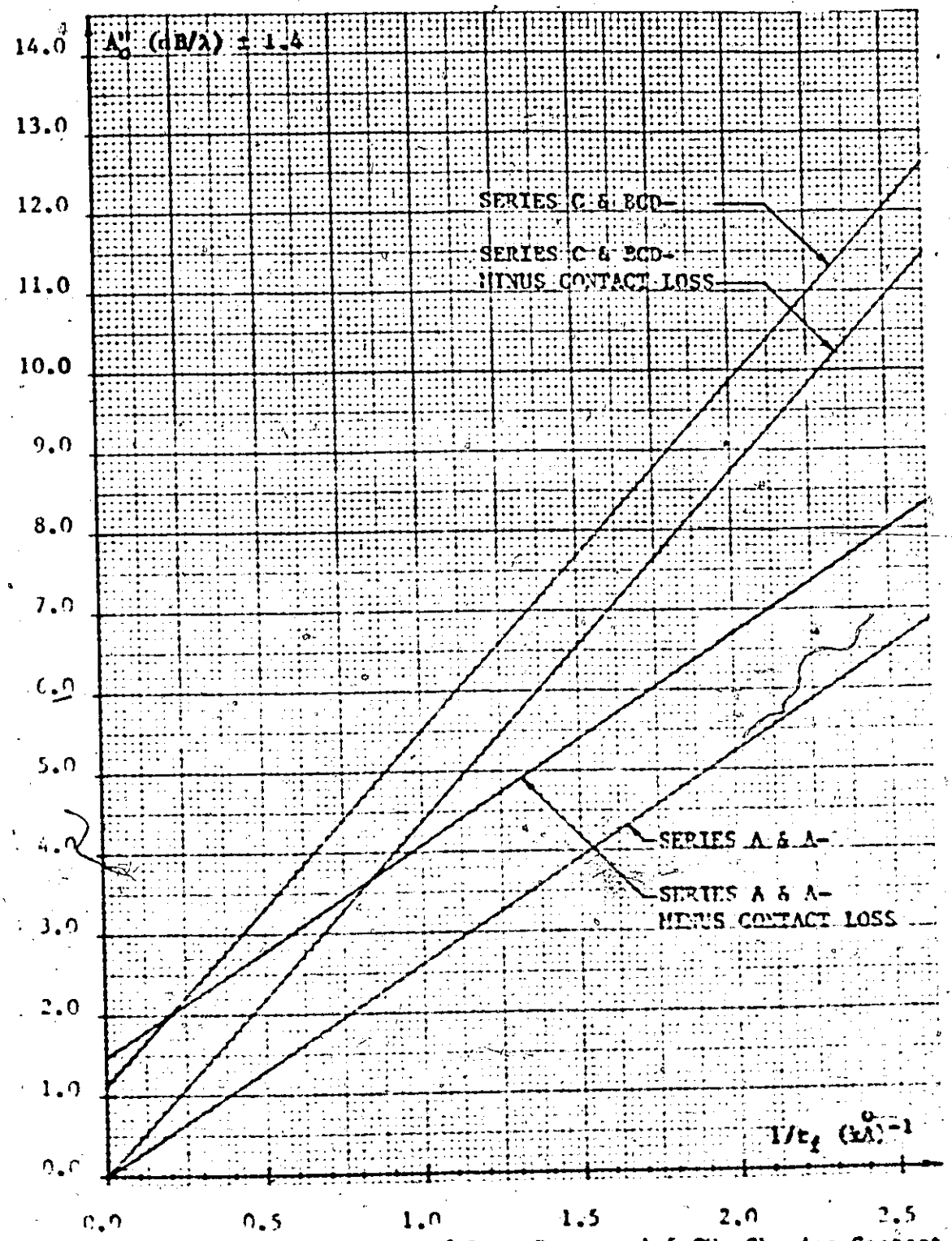

Figure 5.1-2: Least Squares Fit of Loss Data at 1.5 GHz Showing Contact Loss Correction.

normalizing loss values at a particular frequency with respect to wavelength at that frequency has been used. The wavelength employed here at 1.5 GHz is 3.4867", where $\epsilon_r = 9.2$.

The curves through the origin of Figure 5.1-2, which represent transmission loss values corrected for both mismatch loss and contact loss, were replotted as a function of t_f on a log-log basis in Figure 5.1-3 for comparison with theoretical curves placed on the same graph. The dashed lines indicate that measurements were made for thin film thicknesses up to 18 kÅ only, and extrapolation beyond this value is not necessarily valid since it is expected that the lines will level off to a fixed attenuation value when film thickness exceeds one skin depth. The original experimentally measured transmission loss data is also shown on the graph with an appropriate legend shown at the right to enable the behaviour of each series of samples to be distinguished. As outlined in section 2.4 of Chapter II, the theoretical curves were calculated on a d.c. resistance basis, assuming a uniform current distribution in the ground planes. The average percentage deviation in the least squares fit of corrected experimental points was calculated to be about ±18.2% for series C and BCD- combined, and ±17.2% for series A and A- combined. The average percentage error in thin film thickness was estimated to be ±12.3%.

Several trends should be noticed in Figure 5.1-3. First of all, there appears to be a wide scattering of transmission loss data which can be attributed to variations in contact loss from sample to sample, variations in mismatch loss from sample to sample, and measurement errors

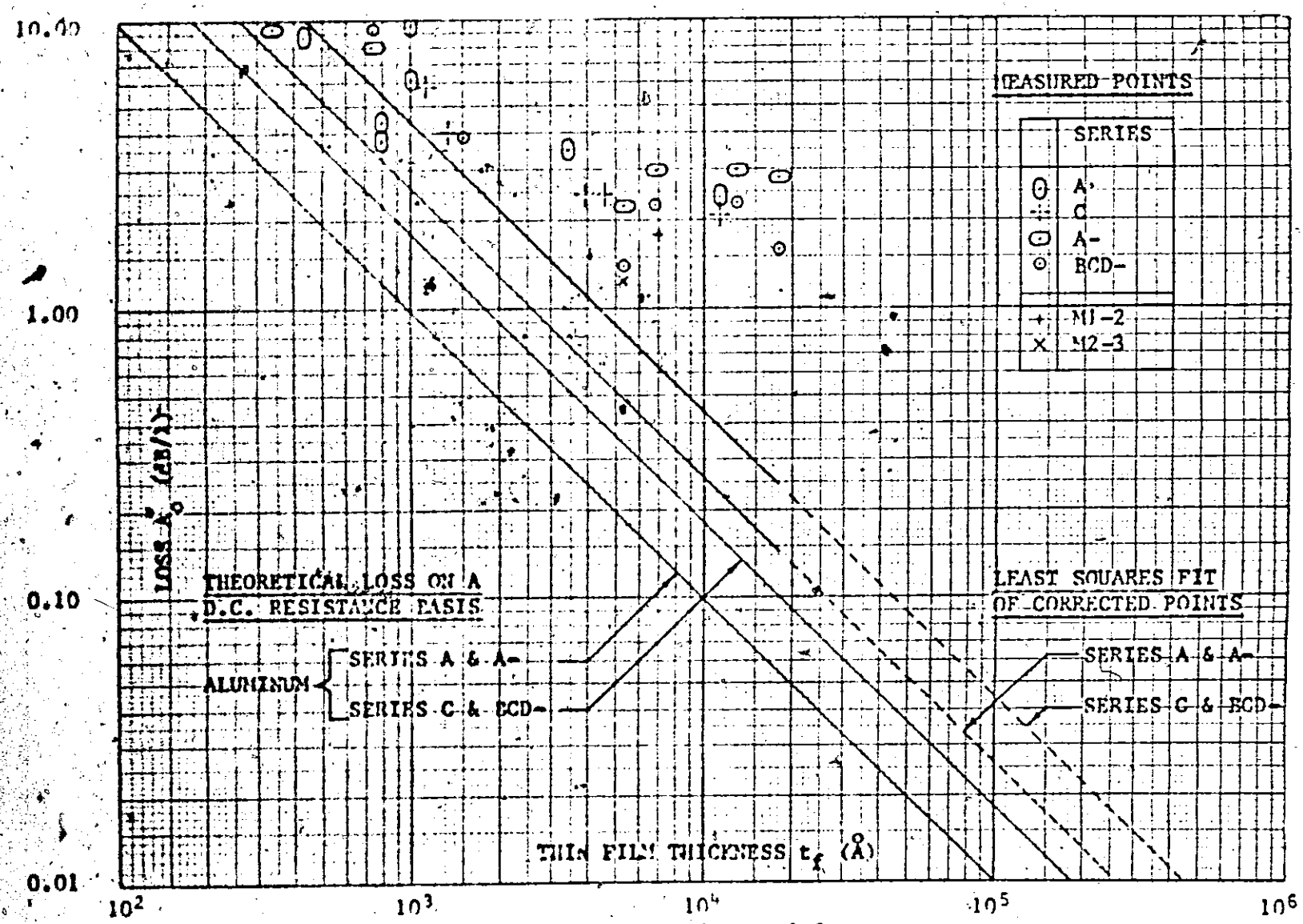

Figure 5.1-3: Losses in Thin Film Coplanar Waveguides at 1.5 GHz as a Function of Film Thickness.

as large as ±1.4 dB/λ. Secondly, one should notice that as t_f increases beyond 4 kÅ, the transmission loss data levels off to an average value of about 2.5 ± 1.4 dB/λ or .717 ± .4 dB/in. This appears to be due to mismatch loss and especially the large contact loss values which were extracted from the least squares fit in Figure 5.1-2. Thirdly, it is clear that the theoretical loss curves underestimate the corresponding least squares curves by a significant amount; by a factor of approximately 2.63 for design A and 2.44 for design BCD. The fact that the slopes of these curves appear equal is not experimentally significant since a log-log plot of any pair of distinct variables always has a slope of ±1.

5.1.3 Accounting for Discrepancies between Theoretical and Corrected Measured Losses

Initially, two major effects were thought to be possible causes of the 2.5 factor discrepancy between the theoretical and corrected measured losses of Figure 5.1-3. What if the actual thin film resistivity was larger than the bulk value of 2.62×10^{-6} Ω-cm used for the theoretical loss calculation at 20° C? Also, could it not be possible that the higher measured losses were also in part due to most of the ground plane current lying in a narrow region in each ground plane at the edge closest to the center strip of the CPW, rather that being uniformly distributed in the ground planes?

The first of these two possibilities was investigated by measuring thin film resistivity with a Sanwa model 360-R-1 multimeter. The d.c

resistance in the center strip of each series A- and BCD- samples was measured and plotted against $1/t_f\ (k\mathring{A})^{-1}$. A linear regression analysis of this data was performed to yield an average slope for each of the two aforementioned series of samples. For the thin aluminum films of series A- this led to an average measured d.c resistivity which was 2.82 times the bulk value of 2.62×10^{-6} Ω-cm. For series BCD-, the measured thin film dc resistivity was 2.54 times the bulk value for aluminum. The overall average resistivity factor for both series was 2.68 ± 5.22%.

In order to check to what extent the higher measured thin film resistivities accounted for the high measured losses, Table 5.1-1 was drawn up. The theoretical and measured values of attenuation $A_o''\ d\Gamma/\lambda$ from Figure 5.1-3 were inserted in the table for the combined series A and A- and the combined series C and BCD-. From the measured values of A_o'' and Figure 2.4-4, the corresponding distributed resistance R_{meas} (Ω/m) was obtained and inserted into the table. Similarly, the theoretical losses of Figure 5.1-3 led to the distributed resistance R_{CSG} for center strip and ground planes combined. For infinite ground planes, Figure 2.4-5 was used in conjunction with Figure 2.4-4 to yield R_{CS} values corresponding to center strip losses. R'_{CS} and R'_{CSG} represented the values of R_{CS} and R_{CSG} corrected for the high measured thin film resistivities obtained previously for series A- and series BCD-. The ratios R_{meas}/R_{CS} and R_{meas}/R_{CSG} were of the order of 3.3 to 2.5, whereas the first resistivity corrected ratio R_{meas}/R'_{CS} was only slightly larger than unity and the second resistivity corrected ratio R'_{meas}/R'_{CSG}

Combined Series	C and BCD-	A and A-
Measured Value of A''_o (dB/λ) @ t_f = 10.0 ± 1.23 kÅ	.44 ± .080	.258 ± .044
Theoretical Value of A''_o (dB/λ) @ t_f = 10.0 ± 1.23 kÅ	.18	.099
R_{meas} ± 18% (Ω/m)	57.0 ± 17.5 %	33.5 ± 16.5%
R_{CS} (Ω/m)	21.0	10.2
R_{CSC} (Ω/m)	23.0	12.8
R'_{CS} ± 5% (Ω/m)	53.3 ± 5.22%	28.8
R'_{CSC} ± 5% (Ω/m)	58.5 ± 5.22%	32.2
R_{meas}/R_{CS}	2.71 ± 17.5 %	3.25 ± 16.5%
R_{meas}/R_{CSC}	2.48 ± 17.5 %	2.62 ± 16.5%
R_{meas}/R'_{CS}	1.07 ± 22.7 %	1.16 ± 21.7%
R_{meas}/R'_{CSC}	0.98 ± 22.7 %	1.04 ± 21.7%

Table 5.1-1: Accounting for High Loss Measurements in Two CPW Designs with Thin Film Resistivity Corrections by Comparing the Measured Distributed Resistance R_{meas} to the Theoretical Distributed Resistances R_{CS} in the Center Strip, R_{CSC} in the Ground Planes and Center Strips, as well as the Corresponding Resistivity Corrected Values R'_{CS} and R'_{CSC}.

was surprisingly close to unity. Furthermore, ranges of uncertainty for these ratios were estimated to vary from ± 16.5% to ± 22.7% in the table. In other words, the higher measured thin film resistivities totally accounted for the approximate 2.5 discrepancy factor between high measured losses and lower theoretical losses within experimental error.

The possibility of ground plane currents lying in a narrow region of the ground planes near the center strips was not detected via Table 5.1-1, implying that if this effect did exist, its contribution to discrepancies between theoretical and experimental losses was smaller than the experimental error of 22.7% and hence not detectable. For instance, if the ground plane currents lay within a region of width $b-a_1$ in each ground plane, the actual measured losses would have been twice the value of the theoretical resistivity corrected losses obtained for the infinite ground plane case; ie R_{meas}/ρ'_{CS} would have had a value of 2.0 within ± 22.7% error. Since the value R_{meas}/ρ'_{CSG} involved finite ground plane loss calculations as well as resistivity corrections, and since this same ratio turned out to be unity within 22.7% error, it appears that for practical loss calculations uniform ground plane currents can be assumed, and the loss theory of section 2.4 of Chapter II is valid for thin films.

5.1.4 Conclusions Drawn from Singer Instrumentation Measurements

The Singer Instrumentation measurements first of all illustrated the importance of understanding the limitations of the measuring equipment. For instance, it was necessary to know that the modulus of a net reflection

coefficient $|\rho|$ was being measured and not $|\rho_1|$ or $|\rho_o|$. In the case of the meandered samples, theoretical considerations showed that additional small reflections probably originating in the Singer Instrumentation could be detected. The theory of Appendix E predicted the shape of the measured $|\rho|$ vs frequency plots quite well for straight 1" long CPW samples where reflections were large over the entire 1-2 GHz band whereas the experimental curves of Figure D.5 appeared slightly distorted in regions of the 1-2 GHz frequency band where reflections were small.

Secondly, the treatment of the experimental data for extracting pertinent information about the various CPW designs required much consideration. For example, how much experimental deviation from a smooth curve performance was due to randomly efficient electrical contacts and how much of the experimental variation was due solely to experimental error? How could the experimental data be best treated statistically? What would be the resulting average deviation? Would this average deviation be small enough to allow meaningful conclusions about the various CPW designs to be drawn? As it turned out, all of these questions were answered and a least squares fit of the loss and resistivity data led to meaningful conclusions about losses in thin film CPW structures.

It was shown from the theory of Appendix E that $\frac{1}{2}\cdot|\rho|_{max}$ was a good estimate of $|\rho_1|$ within 10% error for films thicker than the amount specified in Figure 5.1-1. For the design A samples the values of characteristic impedance corresponding to the range of $|\rho_1|$ values in the same figure varied approximately from 64 Ω to 68 Ω. For the design BCD samples, the characteristic impedance varied mainly from 57 Ω to 64 Ω.

As would be expected the term $\frac{1}{2}|\rho|_{max}$ increased gradually with decreasing thin film thickness but simultaneously $|\rho_i|$ was underestimated more significantly by this term. CPW samples with very thin films of aluminum less than about 1 kÅ in thickness exhibited a significant attenuation of the output reflected wave, consequently causing $\frac{1}{2}|\rho|_{max}$ to underestimate $|\rho_i|$ by about 10% or more.

The lower bound of the aforementioned range of characteristic impedance values indicates that for thick aluminum films, both design A and design BCD samples exhibit an impedance mismatch relative to a 50 Ω line. A mismatch of about 7 Ω is exhibited by design BCD samples and a mismatch of about twice this value is exhibited by design A samples. In section 5.4, TDR measurements will be used to show that this mismatch is due to a finite substrate thickness less than the width of the center strip, and that the 100 mil wide center strip of design A samples causes a mismatch problem about twice as significant as the 50 mil wide strip of the design BCD samples.

The Singer instrumentation also allowed the losses in design A and design BCD samples to be measured as a function of thin film thickness from 0.35 kÅ to 18.0 kÅ with reasonable accuracy. This accuracy was enhanced by knowledge of mismatch loss, contact loss and linear regression analysis. Final corrections were made from resistivity information obtained from a linear regression analysis on thin film resistivity data. It was found that as far as loss calculations were concerned, ground plane currents for both A and BCD designs appeared to be uniformly distributed within the ground planes. An approximate 23% range of

uncertainty was proposed along with these conclusions due to deviation of the loss and resistivity data from a smooth curve performance, but since statistical averaging techniques were used throughout the work, this uncertainty is likely to be much less than 23%. This is evidenced by the fact that in Table 5.1-1, R_{meas}/R'_{CS} and R_{meas}/R'_{CSG} both turned out to be very close to unity for both combined series of samples.

5.2 Results of TDR Reflection Coefficient Measurements

Reflection coefficient information taken from the numerous TDR traces recorded in Appendices B and C is summarized in this section. A total of 26 CPW samples were measured using TDR techniques. The resulting TDR data may be separated into two major groups. The summarized data from these two groups will be compared to the Singer instrumentation measurements summarized in Figure 5.1-1 of section 5.1.

5.2.1 First Group of TDR Data

The first group of TDR data consists of series A and series C samples fabricated by masking techniques as discussed in section 3.2.2 of Chapter III. All of these samples were mounted in the Wavetek microstrip test fixture as in Figure 3.5-2 and measured by means of the HP 1415A TDR. The corresponding TDR traces were recorded in Appendix D for reference purposes. The rise time of this TDR system was approximately 150 ps and the return propagation time for the measured samples was about 400 ps. It was then possible to measure reflections at the input of these short 1" long CPW samples quite accurately.

Table 5.2-1 summarizes this reflection data with respect to thin film thickness t_f and characteristic impedance Z_o for each sample. The symbol $|\rho_i|$ simply represents input reflection coefficient. Values of Z_o ranging from 55.5 Ω to 71.0 Ω were obtained for series C samples, and values of Z ranging from 63.5 Ω to 81.5 Ω were obtained for series A samples. At first glance, it appears that series C samples were better because they had characteristic impedance values closer to 50 Ω. However, some of the series A samples had thinner films than the series C samples and a plot of reflection coefficient vs the inverse of thin film thickness is more instructive.

Figure 5.2-1 illustrates this technique. The first apparent property of the reflection data points is that they exhibit a wide scattering. This was thought to be mainly due to the variability of contact resistance associated with the Wavetek microstrip test fixture. It could also have been due to varied specular migration from sample to sample since this also varies randomly. Less scattering of data points was obtained with the samples fabricated by means of direct photographic etching and mounted by means of the CPW launchers, as will be seen when the second group of data is looked at. Secondly, the reflection coefficient increases with decreasing thin film thickness due to a corresponding increase in distributed resistance. Also, the data appears to have a non-zero intercept on the $|\rho_i|$ axis. This indicates that even for thicker aluminum films of 20 kÅ or more, a finite reflection coefficient would be obtained for the same design geometry. A linear regression analysis has been used to estimate the intercept for both series of samples.

Sample	$\lvert\rho_1\rvert$	$Z_o(\Omega)$	t_f(nS)
A_{12}	.258	74.5	0.796 ± 0.098
A_{23}	.159	69.0	1.015 ± 0.125
A_6	.239	81.5	0.438 ± 0.054
A_8	.163	69.5	1.330 ± 0.164
A_{10}	.119	63.5	1.60 ± 1.43
A_{11}	.157	69.0	3.44 ± 0.423
C_2	.139	66.0	1.357 ± 0.167
C_3	.129	65.0	3.905 ± 0.481
C_4	.099	61.0	4.593 ± 0.565
C_5	.053	55.5	11.50 ± 1.41
C_6	.172	71.0	1.133 ± 0.139

Table 5.2-1: Tabulation of the 1415A TDR Measurements of the Input Reflection Coefficient $\lvert\rho_1\rvert$, for Series A and Series C CPW Samples, Mounted by means of the Wavetek Microstrip Mount.

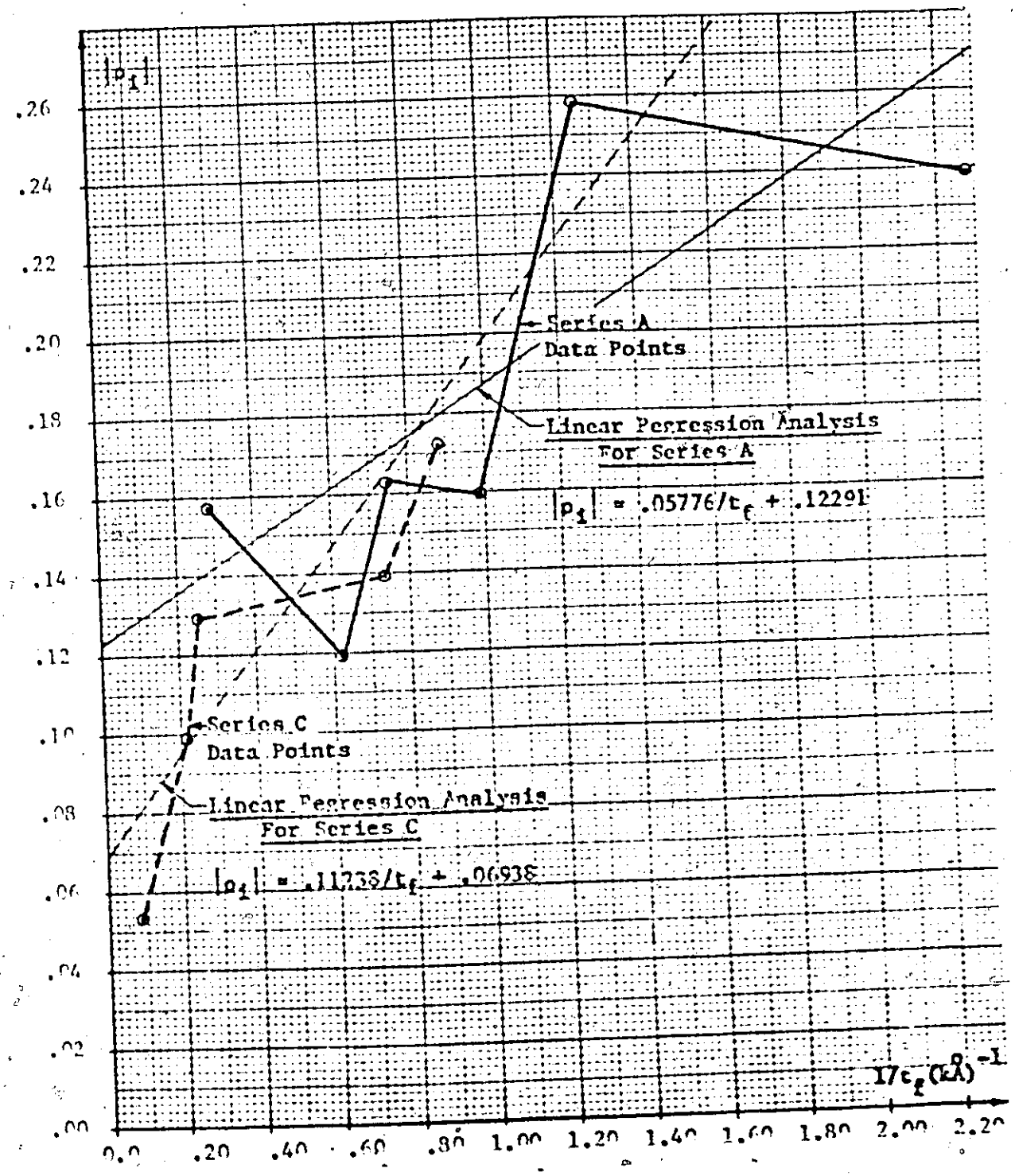

Figure 5.2-1 : Plot of the 1415A TDR Measurements of the Input Reflection Coefficient $|\rho_1|$, vs the Inverse of Thin Film Thickness $1/t_f$, for Series A and Series C CPW Samples, Mounted by means of the Wavetek Microstrip Mount.

Series A given a reflection coefficient of .123 for infinitely thick aluminum films and series C gives a reflection coefficient of .069 for infinitely thick aluminum films. These residual reflection coefficients correspond to characteristic impedance values of 64 Ω and 57.5 Ω for series A and series C respectively.

In other words, if design A or design C were fabricated with aluminum films thicker than 20 kÅ, a residual reflection coefficient would be measured because of contact resistance, geometrical tolerances or a significant deviation of ϵ_r from the design value of 9.2. Since the CPW geometry was carefully shaped in accordance with tolerance specifications of Chapter II, contact resistance, and a deviation in ϵ_r, are most likely the causes of this residual mismatch. In fact, the contribution of ϵ_r to this problem is most significant and will be clarified in detail in section 5.4.

The effect of ϵ_r will only be discussed briefly here. The fact that the residual mismatch is about twice as large for series A samples than for series C samples is quite important. Series A samples employ a center strip which is approximately 100 mils wide whereas series C samples employ a center strip about half as wide:50 mils. The substrate thickness is in turn half this latter figure:25 mils. This finite substrate thickness makes ϵ_r dependent on center strip width since theoretical considerations assumed an infinitely thick dielectric substrate, and the actual dielectric substrate consists of a 25 mil thickness of alumina followed by a thick underlying layer of air. This tends to reduce the actual relative dielectric constant, which in turn increases the characteristic impedance of the CPW. Knowledge of this effect promises to make

possible the accurate design of CPW's within specified characteristic impedance levels.

Comparison of Figure 5.2-1 with corresponding curves in Figure 5.1-1 will show that the 1415A TDR measurements of the series A and series C samples are compatible with the Singer instrumentation measurements of the same samples for values of t_f larger than 1 kA. For t_f smaller than 1 kA the Singer instrumentation measurements appear to underestimate the TDR measurements significantly. Notice also that approximately the same residual reflections occur for $1/t_f=0$ in both diagrams, again illustrating consistancy between the results obtained from two different types of instrumentation. However, the TDR methods appear to be generally better because of the ease with which the TDR results can be interpreted accurately.

5.2.2 Second Group of TDR Data

The second group of TDR measurements were made on 2 meandered samples plus A- and PCD- samples, all fabricated by direct photographic etching techniques as discussed in section 3.2.3 of Chapter III. All of these samples were mounted by means of CPW launchers as in Figure 3.5-5 and measured by means of the HP 1815P TDR/SAMPLER. The corresponding TDR traces were recorded in Appendix C for reference purposes. The rise time of this TDR system was approximately 35 ps and the return propagation time for these measured samples was about 360 ps. It was therefore possible to measure reflections in these short 1" long CPW samples very accurately. Since the rise time of this new TDR system was approximately four times

smaller than the rise time of the HP 1415A TDR, the new TDR system was in comparison quite sensitive to small discontinuities in the samples, launchers, and connectors. The TDR traces for this group of samples were as a result not as smooth as the traces obtained with the HP 1415A TDR.

In fact, the high sensitivity of the new TDR system enabled a slight impedance mismatch to be detected at the junction between each CPW launcher center pin and the CPW sample center strip. The mismatch was thought to be due to the transition from a cylindrical conducting center pin to the flat conducting center strip of the CPW samples. Due to the skin effect, high frequency currents were forced to make a transition from a cylindrical shell of 50 mils diameter to a rectangular shell less that 20 kÅ thick. It was believed that this problem could have been eliminated by gradually tapering the cylindrical center pin to a flat edge with a file. This was an added refinement which was not attempted in this thesis. Significant reflection and propagation data was still obtained without this refinement. The small ripple in the TDR trace due to the slight center pin-center strip mismatch was simply regarded as a small measurement error, and the extreme values of the reflection coefficient in this ripple were recorded so that the average value could be taken.

Table 5.2-2 summarizes this set of data in terms of sample name, extremes in input reflection coefficient $|\rho_1|$ and measured characteristic impedance Z_0, average characteristic impedance $\bar{Z}_0$, and thin film thickness t_f(kÅ). Measurements were also made for the same samples with twice the substrate thickness. For one substrate thickness values of $\bar{Z}_0$ ranging from 61.1 Ω to 78.0 Ω were obtained for series A- samples, and values of $\bar{Z}_0$

Sample and no. of Substrates		$\lvert\rho_f\rvert$ Min → Max	$Z_o(\Omega)$ Min Max	$\bar{Z}_o(\Omega)$	$t_f(k\mathring{A})$
A-3	1	.137→.201	66.0→75.0	70.5± 4.5	5.340 ± 0.657
	2	.120→.160	64.0→69.0	66.5± 2.5	
A-2	1	.112→.150	63.0→67.5	65.2± 2.3	6.877 ± 0.846
	2	.081→.132	59.0→65.5	62.3± 3.3	
A-6	1	.108→.128	62.0→64.5	63.3± 1.3	12.826 ± 1.283
	2	.053→.081	56.0→59.0	57.5± 1.5	
A-11	1	.149→.192	67.5→72.0	69.8± 2.3	18.011 ± 2.216
	2	.073→.105	58.0→62.0	60.0± 2.0	
A-8	1	.111→.152	62.5→68.0	65.3± 2.8	1.509 ± 0.186
	2	.068→.116	57.0→63.0	60.0± 3.0	
A-9	1	.099→.172	61.0→70.5	65.8± 4.8	0.739 ± 0.091
	2	.062→.160	56.5→69.0	62.8± 6.3	
A-10	1	.168→.265	70.0→86.0	78.0± 8.0	0.369 ± 0.045
	2	.125→.220	64.5→78.0	71.3± 6.8	
BCD-3	1	.029→.108	53.0→72.0	62.5± 9.5	5.340 ± 0.657
	2	-.003→.073	49.7→58.0	53.9± 4.2	
BCD-2	1	.027→.085	52.8→59.0	55.9± 3.1	6.877 ± 0.846
	2	.001→.072	50.1→58.0	54.1± 4.0	
BCD-6	1	.006→.071	50.6→58.0	54.3± 3.7	12.826 ± 1.283
	2	-.006→.076	49.4→58.0	53.7± 4.3	
BCD-11	1	.021→.091	52.2→60.0	56.1± 3.9	18.011 ± 2.216
	2	-.009→.071	49.1→58.0	53.6± 4.5	
BCD-8	1	.034→.114	53.6→63.0	58.3± 4.7	1.509 ± 0.186
	2	.008→.094	50.8→60.5	55.7± 4.9	
BCD-9	1	-.027→.189	48.6→73.0	60.8±12.2	0.739 ± 0.091
	2	-.027→.170	48.6→70.5	59.6±11.0	
BCD-10	1	.133→.302	65.5→93.0	79.3±13.7	0.369 ± 0.045
	2	.101→.289	61.5→90.0	75.8±14.3	
M1-2	1	.000→.063	50.0→57.0	53.5± 3.5	6.876 ± 0.846
	2	-.012→.039	48.8→54.0	51.4± 2.6	
M2-3	1	.008→.072	50.8→58.0	54.4± 3.6	5.340 ± 0.657
	2	-.005→.053	50.5→55.5	53.0± 2.5	

Table 5.2-2: Tabulation of the 1815P TDR/Sampler Measurements of the Input Reflection Coefficient $\lvert\rho_f\rvert$, for Series A- and Series BCD- Samples, with 1 and 2 Substrate Thicknesses of 25 Mils Each and Mounted by Means of the New CPW Launchers.

ranging from 54.3 to 79.3 Ω were obtained for series PCD- samples. The two meandered samples indicated $\overline{Z}_o$ values of 53.5 Ω and 54.4 Ω. When the substrate thickness was doubled by the insertion of an extra substrate beneath each sample, and in close contact with each sample, $\overline{Z}_o$ was reduced significantly toward 50 Ω. It was assumed that increasing the substrate thickness to a large value and using thin films of 1 skin depth or more would enable a 50 Ω line to be achieved. In practice making the substrate thickness four or five times the center strip width would be sufficient to achieve this purpose, as will be seen in section 5.4.

Figures 5.2-2 and 5.2-3 summarize the important aspects of the data from table 5.2-2. The first apparent property of the data points is a slight scattering due to measurement error and variability of contact resistance associated with the CPW launchers. This scattering of data points appears to be less than the amount of scattering obtained from the first group of data for samples mounted by means of the wavetek microstrip mount. The reflection coefficient in Figures 5.2-2 and 5.2-3 increases slowly with decreasing film thickness. This is due to a corresponding increase in thin film distributed resistance with decreasing thin film thickness. Thirdly, the data appears to have a non-zero intercept on the $|\rho_1|$ axis indicating a residual mismatch due to contact resistance, geometrical tolerances, and a significant deviation of ϵ_r from the design value of 9.2. Series A- and PCD- samples exhibit a residual reflection coefficient of about .1130 and .0435 respectively corresponding to characteristic impedance values of 63 Ω and 54.5 Ω. These values are just slightly less than the corresponding values obtained for the series A and series C samples in section 5.2-1. As previously discussed for the

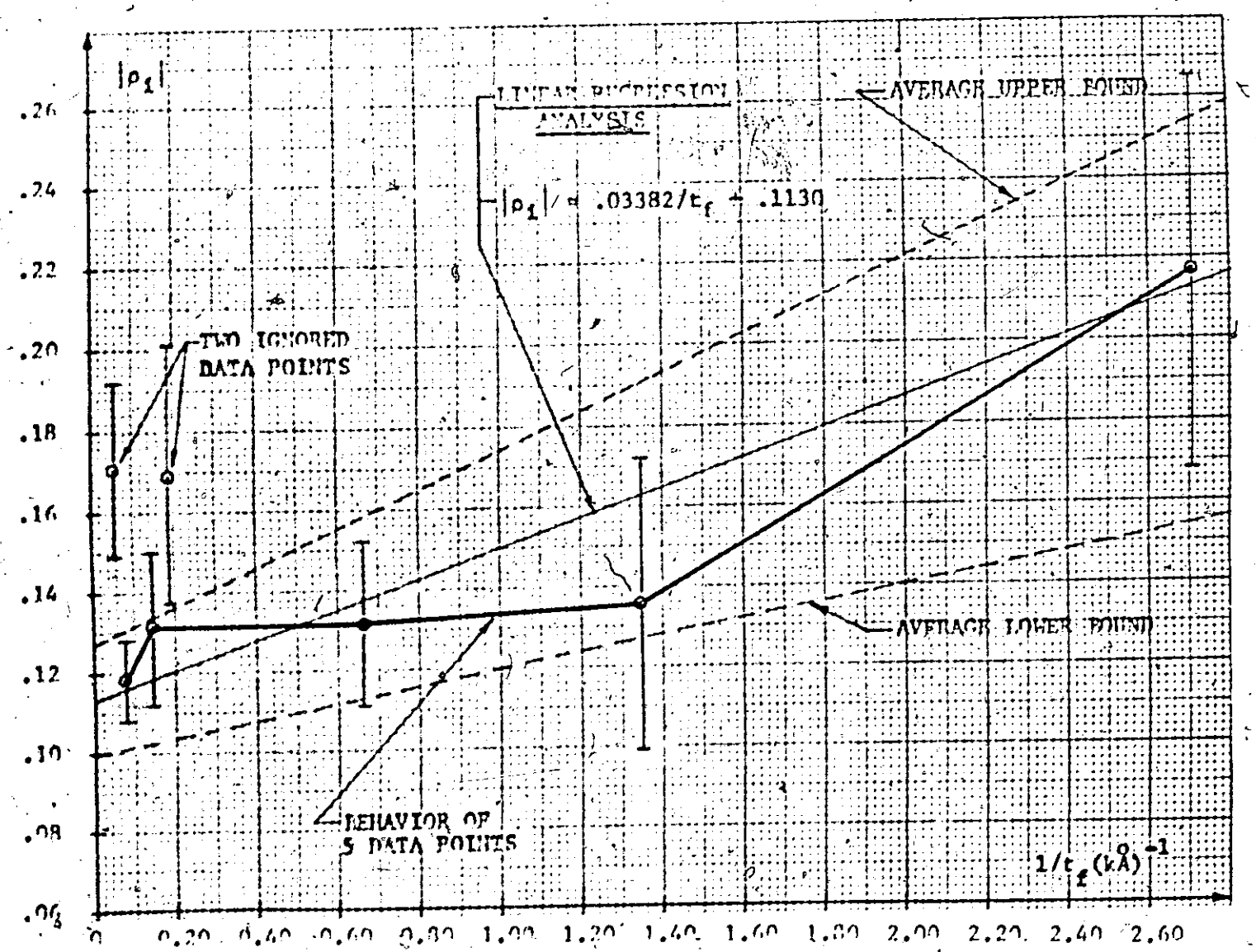

Figure 5.2-2: Plot of the [illegible] Measurements of the Average Measured Value of Input Reflection Coefficient $|\rho_1|$, vs the Inverse of Thin Film Thickness $1/t_f$, for Series A- Samples, with 25 Mil Thick Substrates and Mounted by Means of the New CPW Launchers.

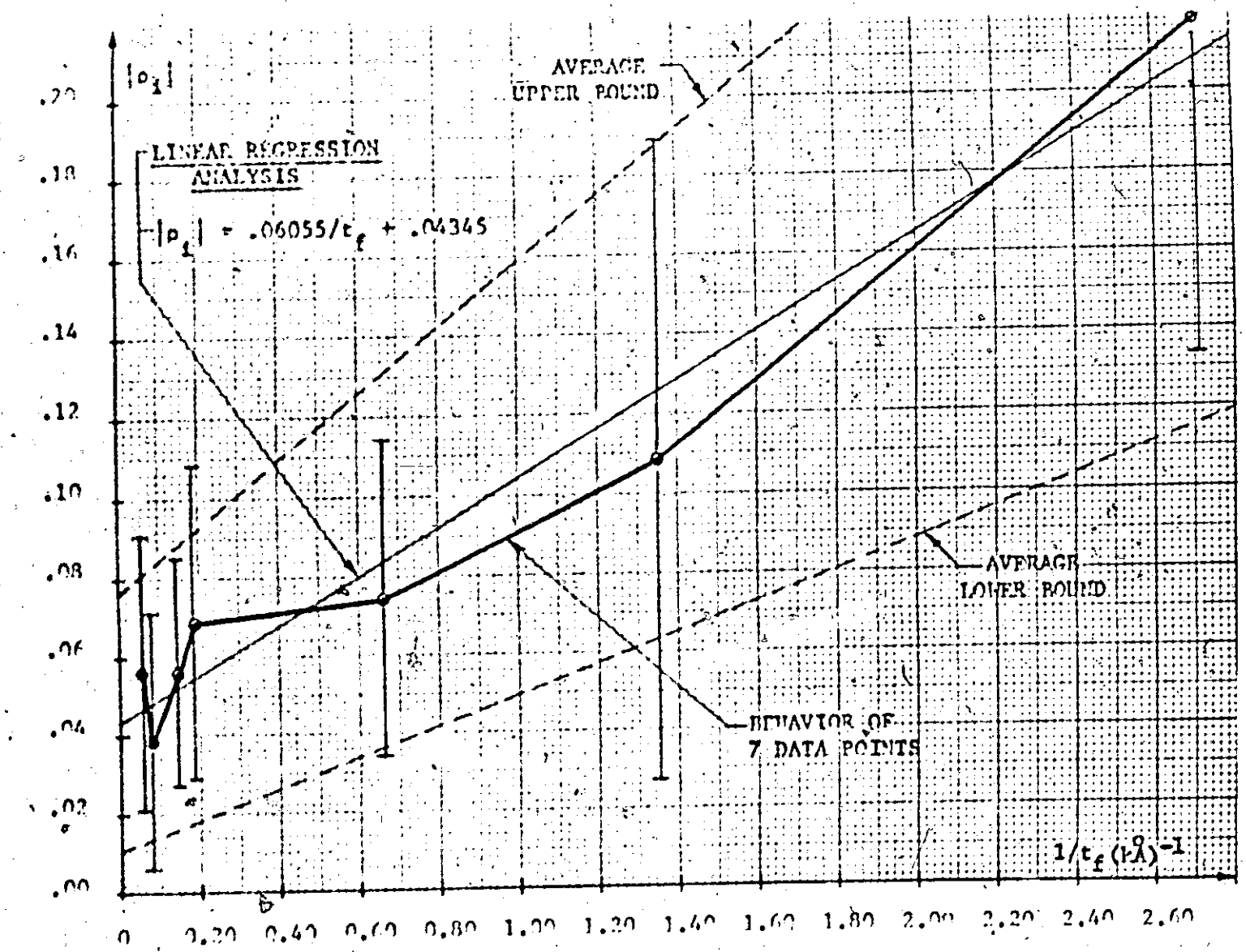

Figure 5.2-4: Plot of the 1015B TDR/SAMPLER measurements of the Average Measured Value of Input Reflection Coefficient $|\rho_1|$, vs the Inverse of Thin Film Thickness $1/t_f$, for Series PCB- Samples, with 25 Mil Thick Substrates and Mounted by Means of the New CPW Launchers.

first group of data in section 5.2-1, this residual mismatch for thin film thicknesses larger than 20 kÅ was due mainly to a decrease in ε_r as a result of a small finite substrate thickness. Data of Table 5.2-2 for two substrate thicknesses indicates an improvement in $\overline{Z}_o$ because this tends to come closer to the design theory which assumed infinite substrate thickness. In section 5.4, TDR measured propagation times will shed light on how design corrections can be made for the finite substrate thickness effect.

A comparison of Figures 5.2-2 and 5.2-3 with Figure 5.2-1 indicates that the TDR reflection coefficient measurements were compatible with the same measurements performed by means of the Singer instrumentation. Again, the group of the Singer instrumentation measurements appeared to underestimate the TDR measurements significantly for thin films less than 1 kÅ thick, because $|\rho|_{max} + 2$ was only a theoretical estimate which was known to be bad for such thin films anyway.

Mention should be made of the measurements made on meandered samples M1-2 and M2-3. Table 5.2-2 indicates characteristic impedance levels which are very close to 50 Ω for these two samples. TDR traces in Figure C.10 in Appendix C did not indicate detectable reflections at the bends of these meandered samples, though slight mismatches were definitely indicated at each transition between CPW launcher and CPW sample making reflections at the meandered line bends difficult to detect. The CPW launchers would have to be improved by tapering the center pins before it could be said that TDR measurements actually indicated small reflections at the meandered line bends. It would be also worthwhile

correcting the coplanar geometry for large values of Z_o first, in order to create a characteristic impedance of 50 Ω in the straight CPW sections. It is usually rather difficult to analyze more than one reflection with TDR techniques.

5.2.3 Conclusions

Reflection coefficient measurements show that a thin aluminum film thickness ≥10 kÅ should be used for CPW samples operating in the 1-2GHz range. Reflections at bends in meandered line samples could not be detected by TDR techniques and hence were small if they existed. However the effect of finite substrate thickness was detected. In section 5.4 simple design corrections will be shown to be possible. The problem of large and variable contact resistance has not been solved completely though it has been improved by means of the CPW launchers. Geometrical deviations were not considered to be a problem since a close check of these was maintained throughout the manufacturing procedure. It will be shown in section 5.4 that C.P. Wen's (CPW) theory is quite accurate if corrections are made for the effect of finite substrate thickness. It will also be shown that ground planes can be quite narrow without affecting the value of the characteristic impedance of the CPW.

5.3 Measurements with the HP 8545A Network Analyzer and the New CPW Launchers on Two Meandered CPW Samples and One Comparable Straight CPW Sample.

The HP 8545A Network Analyzer was used in the manual mode to obtain the phase and magnitude of the net reflection coefficient ρ in the 1-2 GHz band for samples M1-2, M2-3 and BCD-6. The latter sample was a straight coplanar transmission line 1" long, whereas the other two samples were meandered samples. Sample M1-2 had one semicircular bend and was 2.0549" long along its center line. Sample M2-3 had two right angle bends and a center line length of 2.6798". All three samples had 50 mil wide center strips. It will be shown that the performance of all three samples could be improved significantly by increasing substrate thickness from 25 mils to 50 mils. Also, the measured values of ρ corresponded to the Singer instrumentation measurements on the same samples, as presented in Appendix D. Reflections at the bends of the meandered samples could not be detected by the HP 8545A Automatic Network Analyzer measurements, due to other more significant reflections masking any reflections at the bends, which may or may not have existed.

A polar plot was used here to display the magnitude and phase of ρ in one diagram. Phase was referenced by means of the adjustable reference plane extension arm on the S Parameter Test Set of the Network Analyzer. The reference plane extension was adjusted so that a S/C at the input CPW launcher caused ρ=-1 to appear on the polar display. Then an expanded polar plot was utilized. The reflection coefficient ρ was actually the same as the S-parameter S_{11}. The forward transmission

gain S_{21} was not measured nor were the S-parameters S_{12} or S_{22} measured.

5.3.1 Coplanar Line with One Semicircular Bend

Figure 5.3-1 summarizes the HP Network Analyzer's measurements of S_{11} for sample M1-2 which had a thin film thickness of 6.876 KÅ. The dashed trace represents the value of S_{11} for a 50 mil substrate thickness in the 1-2 GHz band whereas the solid line represents the value of S_{11} for a 25 mil substrate thickness in the same frequency band. Various frequencies have been labelled on the traces in order to illustrate the frequencies for which $|\rho|$ is a maximum. M1-2 shows a maximum SWR of 1.45 at approximately 1.63 GHz, corresponding to a maximum net reflection of $|\rho|_{max}$=.184 and an input reflection of .092. This corresponded to a characteristic impedance of 60 Ω.

When 2 substrate thicknesses were used a maximum SWR value of 1.28 at 1.44 GHz was obtained. This corresponded to a value of $|\rho|_{max}$=.123 which in turn corresponded to a net input reflection coefficient of .0615 Ω. If thicker substrates had been used, one would have expected a characteristic impedance even closer to 50 Ω.

Figure D.5 of Appendix D displays the Singer instrumentation measurements of $|\rho|$ for sample M1-2 for a 25 mil substrate thickness. A maximum value for $|\rho|$ of 1.62 was obtained at 1.67 GHz. This corresponds to an SWR value of 1.385, which is very close to the above 8545A Network Analyzer result of 1.45 at 1.63 GHz. However, the Singer instrumentation measurements for M1-2 do show more significant discrepancies with the 8545A Network analyzer results elsewhere in the 1-2 GHz frequency

Figure 5.3-1 : Polar Plot of ρ for Sample M1-2 Measured by the HP 8545A Automatic Network Analyzer.

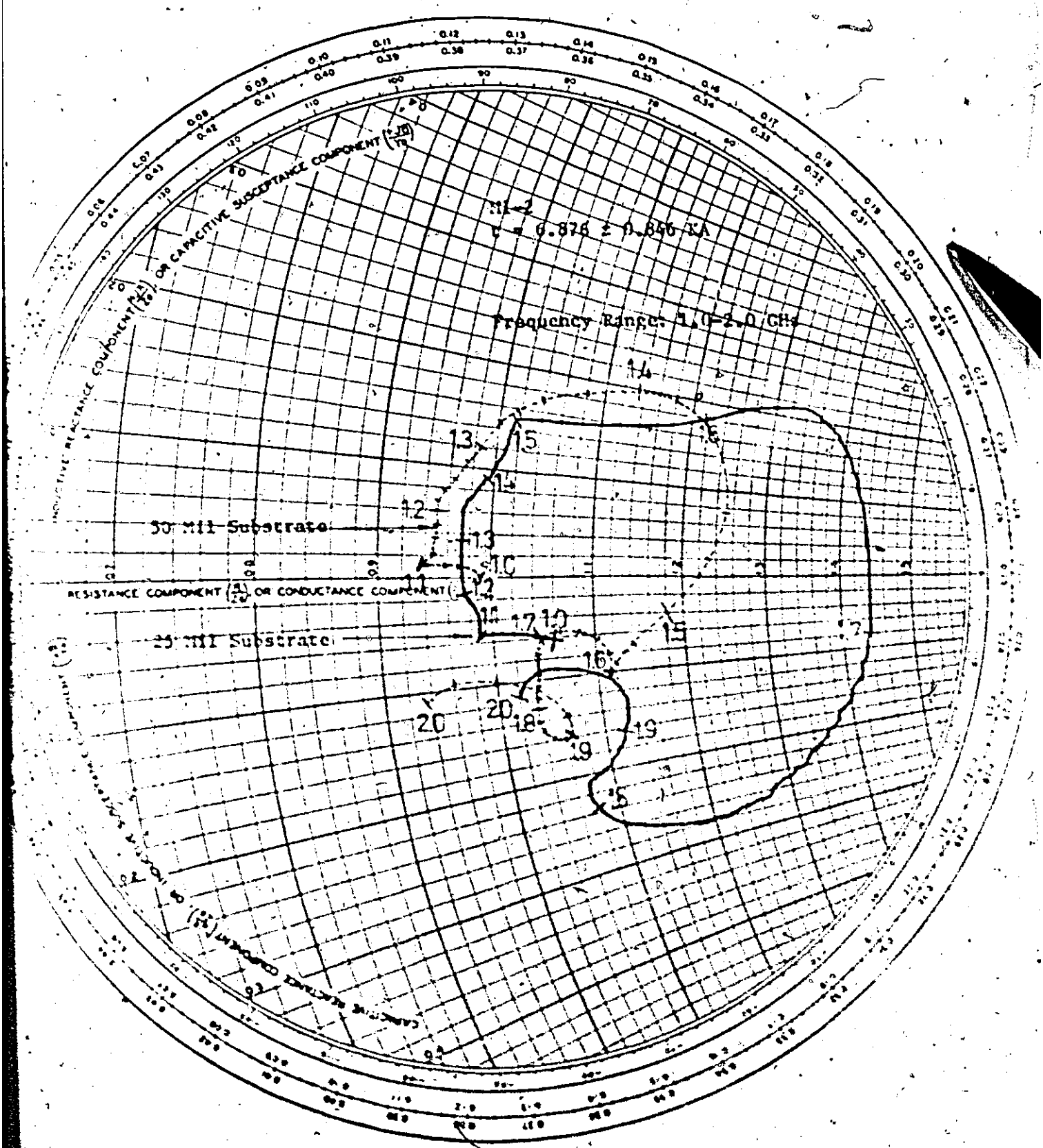
Frequency Range: 1.0-2.0 GHz
50 Mil Substrate
25 Mil Substrate
RESISTANCE COMPONENT OR CONDUCTANCE COMPONENT
INDUCTIVE REACTANCE COMPONENT OR CAPACITIVE SUSCEPTANCE COMPONENT

Figure 5.3-2: Polar Plot of ρ for Sample M2-3 Measured by the HP 8545A Automatic Network Analyzer.

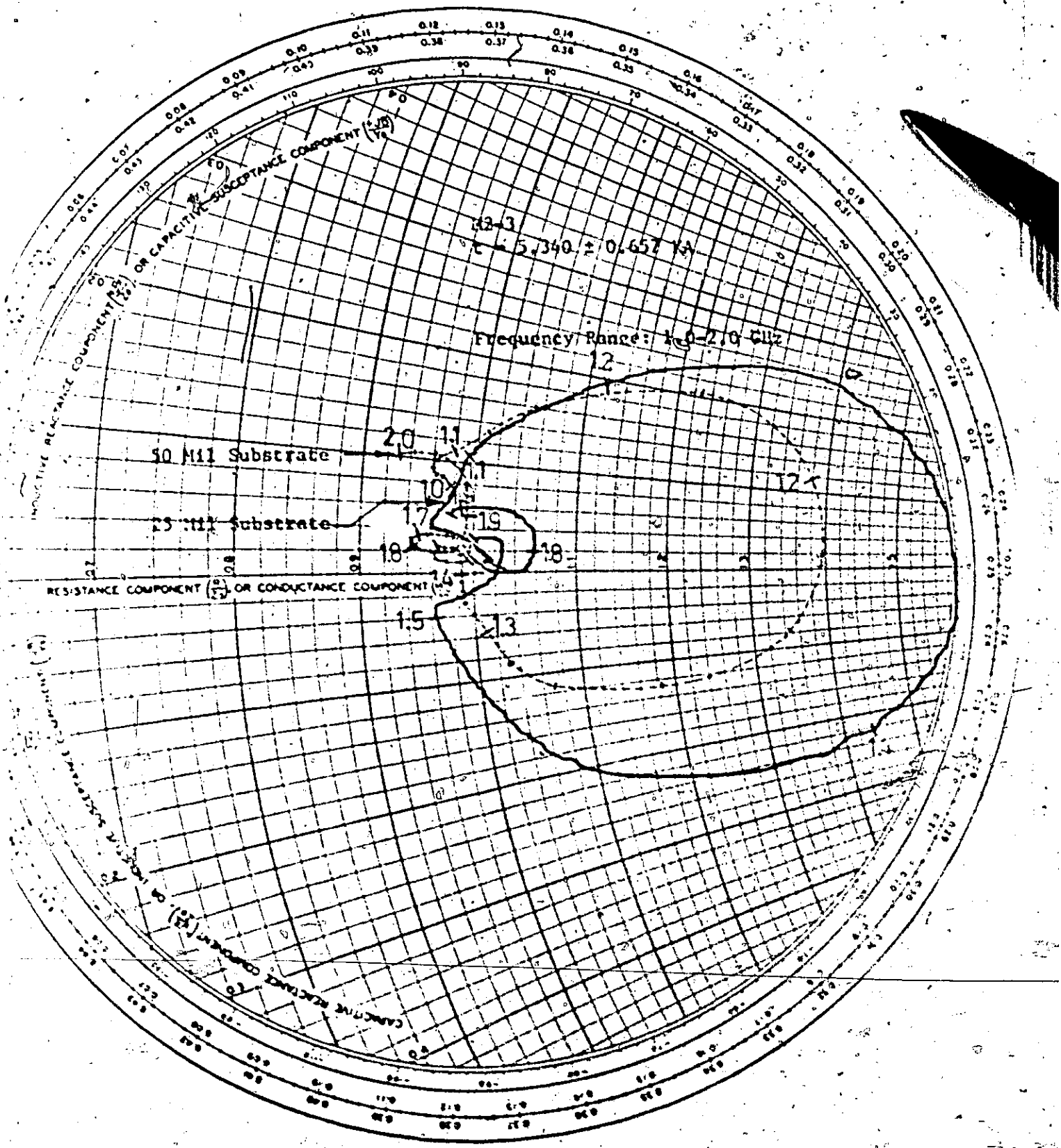
43-3
Z = 5.340 ± 0.657 YA
Frequency Range: 1.0-2.0 GHz
50 Mil Substrate
25 Mil Substrate
RESISTANCE COMPONENT OR CONDUCTANCE COMPONENT
INDUCTIVE REACTANCE COMPONENT OR CAPACITIVE SUSCEPTANCE COMPONENT

band. The results are close to what one would expect theoretically in accordance with Appendix E. Any discrepencies between theory and practice have been attributed to system errors.

5.3.2 Coplanar Line with Two Right Angle Bends

Figure 5.3-2 gives the phase and magnitude of ρ for sample M2-3. This sample had a thin film thickness of 5.340 kÅ, which was very close to the 6.876 kÅ thin film thickness of sample M1-2. The performance of sample M2-3 appeared to be slightly worse than that of M1-2. Notice that a maximum SWR of 1.6 was obtained at about 1.35 GHz for one substrate thickness of 25 mils. This corresponded to a value of $|\rho|_{max}$=.231, a value of $|\rho_1|$=.115 and a characteristic impedance of 62.9 Ω. With 2 substrate thicknesses the characteristic impedance was reduced to 58.5 Ω.

The Singer instrumentation measurements of sample M2-3 displayed in Figure D.5 of Appendix D imply small surplus reflections other than the normal input and output reflections one would expect for a mismatched lossy CPW. This judgement was made on the basis of Appendix E, which accounts for the input and output reflections in straight coplanar transmission lines. Predicted plots of $|\rho|$ vs frequency for various values of attenuation are shown in the same appendix, and their shape differs slightly from the reflection curves of Figure D.5, implying that other sources of small reflections existed in the Singer instrumentation. This argument is reinforced by the fact that TDR measurements of section 5.2 did not indicate significant reflections at the bends of sample M2-3 or sample M1-2. The HP 8545A measurements of this same sample also showed that it behaved

as a straight uniform CPW sample mismatched only at the input and output where it was connected to a 50 Ω coaxial main line. It then appears that any reflections existing at a CPW rectangular bend are very small in the 1-2 GHz frequency band. Instrumentation errors are more significant.

5.3.3 The Straight Coplanar Line

A straight line was included for comparison with the two meandered lines. Figure 5.3-3 shows the performance of sample BCD-6 for a 25 mil substrate and a 50 mil substrate. Remember that the maximum modulus of the reflection coefficient for these traces represents twice the modulus of the input reflection coefficient $|\rho_1|$. Hence a maximum SWR value of 1.2 actually represents 54.8 Ω rather than 60.0 Ω and a maximum SWR value of 1.13 actually represents 53.2 Ω rather than 56.5 Ω. The trace in Figure 5.3-3 for the 25 mil substrate actually represents a characteristic impedance of 54.8 Ω and the trace for the 50 mil substrate represents a characteristic impedance of 53.2 Ω.

5.3.4 Conclusions

In summary, the HP 8545A Network Analyzer measurements on samples M1-2, M2-3 and BCD-6 indicated characteristic impedance of 60 Ω, 62.9 Ω, and 54.8 Ω respectively when one substrate thickness of 25 mils was used. When a substrate thickness of 50 mils was used, characteristic impedance values of 56.5 Ω, 58.5 Ω, and 53.2 Ω were obtained respectively. The respective thin film thicknesses of 6.877 kÅ, 5.340 kÅ, and 12.826 kÅ

Figure 5.3-3: Polar Plot of ρ for sample PCD-6 Measured by the HP 8545A Automatic Network Analyzer.

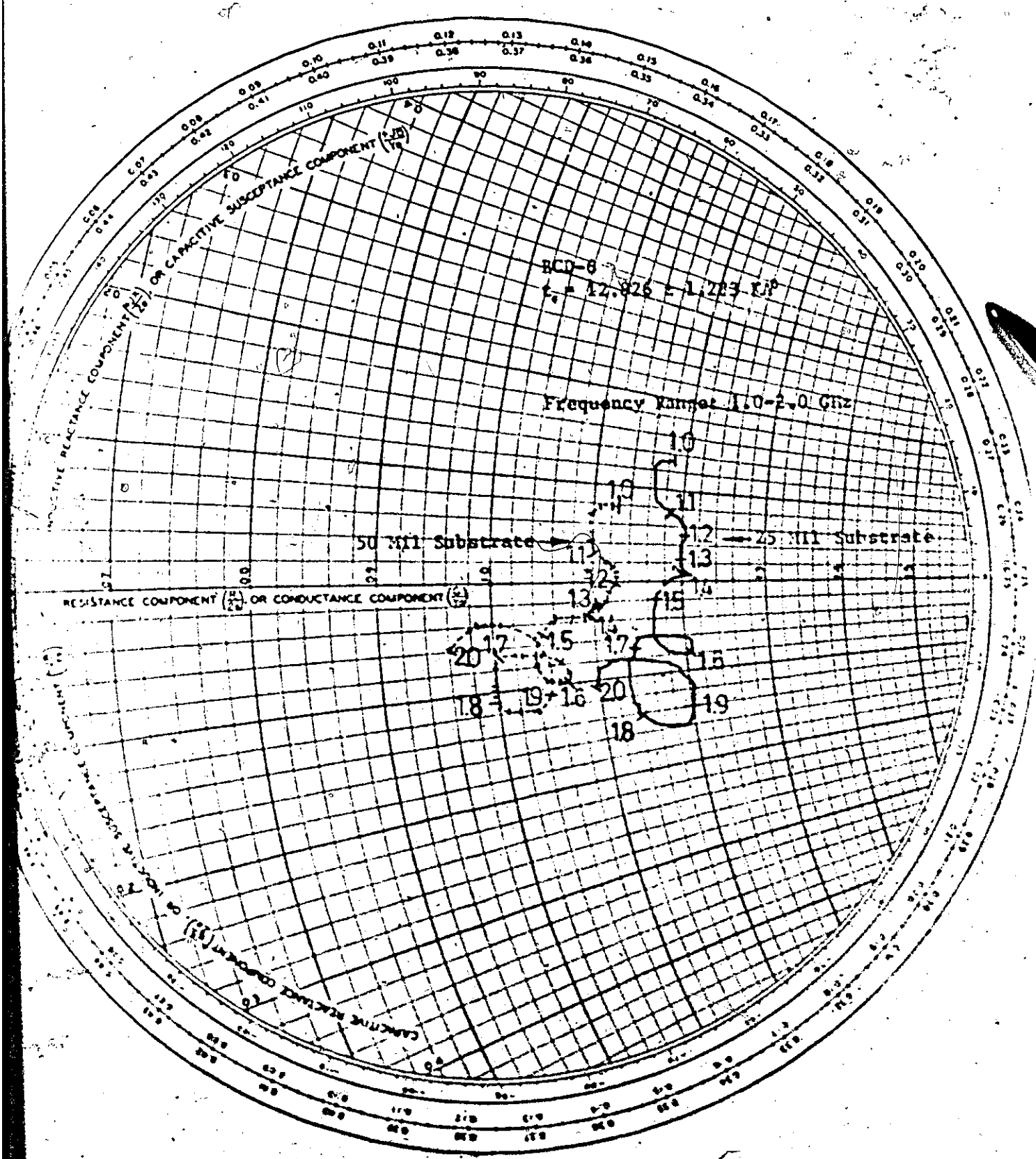
RCD-6
Frequency Range: 1.0-2.0 GHz
50 Mil Substrate
25 Mil Substrate
RESISTANCE COMPONENT OR CONDUCTANCE COMPONENT
CAPACITIVE SUSCEPTANCE COMPONENT OR INDUCTIVE REACTANCE COMPONENT

accounted for sample M2-3 having the higher characteristic impedance, with sample M1-2 having a slightly smaller value, and sample BCD-6 having the smallest value of all three samples. Table 5.2-2 confirms this point if one compares the TDR measured characteristic impedance of straight 1" long CPW samples having the same thin film thickness as the three above samples. The above HP 8545A Network Analyzer results appear to agree within experimental error with the comparable TDR measurements presented in Table 5.2-2.

The agreement of the 8545A measurements with theory and the above agreement between measurements with different types of instrumentation imply that reflections at the bends in the meandered samples were negligeable in the 1-2 GHz range. Perhaps at higher frequencies where the possibility of the conversion of a CPW bend into an antenna exists, a significant mismatch would occur at the bend along with significant radiation of electromagnetic energy. The frequencies at which this might occur can be estimated easily by using C.P. Wen's criterion for radiation. Wen stated that the design of CPW's involved making $2b_1 << \lambda/2$. If $2b_1 = \lambda/2$, Wen claims that significant radiation will occur. For 50 mil wide center strips $2b_1$ had a value of .0300", as in Figure 4.3-2. This means that radiation problems would be encountered at 20.00 GHz. For 103 mil wide center strips, the critical radiation frequency would be 13.27 GHz. The samples measured in this thesis were designed with center strip widths of either 103 mils or 50 mils, and so no radiation problems were expected or detected in the 1-2 GHz frequency band.

5.4 Accounting for Large Measured Values of Characteristic Impedance

C.P. Wen's CPW theory [5] may have previously appeared erroneous since values of Zo larger than 50 Ω were measured for every CPW sample discussed in the foregoing sections. However, Wen's theory had assumed infinitely wide ground planes, an infinitely thick dielectric substrate, and a lossless propagation medium; including zero contact loss. Herein, tests will be performed to show that Wen's theory is not invalid if approximations to these 3 assumed conditions are built into CPW design.

Specifically, this section will concern itself with design guidelines for suitable ground plane widths and suitable substrate thicknesses. It has already been shown in section 5.1 that propagation loss can be made negligible by the use of aluminum films thicker than 10 kÅ. Though contact loss is more critical than propagation loss in short 1" long CPW's, TDR measurements permit the separation of contact resistance from characteristic impedance. No attempt will be made in this thesis to improve electrical contacts over and above what has already been achieved by means of the CPW launchers of section 3.5.

5.4.1 Propagation Time Measurements Lead to Design Corrections for Substrate Thickness

Previous to this test, measured values of the characteristic impedance of the coplanar lines deviated from the theoretical value by a significant positive amount. As shown previously in Table 5.2-2, positive deviations from 50 Ω as small as 12.8 Ω and as large as 28.0 Ω were obtained for design A samples. These samples had a substrate thickness of 25 mils. Similarly, design PCD samples showed deviations ranging from 4.3 Ω to 29.3 Ω. These samples also had a substrate thickness of 25 mils. For both series of samples the magnitude of the deviations increased as thin film thickness decreased below 10 kÅ. Herein, propagation times have been measured for series A- and PCD- samples plus meandered samples M1-2 and M2-3. The purpose was to establish a relationship between the relative dielectric constant ϵ_r of the alumina substrate, and the resulting characteristic impedance of the lines. It will be shown that this approach can be used to correct future designs for the effect of finite substrate thickness.

The A- series of coplanar lines had a 103 mil center strip and a wide ground plane separation of approximately 180 mils. Consequently, its electric field lines were more widely spaced than in the PCD- series, where the center strip width and ground plane separation were both half as large. It was then expected that the resulting field lines in the PCD- series would lie closer to the alumina surface on the side of the thin aluminum film, and that fewer of them would leave the alumina dielectric on the bottom side. A closer approximation to the theoretically assumed, infinitely thick, dielectric medium was then

thought to have been achieved in the BCD- series than in the A- series. Meandered samples M1-2 and M2-3 had 50 mil center strip widths and so it was expected that these samples would compare experimentally with the BCD- samples.

A series of tests were performed to prove this hypothesis. If some of the electric field lines did in fact leave the dielectric substrate on the bottom side and then re-entered the dielectric on the same side, one might expect the effective, relative, dielectric constant ϵ_r to be lower than the 9.2 value specified by the manufacturer of the alumina substrates. This is in fact what was found. The phase velocity equation

$$\frac{v}{c} = \left[\frac{2}{1 + \epsilon_r}\right]^{\frac{1}{2}} \qquad (5.4\text{-}1)$$

was rewritten as

$$\epsilon_r = 2 \cdot \left[\frac{c}{v}\right]^2 - 1 \qquad (5.4\text{-}2)$$

which became

$$\epsilon_r = 2 \cdot c^2 \cdot \left[\frac{2 \cdot t}{2 \cdot L'}\right] - 1 \qquad (5.4\text{-}3)$$

where $2L'$ was twice the length of the coplanar transmission line, and $2t$ was the return time of the TDR step for an open circuit load at the end of the line. Equation (5.4-3) allowed ϵ_r to be calculated for each sample from TDR measured return propagation times. This calculated value

of ϵ_r was used in combination with the known value of the aspect ratio k to calculate an expected characteristic impedance for each sample. The ratio k was measured by means of an optical comparator accurate to .05 mils. This test was performed on all of the samples mentioned above for one and two substrate thicknesses; ie 25 mils thick and 50 mils thick.

This calculated characteristic impedance was then compared to the TDR measured characteristic impedance as tabulated in Table 5.4-1. The results compared within experimental error. The relative dielectric constants were then averaged for each design and for one and two substrate thicknesses. The average results were tabulated for use in future designs in Table 5.4-2. As was expected, the effective value of ϵ_r decreased significantly with increasing center strip width and decreasing substrate thickness. Thin film thickness t_f did not appear to affect the effective value of ϵ_r.

Presently, it appears that a partially empirical approach to CPW design is necessary for low values of ϵ_r. A designer would first design and fabricate a CPW according to Wen's theory with the bulk value of ϵ_r. Then he would measure the signal propagation time of this CPW. The effective value of ϵ_r would then be calculated, and a redesign would be necessary. Ideally one would like to have a theoretical or empirical equation expressing the effective value of ϵ_r as a function of ground plane separation and substrate thickness, but as of this writing such an equation is not available. For large values of ϵ_r of 100 or more, the problem of finite substrate thickness may be less severe and even insignificant since it is expected that the dielectric substrate will

Sample Number	Measured k	Film Thickness t_f(kÅ)	No. Substrate.	2t±35 (ps)	ϵ_r Net ±1.65	Zo (Ω) Expected ±8.0	Zo (Ω) Measured (TDR)
A-3	.53803	5.340 ± 0.657	1	315	5.921	61.996	70.5 ± 4.5
			2	340	7.063	57.438	66.5 ± 2.5
A-2	.53803	6.877 ± 0.846	1	315	6.921	57.950	65.2 ± 2.3
			2	340	7.063	57.438	62.3 ± 3.3
A-6	.53803	12.826 ± 1.283	1	325	6.367	60.090	63.3 ± 1.3
			2	340	7.063	57.438	57.5 ± 1.5
A-11	.53803	18.011 ± 2.216	1	310	5.703	62.996	69.8 ± 2.3
			2	350	7.544	55.798	60.0 ± 2.0
A-8	.53803	1.509 ± 0.186	1	310	5.703	62.996	65.1 ± 2.8
			2	345	7.302	56.605	60.0 ± 3.0
A-9	.53803	0.739 ± 0.091	1	320	6.142	61.029	65.8 ± 4.8
			2	360	8.040	54.245	62.8 ± 6.3
A-10	.53803	0.369 ± 0.846	1	310	5.703	62.996	78.0 ± 8.0
			2	360	8.040	54.245	71.3 ± 6.8
BCD-3	.54480	5.340 ± 0.657	1	325	6.367	59.624	62.5 ± 9.5
			2	340	7.063	56.992	53.9 ± 4.2
BCD-2	.54480	6.877 ± 0.846	1	330	6.596	58.718	55.9 ± 3.1
			2	345	7.302	56.166	54.1 ± 4.0
BCD-6	.54480	12.826 ± 1.283	1	340	7.063	56.992	54.3 ± 3.7
			2	350	7.544	55.365	53.7 ± 4.3
BCD-11	.54480	18.011 ± 2.216	1	330	6.596	58.718	56.1 ± 3.9
			2	350	7.544	55.365	53.6 ± 4.5
BCD-8	.54480	1.509 ± 0.186	1	335	6.828	57.841	58.3 ± 4.7
			2	355	7.790	54.584	55.7 ± 4.9
BCD-9	.54480	0.739 ± 0.091	1	325	6.367	59.624	60.8 ±12.2
			2	365	8.292	53.089	59.6 ±11.9
BCD-10	.54480	0.369 ± 0.045	1	335	6.828	57.841	79.3 ±13.7
			2	360	8.040	53.824	75.8 ±14.3
M1-2	.57337	6.876 ± 0.846	1	345	7.302	54.344	53.5 ± 3.5
			2	360	8.050	52.049	51.4 ± 2.6
M2-3	.56892	5.240 ± 0.657	1	340	7.063	55.428	54.4 ± 3.6
			2	355	7.790	53.086	53.0 ± 2.5

5.4-1: Comparison of TDR Measured Characteristic Impedance with Characteristic Impedance Calculated from TDR Measured Propagation Times and Optical Comparater Measurements of k.

	Center Strip Width (mils)	Substrate Thickness (mils)	$\overline{2t}$ (ps)	$\overline{\epsilon_r}$ Net
Series A-	103	25	315.0 ± 5.0	5.921 ± .22
		50	347.9 ± 5.0	7.442 ± .26
Series BCD-	50	25	331.4 ± 5.0	6.660 ± .23
		50	352.1 ± 5.0	7.647 ± .25

Table 5.4-2: Average Effective Value of ϵ_r as a Function of Substrate Thickness and Center Strip Width.

then contain most of the electric filed lines joining the center strip and ground planes.

As a further study of the substrate thickness effect, the next section will investigate this problem for various values of aspect ratio k. The problem of finite ground plane widths will also be investigated. In these tests, thin film thickness will be kept constant at a sufficiently large value so that increased reflections from a lossy medium will not compound the problem. Center strip width will also be kept constant for various values of k.

5.4.2 Experimental Investigation of Relative Dielectric Constant and Characteristic Impedance as a Function of Aspect Ratio k and Substrate Thickness.

The aspect ratio k was varied from .1 to .6 in increments of .1, while thin film thickness t_f was kept constant at 18.466 ± 2.272 kÅ and the center strip width was kept constant at 50 mils. Propagation time measurements and characteristic impedance measurements were performed with the width of the ground planes held at the original design value, as well as the larger values designated by the ratio $e_1/b_1 = 10$, where e_1 represents the position of the outside edge of each ground plane and b_1 represents the position of the inside edge. Measurements with these increased ground plane widths indicated no noticeable effect on the characteristic impedance of each sample. The results of all of the above measurements were tabulated in Table 5.4-3. The characteristic impedance Z_o and the return propagation time 2t were measured via the HP 1815B TDR/SAMPLER, and because of the sensitivity of this instrument, an average value $\overline{Z_o}$, had to be taken to cancel the small ringing effects originating from the transition between CPW launchers and CPW samples.

Table 5.4-3 indicates an increase in the value of 2t as substrate thickness is increased, which correspondingly decreases $\overline{Z_o}$ towards its theoretical value. A graph of $\overline{Z_o}$ versus k is more instructive since theoretical curves may then be compared with the measured $\overline{Z_o}$ values. Figures 5.4-1 and 5.4-2 illustrate how well $\overline{Z_o}$ compares with theory for one and two substrate thicknesses respectively.

Figure 5.4-1 shows theoretical characteristic impedance curves for the theoretical value of $\epsilon_r = 9.2$ and for the measured average value

Substrate Thickness	k (Nom)	k (Meas)	Ratio (Nom) e/b,	$\lvert\rho_1\rvert$ Min→Max	2t (ps)	Z_o Min→ Max	$\bar{Z}_o$
	.1	.10229	1.40 or 10	.43→.46	270	124→ 134	129
	.2	.20395	2.80 or 10	.31→.34	280	95→ 101	98
1x25 Mil	.3	.30387	4.22 or 10	.20→.25	300	75→ 83	79
	.4	.40503	5.60 or 10	.11→.18	320	62→ 72	67
	.5	.49500	7.00 or 10	.05→.13	330	55→ 65	60
	.6	.59350	8.40 or 10	-.05→.09	330	45→ 60	52.5
	.1	.10229	1.40 or 10	.39→.41	310	118→ 112	115
	.2	.20395	2.80 or 10	.25→.29	320	83→ 90	86.5
2x25 Mil	.3	.30387	4.22 or 10	.15→.20	330	67→ 75	71
	.4	.40503	5.60 or 10	.05→.14	340	55→ 66	60.5
	.5	.49500	7.00 or 10	.03→.10	340	53→ 61	57
	.6	.59350	8.40 or 10	-.08→.06	350	43→ 56	49.5
	.1	.10229	1.40 or 10	.33→.38	315	99→ 110	104.5
	.2	.20395	2.80 or 10	.24→.26	320	81→ 85	83
3x25 Mil	.3	.30387	4.22 or 10	.16→.19	340	69→ 73	71
	.4	.40503	5.60 or 10	.06→.12	340	56→ 64	60
	.5	.49500	7.00 or 10	.02→.09	350	52→ 60	56
	.6	.59350	8.40 or 10	-.06→.04	355	44→ 54	49
	.1	.10229	1.40 or 10	.31→.40	330	95→ 115	105
	.2	.20395	2.80 or 10	.20→.29	340	75→ 91	83
4x25 Mil	.3	.30387	4.22 or 10	.11→.21	350	62→ 76	69
	.4	.40503	5.60 or 10	.05→.15	350	55→ 67	61
	.5	.49500	7.00 or 10	.00→.10	350	50→ 61	55.5
	.6	.59350	8.40 or 10	-.08→.04	360	42→ 54	48.5
	.1	.10229	1.40 or 10	.30→.38	335	93→ 110	101.5
	.2	.20395	2.80 or 10	.22→.27	340	78→ 87	82.5
5x25 Mil	.3	.30387	4.22 or 10	.11→.18	350	62→ 72	67
	.4	.40503	5.60 or 10	.05→.13	350	55→ 65	60
	.5	.49500	7.00 or 10	.01→.09	360	51→ 60	55.5
	.6	.59350	8.40 or 10	-.07→.04	360	43→ 54	48.5

Table 5.4-3: Experimental Investigation of Characteristic Impedance as a Function of Aspect Ratio k for 5 Different Substrate Thicknesses, Various Ground Plane Widths and Film Thickness of 18.446 ± 2.272 kÅ. Only 50 Mil Center Strip Widths Were Used.

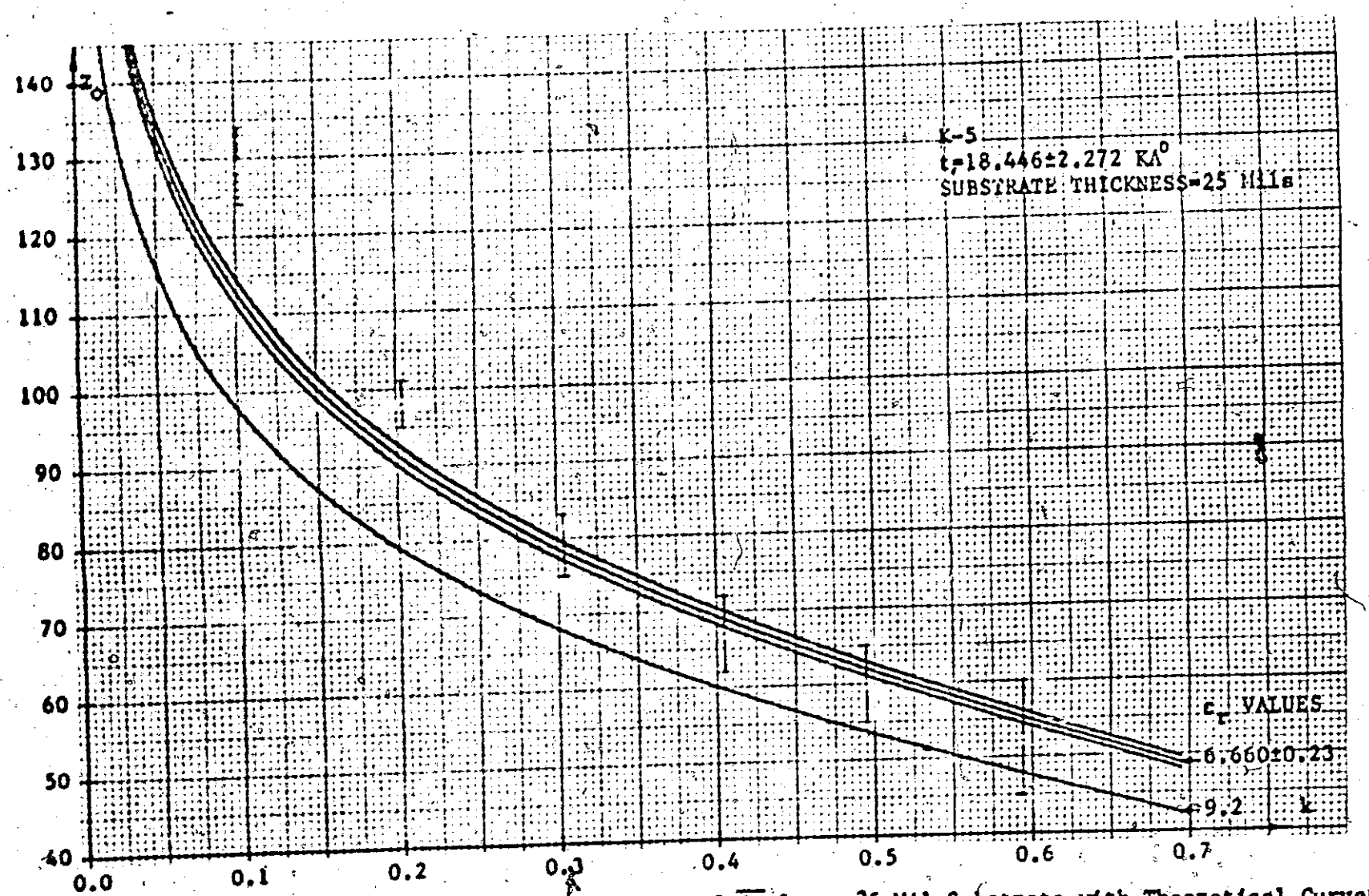

Figure 5.4-1: Comparison of TDR Measured Values of $\overline{Zo}$ for a 25 Mil Substrate with Theoretical Curves Calculated for the Corrected Value of ϵ_r as well as the Bulk Value.

$\epsilon_r = 6.660 \pm 0.230$. Error bars have been placed on the measured points to show the range of agreement with theory. It appears that out of six data points, 1 point could correspond to $\epsilon_r = 9.2$, 4 points could correspond to $\epsilon_r = 6.660$ and the 2 points having the smallest k values don't correspond with any of the theoretical curves. The problem here is that for small values of k, the ground plane separation is quite large compared to substrate thickness and the effective value of ϵ_r is reduced significantly. Figure 5.4-1 shows that good designs may be achieved with 25 mil substrate thicknesses for $k > .3$ if the TDR measured value of ϵ_r is used rather than the bulk value of 9.2.

Figure 5.4-2 shows the results for a 50 mil substrate. Here $\epsilon_r = 7.647$ is the average TDR measured value taken from Table 5.4-2, and $\epsilon_r = 9.2$ is the bulk value specified by the manufacturer of the alumina substrates. It seems that 5 out of 6 data points have the best correspondence with the theoretical curve having $\epsilon_r = 7.647$. Again, for very low values of k, two substrate thicknesses do not appear sufficient to maintain a close correspondence between theory and measurements. However it appears that good designs might be achieved for values of $k > .2$, if the TDR measured value of ϵ_r of 7.647 were used along with 50 mil thick alumina substrates of 96% purity.

If the effective value of ϵ_r cannot be measured, a good rule of thumb is to make certain that the ground plane separation is no more than twice the substrate thickness. Table 5.4-3 illustrates that for good results, $2b_1$ should be equal to or less that about 2 or 3 times the substrate thickness. For example, for $k = .5$ there is not much significant

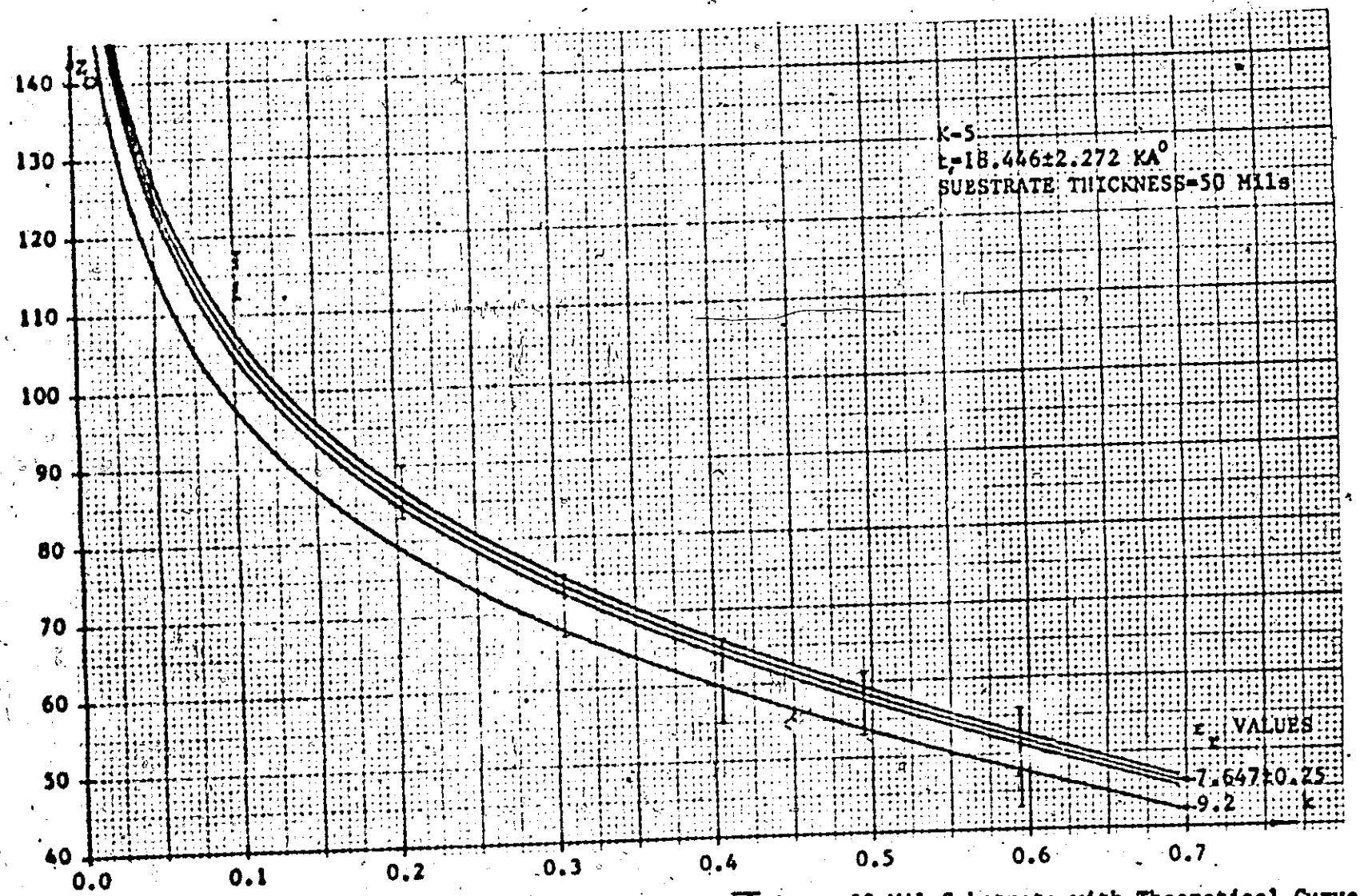

Figure 5.4-2: Comparison of TDR Measured Values of $\overline{Zo}$ for a 50 Mil Substrate with Theoretical Curves Calculated for the Corrected Value of ϵ_r as well as the Bulk Value.

improvement in $\overline{Z_o}$ when more than 2 substrate thicknesses are used. For this case the limiting ratio of $2b_1$ to substrate thickness is approximately 2.0. For k = .2, 4-25 mil substrates are necessary and the limiting ratio is approximately 2.5.

If the values of $\overline{Z}o$ measured for a substrate thickness of 5 x 25 mils are taken from Table 5.4-3 with their respective values of k, the corresponding values of ϵ_r can be calculated using an iterative scheme. This has been achieved in Table 5.4-4 below. The resulting average value of ϵ_r has been calculated to be 8.8 ± .8, which is close to the nominal value of 9.2.

k	$\overline{Z}o \pm 2(\Omega)$	$\epsilon_r \pm .8$
.1	101.5	8.485
.2	82.5	8.415
.3	67.0	9.55
.4	60.0	9.20
.5	55.5	8.42
.6	48.5	8.795

Table 5.4-4: Calculation of ϵ_r from Measured $\overline{Z}o$ Values for an Infinitely Thick Dielectric Substrate.

5.4.3 Conclusions

C.P. Wen's theory of coplanar waveguides has been shown herein to be accurate to within a measurement accuracy of ±2 Ω in the 1-2 GHz band of frequencies when the ground plane separation $2b_1$ < substrate thickness, .1 < k < .6, and ϵ_r > 9.2. It is to be expected that larger ground plane separations could be used for larger values of ϵ_r since the dielectric substrate would then tend to concentrate the electric field lines more, but to what extent this would occur has not been studied quantitatively herein. Only relative dielectric constants of 9.2 have been investigated.

Designs based on the above rule of thumb not only guarantee accurate designs, but the extension of the electric field beneath each CPW is guaranteed to be negligible, thus removing the problem of interference with underlying circuits. On the surface of the CPW, the electric field is not conveniently captured as in the dielectric substrate, but its intensity is expected to be approximately < 1/10.2 of the electric field intensity in the substrate of ϵ_r > 9.2. However, the juxtaposition of a large metallic body near the surface of a CPW can still load the CPW significantly if care is not excercised. This problem was investigated via TDR techniques and it was found that loading caused a change in reflection coefficient of less than -.005 at a distance $2b_1$ from the surface of a properly designed CPW. Wen [5] claims more than this when he states that loading will be negligible 2 slot widths away from the surface of a CPW, but he was using rutile substrates which have a relative dielectric constant of 100. In general

it can be stated that for $\epsilon_r > 9.2$, the metallic encapsulation of a CPW, or the juxtaposition of other CPW circuits will cause negligible loading at a distance $2b_1$ from the surface of the CPW.

The design of CPW's by means of effective corrected values of ϵ_r when substrates have insufficient thickness is not recommended. This can cause significant loading and interference problems between the CPW and nearby metallic objects or circuits.

It has also been shown that very wide ground planes are unnecessary. Design A and design BCD samples had sufficiently wide ground planes to make Wen's CPW theory valid. However, to make ground plane loss small compared to center strip loss, the ground planes should be at least 5X larger than the center strip width $2a_1$. For short CPW's with lengths of the order of 1" or 2", contact loss appears to be a more severe problem. This is especially noticeable for aluminum films thicker than 10 kÅ.

5.5 General Conclusions

This thesis has covered a variety of topics related to the design, fabrication and testing of thin film coplanar waveguides in the 1-2 GHz band of frequencies. Initially, C.P. Wen's theory [5] was analyzed and reproduced graphically. A tolerance analysis of this theory was then performed with the use of the author's own tolerance analysis technique, which is described for reference purposes in Appendix A. Tolerances on $2a_1$ and $2b_1$ were obtained for a specified CPW design of 50 Ω ± 10%, where it was assumed that the nominal ϵ_r value of 9.2 was at least accurate to within ± 10%. The corresponding tolerance analysis yielded an optimum tolerance of ± 3.35% for both $2a_1$ and $2b_1$. This optimum tolerance represented a goal to be achieved at the fabrication stage.

Two related fabrication techniques were investigated; masking and direct photographic etching. The latter method was found to be easier, cleaner and more precise. Tolerance checks were maintained throughout the fabrication process in order to ensure that the calculated tolerance goals were being achieved. Of the 43 samples fabricated, the 32 best samples were tested. Special CPW launchers were designed and accurately machined for easy and reliable mounting of the samples to be tested.

Measurements were made by means of four different groups of instrumentation; the Singer 8000/705 sweep network analyzer, the HP 8545A automatic network analyzer, the HP 1415A TDR and the HP 1815B TDR/SAMPLER. The Singer network analyzer measurements yielded fairly accurate characteristic impedance information, but the most important contribution

of the Singer instrumentation to this thesis came from its ability to measure transmission loss to within .4 dB. A statistical treatment of this transmission loss data coupled with a graphical method for extracting contact loss yielded accurate attenuation information as a function of thin film thickness. The loss theory developed in Chapter II was shown to be quite valid for thin films with thicknesses of 1 skin depth or less. Moreover, the resistivity of thin evaporated aluminum films was shown to be approximately 2.68 ± 5.2% times higher than the bulk value for aluminum, thus increasing attenuation significantly. The HP TDR systems were used primarily to obtain precise reflection information for the accurate determination of characteristic impedance and the verification of Wen's theory.

The TDR measurements led to the verification of Wen's theory and some simple design guidelines for realizing some basic assumptions made by Wen in his derviation. These guidelines are presented in section 5.4. Interference of CPW performance by nearby metallic objects is also treated in the same section. It was found that for $\epsilon_r > 9.2$, metallic objects can be placed at a distance as small as the ground plane spacing $2b_1$ from the surface of the CPW, allowing properly designed CPW circuits to be encapsulated into small packages or densely packed if necessary.

Coplanar waveguides have been shown herein to display attenuation characteristics which are comparable to microstrip circuits. For a 50 Ω microstrip transmission line propagating in the quasi-TEM mode at 2 GHz, a typical value for attenuation would be .13 dB/λ for a 25 mil substrate thickness [2]. For the 50 Ω CPW's measured herein at 1.5 GHz, .21 dB/λ

was measured for t_f = 1 skin depth with a 50 mil wide center strip, and .125 dB/λ was measured for t_f = 1 skin depth with a 100 mil wide center strip; see Figure 5.1-3 at t_f = 21 kÅ.

The simple CPW theory of Chapter II has been shown to be accurate when the proper design guidelines of section 5.4 are used. CPW's also have the advantage that discrete components may be bonded between center conductor and ground planes on the same dielectric surface, making the drilling of holes unnecessary, and interference with electric fields minimal. With proper design, CPW's can be encapsulated into small lightweight packages or placed close to one another without significant interference. They can also be meandered without detectable reflections. In conclusion, this survey has shown that properly designed CPW's perform as well as other strip transmission lines currently in use and have very definite advantages as well.

APPENDIX A

EXACT TOLERANCE ANALYSIS AND OPTIMUM TOLERANCE SETS WITH EXAMPLES

A.1 The Sequential Unconstrained Minimization Technique

The 'Sequential Unconstrained Minimization Technique' (SUMT) is simply a method by which the familiar 'Minimax Formulation' can be implemented. Figure A.1-1 illustrates this point by introducing a real positive boundary parameter P, which is to be added to the upper specification boundary, $S_U(\omega)$, and subtracted from the lower specification boundary, $S_L(\omega)$. This defines new temporary upper and lower boundaries,

$$S_U'(\omega, P) = [S_U(\omega) + P] \qquad (A.1\text{-}1)$$

and

$$S_L'(\omega, P) = [S_L(\omega) - P] \qquad (A.1\text{-}2)$$

respectively. There is an additional requirement that P is chosen large enough initially to ensure that the new temporary boundaries enclose the general response function $F(\underline{\theta}, \omega)$. The SUMT ensures that P is then reduced until it is zero or negative, subject to the constraint that the new temporary boundaries always enclose the response function $F(\underline{\theta}, \omega)$ during the minimization of P. The effect is therefore to use the temporary boundaries to press the response function $F(\underline{\theta}, \omega)$ into the region bounded by $S_U(\omega)$, $S_L(\omega)$, ω_L, and ω_U. When P has been reduced to zero, the overall specifications imposed upon $F(\underline{\theta}, \omega)$ have been met exactly, and when P has been minimized to a negative real number the

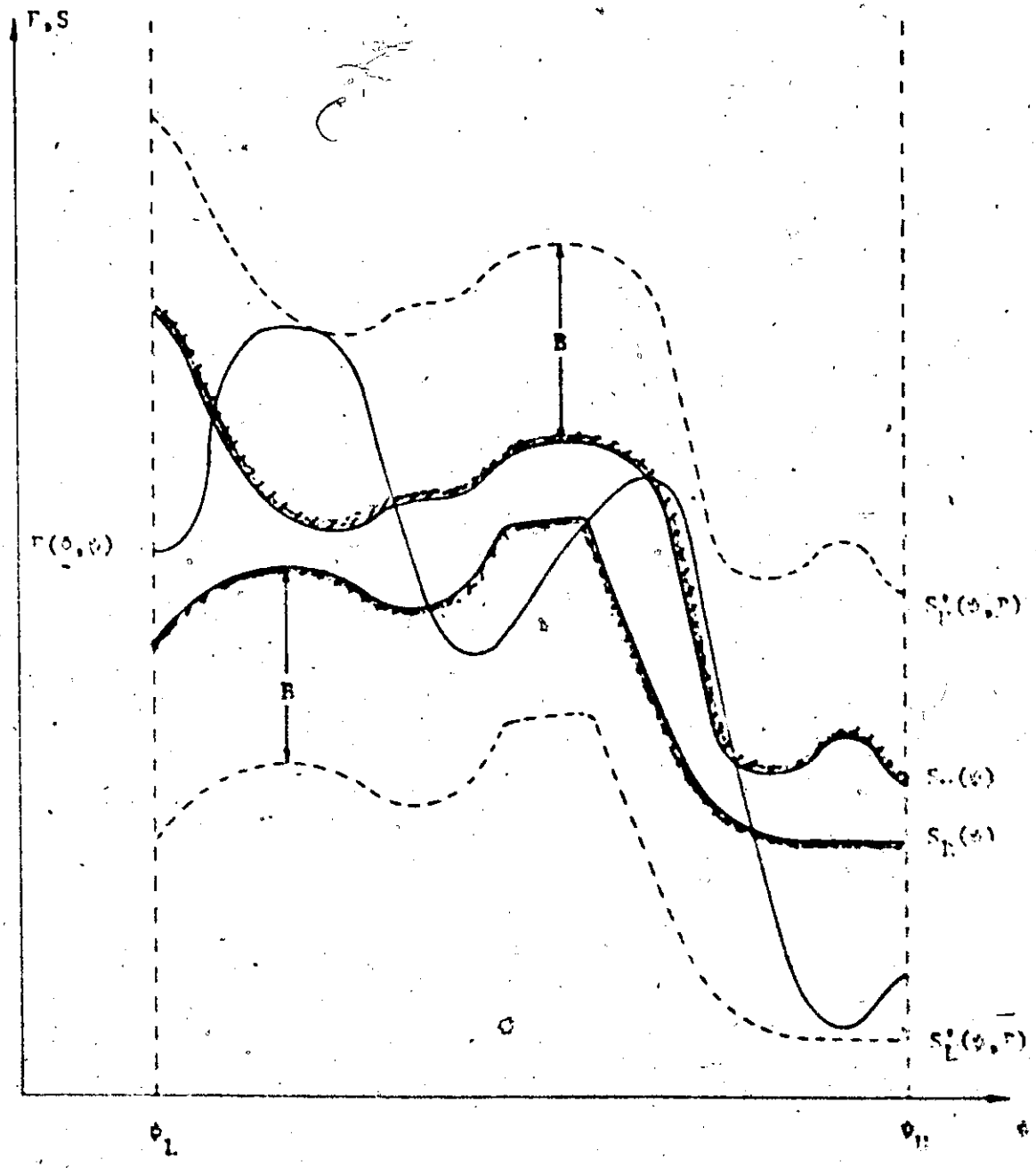

Figure A.1-1: Graphical Illustration of the Use of the Sequential Unconstrained Minimization Technique (SUMT) for Tolerance Analysis.

overall specifications imposed upon $F(\underline{a},\phi)$ have been exceeded. Equality and inequality constraints may also be imposed upon the minimization of F, as will be seen shortly. First the 'Minimax Formulation' will be discussed.

The 'Minimax Formulation' may be defined by an objective function of the form

(A.1-3)

$$U = U(\underline{a},\phi) = \underset{[\phi_L,\phi_U]}{MAX} \left[W_U(\phi) \{F(\underline{a},\phi) - S_U(\phi)\} , W_L(\phi) \{S_L(\phi) - F(\underline{a},\phi)\} \right]$$

where $\underline{a}$ is an n x 1 parameter vector,

$F(\underline{a},\phi)$ is a real approximating function,

$S_U(\phi)$ is a real upper specified function,

$S_L(\phi)$ is a real lower specified function,

$W_U(\phi)$ is a weighting function for $S_U(\phi)$, $W_U(\phi)>0$,

$W_L(\phi)$ is a weighting function for $S_L(\phi)$, $W_L(\phi)>0$,

$S_U(\phi) > S_L(\phi)$, ϕ is a variable sampled ns times,

and U is a real objective function to be minimized. It then follows that when U is minimized, the maximum amount by which $F(\underline{a},\phi)$ fails to meet the specifications, $S_U(\phi)$ and $S_L(\phi)$, is minimized. Similarly, the minimum amount by which $F(\underline{a},\phi)$ exceeds the specifications is maximized. One must be cautious while minimizing U however, since U is a function of ϕ and discrete values of ϕ are used. Hence the maximum deviation between specifications and response function can change abruptly from one point on the ϕ axis to another sampled point. When this happens discontinuous derivatives of U are generated in the response hypersurface, and there are few multidimensional minimization methods available which can handle such a problem. It should be also noted that if R is constant,

$S'_U(\psi,P)$ and $S'_L(\psi,P)$ from (A.1-1) and (A.1-2) may be substituted into (A.1-3) in place of $S_U(\psi)$ and $S_L(\psi)$ without loss of generality. After each minimization of U, B may be reduced and U minimized once more.

In general, the minimization of U is also subject to equality and inequality constraints, defined as follows:

Inequality Constraints:

$$\underline{g}(\underline{\phi},\psi) \triangleq \begin{matrix} g_1(\underline{\phi},\psi) \\ g_2(\underline{\phi},\psi) \\ g_3(\underline{\phi},\psi) \\ \vdots \\ g_m(\underline{\phi},\psi) \end{matrix} \qquad \text{(A.1-4)}$$

Equality Constraints:

$$\underline{h}(\underline{\phi}) \triangleq \begin{matrix} h_1(\underline{\phi}) \\ h_2(\underline{\phi}) \\ h_3(\underline{\phi}) \\ \vdots \\ h_q(\underline{\phi}) \end{matrix} \qquad \text{(A.1-5)}$$

such that a feasible or acceptable region of design

$$R_A \triangleq \{\underline{\phi} \mid \underline{g}(\underline{\phi},\psi) > \underline{0},\ \underline{h}(\cdot) = \underline{0}\}. \qquad \text{(A.1-6)}$$

It should be noted that ψ-dependent constraints have been included in $\underline{g}(\underline{\phi},\psi)$. If it is wished that this dependency be removed, the terms containing ψ may have their coefficients set to zero. Hence, there is no loss of generality in writing the inequality constraints as $\underline{g}(\underline{\phi},\psi) > \underline{0}$.

The SUMT is only a practical extension of the 'Minimax Formulation' except that B is a variable parameter. The SUMT may be defined in a generalized fashion by the objective function

$$P = P(\underline{\phi},\underline{\psi},B,r) = B + r \sum_{j=1}^{m+2ns} [g_j(\underline{\phi},B,\underline{\psi})]^{-1} + r^{-\frac{1}{2}} \sum_{k=1}^{q} h_k^2(\underline{\phi}) \qquad (A.1\text{-}7)$$

where there are m given inequality constraints, q given equality constraints and 2ns minimax inequality constraints. The first term of P ensures that B is minimized when P is minimized. The second term ensures that all inequality constraints are maintained throughout the minimization process. Notice that B has been inserted into the arguments of g_j as an extra parameter. This ensures that the minimax criterion has been embodied into P, as will be seen shortly. The weight r is utilized to emphasize the inequality constraints to an adjustable degree. The third term of P emphasizes the equality constraints $h_k(\underline{\phi})$ for $k = 1,2,\ldots q$. The symbol $\underline{\psi}$ represents a vector of ns sampled ψ values. The factor $r^{-\frac{1}{2}}$ is also an adjustable weighting factor.

During the minimization of P, r must be reduced from a large number such as 1000 to a very small number such as .001 or less. The process involves minimizing P for a fixed value of r. Then r may be reduced by a factor of 10 and P is again minimized. This stepped process is continued until r is very small. When r is large the inequality constraints are emphasized and so the point $\underline{\phi}$ moves into the center of the n- dimensional feasible region R_A. As r is reduced, the point $\underline{\phi}$ is free to move more liberally in R_A and more attention is simultaneously placed on the equality constraints since $r^{-\frac{1}{2}}$ is increasing. When r is

very small ϕ is extremely close to the boundary of R_A, though still inside this feasible region, and the equality constraints are for all practical purposes satisfied. Attention is then focused on the minimization of B since P = B when r is small and the equality constraints are met. Further minimization of P then minimizes B subject to maintaining all imposed constraints. When B goes negative, the overall function specifications on $F(\underline{\phi},\underline{\omega})$ have been exceeded. B should be made as negative as possible since then the specifications will have been exceeded by the maximum possible amount and the best possible solution will have been attained. This is also necessary for introducing tolerance into a solution of the above type. If B = 0, the solution has no tolerance capability. If B < 0 it is possible to impose positive and negative tolerances on the various parameters of the response function and still meet the overall function specifications.

To illustrate how the minimax criterion has been introduced into the SHIFT it is necessary to define an upper bound error

$$e_U(\underline{\phi},\underline{\omega}) \triangleq W_U(\underline{\omega}) \{F(\underline{\phi},\underline{\omega}) - S_U(\underline{\omega})\} \qquad \text{(A.1-8)}$$

and a lower bound error

$$e_L(\underline{\phi},\underline{\omega}) \triangleq W_L(\underline{\omega}) \{S_L(\underline{\omega}) - F(\underline{\phi},\underline{\omega})\}. \qquad \text{(A.1-9)}$$

The right hand sides of (A.1-8) and (A.1-9) have already been presented in expression (A.1-3) for the minimax criterion. Hence all symbols in

(A.1-8) and (A.1-9) have already been defined by (A.1-3). Both the upper bound and lower bound errors are positive if the specifications on $F(\underline{\phi},\psi)$ have not been met and negative if these specifications have been exceeded. It is then possible to use the positive real number B in conjunction with these two error terms by defining extra inequality constraints as follows:

$$g_j(\underline{\phi},B,\psi) \triangleq B - e_U(\underline{\phi},\psi) \geq 0, \quad j = [m+1,\ m+ns] \tag{A.1-10}$$

$$g_j(\underline{\phi},B,\psi) \triangleq P - e_L(\underline{\phi},\psi) \geq 0, \quad j = [m+ns+1,\ m+2ns] \tag{A.1-11}$$

ns $\triangleq$ the number of sampling points ψ_{is}, (is = 1,2,...,ns). (A.1-12)

From (A.1-10) and (A.1-11) it is easily seen that as B is reduced from a large initial positive value towards zero, and hopefully a negative value, the upper and lower bound errors must also become more negative, and so B actually compresses the response function $F(\underline{\phi},\psi)$ into the region bounded by $S_U(\psi)$, $S_L(\psi)$, ψ_L and ψ_U. For a fixed and sufficiently small value of r, the value of P obtained for a minimum value of P must cause the new temporary upper and lower boundaries of Figure (A.1-1) to almost touch the response function at least at one point along these boundaries. Otherwise P could be minimized further.

The SIMT expression, (A.1-7), has the advantage that the partial derivatives of P are well defined providing the partial derivatives of $g_j(\underline{\phi},B,\psi)$ and $h_k(\underline{\phi})$ are well defined. Hence, efficient subroutines such as the Fletcher-Powell minimization technique may be used to minimize P.

Expression (A.1-7) does have the disadvantage of being computationally time consuming, but once minimization has commenced, a minimum value for P and B is likely to be found. In other words, the technique is quite reliable but is costly in terms of computer time. This aspect of monetary expense is however compensated by the fact that the minimization of P gives useful insight into the tolerance problem and even promises to give meaningful and accurate tolerance information. Perhaps other more efficient strategies should be used to locate an initial suboptimal solution $\underline{\phi}_s^*$ for the given response function $F(\underline{\lambda},\underline{\phi})$. The "least p^{th}" technique appears to be applicable here [33]. The SUMT could then be used only to refine the design by centralizing $\underline{\phi}$ inside R_A for tolerance optimization. A method by which this can be achieved will be described shortly.

A.2 The Basis of Exact Tolerance Analysis in a Multidimensional Parameter Space by Tolerance Box Growth.

In the literature on sensitivity and tolerance, [15]-[39], various approximate and cumbersome techniques were used to desensitize a design. For instance, first and second order sensitivity expressions were used as constraints to locate a desensitized nominal design in a region of parameter space for which $F(\underline{\lambda},\underline{\phi})$ was least sensitive to incremental parameter changes for all values of $\underline{\phi}$. It seemed that a first order sensitivity measure was more useful than a second order sensitivity measure from the standpoint of ease in computation in

relation to the worth of the end result. It should be emphasized that such desensitization methods and others found in the literature, did not produce meaningful tolerance information. All that was achieved was a desensitized nominal design which might not be acceptable anyway due to imposed tolerances.

Mention should be made of the more expensive, but more precise Monte Carlo analysis, customarily used in fixing acceptable design tolerances. Obviously, all of the above techniques have serious drawbacks and it is hoped that the new technique to be presented herein will not only produce exact and meaningful tolerance information, but also produce it at a moderate cost. It should also be mentioned that the creation of this new technique in n dimensions was stimulated by E.M. Butler's exact 2-dimensional tolerance analysis [32].

Figure A.2-1 illustrates the use of the SIMT in 2-space to achieve meaningful tolerance information. The contours of Figure A.2 are herein called feasibility contours. These and the region they enclose represent points (ϕ_1, ϕ_2) for which B has a constant value. The feasibility contours also enclose acceptable design points (ϕ_1, ϕ_2) if $S'_U(\phi,B)$ and $S'_L(\phi,B)$ are suitable boundaries for a selected value of B. Each contour is actually a projection of the 3-dimensional objective function $P(\phi_1,\phi_2,B,r)$ when P is infinite, onto a 2-dimensional parameter space ϕ for a predetermined set of sampled ϕ values ϕ_i and a constant value of B. If n parameters are involved, P is (n + 1)-dimensional and any point ϕ which makes P infinite must lie on a contour bounding R_A. Also these contours generally have some sharp corners because these corners represent the intersection of various imposed constraining functions. It will now

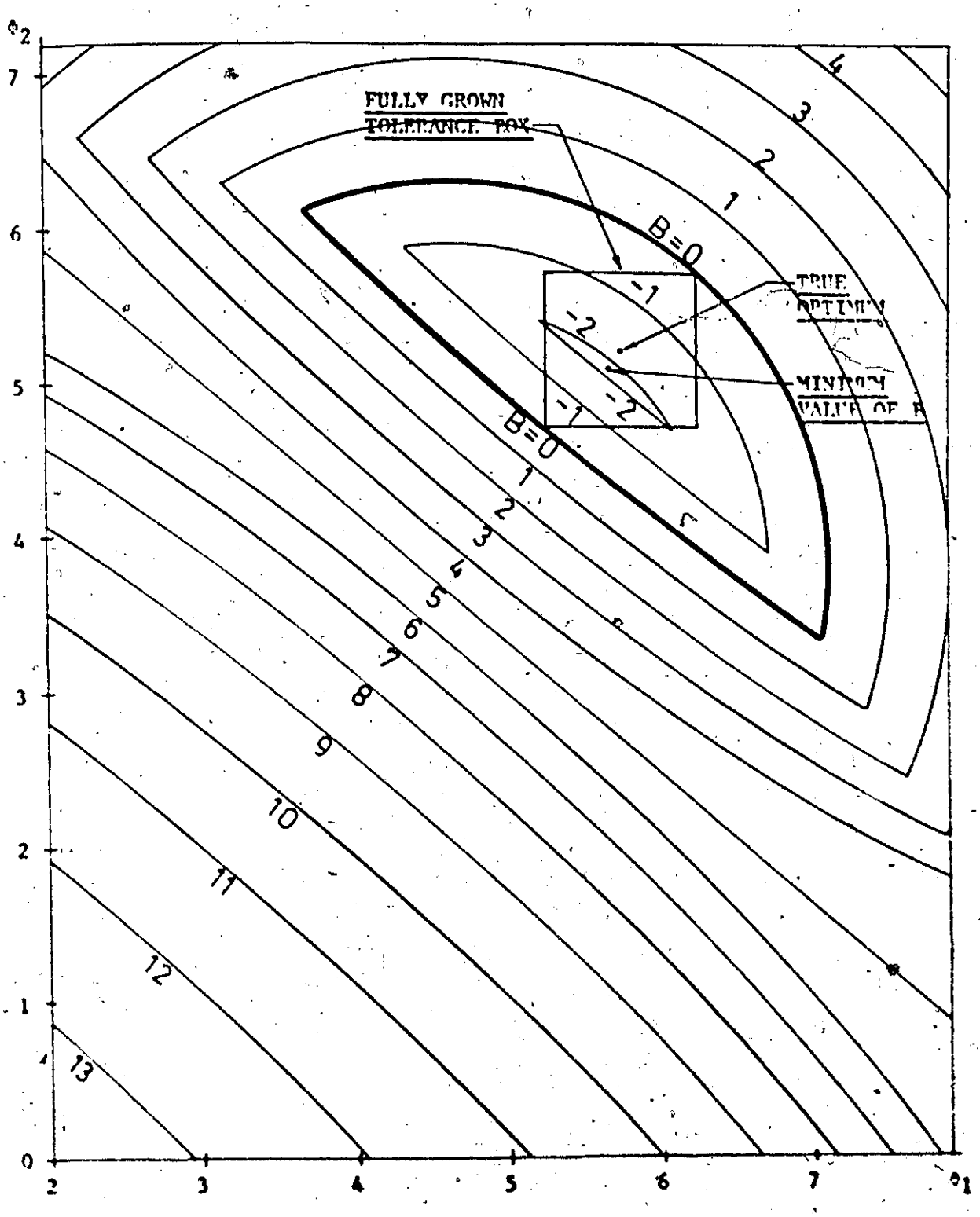

Figure A.2-1: Typical Feasibility Contours in a 2-Dimensional Space.

be shown how a Tolerance Box can be grown within such contours.

It has already been pointed out in section A.1 that when B is positive, the overall specifications on the response function $F(\phi,\psi)$ have not been achieved and when B is negative these same specifications have been exceeded. Hence, any point, ϕ, inside the region $B<0$ represents an acceptable solution from the viewpoint that at least the specifications on $F(\phi,\psi)$ have been satisfied. A tolerance rectangle may be grown from almost zero size inside this acceptable region R_A until the sides of the rectangle are a weighted maximum. The center of the rectangle can then be used as the true nominal design, and any point, ϕ, inside the rectangle represents an acceptable deviation from the nominal design. In Figure A.2-1, the sides of the rectangle are weighted according to the ratio $c_1 : c_2 = 2:1$, where c_1 and c_2 are expected tolerances for parameters ϕ_1 and ϕ_2 respectively. As will be seen shortly, an extra parameter ϵ, will be introduced to indicate the size of the rectangle. As the tolerance rectangle is grown, ϵ will indicate to what extent the expected tolerances have been achieved. If finally $\epsilon>1$, c_1 and c_2 have been realized.

One must first obtain a sub-optional design by methods outlined in section A.1. This approximation corresponds to the most negative value of B attainable. It should be emphasized that if $B=0$ is the minimum value of B attainable, no tolerance rectangle can be grown unless one relaxes the upper and lower boundary constraints by allowing B to be positive. A minimum of P with $B<0$ establishes the existance of an n-dimensional acceptable region R_A in n-space that is bounded by the

feasibility contour labelled $P=0$, and is defined as the set of all points, ϕ, that satisfy the condition $P<0$. For tolerance box growth this acceptable region is suitably redefined in a more general way by a modified version of (A.1-6) by shifting $S_U(\phi)$ and $S_L(\phi)$ by a reference quantity P_o, such that

$$R_A \triangleq \{\phi \mid g(\phi,B,\phi) > 0\}, \qquad (A.2\text{-}1)$$

$$B < P_o,\ P_o = \text{constant}. \qquad (A.2\text{-}2)$$

The selection of this constant allows the temporary upper and lower boundaries $S'_U(\phi,P)$ and $S'_L(\phi,P)$ to be moved up or down if a redesign is necessary. Notice that equality constraints have been removed since they do not allow tolerances to exist except perhaps along a fixed hypersurface in n-space. Also if the minimum for P is at $P=P_o$, the feasibility contour $P=P_o$ is a single point ϕ^*_s, and the region R_A is also only a single point ϕ^*_s. In this case the corresponding tolerance rectangle that may be grown has zero size and so only zero tolerance may be utilized.

As briefly mentioned above, if tolerance is to be accomodated in a design, no equality constraints can be assured except perhaps at the nominal design value. This is because the tolerance imposed on the design defines a rectangular region of parameter space that is always broader that the region defined by the equality constraints. For example, in a 2-parameter problem, an equality constraint defines a curved or straight line relating the 2 parameters to each other, whereas the imposed tolerances define a rectangular area in 2-space. For a 3-parameter problem, an equality constraint defines a 3-dimensional box. The intersection of several equality constraints is even more restrictive. One may in general extend these concepts to an n-dimensional problem by stating

that if equality constraints are to be maintained in an n-dimensional design, only zero tolerance is acceptable on each of the n parameters of the design. As a result no attempt will be made in this tolerance analysis to impose equality constraints except maybe at the design center value.

The n-dimensional tolerance box mentioned above is really a rectangular hyperparallelipiped, but will herein be called a 'tolerance box'. The tolerance box may be defined mathematically as the hypersurface

$$\lim_{a\to\infty} \sum_{i=1}^{n} \left| \frac{\phi_i - \phi_i^*}{\varepsilon\, c_i\, \phi_i^*} \right|^a = 1 \qquad (A.2\text{-}3)$$

where $a>0$ and is an even integer, $\varepsilon>0$ is a parameter that controls the tolerance box growth and $\underline{T} = [c_1, c_2, \ldots, c_i, \ldots, c_n]^T$ is a pre-specified tolerance vector. If the limiting case is temporarily ignored and $a=2$, the hypersurface (A.2-3) is a hyperellipsoid, but if a is allowed to be a large even integer, the corners of (A.2-3) become rectangular. Hence as $a\to\infty$ (A.2-3) defines a tolerance box with sides whose lengths are $2\cdot\varepsilon c_i\phi_i^*$. The box has a center $\underline{\phi}^*$ and $\underline{\phi}$ is any point on the surface of the box.

It is desirable to express all of the corners of the tolerance box in a concise formula. There are a total of 2^n such corners for a problem involving n parameters and so an $n \times 2^n$ matrix is required to describe all of the corners of the tolerance box. The corner matrix is then written as

$$\underline{C} \triangleq [\underline{c}^1 \underline{c}^2 \ldots \underline{c}^{2^n}]$$

$$\triangleq [\underline{\phi}^* \underline{\phi}^* \ldots \underline{\phi}^*] + \tfrac{1}{2} A\underline{Z} \qquad \text{(A.2-4)}$$

where the lengths of the axes of the box are given by the diagonal matrix Λ which is expressed as

$$\underline{\Lambda} \triangleq 2c \begin{bmatrix} \varepsilon_1 \phi_1^* & 0 & & 0 \\ 0 & \varepsilon_2 \phi_2^* & \cdots & 0 \\ \cdot & \cdot & & \cdot \\ \cdot & \cdot & & \cdot \\ \cdot & \cdot & & \cdot \\ 0 & 0 & \cdots & \varepsilon_n \phi_n^* \end{bmatrix} \qquad \text{(A.2-5)}$$

and an $n \times 2^n$ matrix of all possible sign combinations is given by

$$\underline{Z} \triangleq \begin{bmatrix} 1 & -1 & 1 & -1 & 1 & -1 & 1 & -1 & \ldots & 1 & -1 \\ 1 & 1 & -1 & -1 & 1 & 1 & -1 & -1 & \ldots & -1 & -1 \\ 1 & 1 & 1 & 1 & -1 & -1 & -1 & -1 & \ldots & -1 & -1 \\ 1 & 1 & 1 & 1 & 1 & 1 & 1 & 1 & \ldots & -1 & -1 \\ \cdot & \cdot & \cdot & \cdot & \cdot & \cdot & \cdot & \cdot & & \cdot & \cdot \\ \cdot & \cdot & \cdot & \cdot & \cdot & \cdot & \cdot & \cdot & & \cdot & \cdot \\ \cdot & \cdot & \cdot & \cdot & \cdot & \cdot & \cdot & \cdot & & \cdot & \cdot \\ 1 & 1 & 1 & 1 & 1 & 1 & 1 & 1 & \ldots & -1 & -1 \end{bmatrix} = [Z_{it}]_{\substack{i=1,2,\ldots n \\ t=1,2,\ldots 2^n}} \qquad \text{(A.2.6)}$$

hence

$$\underline{C} = \begin{bmatrix} \phi_1^* + \varepsilon\varepsilon_1\phi_1^* & \phi_1^* - \varepsilon\varepsilon_1\phi_1^* & \cdots & \phi_1^* - \varepsilon\varepsilon_1\phi_1^* \\ \phi_2^* + \varepsilon\varepsilon_2\phi_2^* & \phi_2^* + \varepsilon\varepsilon_2\phi_2^* & \cdots & \phi_2^* - \varepsilon\varepsilon_2\phi_2^* \\ \phi_3^* + \varepsilon\varepsilon_3\phi_3^* & \phi_3^* + \varepsilon\varepsilon_3\phi_3^* & \cdots & \phi_3^* - \varepsilon\varepsilon_3\phi_3^* \\ \phi_4^* + \varepsilon\varepsilon_4\phi_4^* & \phi_4^* + \varepsilon\varepsilon_4\phi_4^* & \cdots & \phi_4^* - \varepsilon\varepsilon_4\phi_4^* \\ \vdots & \vdots & & \vdots \\ \phi_n^* + \varepsilon\varepsilon_n\phi_n^* & \phi_n^* + \varepsilon\varepsilon_n\phi_n^* & \cdots & \phi_n^* - \varepsilon\varepsilon_n\phi_n^* \end{bmatrix}_{\substack{i=[1,n] \\ t=[1,2^n]}}$$

$$= [\phi_1^*(1+\varepsilon\varepsilon_i Z_{it})]$$

$$\Delta [\quad \underline{C}^1 \quad \underline{C}^2 \quad \cdots \quad \underline{C}^{2^n} \quad]$$

$$\Delta [\, \underline{C}^t \,]_{t=[1,2^n]} \qquad (A.2.7)$$

where the column vector $\underline{C}^t$ for $t=1,2,\ldots 2^n$ is the t^{th} corner of the box. Note that the matrix $\underline{Z}$ can be generated by the same principle that governs a binary counter. There are two states to be accounted for; +1 and -1. All possible combinations of n of these binary digits yields 2^n states which may be generated sequentially by a binary counter.

It is easily seen from (A.2.3) and (A.2.7) how the growth of the tolerance box can be accomplished. The axes of the tolerance box are weighted according to the expected tolerances $\pm\varepsilon_i$ and the growth of the tolerance box is controlled by the parameter ε. The parameter ε is given an initial value which is almost zero and is gradually

increased until the tolerance box can no longer be grown inside R_A. It is also desirable to shift the design center value $\underline{\phi}^*$. This is accomplished simultaneously with the growth of ϵ by using a modified format of the sequential unconstrained minimization technique of section A.1. In this format R is a constant and $-\epsilon$ is minimized instead of R.

$$P_{TB}(\underline{\phi}^*,\epsilon,\psi,B,r) \triangleq -\epsilon + \left[r\sum_{j=1}^{m+2ns} \frac{-1}{[F_j(\underline{\phi},P,\psi_{js})]} + r^{-1/2} \sum_{k=1}^{q} h_k^2(\underline{\phi}) \right]_{\substack{P=P_0 \\ \underline{\phi}=\underline{\phi}^*}}$$

$$+ \left[\sum_{\underline{\phi}=\underline{C}^1}^{\underline{\phi}=\underline{C}^{2^n}} \left[r\sum_{j=1}^{m+2ns} \frac{-1}{[F_j(\underline{\phi},P,\psi_{js})]} \right] \right]_{P=P_0}$$

$$\triangleq P_{TB} \qquad (A.2\text{-}8)$$

whose derivatives with respect to the elements of $\underline{\phi}^*$ are given by

$$\frac{\partial P_{TB}}{\partial \phi_i^*} = \left[-r\sum_{j=1}^{m+2ns} \frac{1}{F_j^2(\underline{\phi},P,\phi_{js})} \cdot \frac{\partial F_j(\underline{\phi},P,\phi_{js})}{\partial \phi_i} + 2r^{-1/2} \sum_{k=1}^{q} h_k(\underline{\phi}) \frac{\partial h_k(\underline{\phi})}{\partial \phi_i} \right]_{\substack{P=P_0 \\ \underline{\phi}=\underline{\phi}^*}}$$

$$+\left[\begin{array}{c}\phi=C^{2^n}\\ -r\sum\limits_{\phi=C^1}\end{array}\left[\sum_{j=1}^{m+2ns}\frac{1}{R_j^2(\underline{\phi},R,\psi_{is})}\cdot\frac{\partial R_j(\underline{\phi},R,\psi_{is})}{\partial\phi_i}\cdot\frac{\partial\phi_i}{\partial\phi_i^*}\right]\right]\Bigg|_{R=R_o} \qquad (A.2\text{-}9)$$

where

$$\frac{\partial\phi_i}{\partial\phi_i^*} = 1 + \varepsilon\varepsilon_i z_{it},$$

$$i=1,2,\ldots n$$

$$t=1,2,\ldots 2^n. \qquad (A.2\text{-}10)$$

Similarly, the derivative of P with respect to ε is given by

$$\frac{\partial P_{TR}}{\partial\varepsilon} = [-1] + \left[\begin{array}{c}\phi=C^{2^n}\\ -r_l^2\\ \phi=C^1\end{array}\sum_{j=1}^{m}\frac{1}{R_j^2(\underline{\phi},R,\psi_{is})}\cdot\left[\nabla R_j(\underline{\phi},R,\psi_{is})\right]^T\cdot\left[\frac{\partial\underline{\phi}}{\partial\varepsilon}\right]\right]\Bigg|_{R=R_o} \qquad (A.2\text{-}11)$$

where

$$\frac{\partial \phi_i}{\partial \epsilon} = \phi_i^*(0 + c_i Z_{it}),$$

$$i = 1,2,\ldots n,$$

$$t = 1,2,\ldots 2^n \qquad \text{(A.2-12)}$$

The objective function P_{TB} has m inequality constraints and q equality constraints such that these constraints are imposed on the nominal design vector $\underline{x}^*$. Note however that only the inequality constraints are applied to the corners $\underline{C}^t$, where $t=1,2,\ldots 2^n$. Since the equality constraints represent the intersection of hypersurfaces, and the tolerance problem involves a hypervolume, one can't hope to satisfy the equality constraints at the center of the box and corners of the box as well. If equality constraints are to be imposed, a compromise must be made by imposing the equality constraints at the center of the box only. This could limit the size of the box if the equality constraints can be satisfied only near the edge of R_A, but this is what the aforementioned compromise is all about. The objective function P_{TP} allows c to grow from a very small positive value to as large a value as possible while all necessary constraints are maintained. It is better if only inequality constraints are imposed since then the tolerance box will grow to a larger size and larger individual parameter tolerances will be allowed. If equality constraints

are also required, they must be imposed only at the design center ϕ^* if a tolerance box is to be grown at all. Since $P=P_0$ throughout the minimization of P_{TB}, all the corners of the tolerance box as well as the nominal design (center of the box) lie inside the acceptable region R_A throughout the minimization of P_{TB}, where $P=P_0$ is substituted into upper and lower bound constraints $S_U'(\phi,P)$ and $S_L'(\phi,P)$. The existance of continuous derivatives (A.2-9), (A.2-11), and (A.2-12) allows the use of the Fletcher-Powell minimization technique to arrive at a minimum for P_{TB} quickly. These derivatives exist if the required partial derivatives of the response function and all constraining functions exist. If this is true, then P_{TB} is a smooth and continuous function except at the boundaries of R_A.

Originally the problem with tolerance analysis was that the computer was allowed to deal with one point of parameter space at once. The algorithm defined by (A.2-8) allows the computer to cope with $2^n + 1$ points simultaneously, where 2^n corners are involved along with ϕ_0. However, one should be aware of some of the problems that could be encountered with these $2^n + 1$ points. Figure A.3 is a 2-dimensional illustration of potential hazards that could be encountered if P_{TB} is not minimized properly.

In Figure A.2-2, ϕ^1 and ϕ^6 both represent minimum values of P but ϕ^6 lies in an unacceptable region due to the sloped constraining line which enters the region enclosed by the feasibility contour labelled P=0. The next best attainable minimum near ϕ^6 is the constrained minimum ϕ^5. However, ϕ^1 obviously lies in a less sensitive region than ϕ^5 since

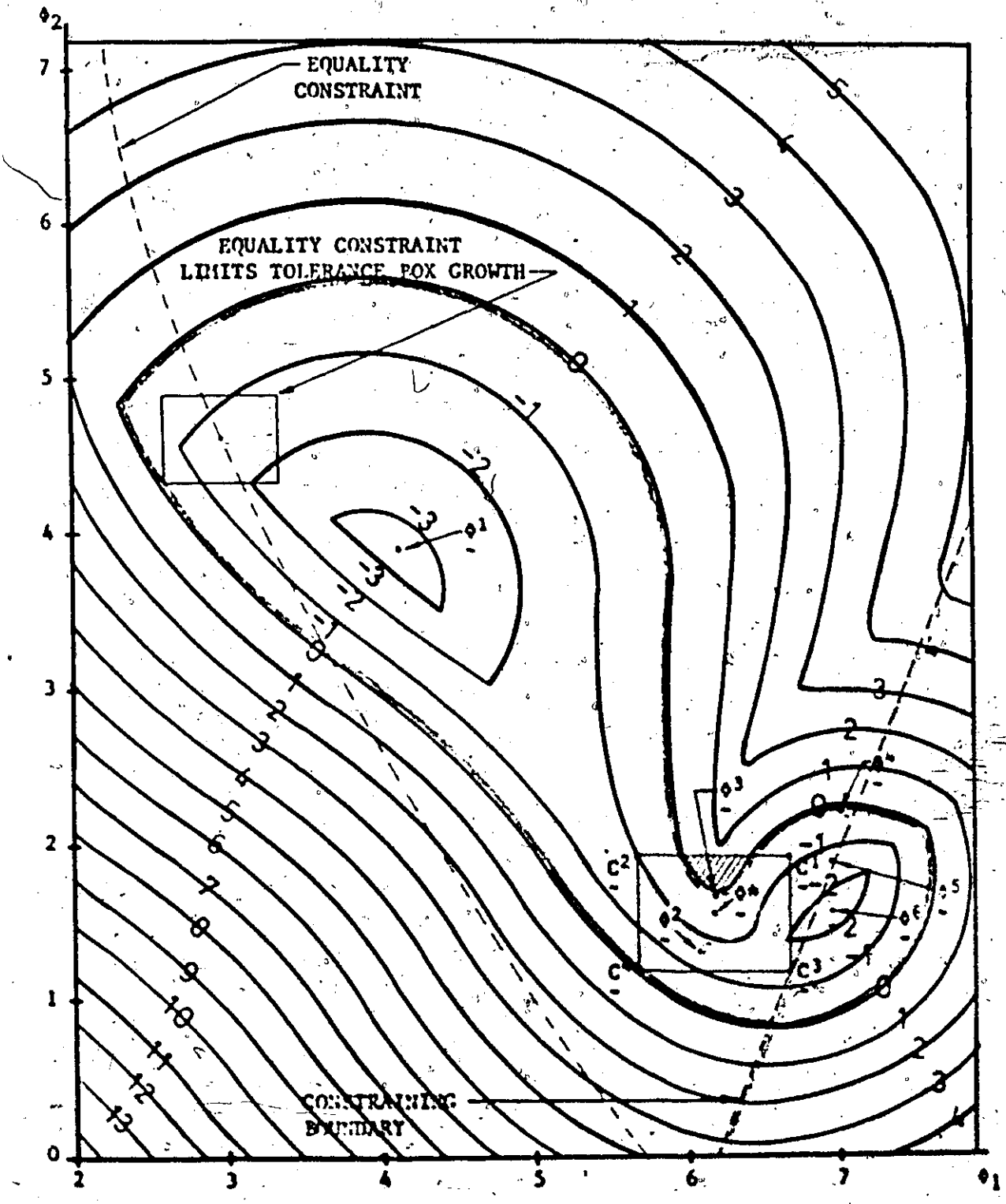

Figure A.2-2: Illustration of Hazards Encountered in Tolerance Analysis.

near ϕ^1 the feasibility contours with negative values of F are spread farther apart from each other than the same contours in the region of ϕ^5 and ϕ^6. Hence it would be preferable to grow a tolerance box in the region of ϕ^1 rather than ϕ^5. Either ϕ^1 or ϕ^5 can be obtained as sub-optimal designs by the methods outlined in section A.1. The methods of A.1 do not necessarily cause the least sensitive region of parameter space to be selected. As mentioned above it is desirable for the region of ϕ^1 to be chosen in preference to the region of ϕ^5 for a sub-optional design. Also, the saddle point ϕ^2 should also be avoided for reasons to be discussed shortly. These objectives can be achieved by using the desensitization methods in the aforementioned literature or by obtaining various solutions by trying the methods of A.1 from various starting points. A tolerance box can then easily be grown from each solution, and the center of the largest tolerance box can then be chosen as the best design. Also, the minimization of F to its most negative value ensures that points such as ϕ^4 of Figure A.2-2 are not chosen as a sub-optional design. ϕ^4 obviously satisfies the overall design specifications on the response function $F(\theta,\phi)$ but it is much easier to grow a tolerance box from a more centralized point such as ϕ^5 or ϕ^1.

In Figure A.2-2, ϕ^2 represents a saddle point and ϕ^3 is just another acceptable point in R_A near the saddle point. The growth of a tolerance box from either of these sub-optimal design values might result in the type of tolerance box shown enclosing these points. First of all, the corners of the box as well as the center of the box ϕ^*, lie in R_A, but obviously there are certain points within the box that lie outside R_A, and the algorithm defined by (A.2-3) is not aware of these points.

The shaded area of the tolerance box represents a loss in production line yield and such a situation should be avoided. The initial desensitization of a design reduces the chances for this hazard to occur. If in Figure A.2-2 the suboptimal starting point to be used for tolerance box growth is itself in the minimum sensitivity region, no problem of yield loss exists since this region is not only larger than the regions near ϕ^2 or ϕ^5, but the B=0 feasibility contour has no narrow lobes which can protrude into the tolerance box. That is, the growing tolerance box will not be in a constricted region as shown in Figure A.2-2 but will be in a broad convex region where it will not encounter the saddle point hazard.

The parameter ϵ should be grown to as large a value as possible in order to try to attain the desired tolerances. The lengths of the sides of the tolerance box as defined by (A.2-3) indicate that if $\epsilon>1$, the expected tolerances have not been achieved. Since mathematically, there are an infinite number of ways by which the sides of the tolerance box can be weighted, it is practical to initially select one set of allowable, realistic weights for the minimization of B and the growth of the tolerance box. For example, tolerance weights could be selected according to cost and availability of tolerances. Another way to select these weights is to measure R_A with tolerance meters which are really just narrow tolerance boxes with one tolerance weighted at least 100:1 over all remaining tolerances. This latter technique was used successfully in section 2.3 of Chapter II to obtain a set of tolerance weights called the optimum tolerance set. These weights multiplied by the value of ϵ_{max}

obtained in growing a tolerance box with these tolerance weights, gave the final optimum tolerances for the design and its imposed constraints.

Another method of selecting optimum tolerance weights is to employ the first order sensitivities of the response function $F(\underline{\phi},\psi)$ such that

$$\epsilon_i \int_0^{\infty} \left| S^F_{\phi_i}(\underline{\phi},\psi) \right| \Xi(\psi)\, d\psi = \epsilon_f \int_0^{\infty} \left| S^F_{\phi_f} \right| \Xi(\psi)\, d\psi \qquad (A.2\text{-}12)$$

$i = 1,2,\ldots,n$

$S^F_{\phi_i}(\underline{\phi},\psi)$ $\triangleq$ the first order sensitivity of F with respect to ϕ_i,

ϕ_i $\triangleq$ the i^{th} parameter,

ϕ_f $\triangleq$ a fixed parameter used as a reference,

ϵ_f $\triangleq$ unity,

$\Xi(\psi)$ $\triangleq$ a window function defining the range of ψ [26].

However, the computation of this first order approximation appears cumbersome compared to the tolerance meter method since more programming is required. The tolerance meter method employs the same program used for tolerance box growth, but is subject to the saddle point hazard.

One may also wish to grow a tolerance box with the tolerances weighted according to both cost and first order sensitivity. The final choice of the above technique for choosing tolerance weights is left to the designers discretion. In any case, all final tolerances ϵ's$_i$ have to be rounded off to the next lowest realistic available tolerances in

order that design specifications are met. The final central design ϕ^* must also be rounded off to realistic available parameters.

As a final comment, P_{TB} may be simplified slightly by omitting the first bracketed term of (A.2-8) if equality constraints are not present. The evaluation of inequality constraints at the point ϕ^* is most unnecessary. The corners of C^* alone imply the position of ϕ^* since ϕ^* is the center of the tolerance box. Hence, the evaluation of the inequality constraints at the corners of the tolerance box is sufficient to grow the box and determine ϕ^*.

A.3 Closed Regions and Open Ended Regions

The contours of Figure A.2-1 and Figure A.2-2 illustrate the case of closed acceptable design regions R_A, where each feasibility contour closes onto itself. Some design problems may involve open ended feasibility regions for which the feasibility contours do not close onto themselves except maybe at infinity. Furthermore the region R_A may have a large or infinite width at the open end. Such a problem arose in the tolerance analysis for CPU design in section 2.3 of Chapter II. In such open ended acceptable design regions, a tolerance box can grow to an extremely large size while the parameters of the central design ϕ^* also increase in magnitude. However, practical physical limits must be placed on these parameters and a reliable method of mathematically incorporating upper and lower bounds on the parameters into the objective function P or the objective function P_{TB} must be used.

Upper and lower bounds on design parameters simply fall into the general category of inequality constraints and so terms of the form

$$g_j^{-1} = \frac{1}{\phi_{Uj} - \phi_j} \qquad (A.3\text{-}1)$$

and

$$g_j^{-1} = \frac{1}{\phi_j - \phi_{Lj}} \qquad (A.3\text{-}2)$$

can easily be incorporated into the previously defined m inequality constraints. Notice that the derivatives of these terms are finite and continuous except at $\phi_j = \phi_{Uj}$ and $\phi_j = \phi_{Lj}$ where they represent imposed boundaries on R_A. This form of upper and lower bound constraints was necessary in the exact tolerance analysis applied to CRW design in section 2.3 of Chapter II. Very successful results were obtained.

A.4 Penalties for Corners Outside of R_A

Occasionally during the minimization of P_{TP}, a minimization subroutine, such as the Fletcher-Powell subroutine, will allow corners of the tolerance box to take steps outside of R_A. It should be remembered that R_A has a fixed size since it is defined by a fixed chosen value of P_f and its boundaries represent infinite values of P_{TP}. On either side of

these boundaries P_{TP} is finite. It is possible to shape the objective function P_{TB} outside of R_A into a large valued function with a steep slope pointing downward into R_A. This was accomplished by replacing violated constraint terms in P_{TP} with penalty terms T_p, of the form

$$T_p = +10^{-12} \left| g_j(\underline{\phi}, P, \psi) \right| \qquad (A.4\text{-}1)$$

which is easily differentiated to give

$$\frac{\partial T_p}{\partial \phi_i} = -10^{12} \left[\frac{\partial g_j(\underline{\phi}, P, \psi)}{\partial \phi_i} \right] \qquad (A.4\text{-}2)$$

where $g_j(\underline{\phi}, P, \psi) < 0$ when the j^{th} inequality constraint has been violated. Tests were made of this technique via a CDC 6400 IBM computer on three separate design examples. It was found that if a starting point for minimization was initially selected inside R_A, and one or several corners of the tolerance box stepped outside R_A during a particular iteration of the minimization process, the corners of the tolerance box were placed back into R_A at the following iteration. On the average, results from 3 separate problems indicated that iterations containing the above type of penalty terms occurred about 10% of the time for large values of r such as r=1, and about 75% of the time for $r=r_{min}=10^{-15}$. This latter value of r was the lowest value of r used for the three different tolerance box growth

examples attempted. As was expected, as r was reduced, ε grew and the chance for more corners of the tolerance box to step outside of P_A increased. Such a small value of r_{min} ensured that every tolerance box grew to a full size with at least some of the corners of the tolerance box touching some of the boundaries of P_A. Penalty terms of the form (A.4-1) for violation of inequality constraint boundaries defining P_A proved to be 100% successful for the 3 computed examples.

A general Fortran computer program for tolerance box growth in an n-dimensional parameter space was written by the author embodying into one complete package the mathematics of sections A.2 and A.3 as well as the penalty terms described above. Apart from this package it was necessary to write a subprogram to calculate the response function and its first order partial derivatives. Specific input data was required such as values for n, δ_S^*, δ_U, δ_L, ns*, α_L, α_U, $\Delta\beta$, ΔP, as well as starting and finishing values for ε, P, and r. Also, the sides of the tolerance box had to be weighted and so tolerance weights also formed part of this necessary input data. This scheme enabled tolerance boxes to be grown for different design examples with minimal effort. For each design example the boxes were grown sequentially for incremented values of P which gave useful information about the linearity of the design region. For simplicity only uniform sampling was used and no inequality constraints other than those arising from α_U, α_L, $S_U^i(\alpha,P)$ and $S_L^i(\alpha,P)$ were employed.

A.5 Computer Time Required to Grow One Tolerance Box

A set of six basic rules will be discussed to minimize the time required for growing a tolerance box. The total computation time t_{TP} for the growth of one tolerance box can be approximated by an expression of the form

$$t_{TP} = [\, a_0 + a_1 \cdot 4 \cdot (n+2) + a_2 \cdot n \cdot 2^n \,]$$

$$+ \{\, [b_0] + \left[\left[\sum_{i=1}^{n} b_i\right] + 2 \cdot ns \cdot b_{n+1}\right] \cdot [2^n + 1] + [\sum_{k=1}^{n} c_k]$$

$$+ \left[\left[\sum_{i=1}^{n} b_i\right] + 2 \cdot ns \cdot b_{n+1}\right] \cdot [2^n + 1] \cdot K$$

$$+ \left[\left[\sum_{i=1}^{n} b_i\right] + 2 \cdot ns \cdot b_{n+1}\right] \cdot [2^n] \cdot n \cdot K \,\} \cdot I \cdot N_r \qquad \text{(A.5-1)}$$

where

a_0 = time for initiating the computer program,

a_1 = average time for establishing control parameters, and the initial values of the design parameters, the upper and lower bounds on θ and the tolerance weights,

a_2 = time for computing one corner of the tolerance box,

b_0 = average time for initiating the calculation and recalculation

of P_{TR} and its derivatives from the minimization subroutine for each iteration,

b_j = time for computing each of the m initially given $g_j(\phi, R, \psi_{is})$ inequality constraints,

b_{m+1} = time for computing each upper and lower bound error inequality constraint,

C_k = a function of n representing time required for computing each of the q equality constraints,

K = 2 is an average constant denoting the ratio of the time taken to calculate both g_j and $\partial g_j/\partial \phi_i$ to the time taken to calculate g_j alone,

l = an integer representing the average number of times the minimizing subroutine calls for the evaluation of P_{TR} and its derivatives in order to find a minimum value of P_{TR} at a constant value of r,

N_r = the number of r values used,

and n, j, m, ns, k and q all have the same meaning as in (A.2-8). Expression (A.5-1) appears rather cumbersome, but fortunately it can be reduced to

$$
\begin{aligned}
t_{TR} &= [a_2 + K_1 K l N_r] \cdot n \cdot 2^n \\
&\quad + [(K_1 + K_1 l) \cdot l N_r] \cdot 2^n \\
&\quad + [4a_1] \cdot n \\
&\quad + [(a_0 + 3a_1) + (b_0 + b_1 + K_1 K + \sum_{k=1}^{n} C_k)\, l N_r]
\end{aligned}
$$

$$
K_1 = [\sum_{j=1}^{m} b_j] + 2 \cdot ns \cdot b_{m+1} \qquad \text{(A.5-3)}
$$

and since a_o, a_1, a_2 and even bo may be ignored in comparison to other more significant terms containing K_1, equation (A.5-2) reduces further to

$$t_{TB} = \{A_o + [A_1 + A_2 \cdot n] \cdot 2^n\} \cdot IN_r \qquad (A.5-4)$$

where A_o, A_1, and A_2 are constants for a given problem. This latter approximation to t_{TB} may be used to give insight into how one might proceed to minimize his computer time for tolerance box growth for n given parameters. First of all

$$A_o = K_I \cdot (K + 1) + \sum_{k=1}^{n} c_k,$$

$$A_1 = K_1 \cdot (K + 1),$$

and

$$A_2 = K_1 \cdot K \qquad (A.5-4)$$

are all linearly dependent on K_1 and hence so is t_{TP}. Also if no derivatives were evaluated K would be unity. Tolerance box growth requires first order partial derivatives and so K=2. A_o is the only time term dependent on the q equality constraints, since these constraints were evaluated at only the design center value for reasons discussed earlier. Hence equality constraints do not use up a large amount of the time required to grow a tolerance box. In many problems equality constraints may not even be present.

It is then obvious that t_{TP} may be reduced linearly if K_1 is reduced linearly. Equation (A.5-1) shows that K_1 may be reduced linearly by a linear reduction in the number ns of sampling points n_{is}. The minimum

required number ns to define R_A precisely can range from 2 to 20 or more. On the average a linear reduction in K_1 can also be acheived by a linear reduction in the number m of initial inequality constraints $g_i(\underline{\phi},\underline{p},\phi_{is})$, though usually all of the m given inequality constraints must be used and a reduction in K_1 by the reduction of m is not a feasible alternative. The best method of keeping K_1 and hence A_0, A_1, and A_2 small appears to be the selection of a minimum necessary value of ns, if one exists. Sometimes it is immediately obvious from the nature of the problem that one exists and sometimes its value is also obvious. For less obvious cases a low suitable value of ns can be estimated from a plot of $F(\underline{\phi},\phi)$ against ϕ for the initial sub-optimal design $\underline{\phi}^*_s$. If $F(\underline{\phi}^*_s,\phi)$ varies drastically for the given range of values of ϕ, then perhaps as many as 20 or more sampling points will be necessary to represent $F(\underline{\phi},\phi)$ accurately in $[\phi_L,\phi_U]$ in order that R_A is also accurately represented. A reliable means of selecting ns sampling points ϕ_{is} for cases when $F(\underline{\phi},\phi)$ is a smooth and continuous function of ϕ and has ns-1 continuous derivatives in $[\phi_L,\phi_U]$ will be given in section A.6. Confidence limits such as 99.0% reliability or better will also be placed on the selection of ns.

The other obvious means of reducing t_{TR} in (A.5-4) is to reduce I or N_r, since t_{TR} varies linearly as the product of I and N_r. I may be reduced by the selection of an efficient minimization subroutine such as the Fletcher-Powell subroutine or better still, Fletcher's latest subroutine called VF01 can be used. The integer I may also be small if the sub-optimal design $\underline{\phi}^*_s$ is already fairly well centralized in R_A and acts as a good starting point for tolerance box growth. Tolerance boxes, which are always grown while s is a constant, may be grown sequentially

by incrementing B by a small amount ΔB so that ϕ_s^* of each previous tolerance box acts as a good starting point for the new box to be grown. This was attempted by the author with 100% success in 3 design examples for various chosen sub-optimal designs ϕ_s^*.

The number of r values N_r can be reduced significantly if at first, not too large a starting value of r is chosen, and secondly, if a test is made during the computation which will stop reducing r by a factor of 10 when

$$\frac{\Delta c}{c} < 10^{-d} \qquad (A.5\text{-}5)$$

where Δc corresponds to the maximum increment in c obtained when r is decreased by 10 and where d is an integer chosen at the designer's discretion. Some typical acceptable values for d would be 3, 4 or 5. However, in the design examples attempted by the author, no such test was made during the execution of the computer program since the tolerance box growth process was being tested for the first time and unnecessary complications were avoided. The results showed that for variations in r from 10^{-2} to 10^{-15}, 10^{-2} to 10^{-15} and from 10^{-2} to 10^{-10} in increments of 10 x, the latter range was better in terms of a low starting value of r, a low final value of r, and also a smaller value of N_r. Too high a starting value of r caused the tolerance box to grow at an unnecessary slow rate at first thus causing I to be large. Eventually a suitable r value was reached when the tolerance box grew quickly, but such time delays were undesirable. The starting value $r=10^{-2}$ appeared to be quite suitable for tolerance box growth. The final value $r=10^{-15}$ corresponded

approximately to d=5 and a final value of $r=10^{-10}$ corresponded to d=4 which was an equally suitable value of d in terms of accuracy. Hence substantial time savings could be achieved for these tolerance box growths by allowing r to range from 10^{-2} to 10^{-10} in increments of 10 x.

In general the computation time t_{TR} for the growth of one tolerance box may be reduced by

(1) selecting a minimum required value of ns for 99.9% reliability or any other acceptable confidence level,

(2) reducing N_r by adjusting the initial value of r as outlined above,

(3) reducing N_r by using equation (A.5-5) as a test condition with d=3 or 4,

(4) reducing I by ensuring that the initial value or r is not too large and

(5) reducing I by ensuring that an efficient minimization subroutine such as Fletcher's VF01 package is used,

(6) reducing I by providing a good starting point for tolerance box growth by initially obtaining ϕ_n^* for a negative value of R and then proving a sequence of tolerance boxes by incrementing R for each new box.

As a final comment, there is one major fact that must be faced about tolerance box growth. There are 2^n corners at which the response function performance is to be evaluated and this fact leads to the linear dependance of t_{TR} on the factor 2^n as shown in (A.5-4). Also partial derivatives of P_{TR} with respect to c lead to the linear dependency of t_{TR} on the factor $n \cdot 2^n$. This means that a 5 parameter problem will take about 88 times as long as a 2 parameter problem. A 10 parameter problem

will take about 2816 times as long as a 2 parameter problem. In other words if a 2 parameter tolerance box growth occupies 10 seconds of computer CP time, a 5 parameter problem should occupy about 4 min. 28 sec. of CP time and a ten parameter problem should occupy 46 min. 56 sec. of computer time. One can therefore see the need for using the above six rules to reduce t_{TB}. If the rules will allow CP time to be reduced by even a factor of 10 a substantial monetary savings will have been accomplished. Examples discussed in section A.7 will show that exact tolerance analysis by tolerance box growth promises to give very accurate parameter tolerance measures at a moderate cost to the designer.

A.6 Reliable Means of Selecting the Minimum Required Number of Sampling Points, n_s^*, when $F(\phi_s^*, \psi)$ is a Smooth and Continuous Function of ψ, and Has at least n_s^*-1 Continuous Derivatives in $[\psi_L, \psi_U]$

How accurate is this new tolerance analysis? How many sampled data points are required to describe $F(\phi_s^*, \psi)$ to within an α^* confidence level over the interval $[\psi_L, \psi_U]$? Will this also describe P_A [unt. as accurately? It is suggested herein that in order to describe P_A by sampling techniques to within a specified degree of reliability α^*, a minimum required value of n_s must be found. Theoretically, this may be accomplished by considering whether or not a polynomial $Y_{n'}(\psi)$ of degree n' can be a good fit to $F(\phi_s^*, \psi)$ to within the α^* confidence level over the interval $[\psi_L, \psi_U]$ for a fixed multinominal design ϕ_s^*. Since a polynomial of degree n' can be determined by $(n'+1)$ sampled points, it follows

that if this polynomial represents $F(\underline{\delta}_s^*, \psi)$ to within $\eta\%$ in $[\psi_L, \psi_U]$, the sampled points, $(\psi_{is}, F(\underline{\delta}_s^*, \psi_{is})$, is=1,2,...$(n' + 1)$, can be used to describe R_A to within $\eta\%$ providing $F(\underline{\delta}_s^*, \psi)$ is smooth and continuous in $[\psi_L, \psi_U]$ and has at least n' continuous derivatives in $[\psi_L, \psi_U]$. If ns represents the total no. of sampled points, a value of ns of at least n' + 1 must be chosen to define R_A within $\eta\%$ accuracy. A typical acceptable value for η might be 99.9% if expected final tolerances are to range from 1% to 10%. This also corresponds to a 0.1% curve fitting error.

A higher level of confidence in this curve fitting process may be selected at the designer's discretion. One may also not wish to employ uniform sampling and as an alternative strategically place some ψ samples in regions of $[\psi_L, \psi_U]$ where changes in $F(\underline{\delta}_s^*, \psi)$ are most critical with upper and lower bound errors having their smallest values in $[\psi_L, \psi_U]$. However it appears that uniform sampling is best for tolerance box growth. It is not only simpler but as will be seen from a gain equalizer design, uniform sampling defines R_A reliably and uniformly. In any case the ψ_L and ψ_U values of ψ must always be included. Also, a computer plot of $F(\underline{\delta}_s^*, \psi)$ in $[\psi_L, \psi_U]$, should be obtained as output from the process used to determine $\underline{\delta}_s^*$. With these preliminaries completed, the most critical ψ values are at least known for one value of $\underline{\delta}_s^*$ and one has an initial guess at ns; called ns_o. One can then move on to the problem of selecting the minimum required quantity ns^* so that R_A can be accurately defined within the confidence level $\eta\%$.

A limited approach is described first. In order to determine

ns*, consider an n'^{th} order Taylor series approximation to $F(\underline{\phi}^*_s,\phi)$ about the central ϕ value, ϕ_c, in the interval $[\phi_L,\phi_U]$. The $(n'+1)^{th}$ term of this truncated Taylor series may be evaluated at ϕ_1, and if this term's relative magnitude to $F(\underline{\phi}^*_s,\phi_1)$ is less than $(100-\eta)\%$, then ns*=n'+1. If this relative magnitude is too large the process can be iterated until ns* has been found. Increasing or decreasing the order of the polynomial $Y_{n'}(\phi)$ by unity until the $(100-\eta)\%$ accuracy restriction is just met will correspond to increasing or decreasing the required number of sampling points by unity until ns* is found. This method is interesting, but is only practical if $F(\underline{\phi}^*_s,\phi)$ is easily differentiated many times, and a simple general formula for each $(n'+1)^{th}$ term in the truncated Taylor series exists.

A second process similar to the above method of selecting ns* for a given value of η is more applicable in cases where the mathematical differentiation of $F(\underline{\phi}^*_s,\phi)$ with respect to ϕ is difficult beyond the first order derivative. This method entails numerical differentiations of $F(\underline{\phi}^*_s,\phi)$ at ϕ_c. Such differentiations can be performed quickly and accurately on a digital computer. Then differentiation n' times yields a derivative $D^{n'}(\phi_c)$, such that

$$\frac{|(\phi-\phi_c)^{n'}\cdot D^{n'}(\phi_c)|}{[n']}\ ;\ |F(\underline{\phi}^*_s,\phi)| < \frac{(100-\eta)}{100} \qquad (A.4\text{-}1)$$

for the largest value of $|\psi - \psi_c|$ in $[\psi_L, \psi_U]$, then the minimum required number of sampling points is

$$ns^* = (n' + 1), \qquad (A.6-2)$$

This second method appears to be the simplest since F and $D^{n'}$ are easily determined numerically and (A.6-1) is easily calculated. Notice that condition (A.6-1) becomes more and more difficult to meet if the region $[\psi_L, \psi_U]$ is widened. Then more sampling points are needed to meet the n^* reliability condition. Errors in $D^{n'}$ may however be large for n' large.

A third different and more accurate method of selecting the minimum required value of ns for a specified value of n^* involves the use of the least n^{th} curve fitting technique [33]. A selection of n' + 1 sampling points are inserted into a least n^{th} polynomial fit of $F(\lambda_s^*, \psi)$ for of polynomial $Y_{n'}(\psi)$ of degree n' centered at ψ_c. The maximum percentage error between $F(\lambda_s^*, \psi)$ and $Y_{n'}(\psi)$ at these n' initial points is then tested for 10(n' + 1) sampling points in $[\psi_L, \psi_U]$. If this percentage error is found to be less than $(100 - n)\%$, n' may be reduced by unity and the entire process iterated again until the percentage error in the curve fitting process across $[\psi_L, \psi_U]$ exceeds $(100 - n)\%$. Conversely if this percentage error is greater than $(100 - n)\%$ the degree n' of the polynomial $Y_{n'}(\psi)$ may be incremented along with ns, and the entire process may again be iterated until the percentage error in the fit becomes less than $(100 - n)\%$. Then a corresponding suitable value of ns

has been found since

$$\hat{n}s^* = (n' + 1) \qquad (A.6-3)$$

when

$$\frac{|F(\underset{\sim}{\phi}^*_{n'}, \psi) - Y_{n'}(\psi)|}{|F(\underset{\sim}{\phi}^*_{n'}, \psi)|} < \frac{100 - n}{100} \qquad (A.6-4)$$

is just met.

Of the three above techniques, the first method is the most cumbersome one because of the need to express the n'^{th} derivative in a simple closed form solution. The use of the least n^{th} fitting technique to find ns^* is the second most difficult method because of a need for considerable programming and computer time for the optimization process. It is based more on a trial and error process than theory. The second method employing numerical differentiation is simply a practical extension of the cumbersome first method, since $\eta^{n'}(\tau_c)$ is obtained by a numerical means rather than a formula. In summary it should be emphasized that the three above methods of selection ns^* are only suggestions. Only three design examples have been attempted for testing the new tolerance box growth and the above suggestions are based on the limited experience obtained with these examples. For simplicity it appears that uniform sampling should be used to determine $\underset{\sim}{P}_A$. It also appears that the easiest method to obtain ns^* is to allow the computer to calculate $\eta^{n'}(\tau_c)$

by incremental methods after ϕ_s^* has been found. Then ns* can be displayed automatically along with the solution ϕ_s^*. In otherwords, the minimum number of samples required to represent $F(\phi_s^*,\psi)$ and hence R_A within (100 - η)% accuracy by a truncated Taylor series about ψ_c can be determined in the same computer run used to find ϕ_s^*. Also, a computer listing of each term of this Taylor series about ψ_c up to ns* terms would provide useful information about convergence. It should be remembered however that $F(\phi_s^*,\psi)$ must be smooth and continuous in $[\psi_L,\psi_U]$.

If all of the above methods do not appear attractive to the designer, he still has the option of growing a tolerance box for various values of ns, and compare the results. This procedure might however be costly if a large number of parameters are involved in the design.

A.7 Examples

Two simple design examples discussed herein were attempted in a 2-dimensional parameter space in order to test the new algorithm P_{TP} in relation to a simple 2-dimensional region R_A. A third 2-dimensional coplanar waveguide example was also analyzed for tolerance, and appears in section 2.3 of Chapter II. All three problems yielded excellent tolerance box growths within moderate computer times; 1-2 seconds per box. These three examples also served to reinforce the concepts presented previously in section A.6 about the accuracy involved when P_A is defined by a finite number of sample data points in $[\psi_L,\psi_U]$.

A.7.1 Fitting a Straight Line Between Two Linear Boundaries

This 2-parameter problem was prepared as an initial test of P_{TP}.

Figure A.7-1 illustrates the task of fitting a straight line

$$F(\underline{\phi}, \psi) = \phi_1 \psi + \phi_2 \qquad (A.7\text{-}1)$$

between

$$F_U(\psi) = \psi + 2 \qquad (A.7\text{-}2)$$

and

$$F_L(\psi) = \psi + .1 \qquad (A.7\text{-}3)$$

over the interval

$$[\psi_L, \psi_U] = [0, 5]. \qquad (A.7\text{-}4)$$

A sub-optimal design was easily found by placing $F(\underline{\phi}, \psi)$ anywhere inside the above bounded performance region. Attention was then focused on the shape of the feasibility contours in parameter space, and the acceptable design region $P_A|_{F=F_0}$ which the contours enclose for each distinct value of F.

Figure A.7-2 illustrates various regions P_A for corresponding values of F ranging from -0.5 to 0.0 in increments of 0.1. Since a straight line is a polynomial of degree 2, and can be determined by two distinct points, samples ψ_L and ψ_U are necessary and sufficient to precisely define P_A. The use of any more samples in $[\psi_L, \psi_U]$ would simply represent wasted effort and expense. For the given linear constraining functions $F_U(\psi)$ and $F_L(\psi)$, $F=0$. Hence, the region enclosed by the feasibility contours labelled $F=0$, correspond to the $F_U(\psi)$ and $F_L(\psi)$ constraints to be imposed upon $F(\underline{\phi}, \psi)$. This region is called $P_A|_{F=0}$.

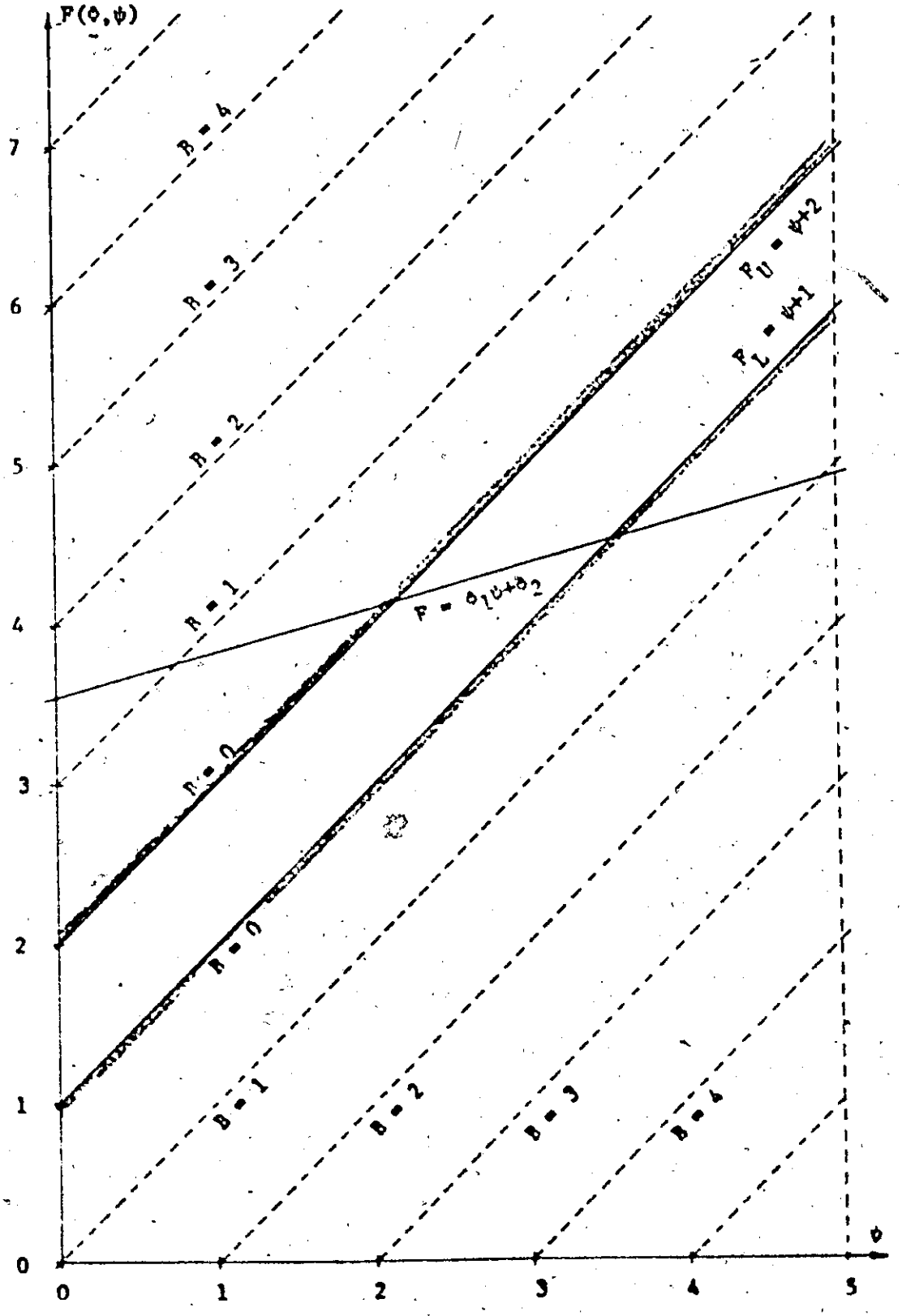

Figure A.7-1: Fitting a Straight Line Between Two Parallel Lines.

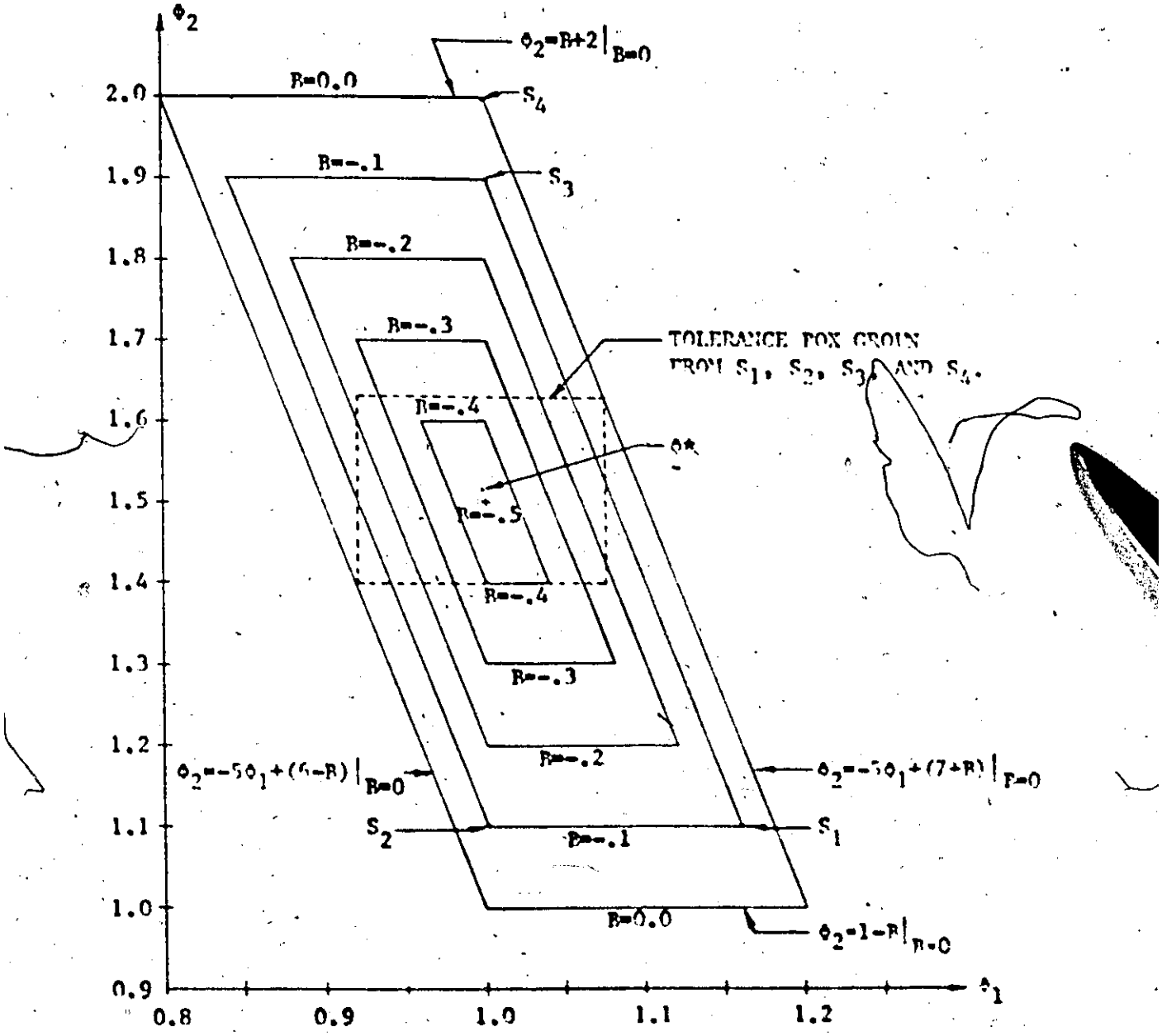

Figure A.7-2: Feasibility Contours for Problem of Fitting a Straight Line Between Two Linear Boundaries with B Ranging from -0.5 to 0.0 in Increments of 0.1.

The rhombic shape of R_A is determined by the possible ranges of δ_1 and δ_2 when the line $F(\underline{\delta},\phi)$ is allowed to change in slope or intercept within the upper and lower boundary specifications, $F_U(\phi)$ and $F_L(\phi)$. The top side of $R_A|_{p=0}$ is determined by holding intercept δ_2 constant at its maximum possible value of 2.0 and then determining the resulting possible range of the slope δ_1. Similarly, the bottom side of $R_A|_{p=0}$ is determined by keeping δ_2 constant at its minimum possible value of 1.0, and then again determining the resulting possible range of δ_1. The left side of the rhombic region $R_A|_{p=0}$ is found by allowing δ_2 to have any general value between 1.0 and 2.0, and determining the corresponding slope δ_1 which causes $F(\underline{\delta},\phi)$ to just violate $F_L(\phi)$ at $\phi = \phi_L$ for each value of δ_2. Similarly, the right boundary of $R_A|_{p=0}$ is found by allowing δ_2 to to again take on any value between 1.0 and 2.0, and determining the corresponding value of δ_1 which will cause $F(\underline{\delta},\phi)$ to just violate $F_U(\phi)$ at $\phi = \phi_U$.

A more concise method of defining R_A for this problem is to consider the upper and lower bound errors $e_{U_{is}}(\underline{\delta},P,\phi_{is})$ and $e_{L_{is}}(\underline{\delta},P,\phi_{is})$ respectively in terms of δ_1 and δ_2 for a constant value of P. Here $is = 1,2: \phi_1 = \phi_L$ and $\phi_2 = \phi_U$. This leads to

$$e_{U_1} = [\delta_1\phi_1 + \delta_2] - [\phi_1 + 2 + P] \qquad (A.7\text{-}6)$$

$$e_{U_2} = [\delta_1\phi_2 + \delta_2] - [\phi_2 + 2 + P] \qquad (A.7\text{-}7)$$

$$e_{L_1} = [\phi_1 + 1 - P] - [\delta_1\phi_1 + \delta_2] \qquad (A.7\text{-}8)$$

$$e_{L_2} = [\phi_2 + 1 - P] - [\delta_1\phi_2 + \delta_2]. \qquad (A.7\text{-}9)$$

If the upper and lower bound errors are all set to zero, and the values of ϕ_1 and ϕ_2 are inserted into these four error expressions, the bound-

aries of R_A are defined for a specific value of R. The four error equations may then be respectively reduced to

$$\phi_2 = R + 2 \qquad (A.7\text{-}10)$$

$$\phi_2 = -5\phi_1 + (7 + R) \qquad (A.7\text{-}11)$$

$$\phi_2 = 1 - R \qquad (A.7\text{-}12)$$

$$\phi_2 = -5\phi_1 + (6 - R) \qquad (A.7\text{-}13)$$

These resulting boundary equations have been indicated in Figure A.7-2 for the case R=0.

Figure A.7-2 also shows a fully grown tolerance box with its central nominal design ϕ^*. This same box was grown from four various starting points S_1, S_2, S_3, and S_4, with 10% tolerance weights for each parameter. Notice that the box has been centrallized in R_A and has attained a maximum size.

Also various tolerance boxes were grown sequentially with these same tolerance weights from these same starting points by incrementing R for the growth of each new box. The results of these sequential tolerance box growths are summarized in a plot of c vs R in Figure A.7-3. The plot turned out to be a straight line indicating that the dimensions of region R_A were linear with respect to R. The plot of c vs R represented a summary of the tolerance information for the above defined problem and could be used to determine c for any given value of R by interpolation within the range of R values tested. As was mentioned earlier, it was more economical to obtain a set of tolerance boxes for incremental values of R in one computer run. For this simple problem, the average computer

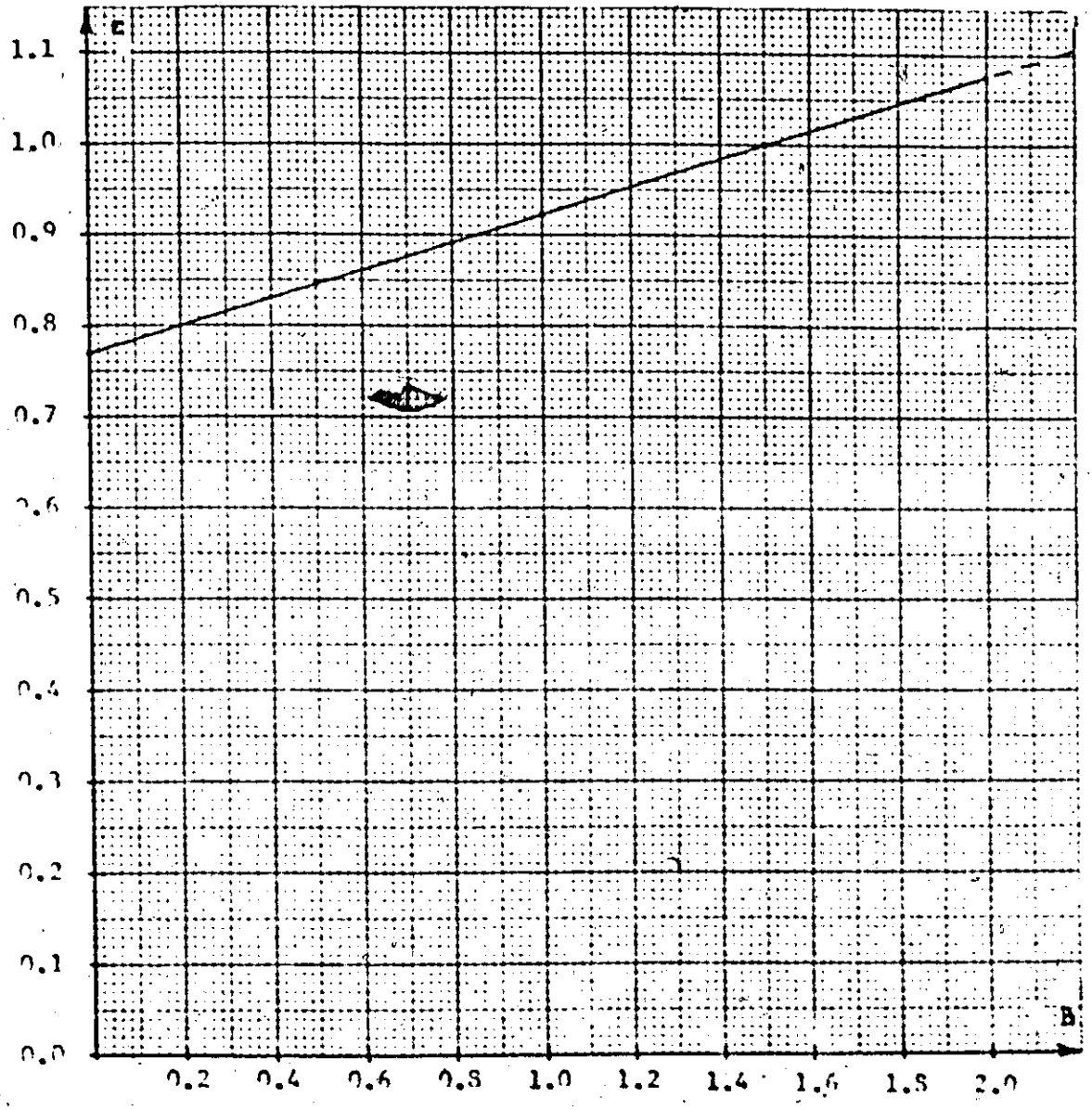

Figure A.7-3: Plot of Maximum Size of Tolerance Box ε vs Boundary Value B for Problem of Fitting a Straight Line Between Two Given Straight Line Boundaries, where 10 % Tolerance Weights have been used.

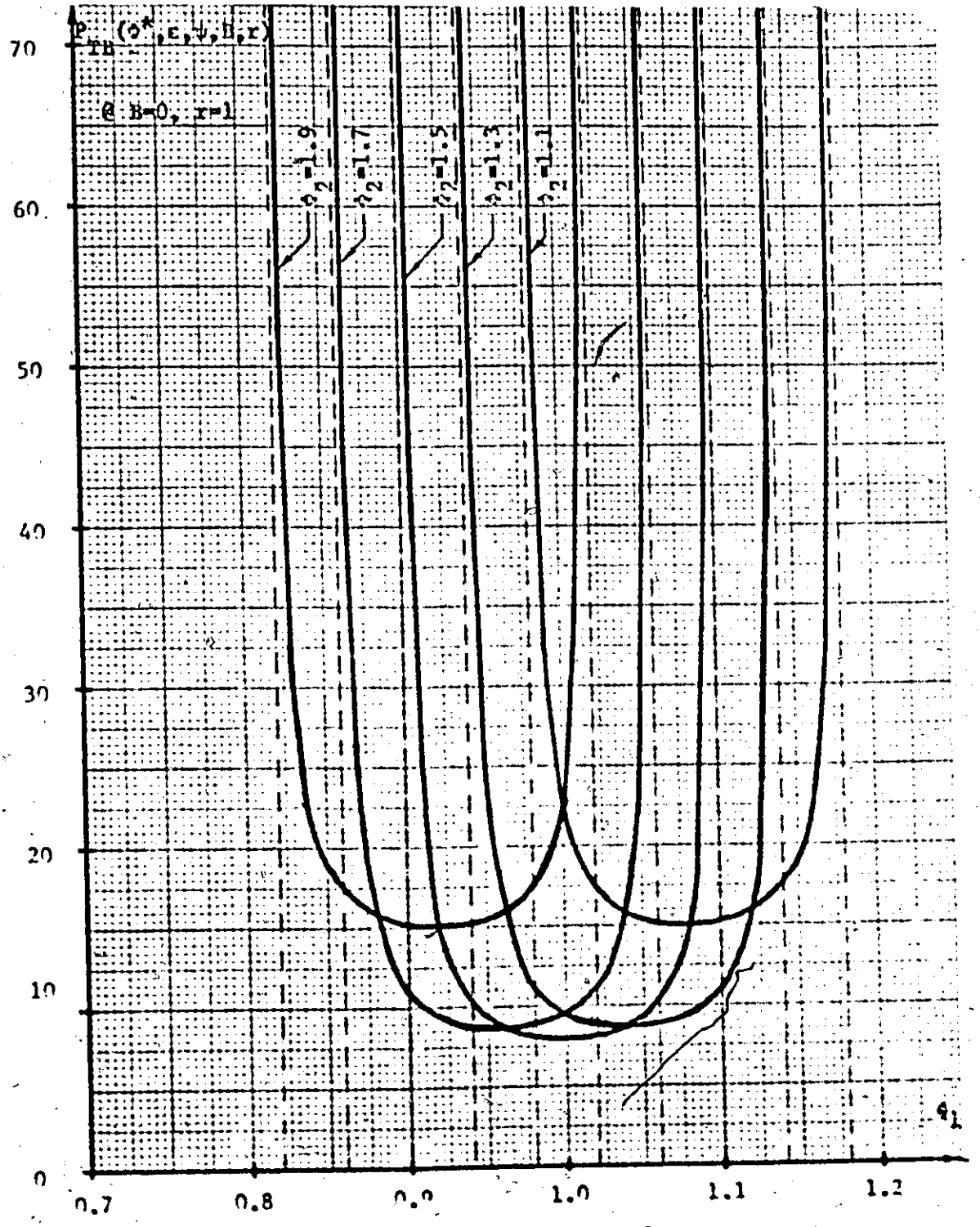

Figure A.7-4: Plot of the Objective Function P_{TB} vs ϕ_1 for Various Constant Values of ϕ_2 for Problem of Fitting a Straight Line Between Two Given Straight Line Boundaries.

time per tolerance box was found to be about 1.6 seconds.

The shape of the hypersurface P_{TB} above R_A for this simple problem was of particular interest. Was P_{TB} smooth and continuous above R_A? Figure A.7-4 shows a plot of the objective function P_{TB} vs δ_1 for various constant values of δ_2 with P=0 and r=1. Here, only error constraints were used to calculate P_{TB}. No other inequality constraints have been included. Directly above the enclosed region R_A, P_{TB} was found to be a finite, smooth and continuous function of δ_1 and δ_2.

A.7.2 Gain Equalizer Design

The following example is a simple gain equalizer problem involving an ideal operational amplifier, 2 discrete resistors, R and R_1, plus one discrete capacitor C_1. A circuit diagram is given in Figure A.7-5 with the desired and actual performance curves over the 1-2 MHz frequency band. In order to minimize computer costs, this 3 dimensional tolerance problem was reduced to a simple 2 dimensional one by considering the scaling factor R to be known to have precisely unity magnitude. An exact tolerance analysis was performed in 2 dimensions on R_1 and C_1 only.

It was a simple matter to show that the theoretical response function had the general form

$$F(\delta,\phi) = 10 \log_{10}\left(\left[\frac{R}{R_1}\right]^2 [\,1 + (\omega R_1 C_1)^2\,]\right). \qquad (A.7\text{-}14)$$

The problem was to fit this theoretical response between

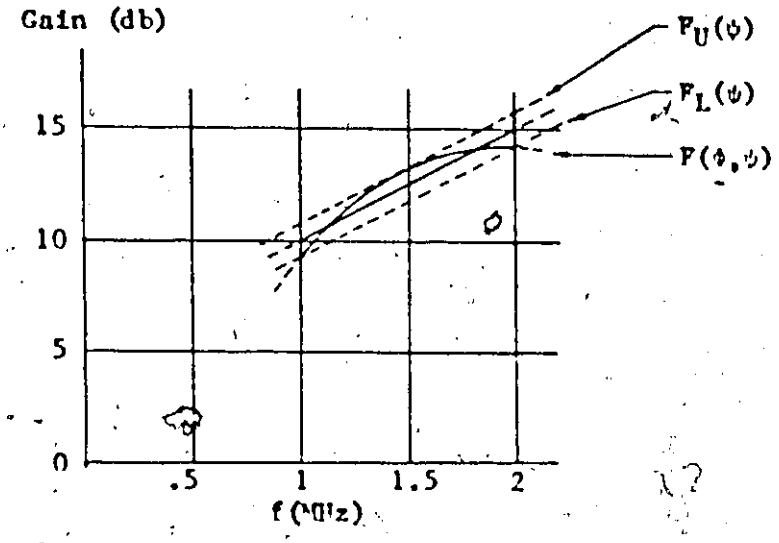

(a)

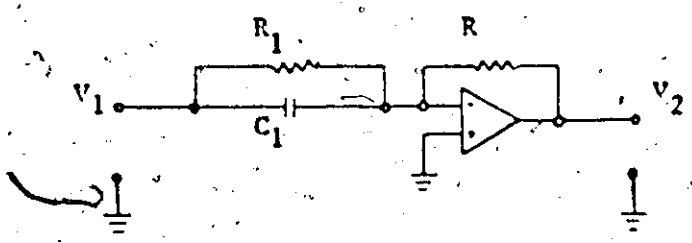

(b)

Figure A.7-5: Response and Specified Gain Characteristics for Active Gain Equalizer Circuit.

$$F_U(\psi) = 5.160 + 5f \qquad (A.7\text{-}15)$$

and

$$F_L(\psi) = 4.840 + 5f \qquad (A.7\text{-}16)$$

over the interval

$$[\psi_L, \psi_U] = [1, 2], \qquad (A.7\text{-}17)$$

where

$$\phi_1 = C_1, \qquad (A.7\text{-}18)$$

$$\phi_2 = R_1, \qquad (A.7\text{-}19)$$

and

$$R = 1. \qquad (A.7\text{-}20)$$

The upper and lower bound errors were determined according to equations (A.1-8) and (A.1-9) for a fixed value of F and for 20 values of ϕ in the interval of interest. A tolerance box was then grown for equal tolerance weights on both ϕ_1 and ϕ_2.

A typical example of this situation is depicted in Figure A.7-6 for B = .10. The dotted curves at the left of the figure represent lower bound error constraints and the solid curves at the right of the figure indicate upper bound error constraints. In the center of the figure, the design region R_A is displayed containing a fully grown tolerance box. This

Figure A.7-6: Acceptable Design Region R_A for Gain Equalizer Circuit with R = 0.10.

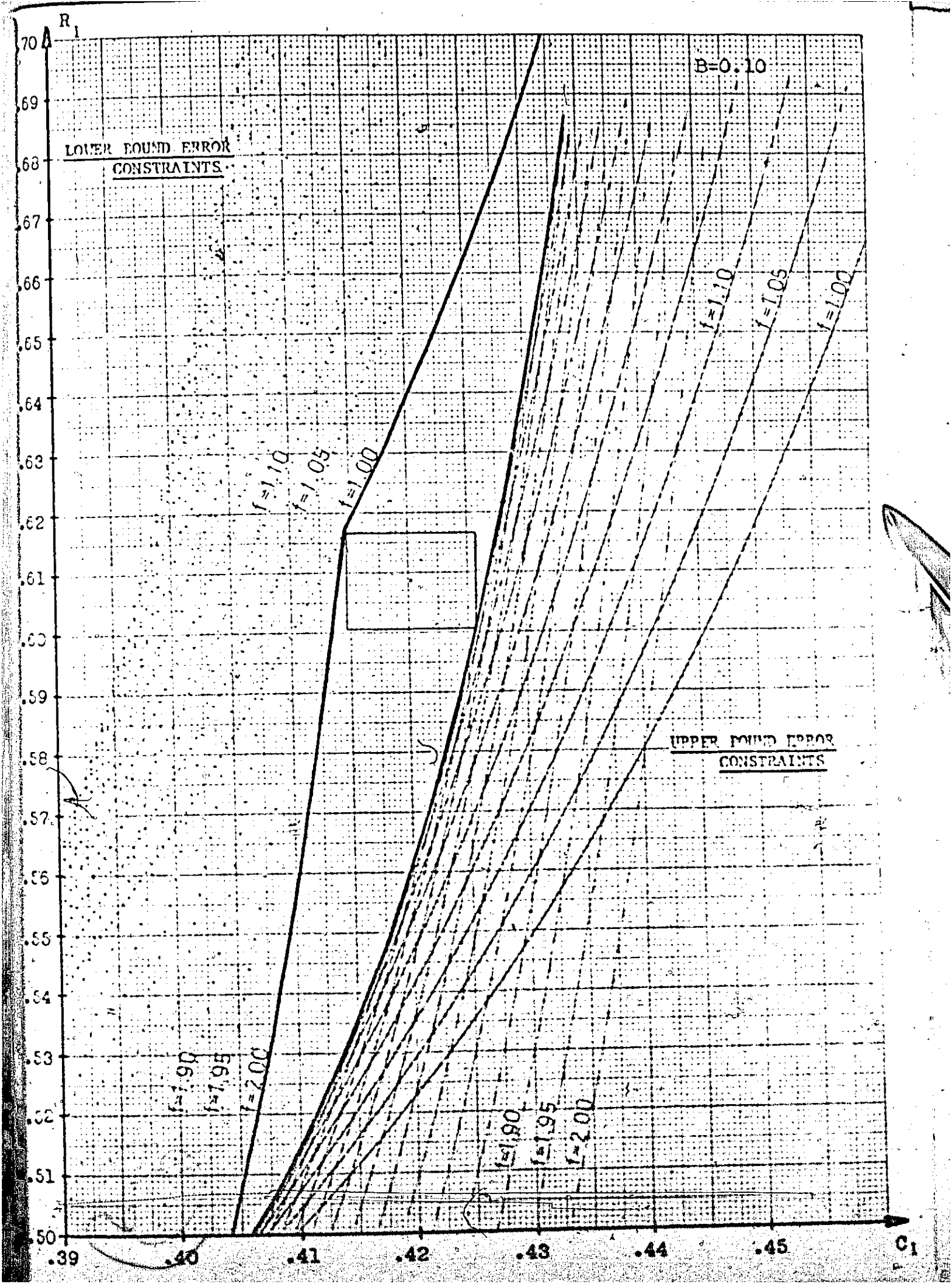
R1
B=0.10
LOWER BOUND ERROR CONSTRAINTS
UPPER BOUND ERROR CONSTRAINTS
f=1.10
f=1.05
f=1.00
f=1.90
f=1.95
f=2.00
C1
.70
.69
.68
.67
.66
.65
.64
.63
.62
.61
.60
.59
.58
.57
.56
.55
.54
.53
.52
.51
.50
.39
.40
.41
.42
.43
.44
.45

Figure A.7-7: Feasibility Contours for Gain Equalizer Circuit for Various Values of B Ranging from 0.00 to 0.50.

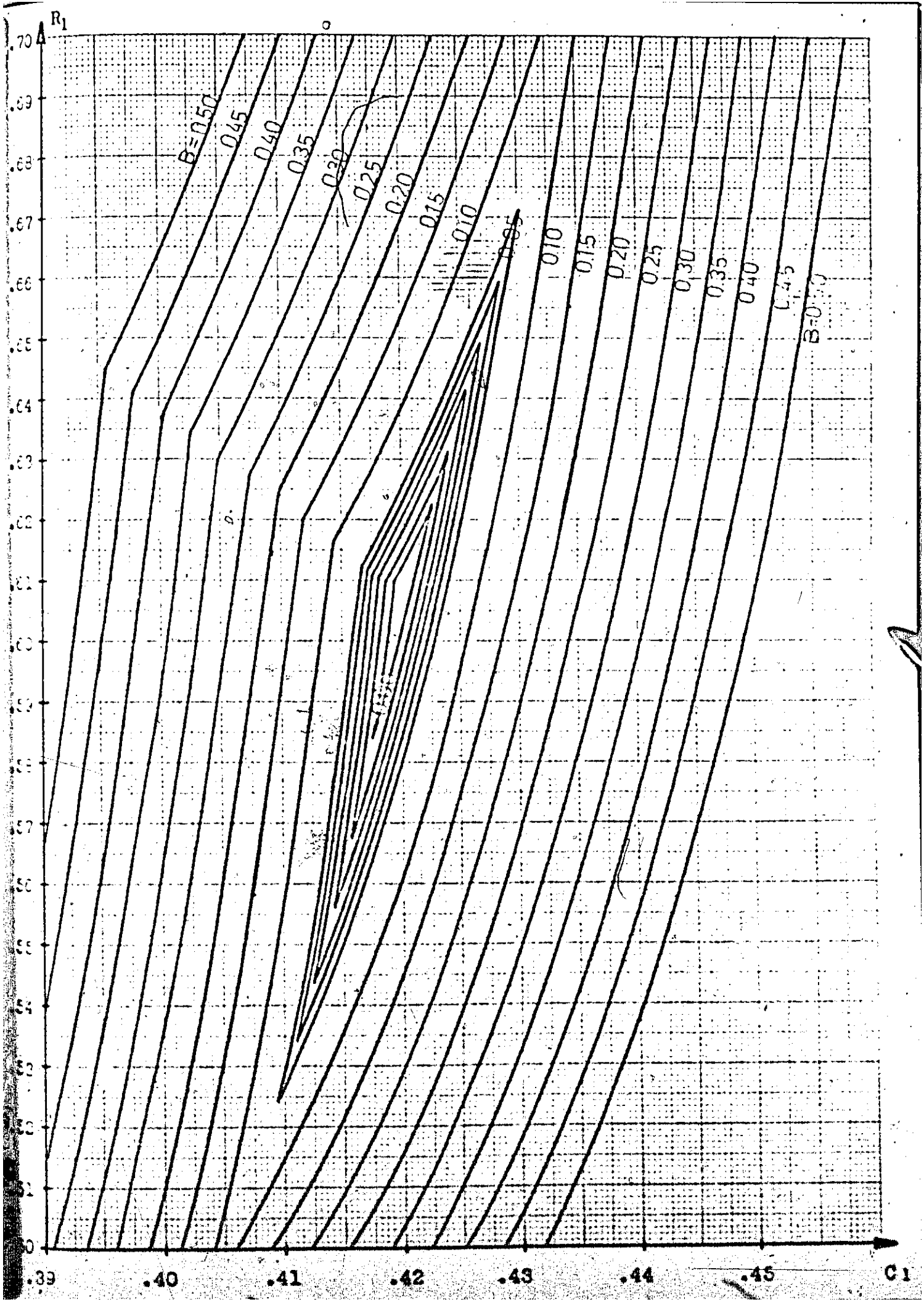
R1
B=0.50
0.45
0.40
0.35
0.30
0.25
0.20
0.15
0.10
0.05
0.10
0.15
0.20
0.25
0.30
0.35
0.40
0.45
.39
.40
.41
.42
.43
.44
.45
C1

Figure A.7-8: Plot of Maximum Size of Tolerance Box ε vs Boundary Value B for the Active Gain Equalizer Problem, where 10 % Tolerance Weights have been used.

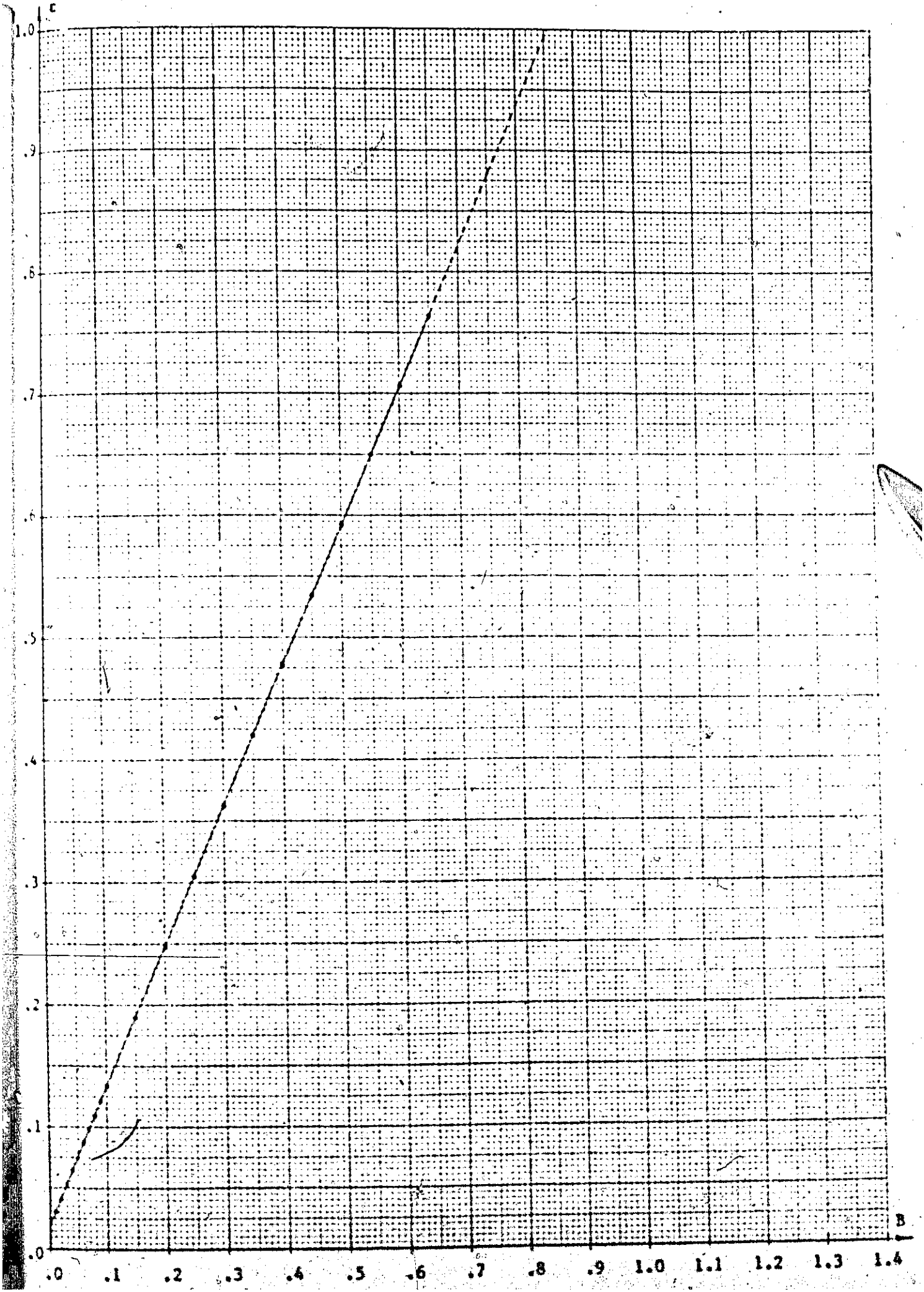
C
1.0
.9
.8
.7
.6
.5
.4
.3
.2
.1
.0
B
.0
.1
.2
.3
.4
.5
.6
.7
.8
.9
1.0
1.1
1.2
1.3
1.4

tolerance box can be grown from any point contained in R_A. Notice that some of the error constraints are labelled with their appropriate frequency. The frequency was varied from 1 to 2 MHz inclusive, in increments of .05 MHz. It should be emphasized that the tolerance box shown has the maximum size possible for the indicated region R_A.

A sequence of such figures can be generated by incrementing P. This yields a set of feasibility contours as in Figure A.7-7. For this latter figure, equal increments in the boundary parameter B appeared to cause equal increments in the linear dimensions of R_A. A check was made of this by plotting fully grown values of c vs B as in Figure (A.7-8). A truly linear relation between c and B was obtained for the above described linear gain fitting problem. On the average, a tolerance box could be grown to its maximum size within 2 seconds of computation.

A.8 Conclusions

The above examples have illustrated the precision and simplicity of this new method of tolerance box growth. Tolerance boxes can be grown easily and economically to give exact tolerance information. On the average, computer times were as low as 1-2 seconds per box grown for 2 component problems. A 3,4, and 5 component problem could then have typical average computation times of 4, 8, and 16 seconds per box respectively. With the aid of the tolerance meters previously described, this new tolerance analysis technique can also grow tolerance boxes in an optimal manner. Furthermore, only a small number of these optimum tolerance boxes need be

grown in order to enable a graph of c vs B to be plotted. Since this graph may not be truly linear for some problems, 5 to 10 data points should be obtained.

The resulting c vs B graph, and the optimum tolerance weights represent the total optimum tolerance solution to a given problem, and this solution can be obtained in one single computer run. In other words, for each value of B imposed on the given problem, a value of c is combined with the calculated optimum tolerance weights, all optimum tolerances are known for a fixed value of B. This establishes a simple relation of optimum tolerances with $S_U(\phi)$ and $S_L'(\phi)$.

The above results were obtained on a CDC 6400 digital computer. This has led to a documented programme which grows optimum tolerance boxes. The user need only supply upper and lower bounds, a response function, the number of parameters, their initial values, the first order partial derivatives of the response function with respect to these parameters, the number of sampling points, plus a small number of control parameters. It is also possible to insert pre-selected tolerances into the program to generate a new c vs B curve. When c has grown to unity the growth of these pre-selected tolerances has been achieved and the positions of $S_U(\phi)$ and $S_L(\phi)$ corresponding to these tolerances has been determined. The choice of the optimum number of sampling points n_s^* is left up to the designer in accordance with the discussion of section A.6.

However, there are two limitations which should be emphasized strongly. First of all, equality constraints should only be placed at ϕ^*, and when this is done, one should expect calculated tolerances to be less than the tolerances grown without these imposed equality constraints.

Secondly, saddle points cause a potential hazard, since they are difficult to observe in more than 2 dimensions. Design desensitization by techniques found in the literature can be used to alleviate this problem, but a simpler technique not yet proposed would be to check the values of $e_U(\phi,\psi)$ and $e_L(\phi,\psi)$ at the mid points of the tolerance box that has grown. If either $e_U(\phi,\psi)$ and $e_L(\phi,\psi)$ are negative at these points for any selected frequency, then at least one side has protruded the boundaries of R_A.

A strategy which grows tolerance boxes by including the mid points of the box in the calculation of P_{TB} may then be used in the remainder of the problem for the growth of all subsequent tolerance boxes. This is a simple extension of what has already been achieved and will roughly increase computer time by the factor $(2 \cdot n + 2^n)/2^n$, since an n dimensional box has 2^n corners and $2 \cdot n$ sides. For a 2 component problem computer time would double. A six component problem would have 12 sides and 64 corners so that computer time would be increased by only 18.8%. For 8, 9, and 10 component problems computer time would increase by only 6.2%, 3.5%, and 1.0% respectively. So, the problem of feasibility contours protruding into the tolerance box in the vicinity of a saddle point may be alleviated significantly at a moderate cost. However, further studies need to be directed towards the creation of a reliable means of circumventing the saddle point hazard altogether.

APPENDIX B

MEASUREMENTS WITH THE WAVETEK MICROSTRIP LINE MOUNTS AND THE SLOWER HP 1415A TIME DOMAIN REFLECTOMETER ON THE ALUMINUM COPLANAR WAVEGUIDE SAMPLES FABRICATED BY MASKING TECHNIQUES

APPENDIX B

The slower HP 1415A TDR system described in section 4.3 of chapter IV was used to determine average input reflection coefficients for all thin film CPW samples fabricated by the masking technique of section 3.2 of chapter III. These included both series A and series C samples. Expanded and unexpanded TDR traces were taken on an HP-Moseley 7030A XY recorder for these series of samples. The symbol $|\rho_t|$ represents the TDR measured reflection coefficient magnitude and t represents elapsed return time. The samples are listed in Table B.1 with their respective thin film thicknesses t_f, and their corresponding alphanumeric figure labels.

The unexpanded traces have various symbols and subscripts to indicate the types of loads applied to the CPW samples for testing. These are

- O/C_I - open circuit at the CPW input,
- O/C_o - open circuit at the CPW output,
- O/C_{oo} - open circuit at the end of the output launcher,
- S/C_I - short circuit at the CPW input,
- S/C_{oo} - short circuit at the end of the output launcher,
- $50\ \Omega_{oo}$ - 50 Ω load at the end of the output launcher.

The expanded traces all involve the $50\ \Omega_{oo}$ condition and are labelled with numerical integer symbols to indicate major regions of interest along each trace. These and their corresponding propagation return times are

1. GR 874 to 3 mm OSM plug/plug adapter (280 ps),
2. OSM 218 male jack/jack adapter (80 ps),

3 OSM 218 adapter, straight plug/plug (150 ps),

4 Input Wavetek terminal post (80 ps),

5 Coplanar Waveguide (400 ps),

6 Output Wavetek terminal post (80 ps)

Figure 4.3-1 of chapter IV illustrated the experimental set up described by these six major subdivisions of the test circuit. The return propagation times shown above are assumed to be only approximate since the rise time of the measuring system was as high as 150 ps.

The series A and series C samples have been labelled with the two appropriate capital letters, A and C, followed by an integer. This integer designates the order in which the samples were fabricated. In addition, sample A1 was mounted and measured twice, and sample A2 was mounted and measured three times. These mounting conditions were indicated by the use of numerical subscripts: 1,2,3. This permitted the effectiveness and reliability of the Wavetek microstrip experimental mount for mounting CPW samples to be studied.

For a 50 Ω_{oo} termination, sample $A1_1$ gave a peak reflection coefficient of .14, but when mounted and measured a second time a peak reflection coefficient of .257 was obtained. Traces for $A2_1$, $A2_2$, and $A2_3$ show similar variations. This indicates the difficulties involved in mounting the series A and series C samples with the Wavetek microstrip mount. One was never quite sure that the best possible electrical contacts were being made the first time a sample was mounted. Several trial and error attempts were necessary on all samples. This problem initiated the design of proper

Sample	Scale	t_f (kÅ)	Figure
$A1_1$	Unexpanded	0.796 ± 0.098	B.A1.1-U
$A1_2$	Expanded	0.796 ± 0.098	B.A1.2-E
$A2_1$	Unexpanded	1.015 ± 0.125	B.A2.1-U
$A2_2$	Unexpanded	1.015 ± 0.125	B.A2.2-U
$A2_3$	Unexpanded	1.015 ± 0.125	B.A2.3-U
$A2_3$	Expanded	1.015 ± 0.125	B.A2.3-E
A6	Unexpanded	0.438 ± 0.054	B.A6-U
A6	Expanded	0.438 ± 0.054	B.A6-E
A8	Unexpanded	1.330 ± 0.164	B.A8-U
A8	Expanded	1.330 ± 0.164	B.A8-E
A10	Unexpanded	11.600 ± 1.43	B.A10-U
A10	Expanded	11.600 ± 1.43	B.A10-E
A11	Unexpanded	3.44 ± 0.423	B.A11-U
A11	Expanded	3.44 ± 0.423	B.A11-E
C2	Unexpanded	1.357 ± 0.167	B.C2-U
C2	Expanded	1.357 ± 0.167	B.C2-E
C3	Unexpanded	3.905 ± 0.481	B.C3-U
C3	Expanded	3.905 ± 0.481	B.C3-E
C4	Unexpanded	4.593 ± 0.565	B.C4-U
C4	Expanded	4.593 ± 0.565	B.C4-E
C5	Unexpanded	11.50 ± 1.41	B.C5-U
C5	Expanded	11.50 ± 1.41	B.C5-E
C6	Unexpanded	1.133 ± 0.139	B.C6-U
C6	Expanded	1.133 ± 0.139	B.C6-E

Table B.1: List of Samples with Their Respective Thin Film Thickness t_f, and Their Corresponding Alphanumeric Figure Labels.

CPW launchers, which were then used to mount and measure series A- and series BCD- CPW samples. The results of these measurements are given in Appendix C. The new CPW launchers, described in section 3.5 of Chapter III, enabled the same TDR performance to be obtained each time a CPW sample was remounted for testing.

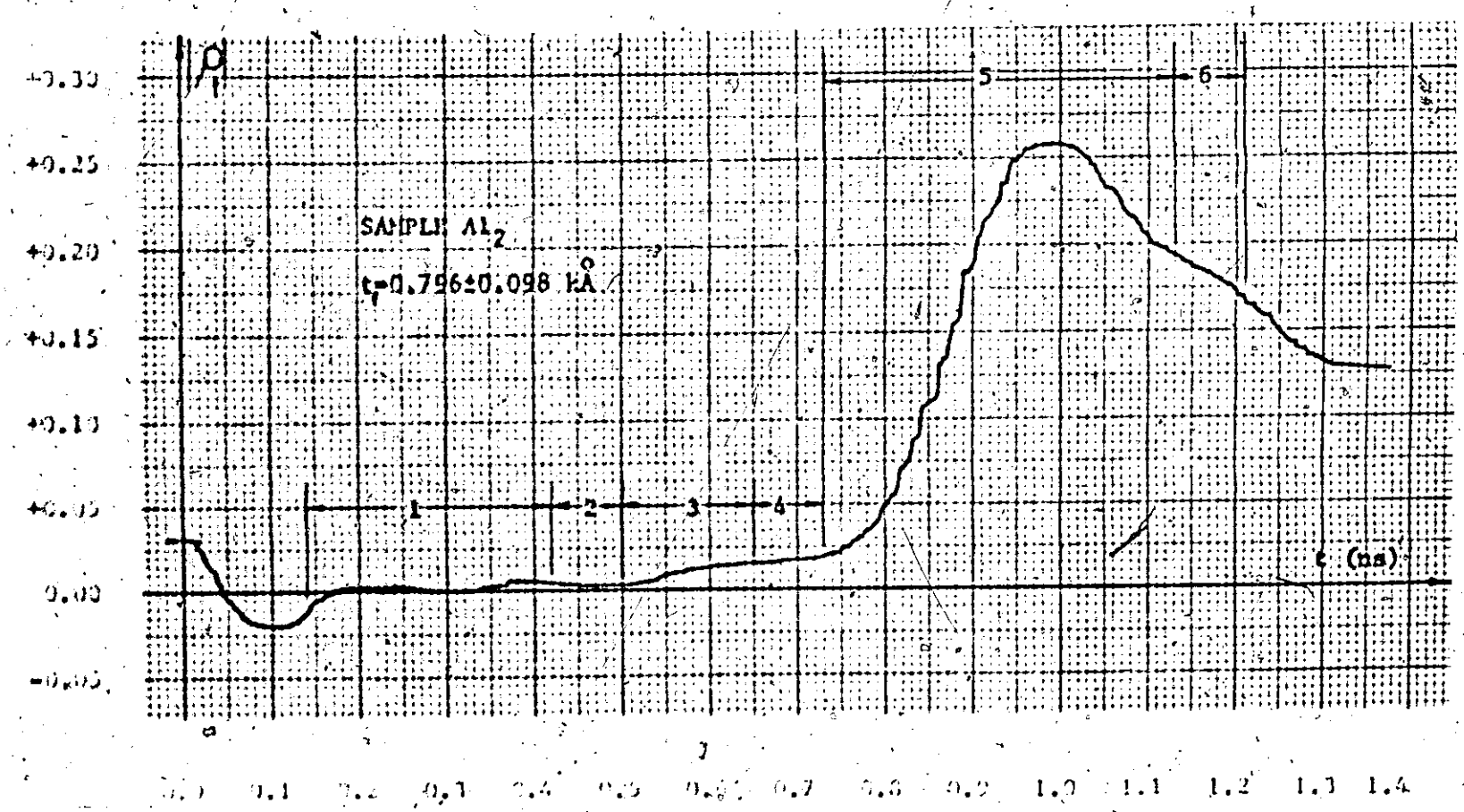

Figure B.A1.2-F: Expanded HP 1415A TDR Trace for a 50 Ω Termination Applied to Thin Film CPW Sample Al_2 Mounted by Means of the Wavetek Microstrip Mount.

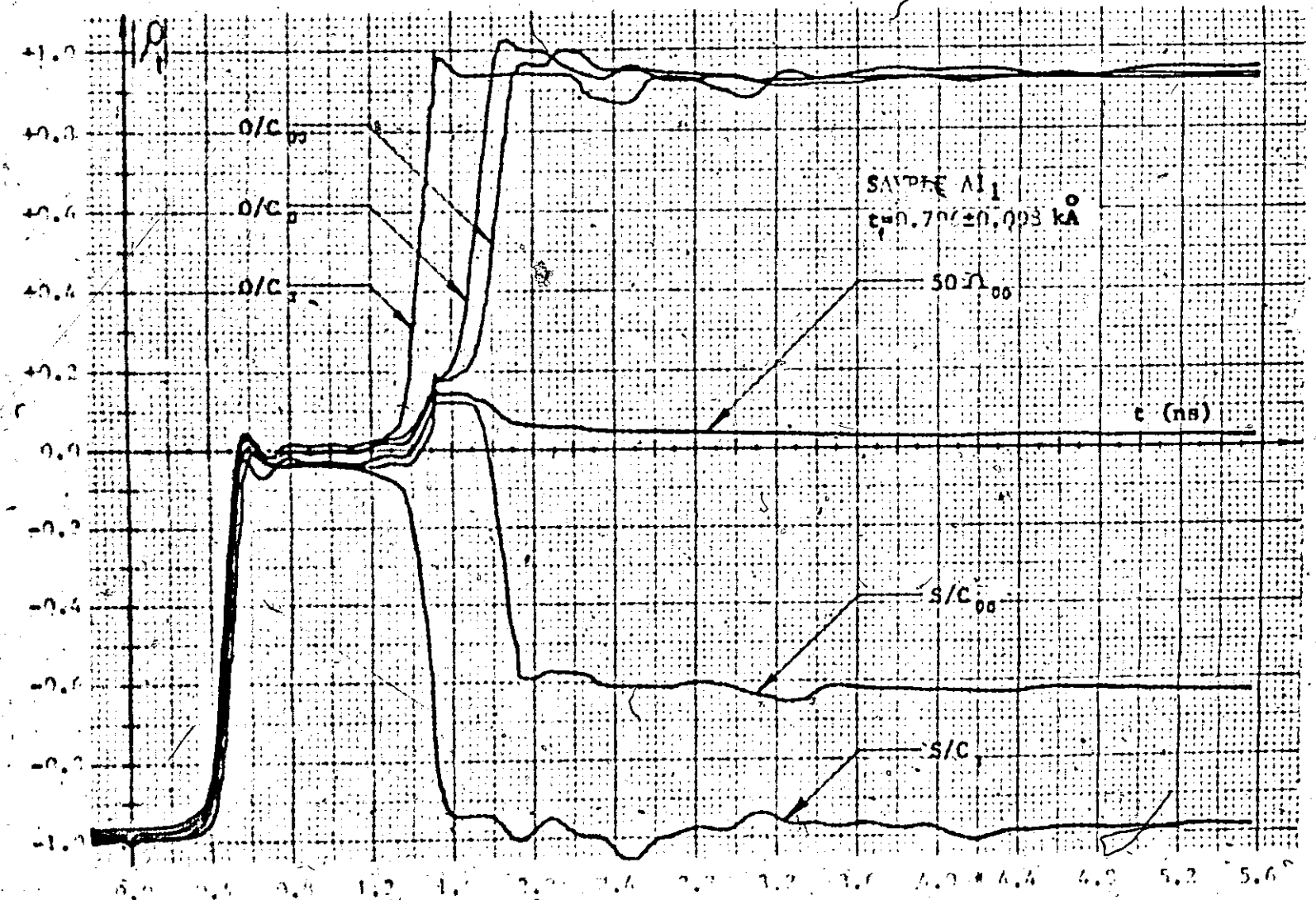

Figure B.Al.1-4: Expanded HP 1415A TDR Traces for 6 Different Loads Applied to Thin Film CPW Sample Al_1 Mounted by Means of the Wavetek Microstrip Mount.

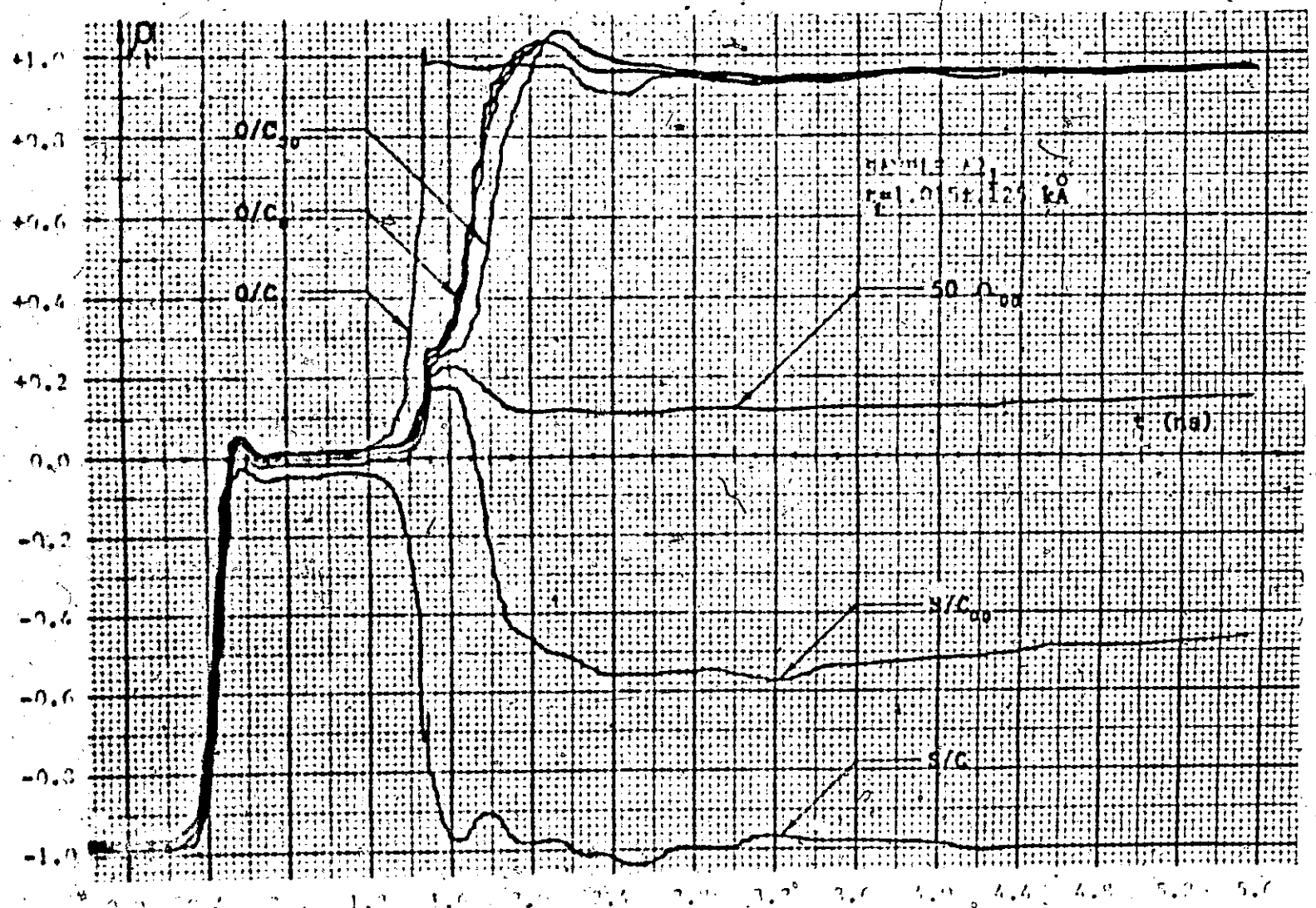

Figure 8.A2.14: Unexpanded HP-1415A TDR Traces for 6 Different Loads Applied to Thin Film CPW Sample $A2_1$ Mounted by Means of the Wavetek Microstrip Mount.

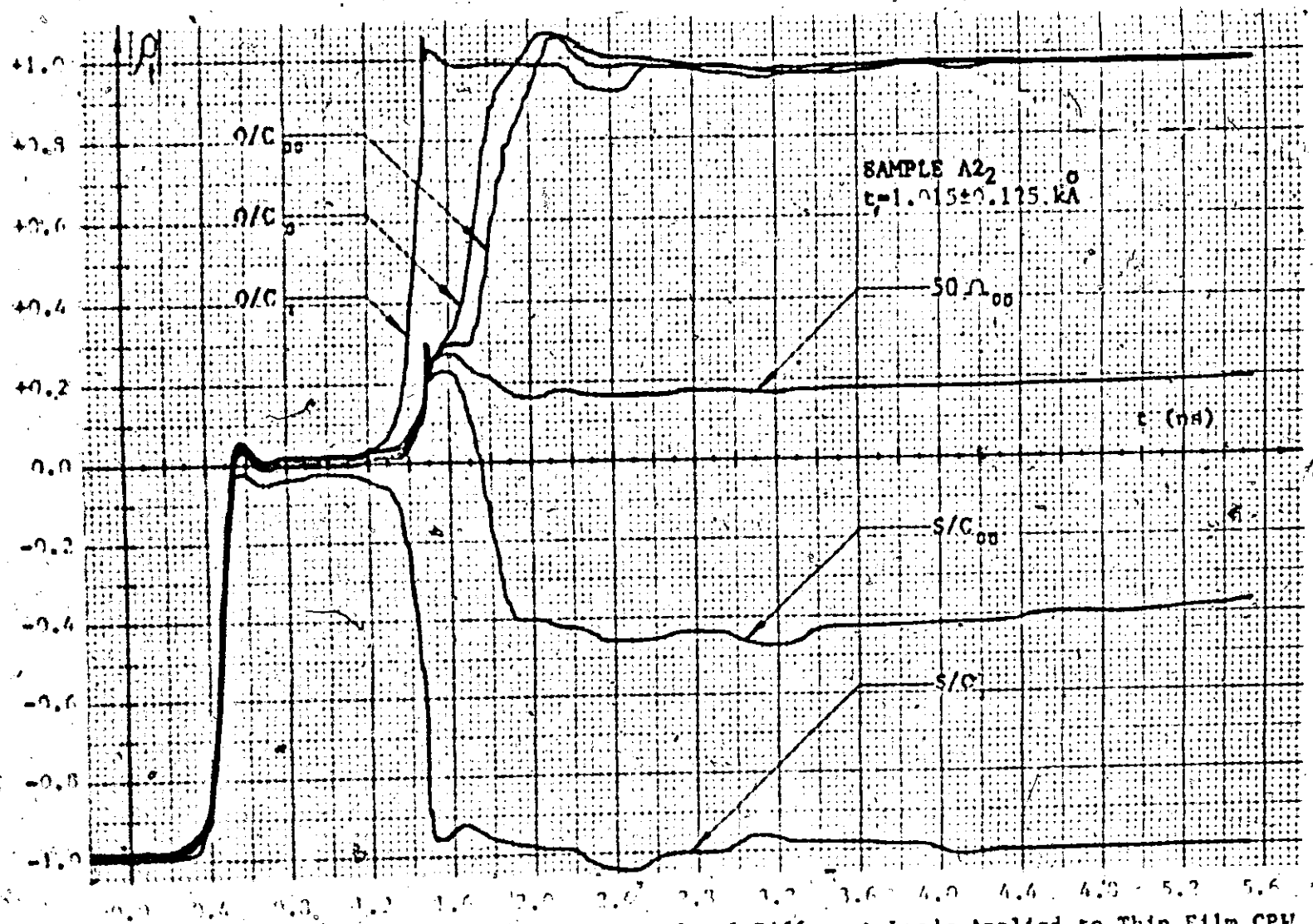

Figure E.A2.2-4: Unexpanded HP 1415A TDR Traces for 6 Different Loads Applied to Thin Film CPW Sample $A2_2$ Mounted by Means of the Wavetek Microstrip Mount.

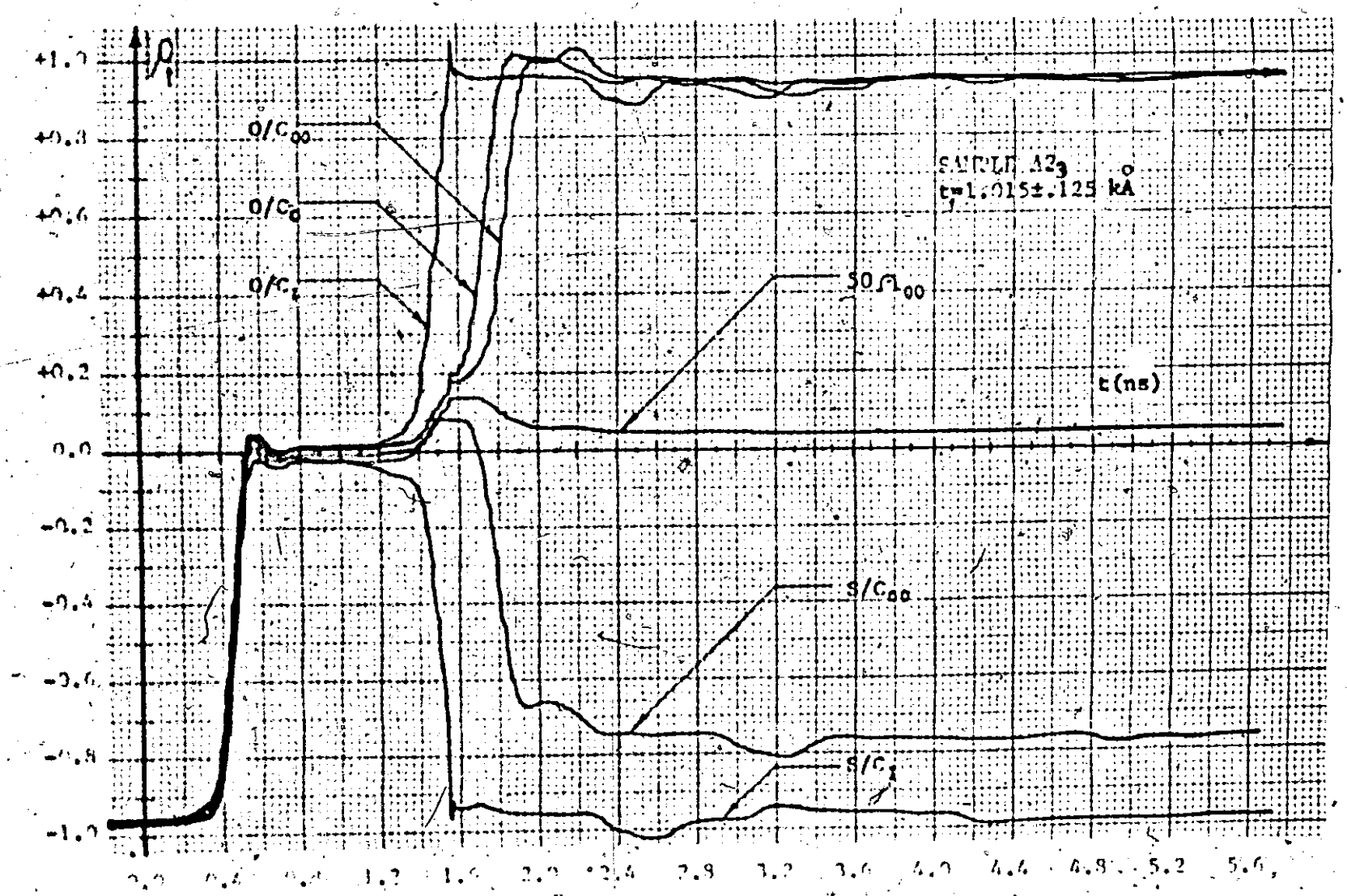

Figure E.A2.3-U: Unexpanded HP 1415A TDR Traces for 6 Different Loads Applied to Thin Film CPW Sample $A2_3$ Mounted by Means of the Wavetek Microstrip Mount.

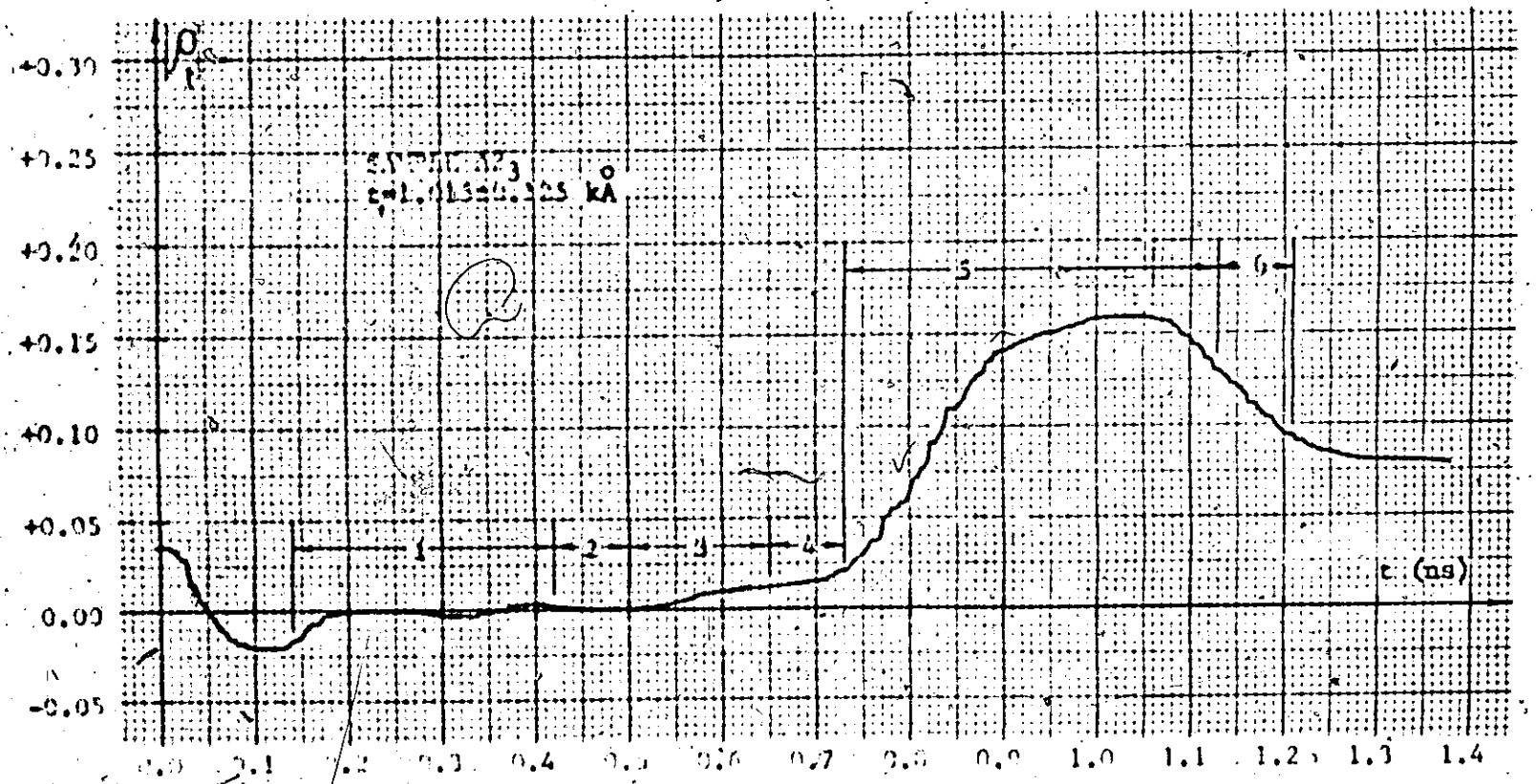

Figure B.A2.3-F: Expanded HP 1415A TDR Trace for a 50 Ω Termination Applied to Thin Film CPW Sample $A2_3$ Mounted by Means of the Wavetek Microstrip Mount.

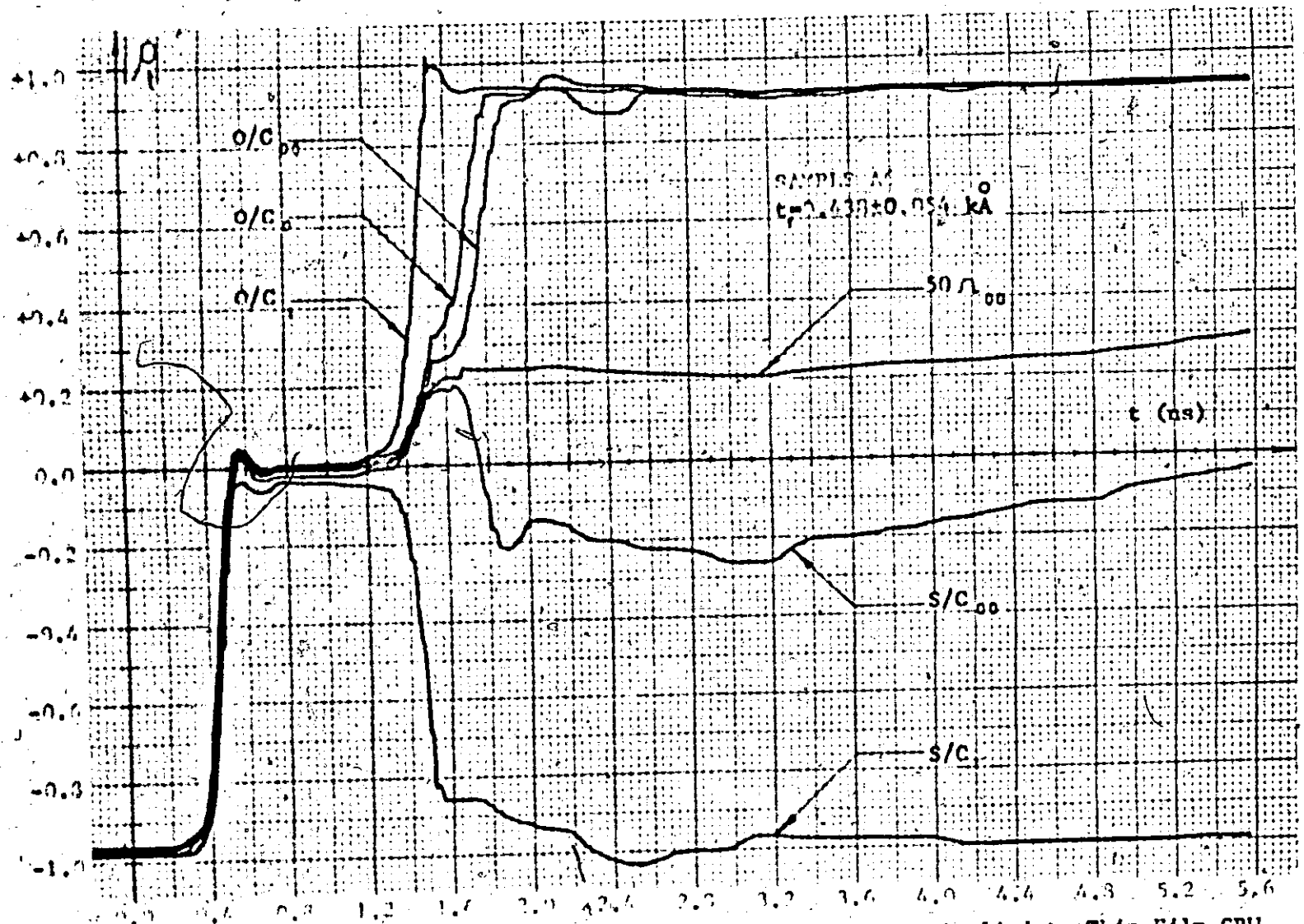

Figure B.A6-B: Unexpanded HP 1415A TDR Traces for 6 Different Loads Applied to Thin Film CPW Sample A6 Mounted by Means of the Wavetek Microstrip Mount.

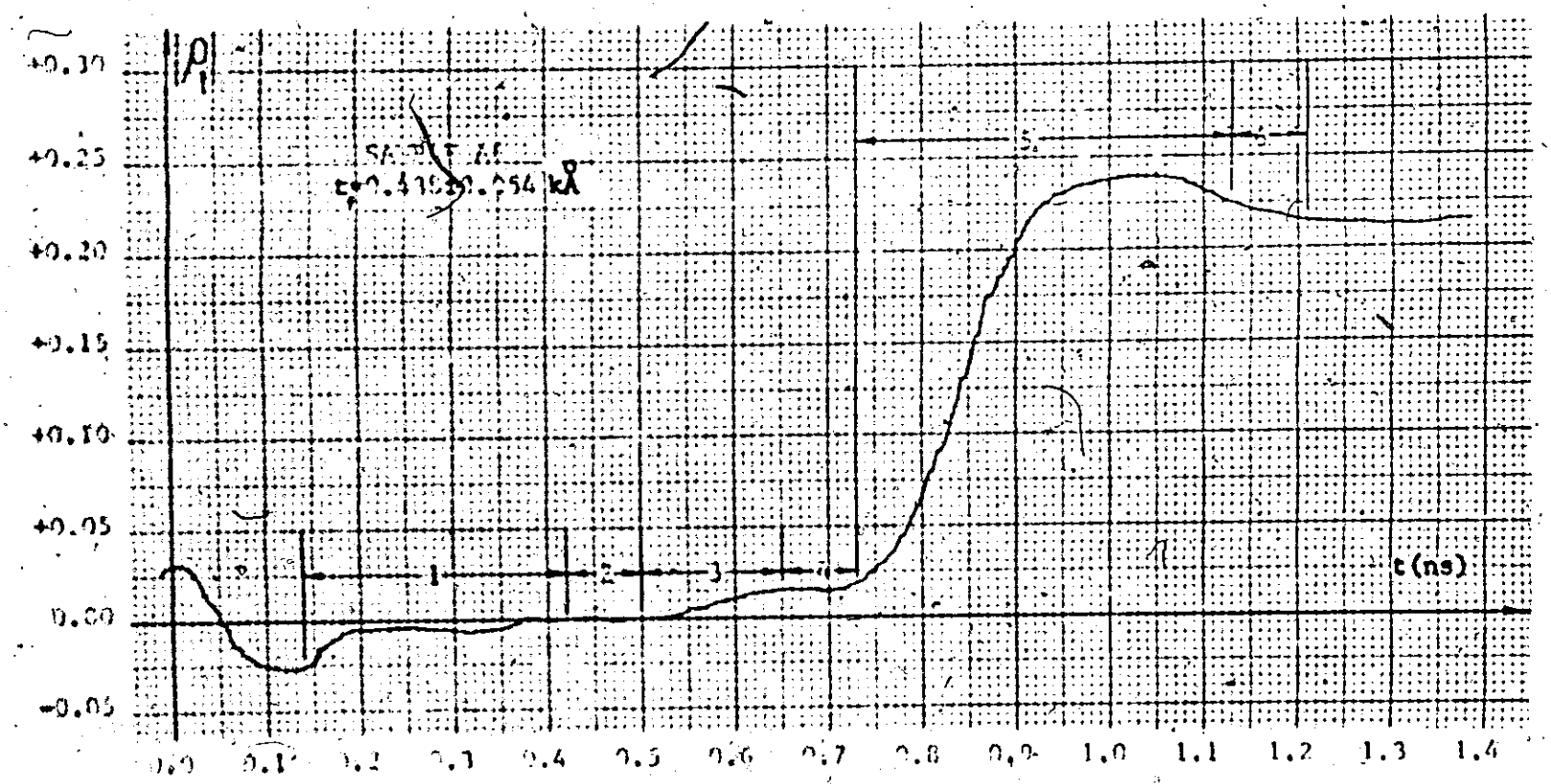

Figure B.A6-E: Expanded HP 1415A TDR Trace for a 50 Ω Termination Applied to Thin Film CPW Sample A6 Mounted by Means of the Wavetek Microstrip Mount.

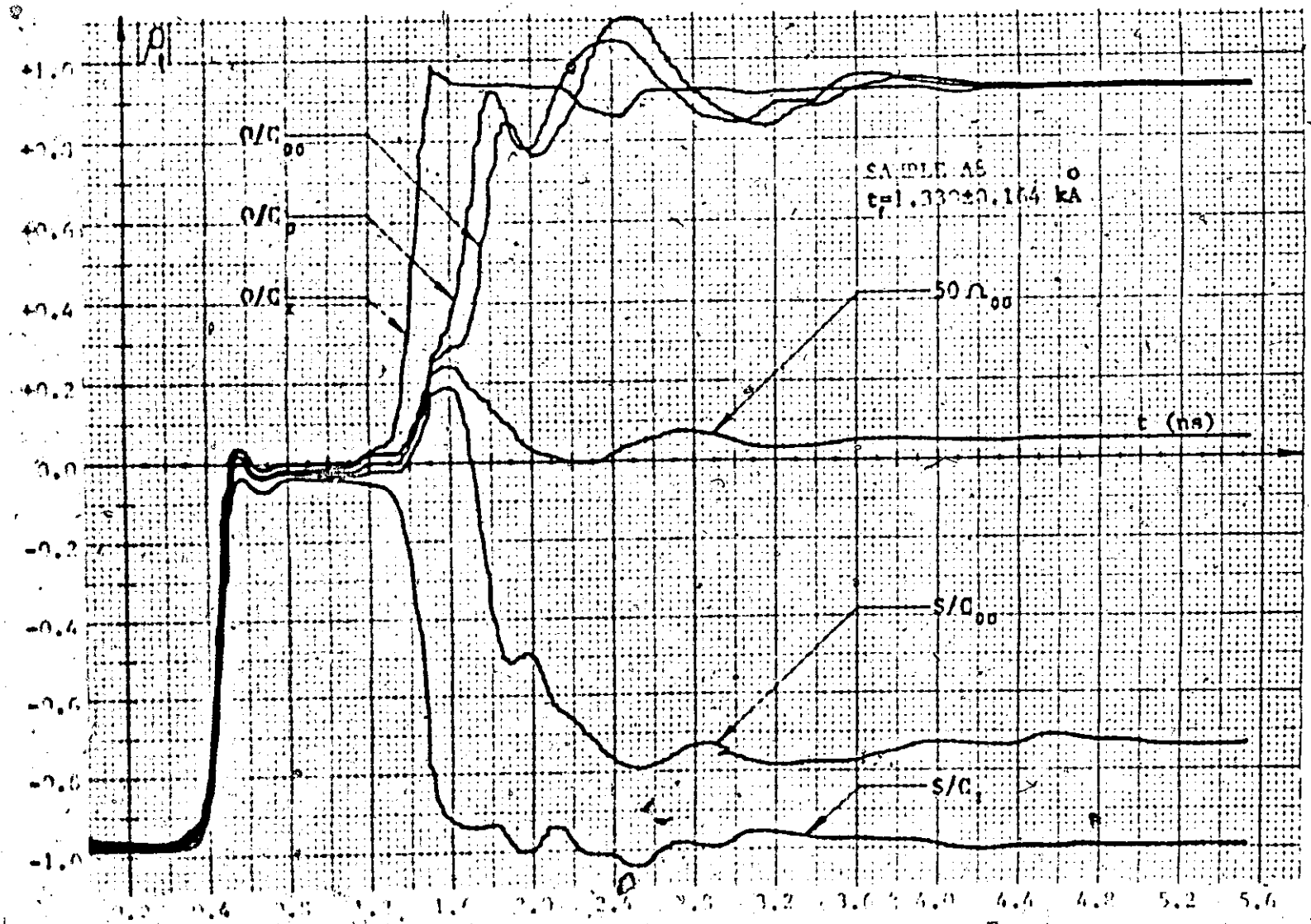

Figure B.AB-1: Unexpanded HP 1415A TDR Traces for 6 Different Loads Applied to Thin Film CPW Sample AB Mounted by Means of the Wavetek Microstrip Mount.

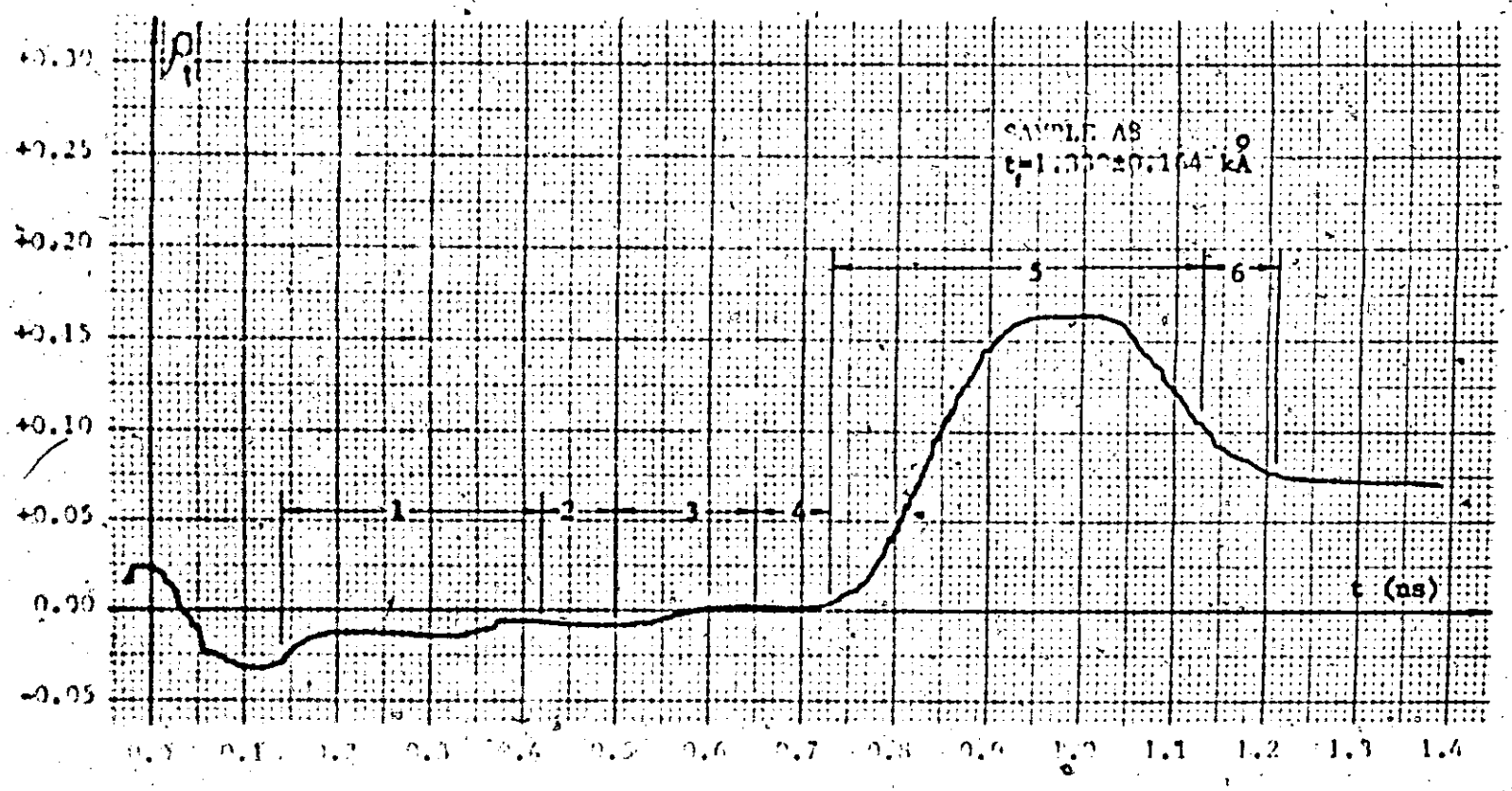

Figure B.A8-E: Expanded HP 1415A TDR Trace for a 50 Ω Termination Applied to Thin Film CPW Sample A8 Mounted by Means of the Wavetek Microstrip Mount.

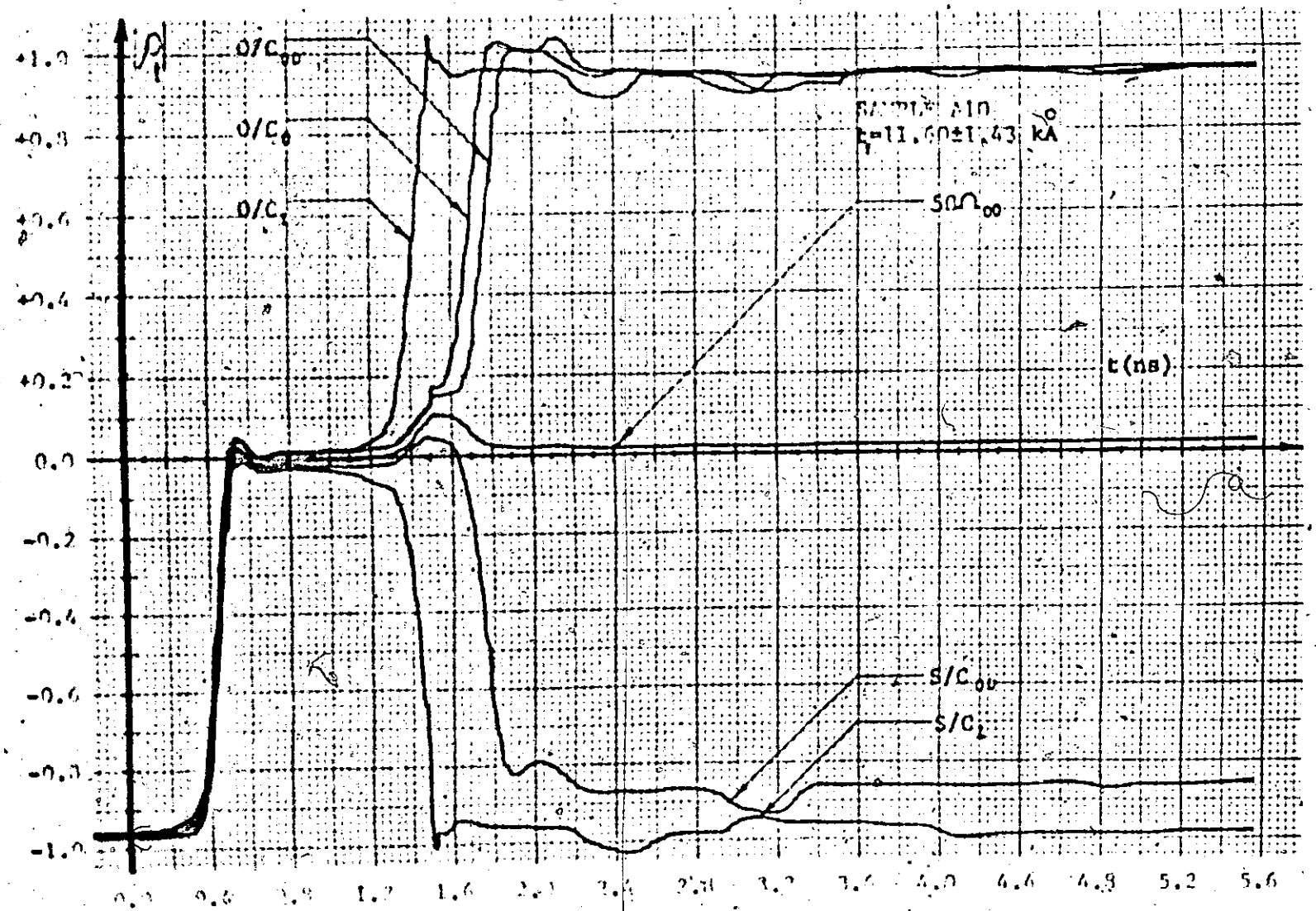

Figure F.A10-4: Unexpanded HP 1415A TDR Traces for 6 Different Loads Applied to Thin Film CPW Sample A10 Mounted by Means of the Wavetek Microstrip Mount.

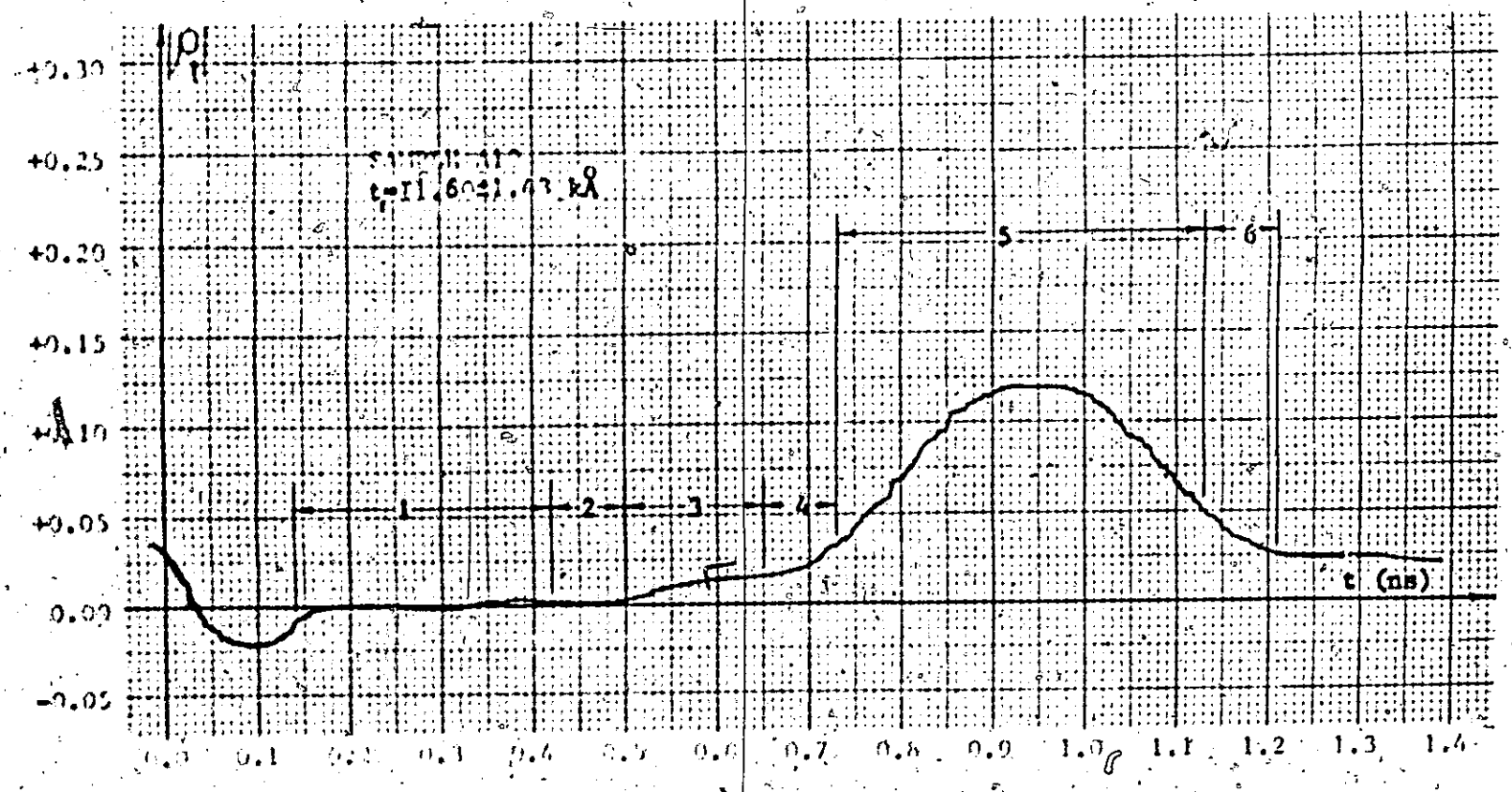

Figure B.A10-E: Expanded HP 1415A TDR Trace for a 50 Ω Termination Applied to Thin Film CPW Sample A10 Mounted by Means of the Wavetek Microstrip Mount.

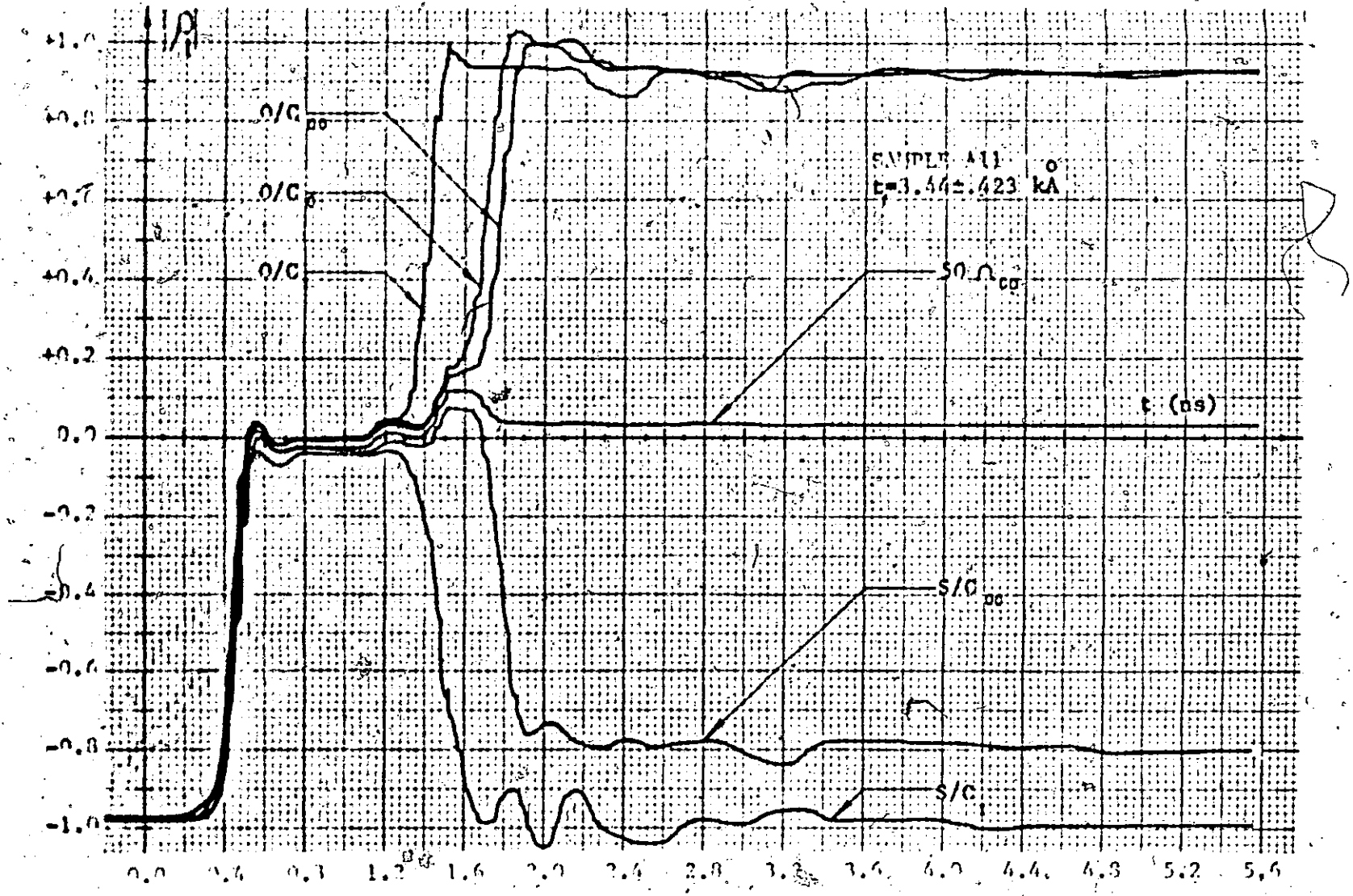

Figure B.A11-D: Unexpanded HP 1415A TDR Traces for 6 Different Loads Applied to Thin Film CPW Sample A11 Mounted by Means of the Wavetek Microstrip Mount.

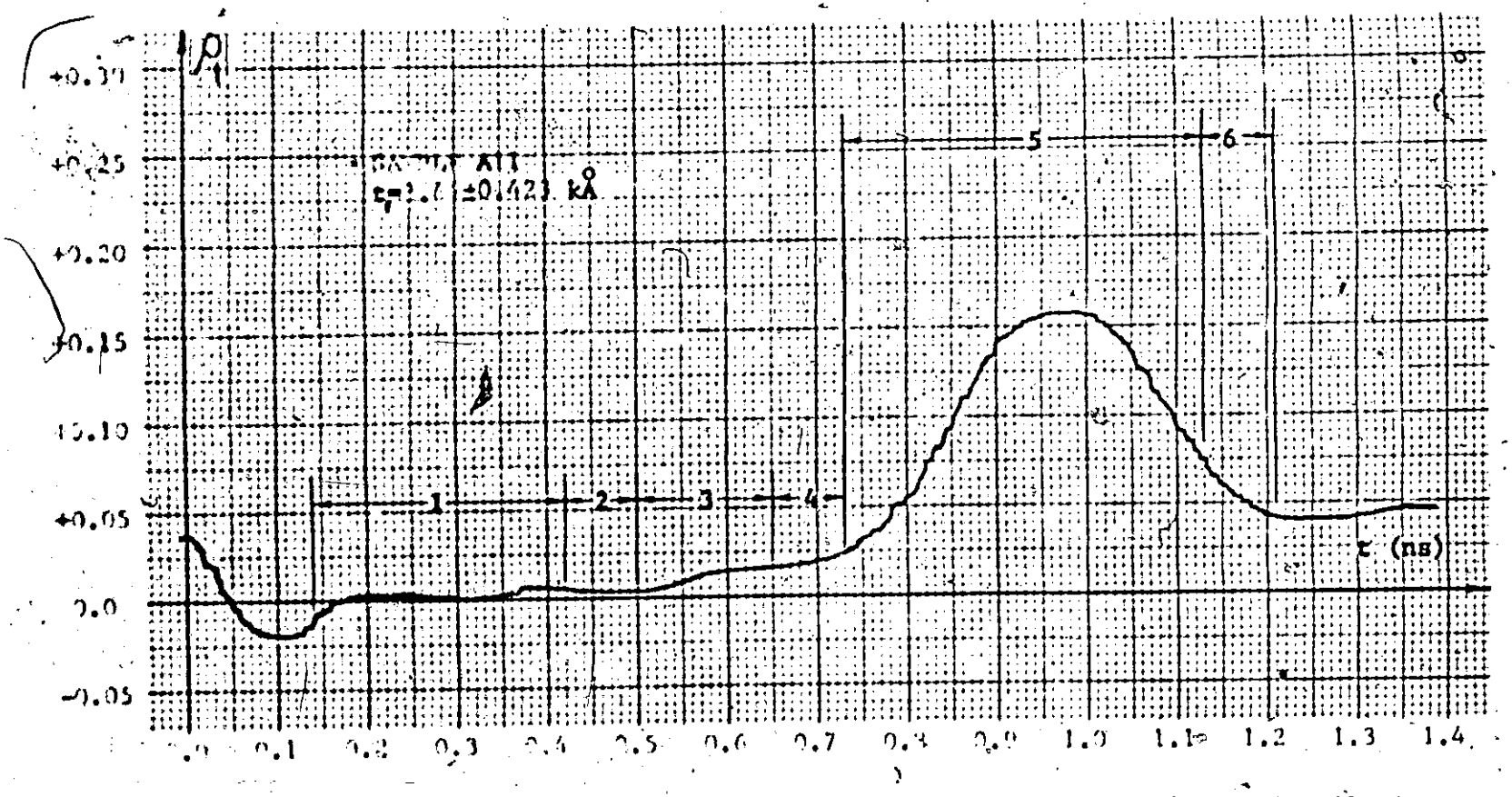

Figure B.A11-F: Expanded HP 1415A TDR Trace for a 50 Ω Termination Applied to Thin Film CPW Sample A11 Mounted by Means of the Wavetek Microstrip Mount.

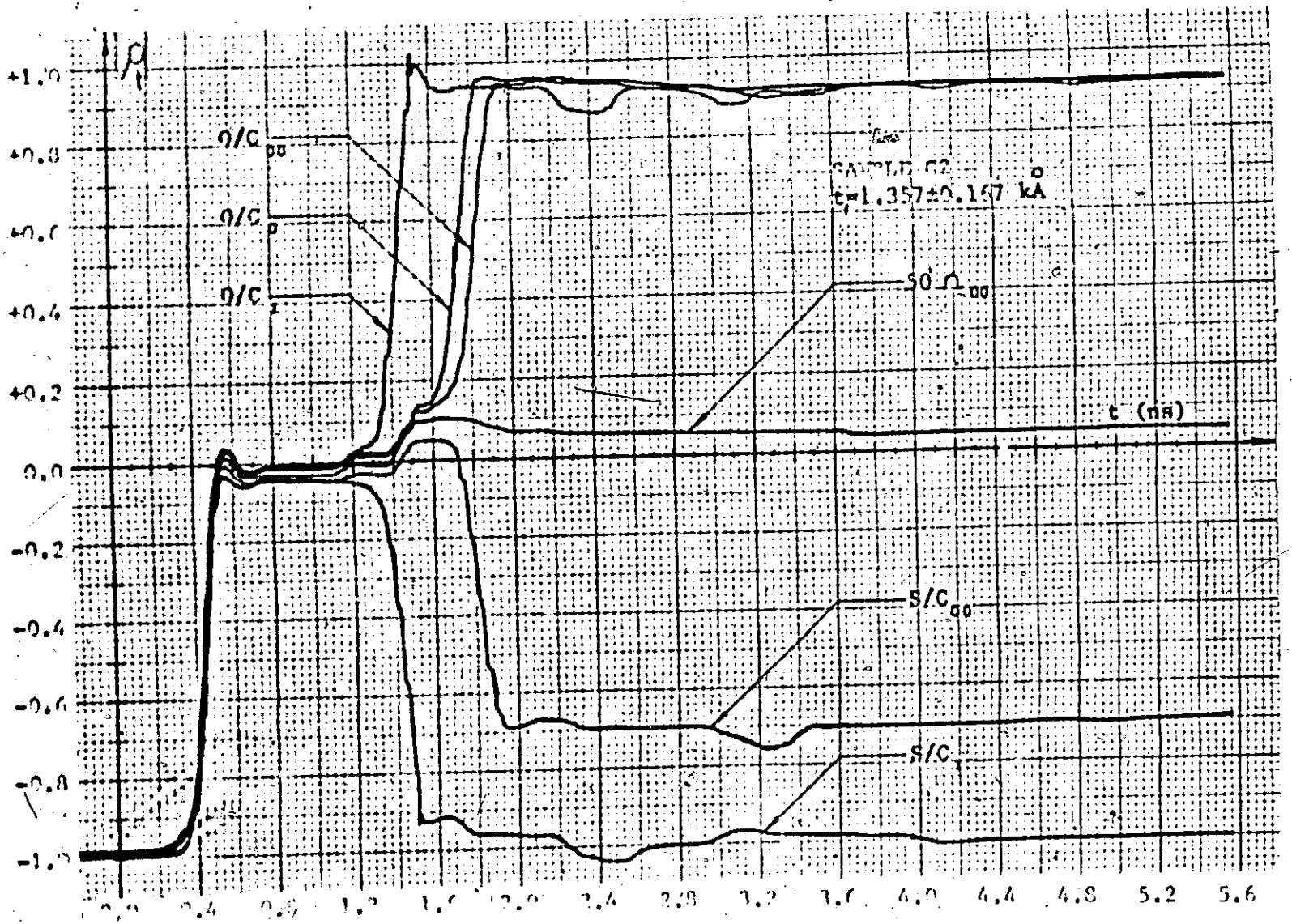

Figure E.C2-U: Unexpanded HP 1415A TDR Traces for 6 Different Loads Applied to Thin Film CPW Sample C2 Mounted by Means of the Wavetek Microstrip Mount.

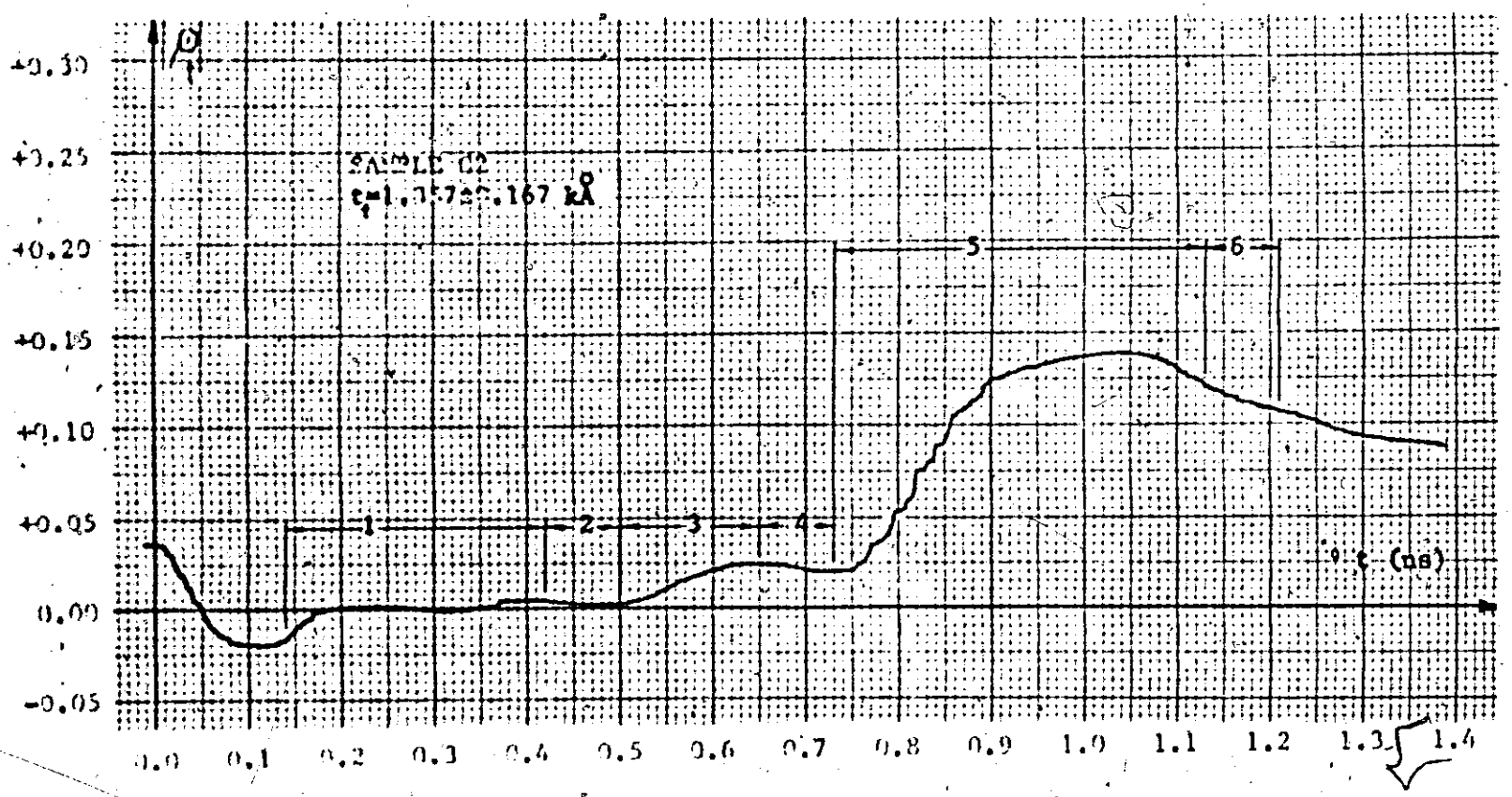

Figure B.C2-E: Expanded HP 1415A TDR Trace for a 50 Ω Termination Applied to Thin Film CPW Sample C2 Mounted by Means of the Wavetek Microstrip Mount.

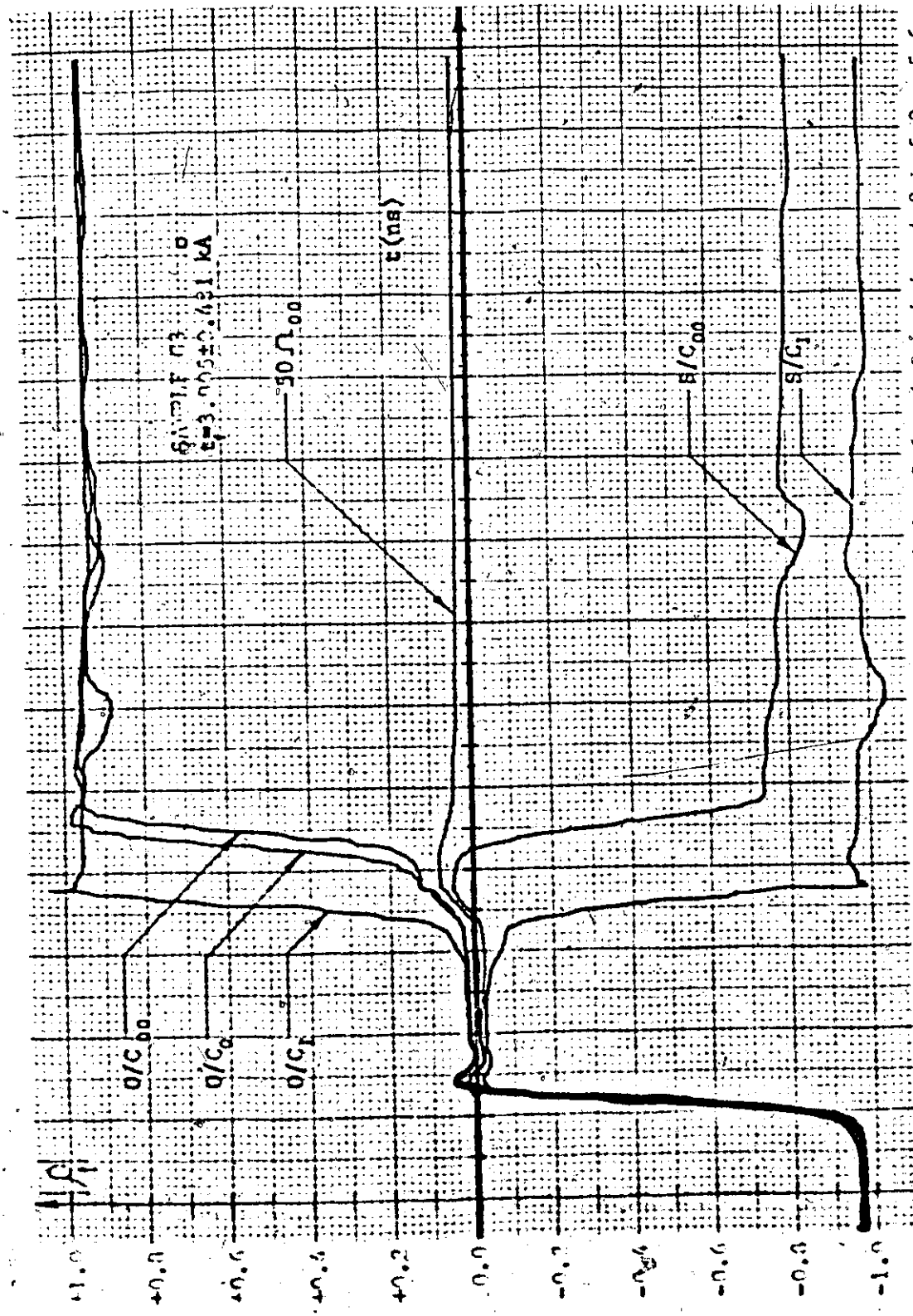

Figure B.C3-11: Unexpanded HP 1415A TDR Traces for 6 Different Loads Applied to Thin Film CPW Sample C3 Mounted by Means of the Wavetek Microstrip Mount.

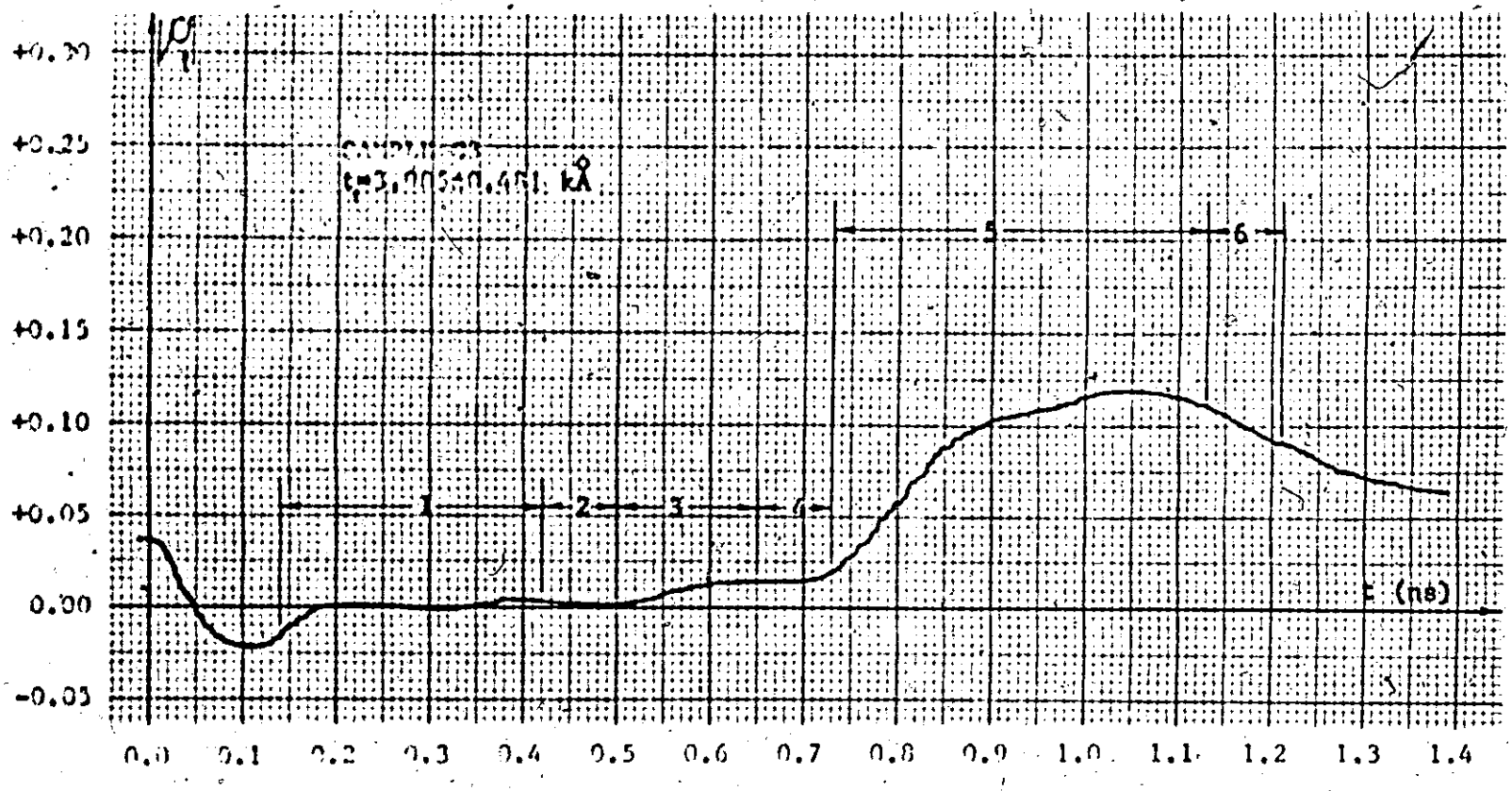

Figure B.C3-E: Expanded HP 1415A TDR Trace for a 50 Ω Termination Applied to Thin Film CPW Sample C3 Mounted by Means of the Wavetek Microstrip Mount.

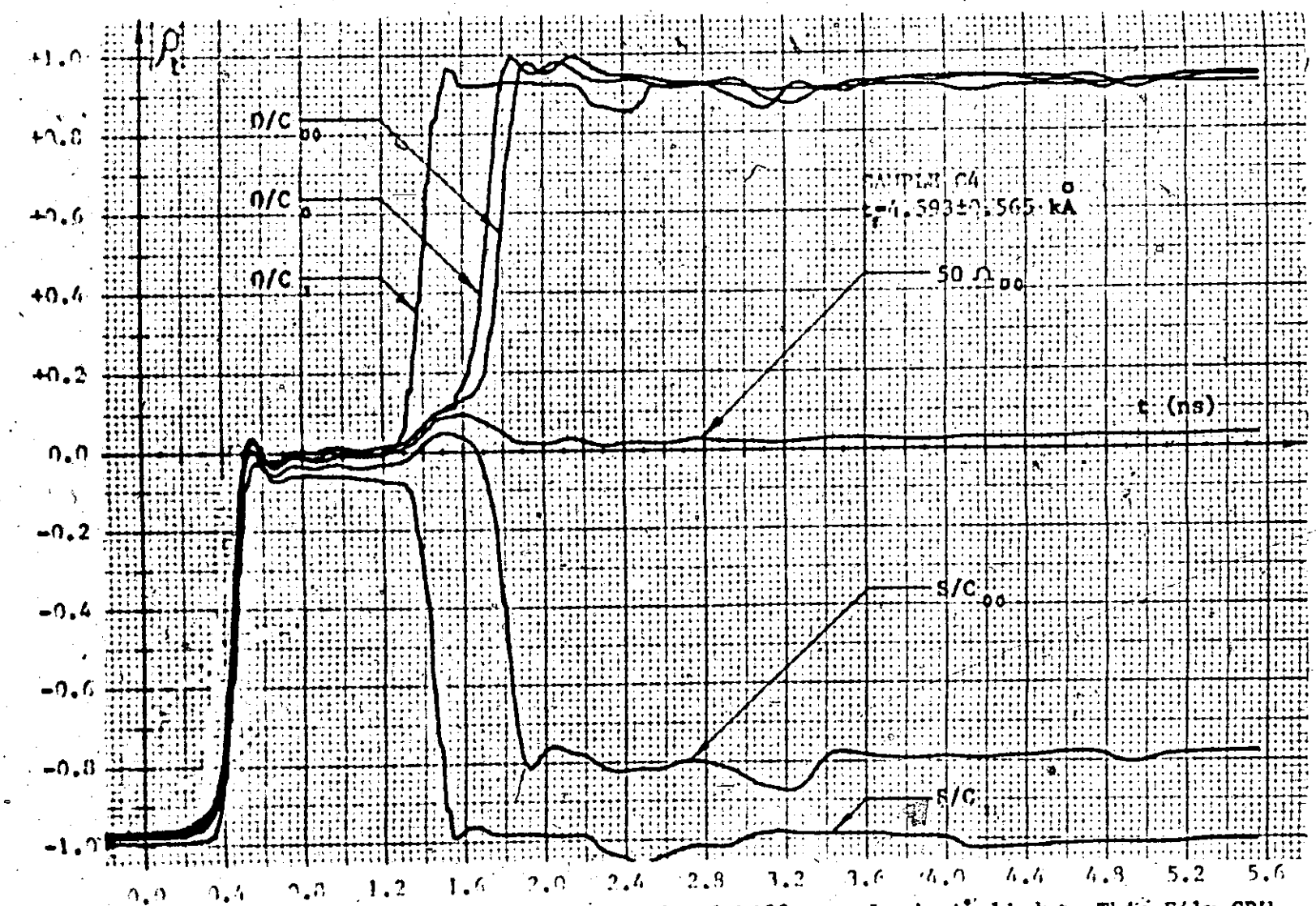

Figure B.C4-U: Unexpanded HP 1415A TDR Traces for 6 Different Loads Applied to Thin Film CPW Sample C4 Mounted by Means of the Wavetek Microstrip Mount.

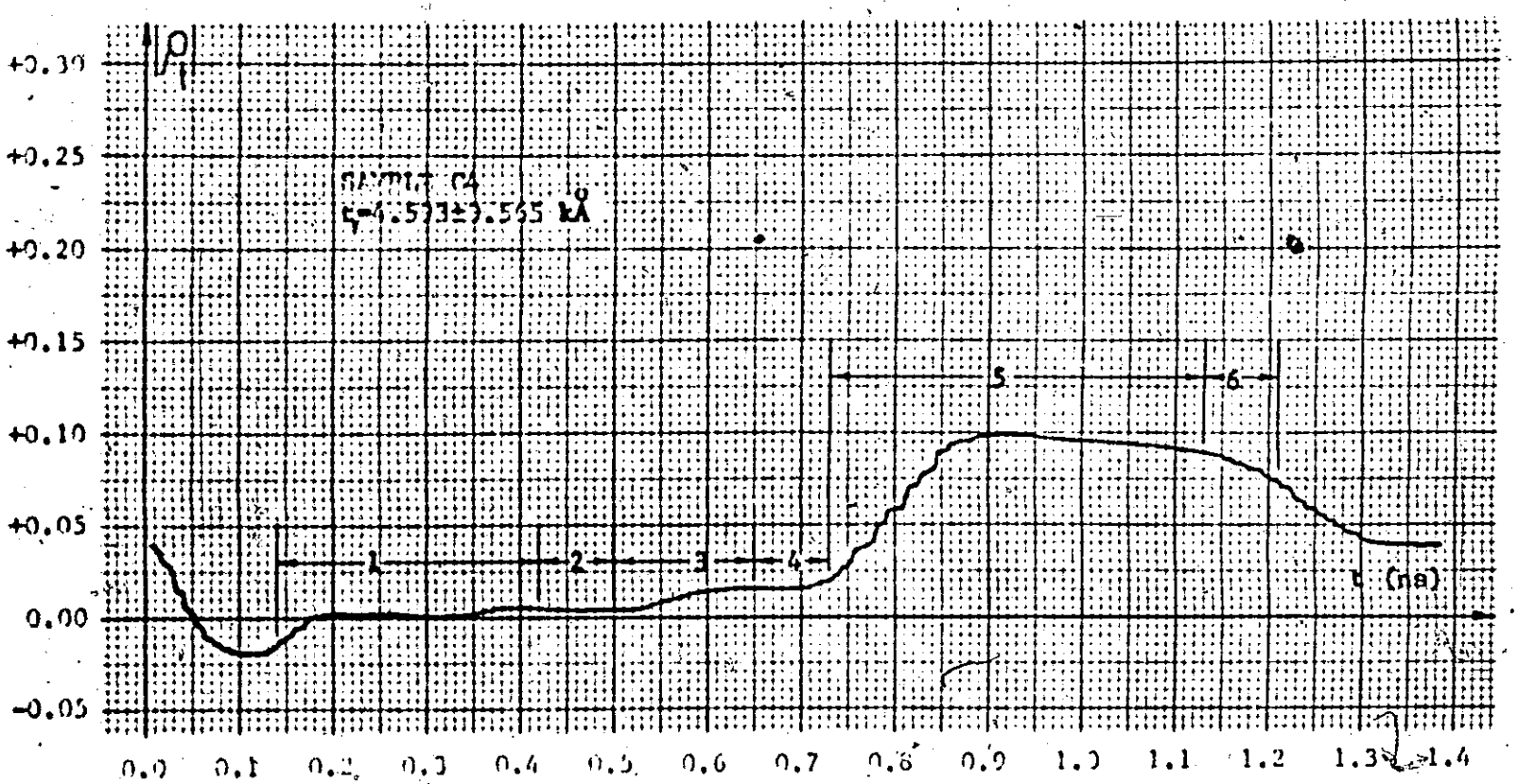

Figure B.C4-E: Expanded HP 1415A TDR Trace for a 50 Ω Termination Applied to Thin Film CPW Sample C4 Mounted by Means of the Wavetek Microstrip Mount.

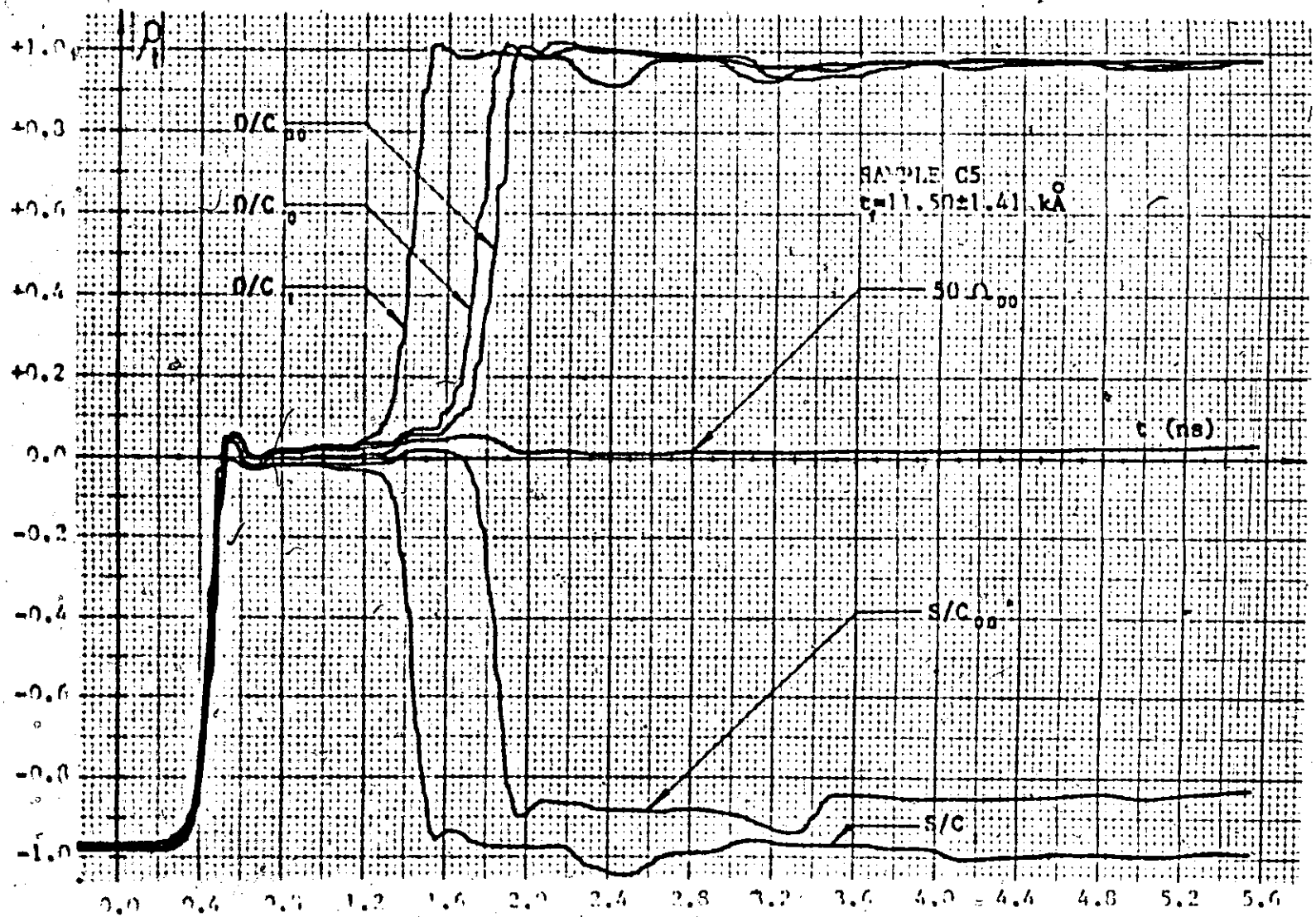

Figure B.C5-U: Unexpanded HP 1415A TDR Traces for 6 Different Loads Applied to Thin Film CPW Sample C5 Mounted by Means of the Wavetek Microstrip Mount.

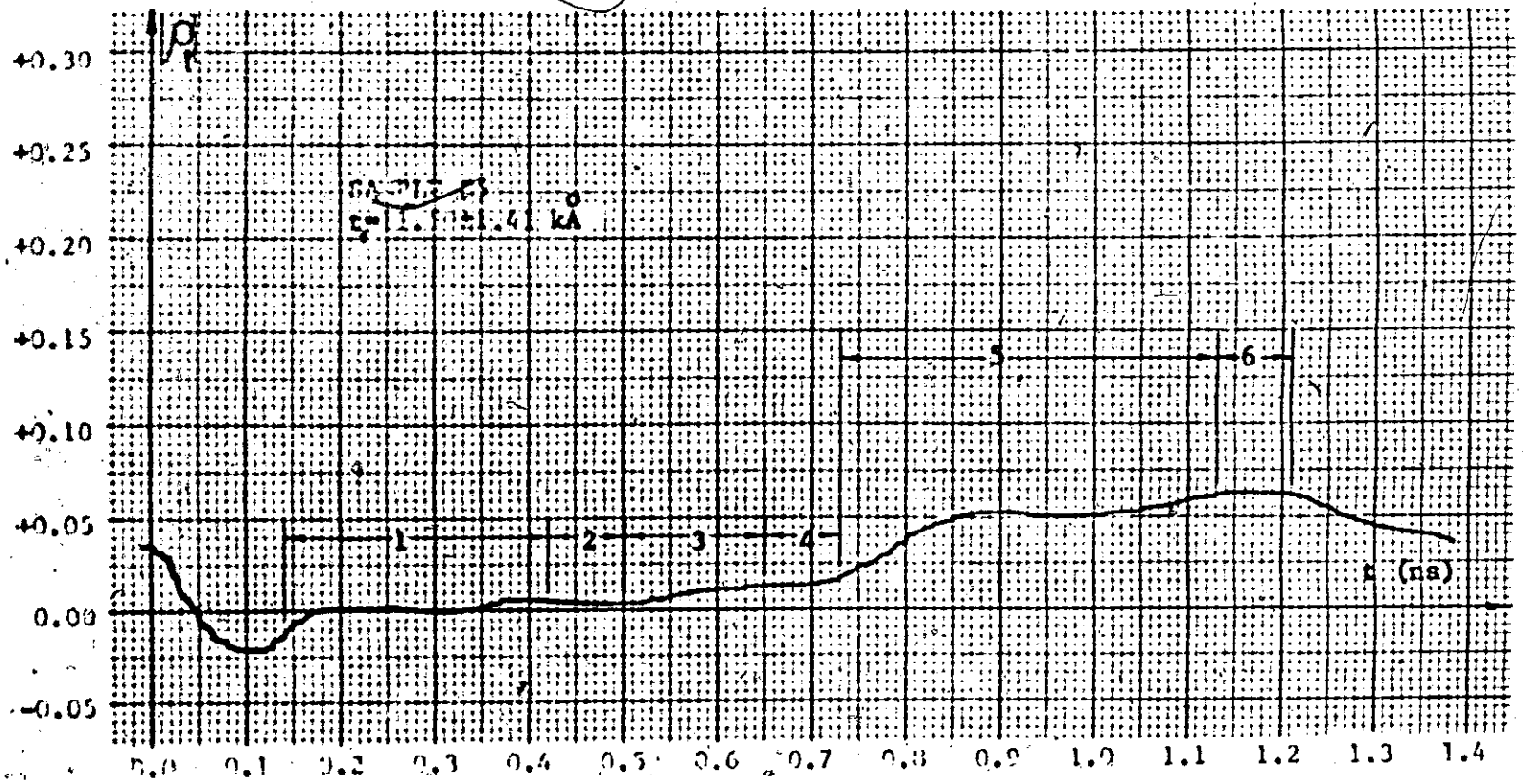

Figure B.C5-E: Expanded HP 1415A TDR Trace for a 50 Ω Termination Applied to Thin Film CPW Sample C5 Mounted by Means of the Wavetek Microstrip Mount.

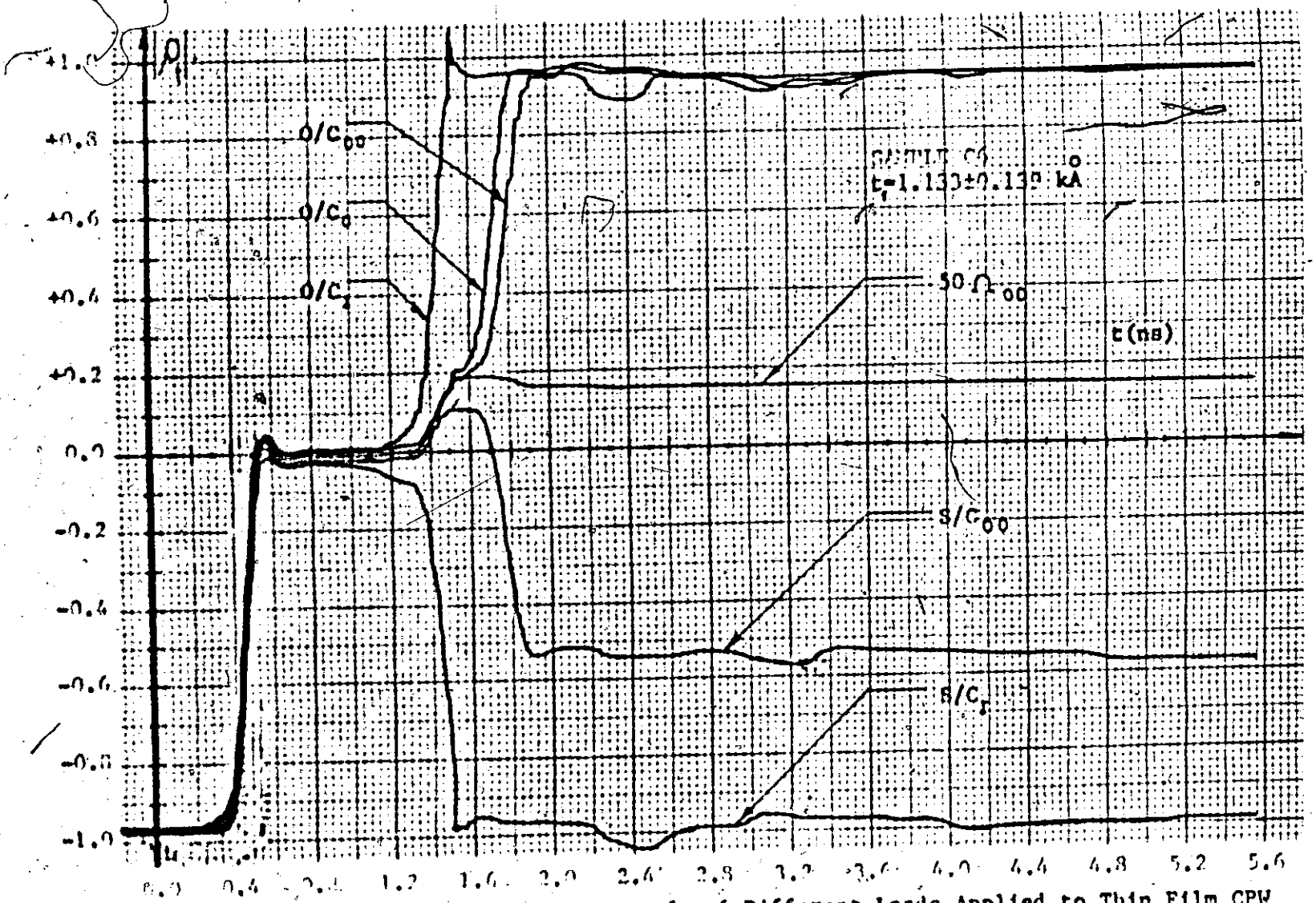

Figure B.C6-D: Unexpanded HP 1415A TDR Traces for 6 Different Loads Applied to Thin Film CPW Sample C6 Mounted by Means of the Wavetek Microstrip Mount.

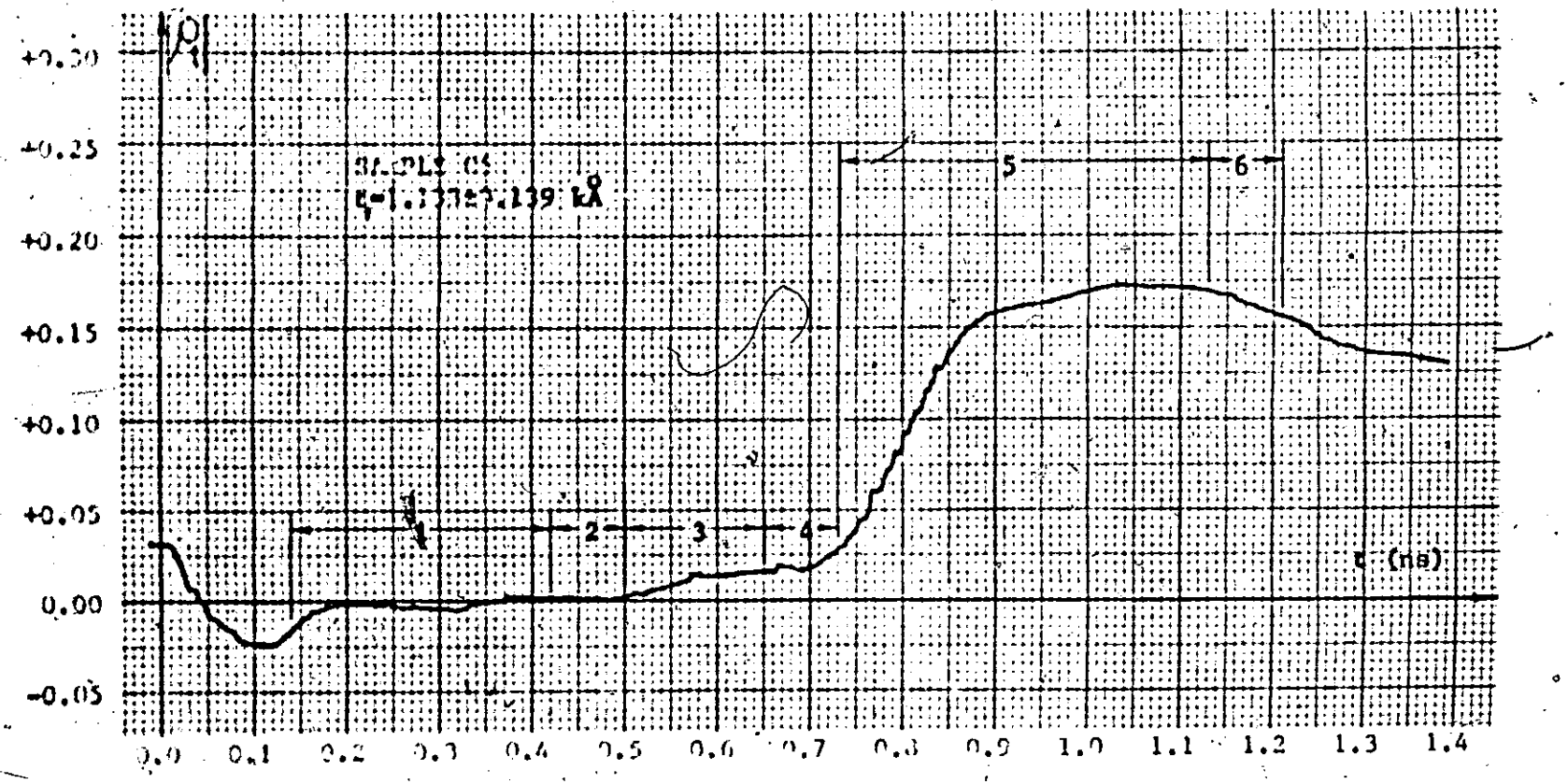

Figure B.C6-E: Expanded HP 1415A TDR Trace for a 50 Ω Termination Applied to Thin Film CPW Sample C6 Mounted by Means of the Wavetek Microstrip Mount.

APPENDIX C

MEASUREMENTS WITH THE NEW COPLANAR WAVEGUIDE LAUNCHERS AND THE FASTER HP 1815B TDR/SAMPLER ON THE ALUMINUM COPLANAR WAVEGUIDES FABRICATED BY DIRECT ETCHING OF ALUMINUM

APPENDIX C

The faster HP 1815B TDR/SAMPLER system described in section 4.3 of chapter IV was used to determine average input reflection coefficients for all thin film CPW samples fabricated by the direct photographic etching technique of section 3.2 of chapter III. Expanded TDR traces in the region of interest for the series A- and BCD- samples were taken on an HP-Moseley 7030A XY recorder. Both expanded and unexpanded traces for meandered lines M1-2 and M2-3 were also taken. Figures C.1 to C.7 contain the performance records for the A- and BCD- samples in order of increasing film thickness. Figures C.8 to C.10 contain the performance records for the meandered lines.

Each graph is labelled with a sample number and corresponding film thickness t_f. The symbols $|\rho_t|$ and t represent TDR measured reflection coefficient magnitude and elapsed return time respectively. The various TDR traces and their parts are labelled by the use of integers from 1 to 7. Their meanings are as follows:

1 One 25 mil substrate thickness is used,

2 Two 25 mil substrate thicknesses are used,

3 Three 25 mil substrate thicknesses are used,

4 Input CPW launcher,

5 CPW sample,

6 Output CPW launcher,

7 A termination of 50 Ω.

The implications of these measurements are presented in section 5.2 of chapter V.

The unexpanded traces for the meandered samples have various symbols and subscripts to indicate the types of loads applied to the CPW samples for testing. These are

O/C_I - open circuit at the CPW input,

O/C_o - open circuit at the CPW output,

O/C_{oo} - open circuit at the end of the output launcher,

S/C_I - short circuit at the CPW input,

S/C_{oo} - short circuit at the end of the output launcher,

$50\ \Omega_{oo}$ - 50 Ω load at the end of the output launcher.

These various loading conditions serve to indicate propagation times through the samples and launchers as well as indicate the degree of matching in each sample. The s/c tests also give an approximate measurement of the d.c. thin film resistance plus d.c. contact resistance of each sample where small multiple reflections introduce a significant degree of error. For both M1-2 and M2-3 the s/c test yields a reflection coefficient of -0.8, which indicates a total d.c. resistance of about 5.5 Ω for each sample.

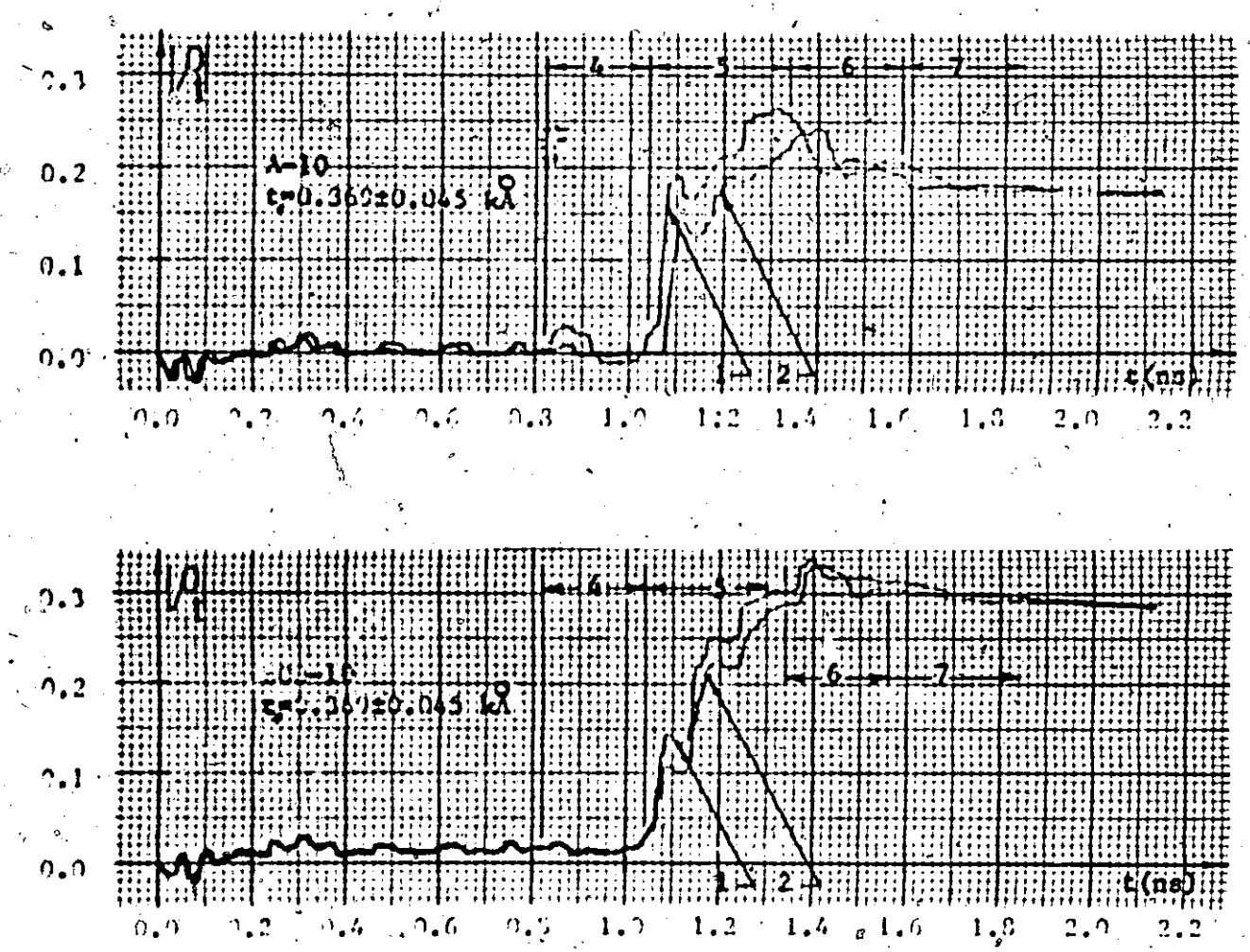

Figure C.1: Expanded TDR Traces for Samples A-10 and BCD-10 Terminated with a 50 Ω Calibrated Load and Measured by the 1815B TDR/SAMPLER.

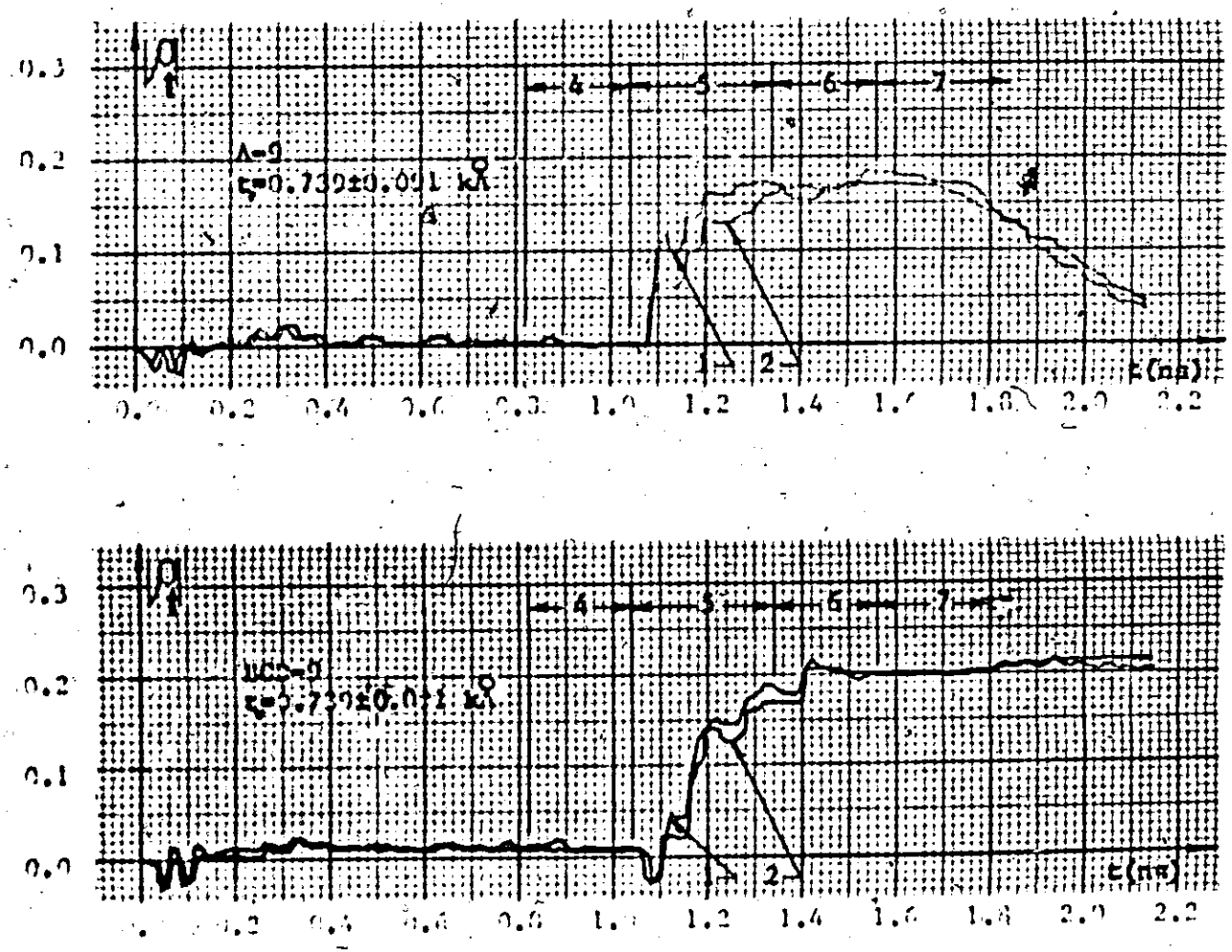

Figure C.2: Expanded TDR Traces for Samples A-9 and BCD-9 Terminated with a 50 Ω Calibrated Load and Measured by the 1815B TDR/SAMPLER.

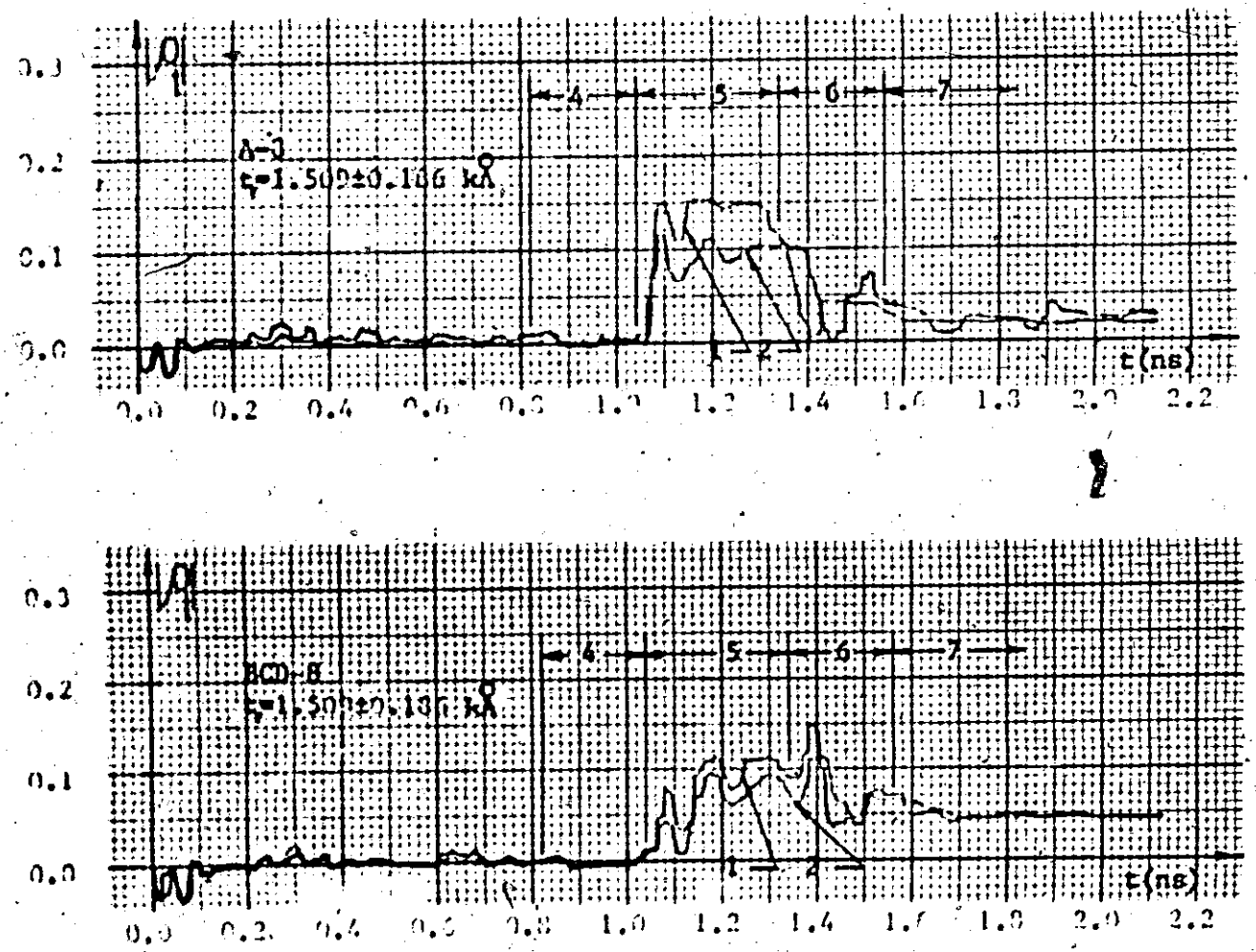

Figure C.3: Expanded TDR Traces for Samples A-8 and PCD-8 Terminated with a 50 Ω Calibrated Load and Measured by the 1815B TDR/SAMPLER.

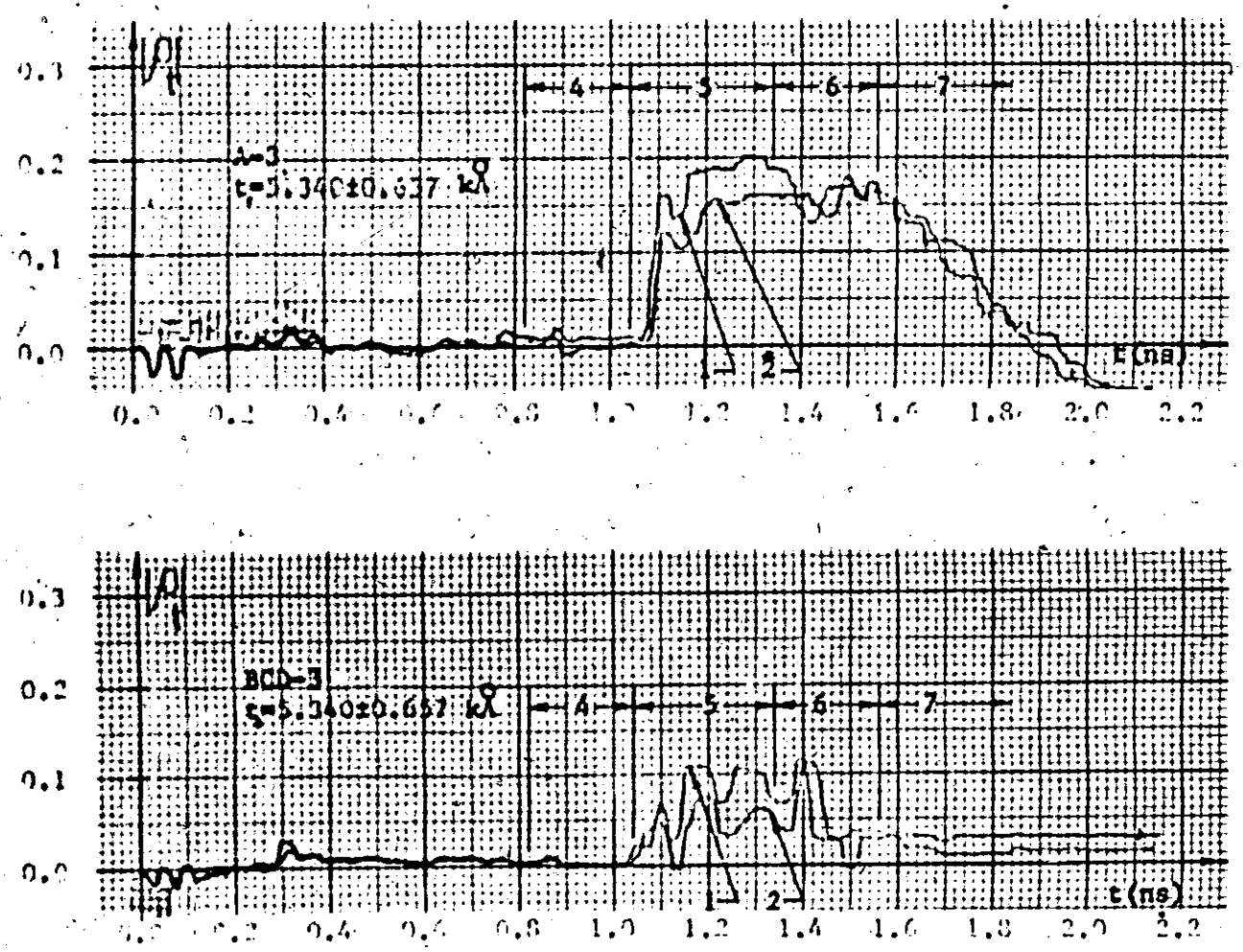

Figure C.4: Expanded TDR Traces for Samples A-3 and BCD-3 Terminated with a 50 Ω Calibrated Load and Measured by the 1815B TDR/SAMPLER.

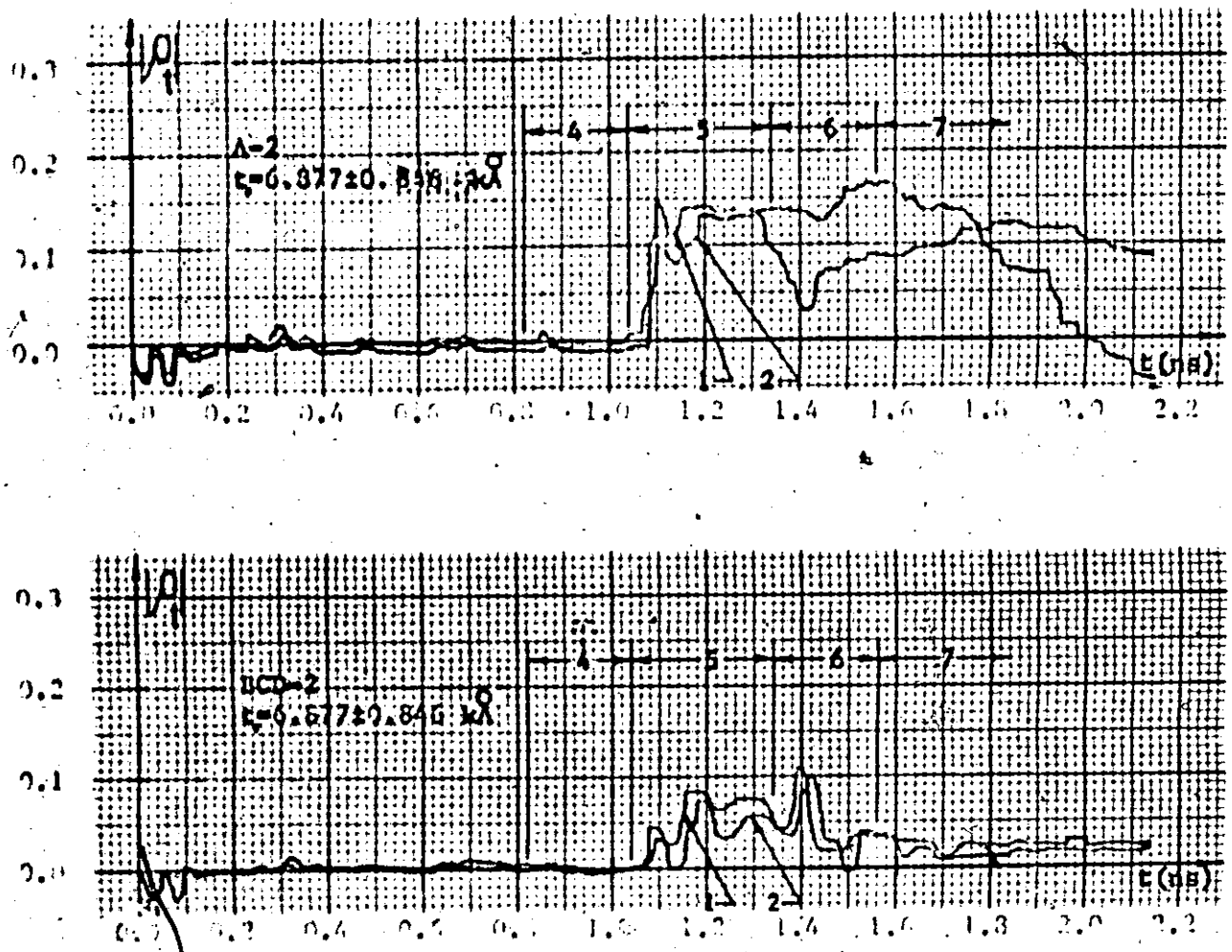

Figure C.5 : Expanded TDR Traces for Samples A-2 and BCD-2 Terminated with a 50 Ω Calibrated Load and Measured by the 1815B TDR/SAMPLER.

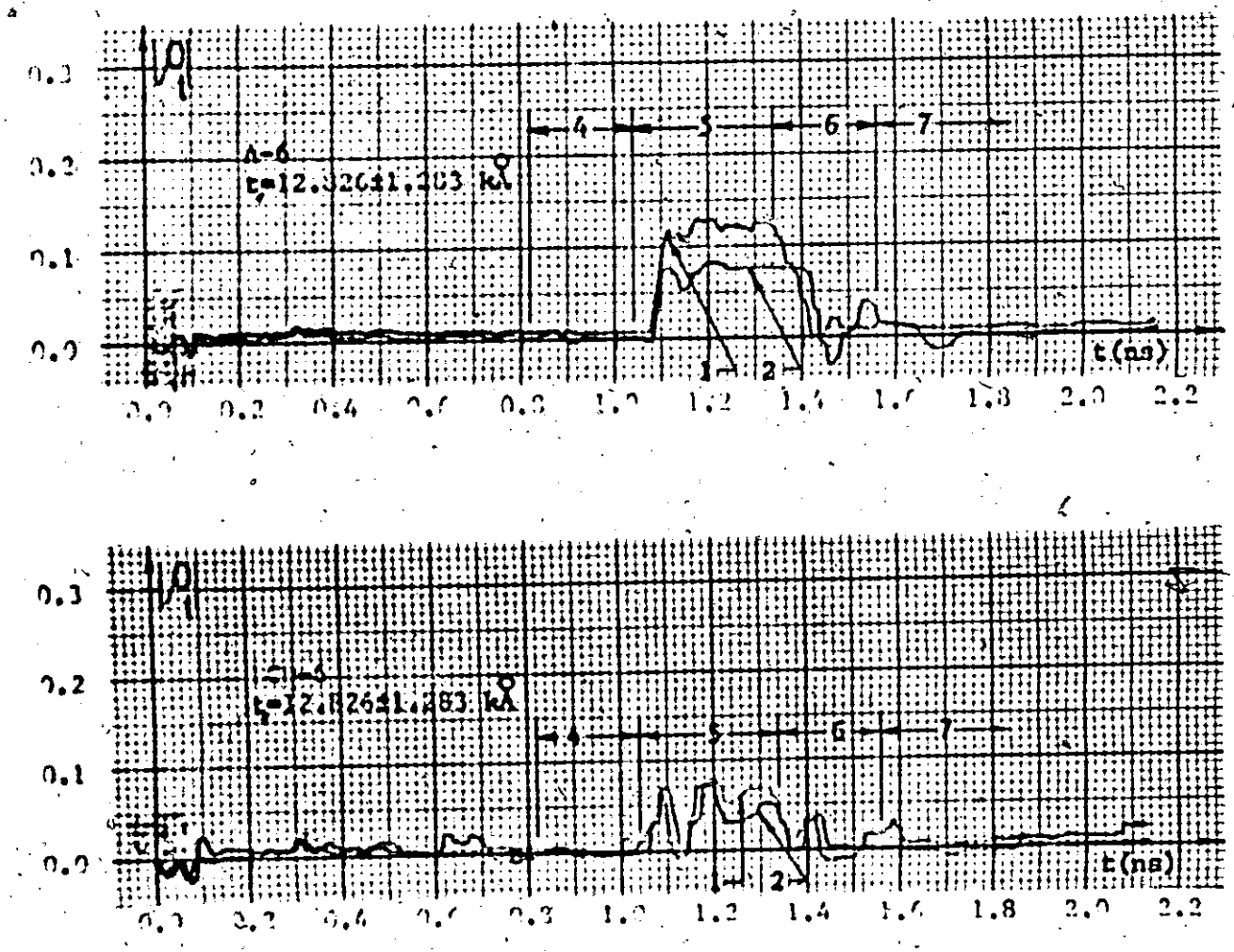

Figure C.6: Expanded TDR Traces for Samples A-6 and BCD-6 Terminated with a 50 Ω Calibrated Load and Measured by the 1815R TDR/SAMPLER.

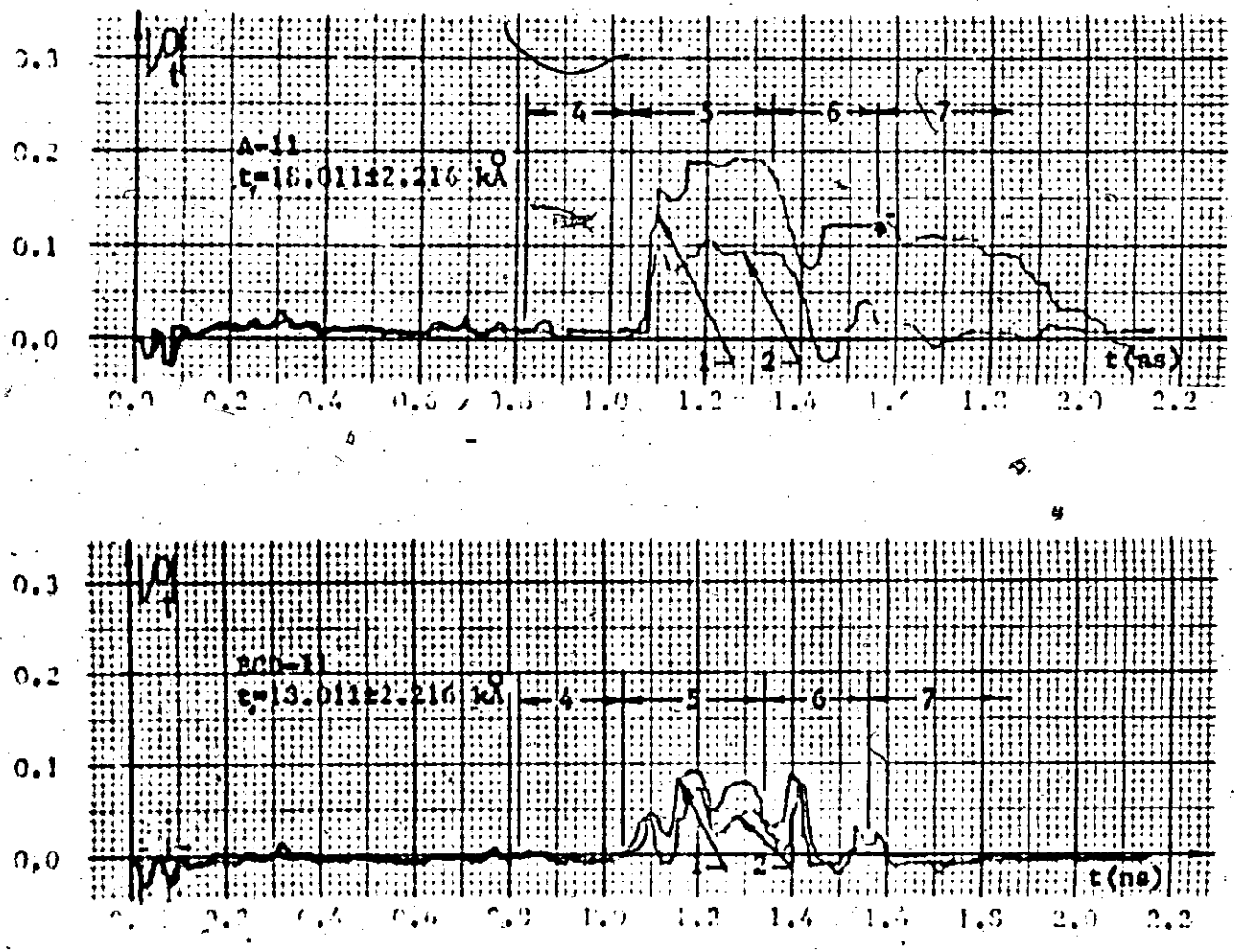

Figure C.7: Expanded TDR Traces for Samples A-11 and PCD-11 Terminated with a 50 Ω Calibrated Load and Measured by the 1815R TDR/Sampler.

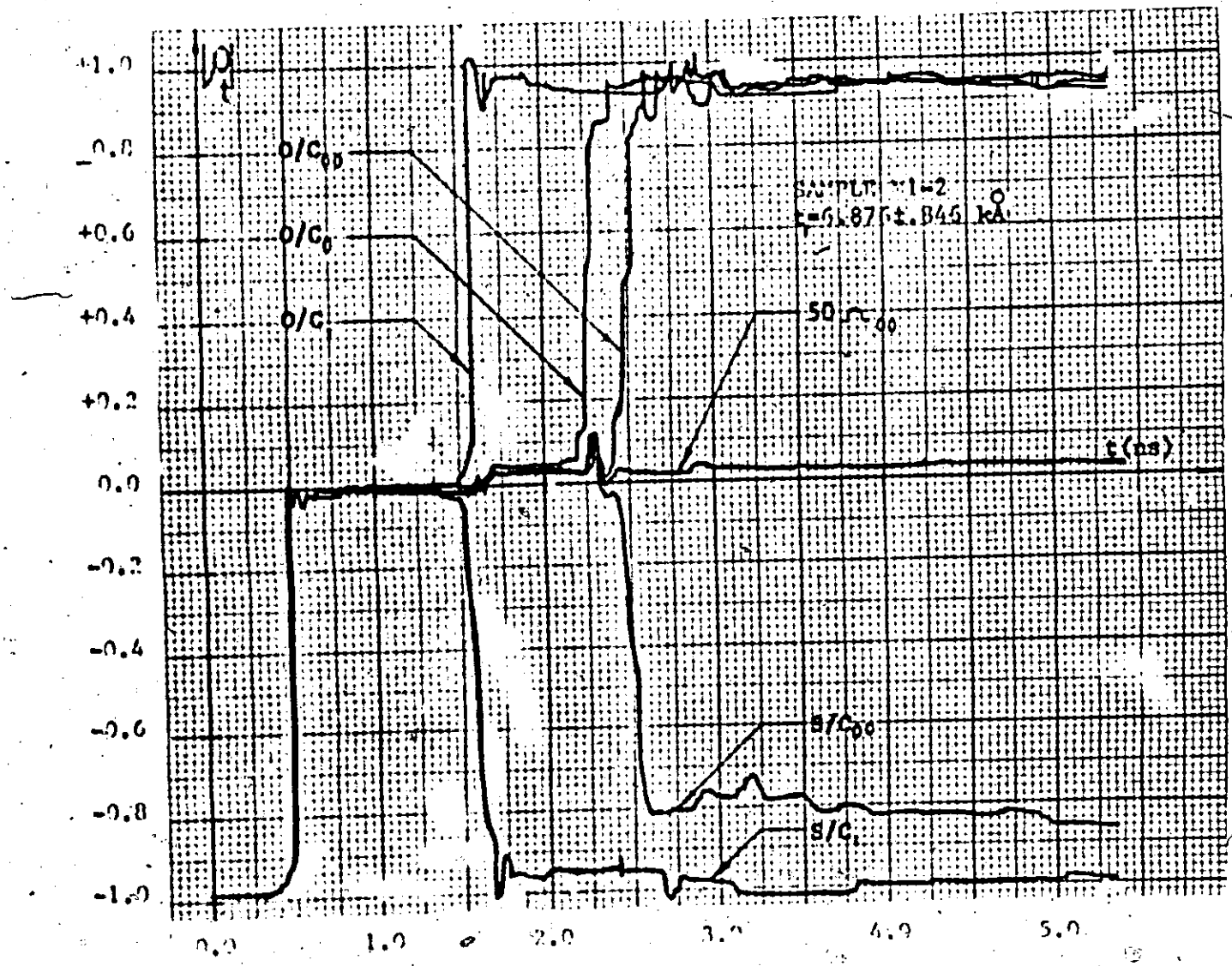

Figure C.8: Unexpanded TDR Traces for Meandered Sample M1-2 with 6 Different Load Conditions and Measured by the 1815R TDR/SAMPLER.

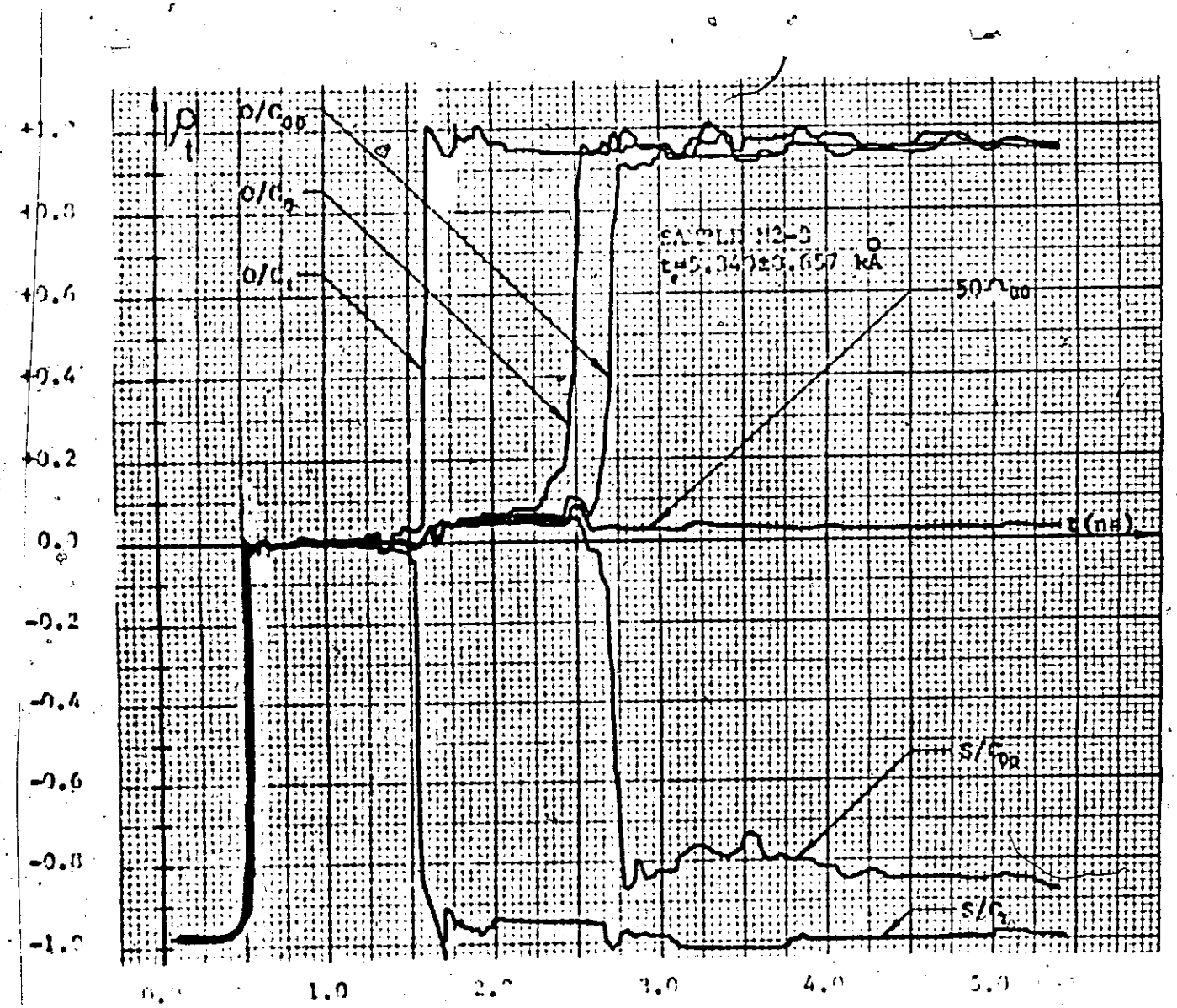

Figure C.9: Unexpanded TDR Traces for Meandered Sample M2-3 with 6 Different Load Conditions and Measured by the 1815R TDR/SAMPLER.

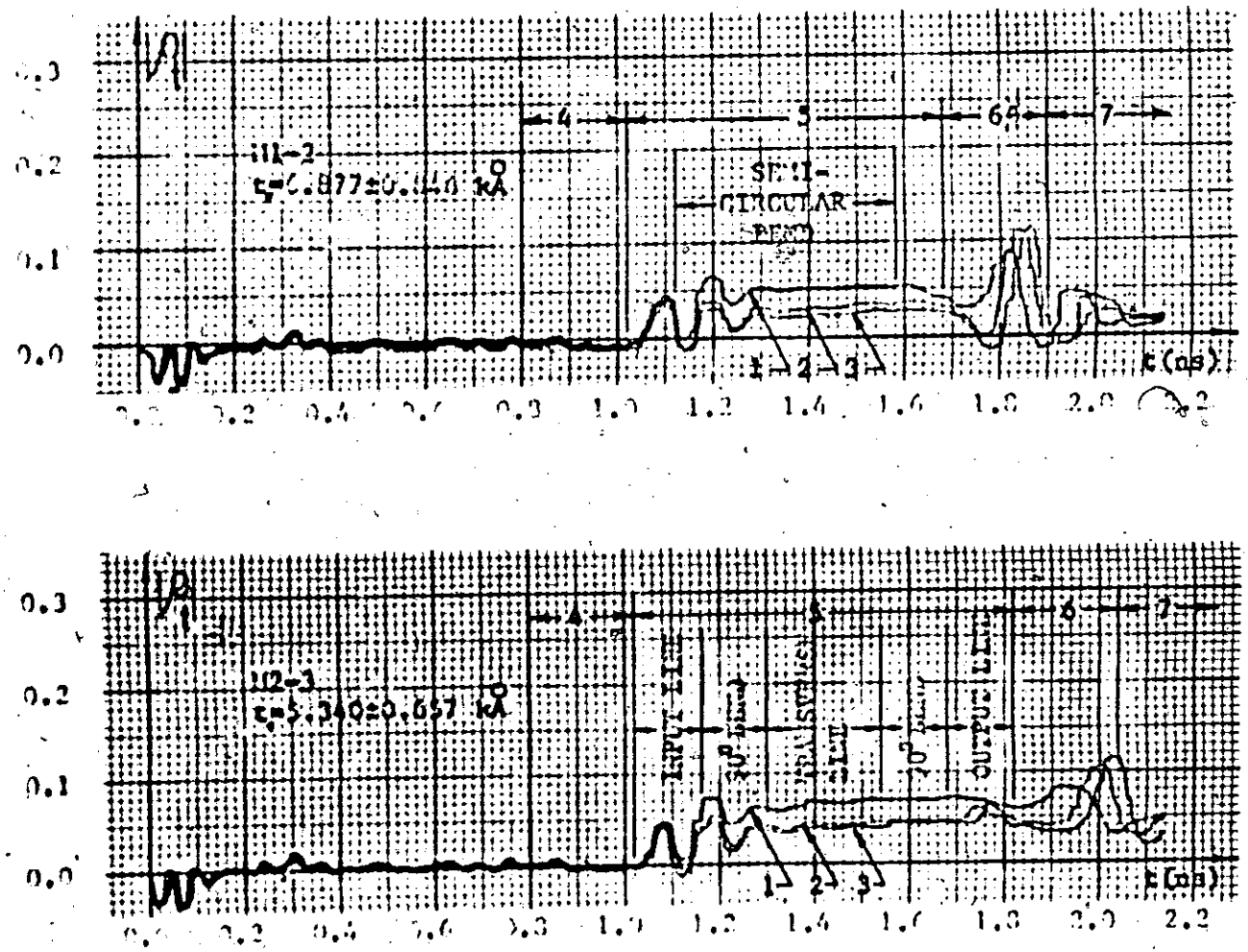

Figure C.10: Expanded TDR Traces for Meandered Samples M1-2 and M2-3 Terminated with a 50 Ω Calibrated Load and Measured by the 1815B TDR/SAMPLER.

APPENDIX D

LOSS MEASUREMENTS FROM ONE TO TWO GHZ WITH A 20 dB BI-DIRECTIONAL COAXIAL COUPLER A MODEL 6608D SINGER SWEEP OSCILLATOR AND A MODEL 7051 SINGER NETWORK ANALYSER ON STRAIGHT AND MEANDERED COPLANAR LINES

APPENDIX D

The Singer instrumentation discussed in section 4.1 of chapter IV was used to measure reflection coefficient magnitudes and transmission loss in the 1-2 GHz frequency band for 24 straight 1" long CPW samples of various thin film thicknesses and also for two meandered samples M1-2 and M2-3. In this appendix these measurements have been recorded graphically for reference purposes. Their significance is discussed in chapter V, section 5.1. Legends have been placed at the right of each graph to enable the identification of each curve in relation to thin film thickness in kÅ.

Figure D.1 summarizes loss and reflection measurements made on the series of samples fabricated by masking techniques with mask A from design A, and as a result are called series A samples. The numbers from 1 to 11 behind the letter A relate to the sequence in which the samples were fabricated. Only samples A1, A6, A8, A10, and A11 were tested in this series because the other remaining six samples showed significant signs of specular migration and were not considered suitable tolerance-wise.

Figure D.2 summarizes loss and reflection measurements made on the series of samples fabricated by masking techniques with mask C from design BCD, and as a result are called series C samples. Masks B and D were rejects because of pre-established tolerance specifications and only mask C was acceptable tolerance-wise. The numbers from 2 to 6 behind the letter C in Figure D.2 relate to the sequence in which the samples were fabricated. Sample C1 was rejected because of significant

specular migration and as a result only C2, C3, C4, C5 and C6 were tested.

Figure D.3 summarizes loss and reflection measurements made on the series of samples fabricated by direct photographic etching from design A. This series is called the A- series. For this different fabrication technique, thin films of aluminum of various thicknesses were evaporated before etching and these films were given a code number in the sequence in which they were created. Each code number then represents a specific thin film thickness and is written after the hyphen in the A- series to identify a specific sample and its corresponding thin film thickness. Of the 11 thicknesses deposited seven were selected in order to obtain a wide selection of thin film thicknesses for the investigation of the effects of thin film thickness on attenuation in CPW's.

Figure D.4 summarizes loss and reflection measurements made on the RCD- series of samples fabricated by direct photographic etching from design RCD. Each code number and corresponding thin film thickness is the same as in the A- series. The purpose here was to also study the relationship between attenuation and thin film thickness in CPW's.

The loss and reflection measurements on the two meandered lines M1-2 and M2-3 are given in Figure D.5. Design M1 has a semicircular bend and design M2 contains two right angle bends. The code numbers 2 and 3 represent the same thin film thicknesses found in the A- and RCD- series. These meandered line measurements are of great interest since the meandering of transmission lines is necessary for the design and fabrication of microwave integrated circuits.

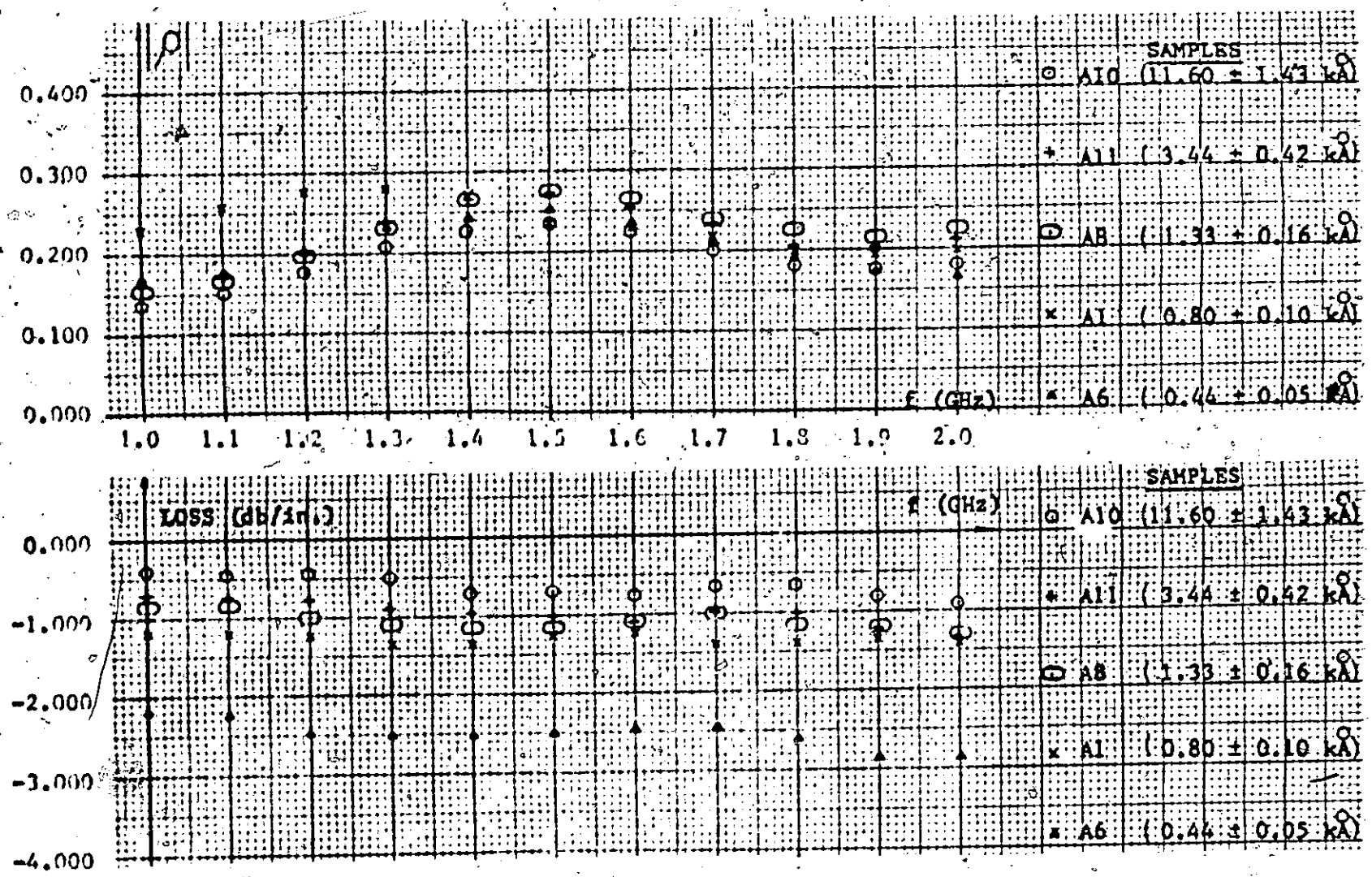

Figure D.1: Singer Instrumentation Measurements in the 1-2 GHz Frequency Band Showing the Effect of Thin Film Thickness (kÅ) on Transmission Loss and the Modulus of the Net Reflection Coefficient ρ for Various CPW Samples of Series A.

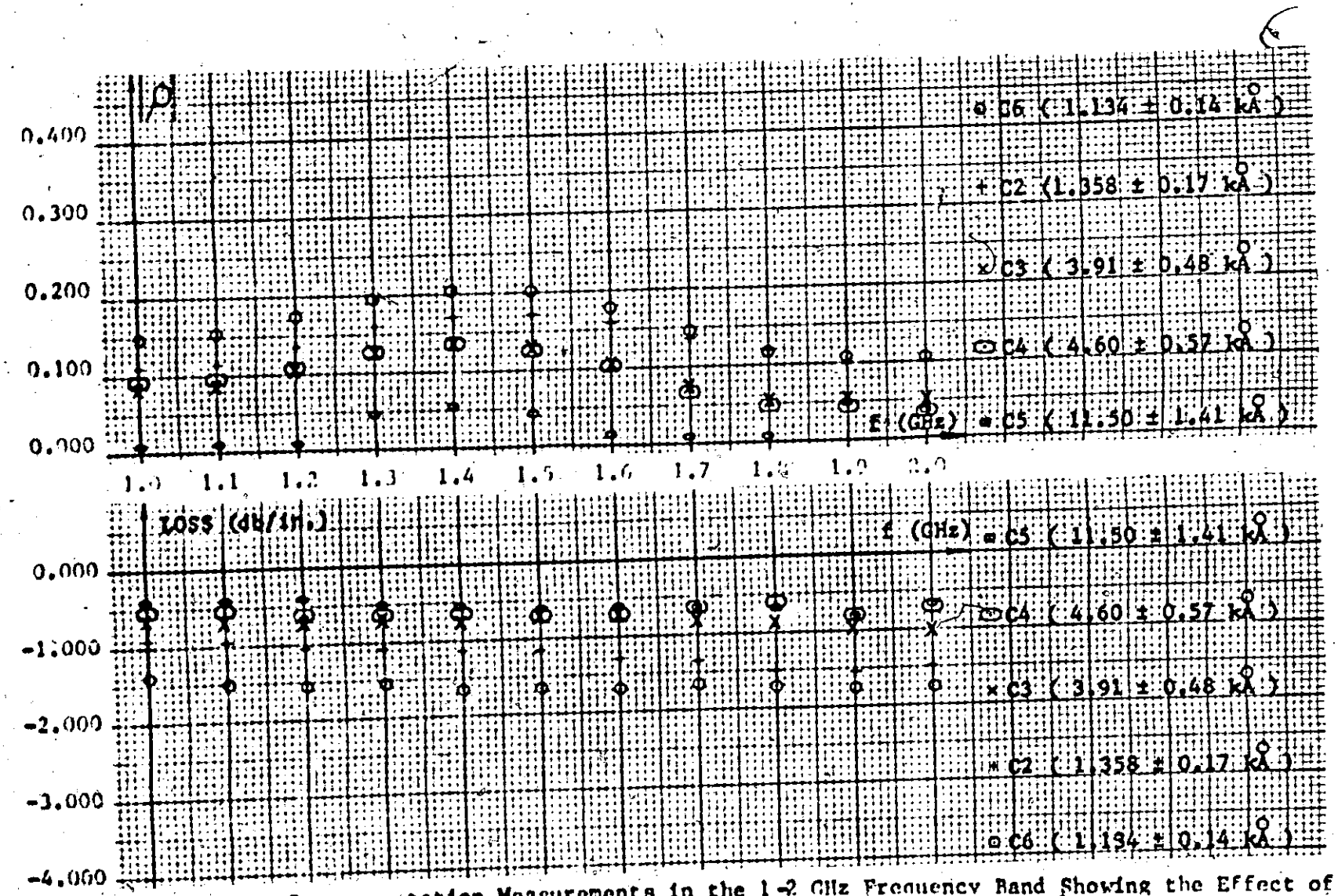

Figure D.2: Singer Instrumentation Measurements in the 1-2 GHz Frequency Band Showing the Effect of Thin Film Thickness (kÅ) on Transmission Loss and the Modulus of the Net Reflection Coefficient ρ for Various CPW Samples of Series C.

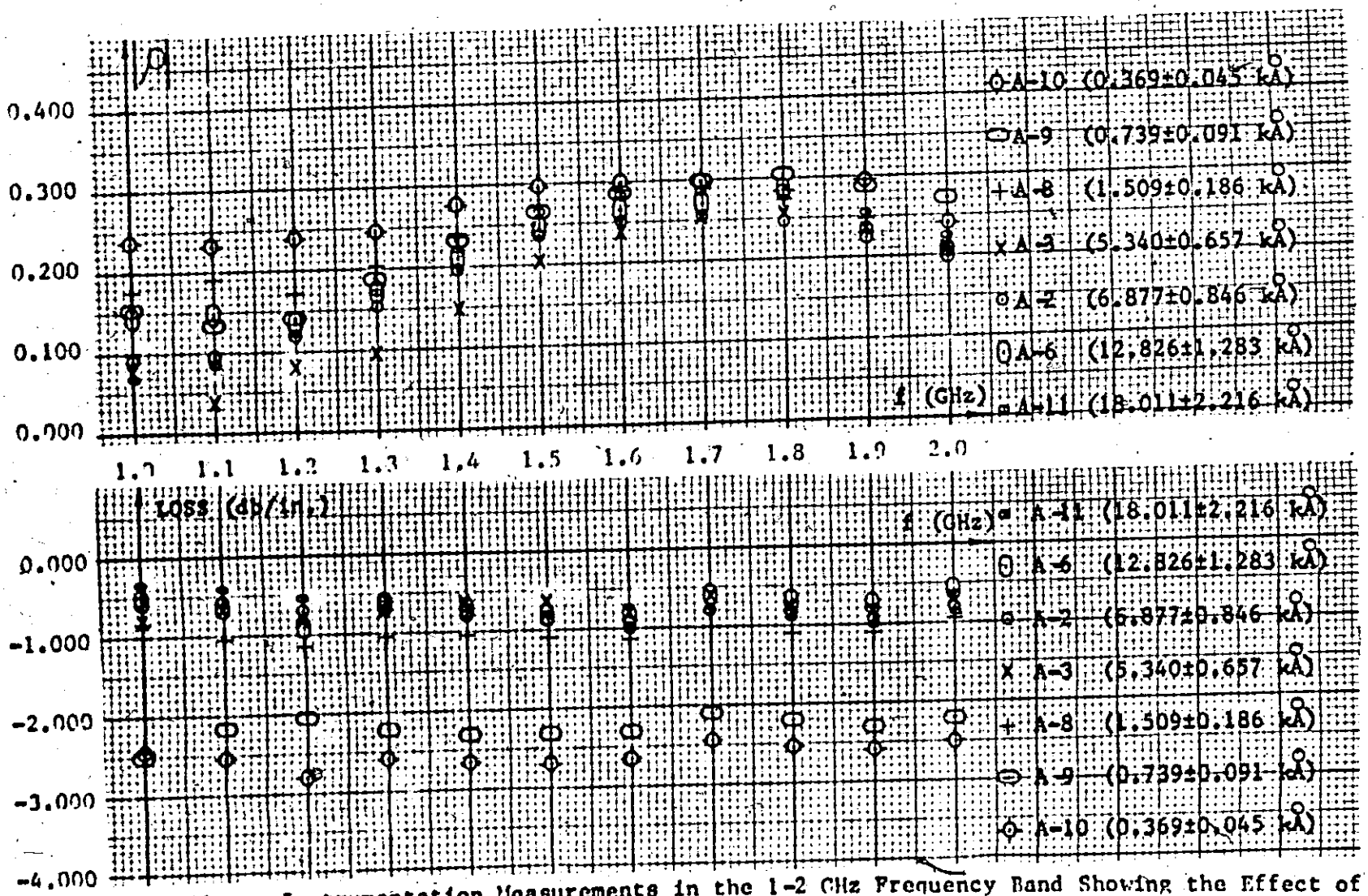

Figure D.3: Singer Instrumentation Measurements in the 1-2 GHz Frequency Band Showing the Effect of Thin Film Thickness (kÅ) on Transmission Loss and the Modulus of the Net Reflection Coefficient ρ for Various CPW Samples of Series A-.

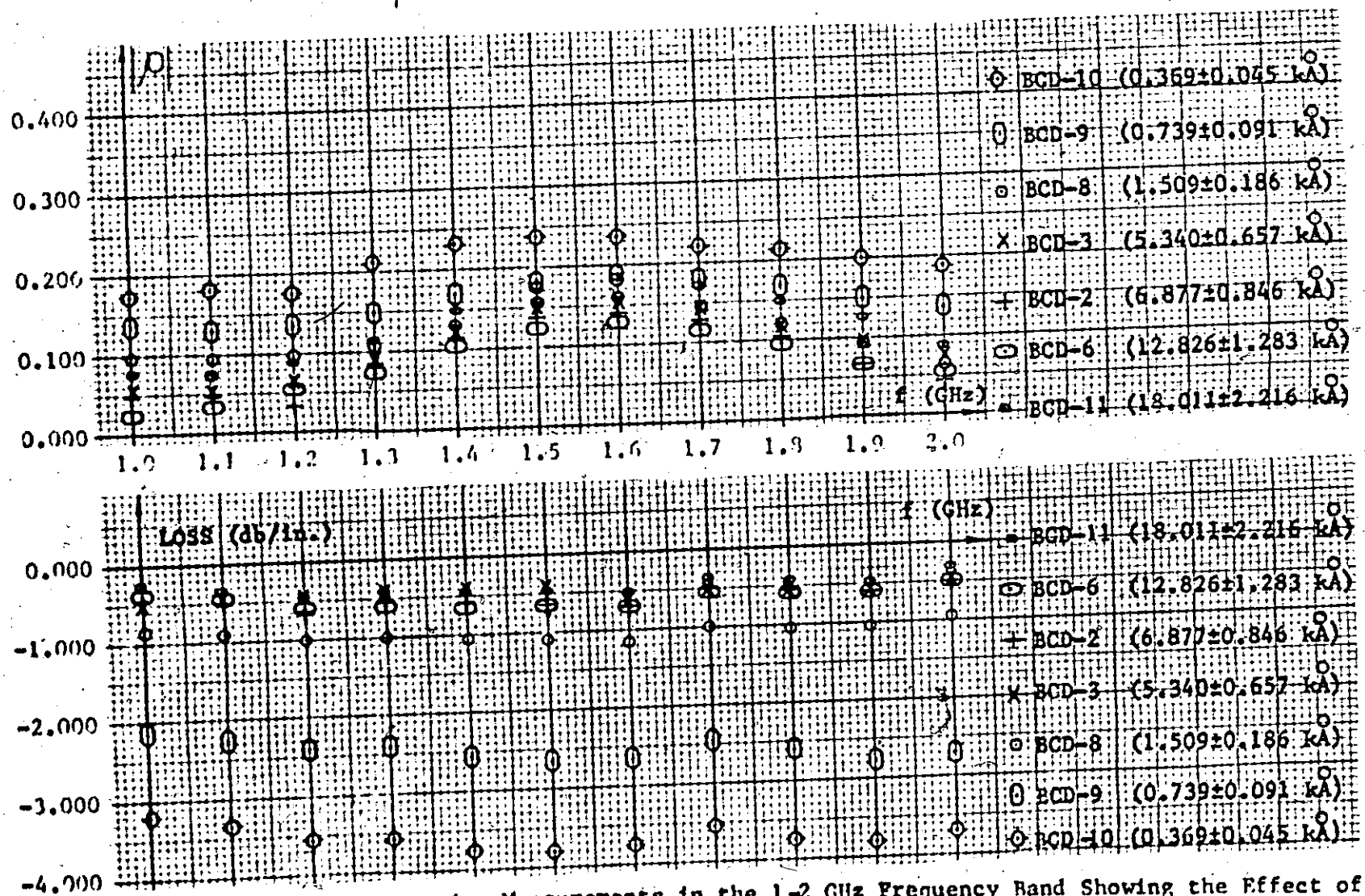

Figure D.4: Singer Instrumentation Measurements in the 1-2 GHz Frequency Band Showing the Effect of Thin Film Thickness (kÅ) on Transmission Loss and the Modulus of the Net Reflection Coefficient ρ for Various CPW Samples of Series BCD-.

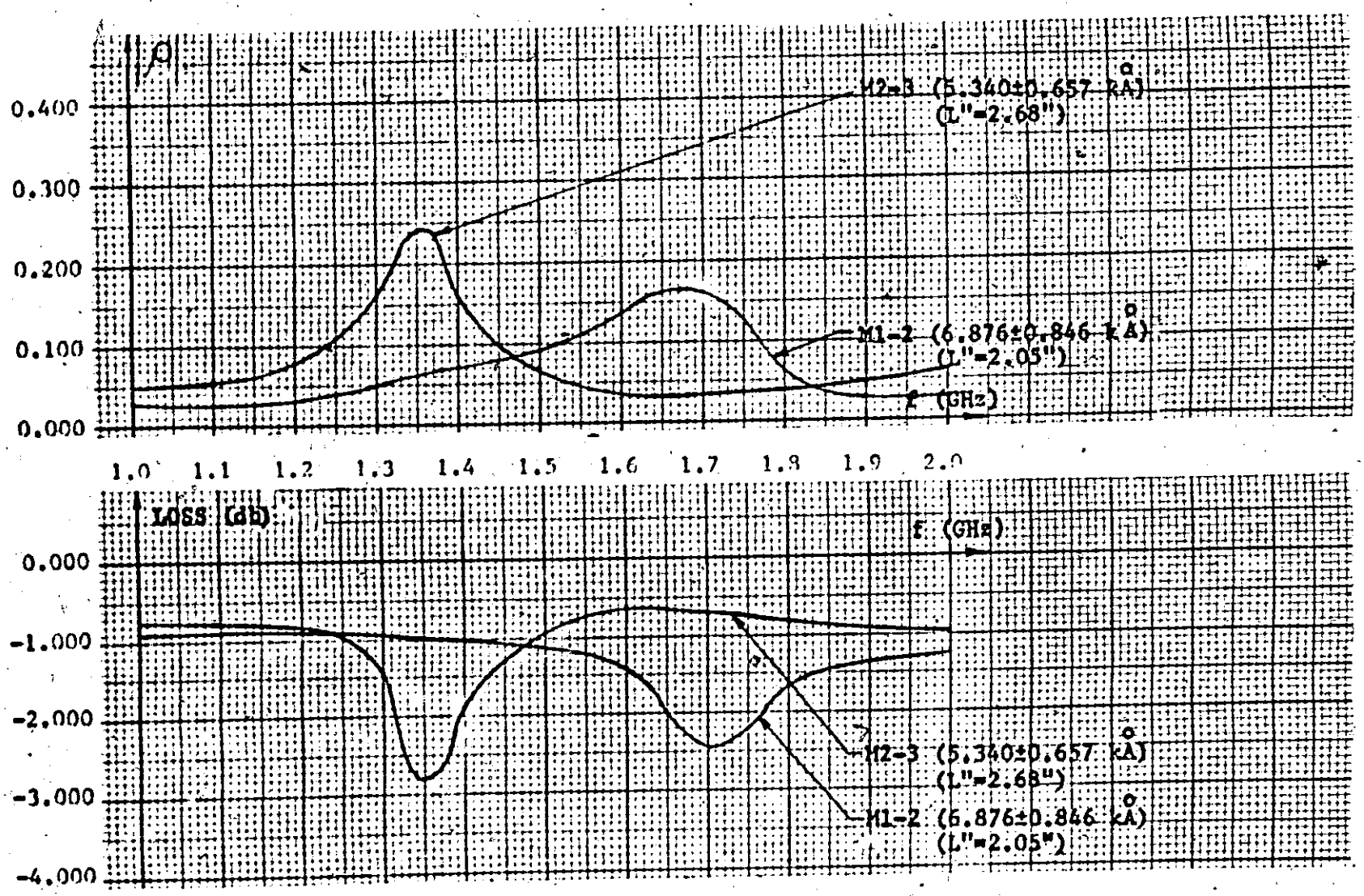

Figure D.5: Singer Instrumentation Measurements in the 1-2 GHz Frequency Band Showing the Effect of Thin Film Thickness (kÅ) on Transmission Loss and the Modulus of the Net Reflection Coefficient ρ for Two Meandered CPW Samples M1-2 and M2-3.

APPENDIX E

ACCOUNTING FOR INPUT AND OUTPUT REFLECTIONS IN A LOSSY MISMATCHED CPW

E.0 Introduction

The Singer Instrumentation of section 4.1 and the HP 8545A automatic network analyzer of section 4.2 did not directly measure the input and output reflection coefficients of each CPW sample; ρ_i and ρ_o respectively. Instead, the modulus of the net reflection coefficient ρ of each CPW sample was measured in the frequency band of interest by this equipment. Furthermore, the total phase ϕ could not be measured by the Singer instrumentation. A polar plot of ρ from the 8545A gave both the phase and magnitude of ρ with respect to an imaginary calibrated reference plane in the frequency band of interest. In section 4.1 a theory was developed for the interpretation of these measurements in terms of Z_{LC}, ρ_i, ρ_o and the attenuation in each CPW sample.

Equation (4.1-8) allowed $|\rho|/|\rho_i|$ to be easily calculated as a function of frequency with α' (N_p/in) as parameter. Similarly, (4.1-9) allowed $(\phi-\phi_i)$ to be calculated in the frequency band of interest with α' (N_p/in) as parameter. Figures E.1 to E.7 represent the results of these calculations graphically for various sample lengths L", and various relative dielectric constants ϵ_r.

Figures E.1, E.2, and E.3 are for 1" long CPW samples of various ϵ_r values. The ϵ_r value of 9.2 is a nominal value specified by the manufacturer whereas the values 6.660 and 5.921 are average values measured via TDR techniques for series BCD- and A- respectively. These values are lower because of the finite substrate thickness used for these samples.

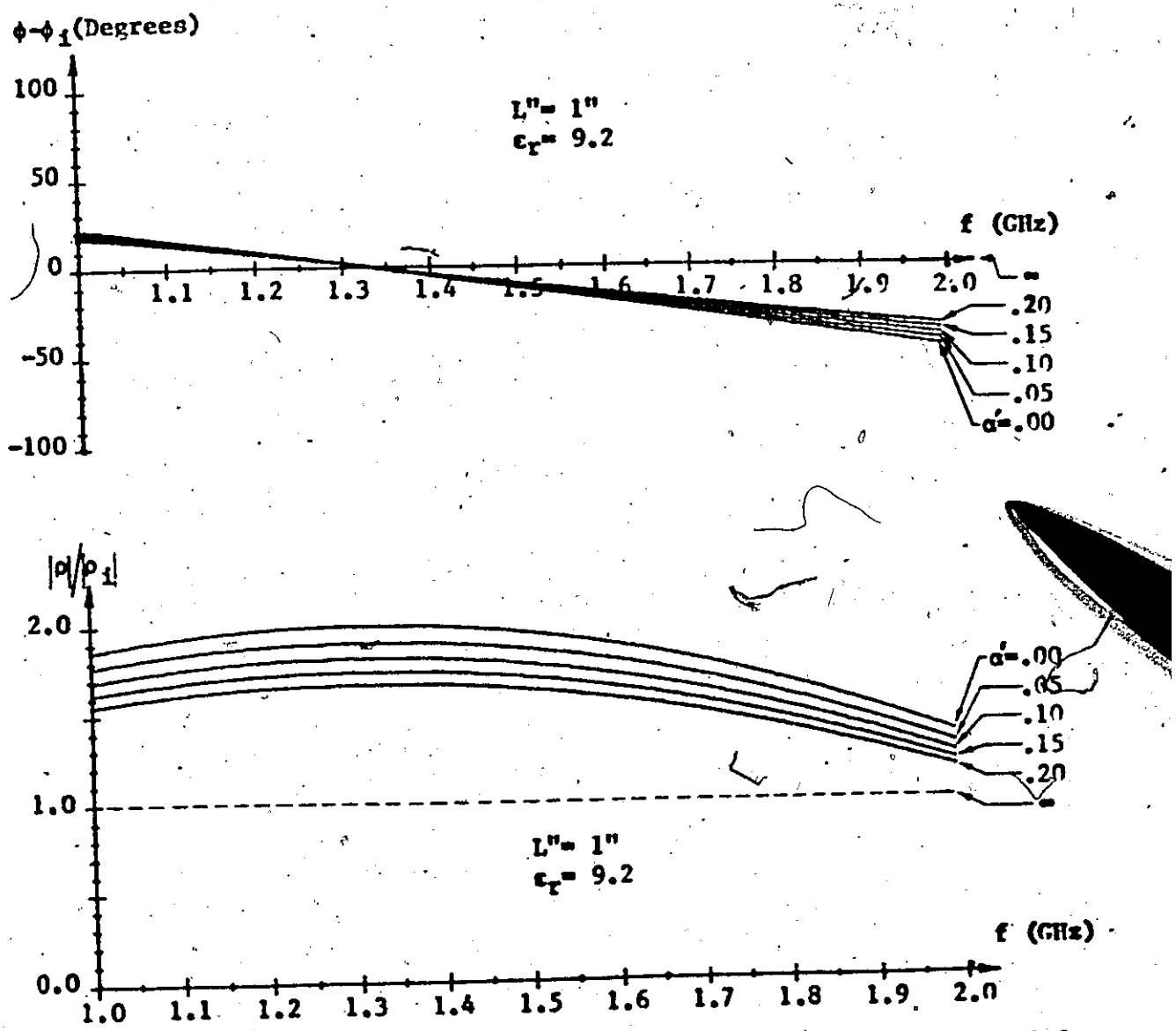

Figure E.1: Theoretical Frequency Response of the Ratio ρ/ρ_i in the 1-2 GHz Band with α' (Np/in) as Parameter, where ϵ_r= 9.2 and the CPW is 1" Long.

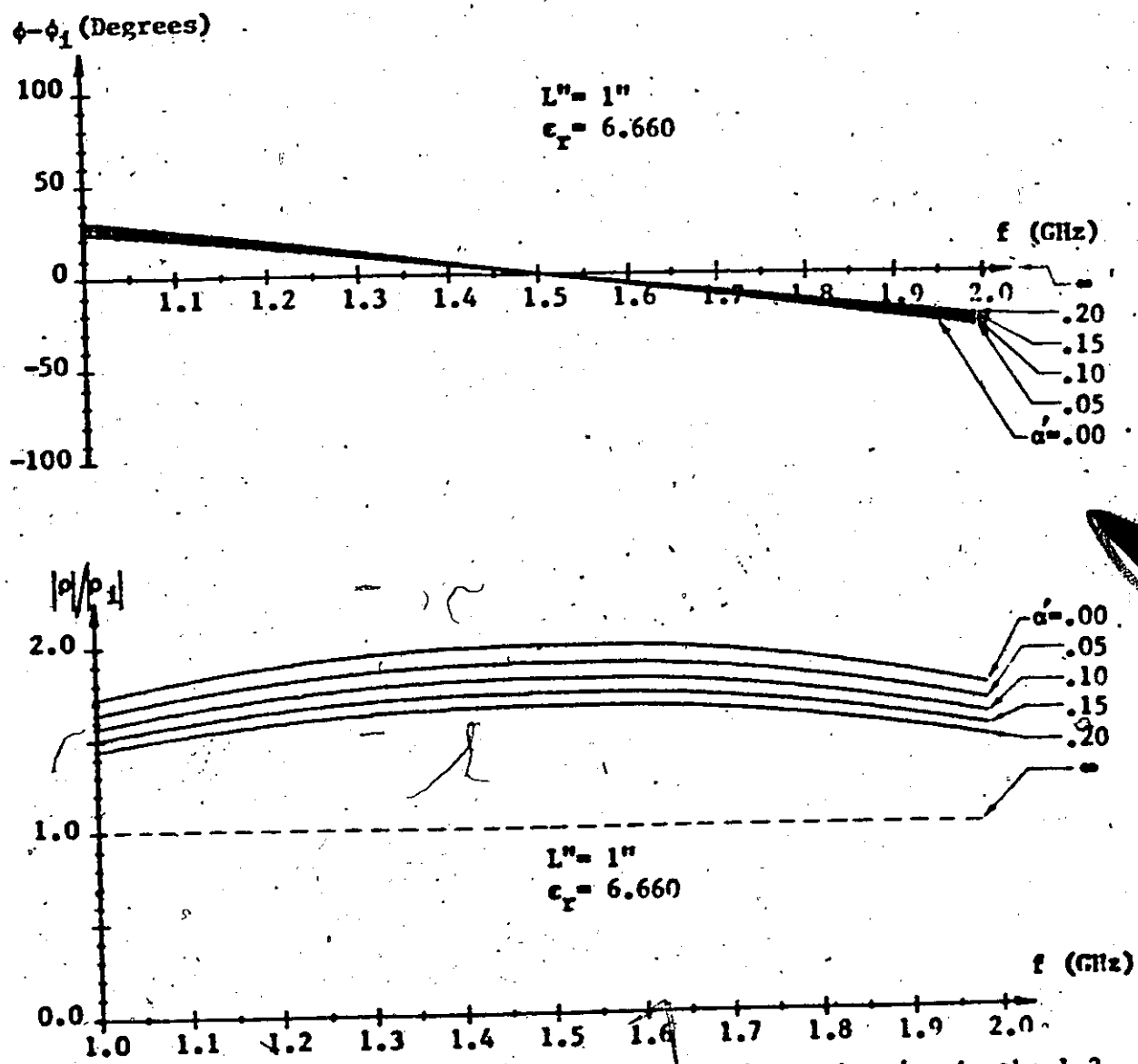

Figure E.2: Theoretical Frequency Response of the Ratio ρ/ρ_1 in the 1-2 GHz Band with α' (Np/in) as Parameter, where ϵ_r= 6.660 and the CPW is 1" Long.

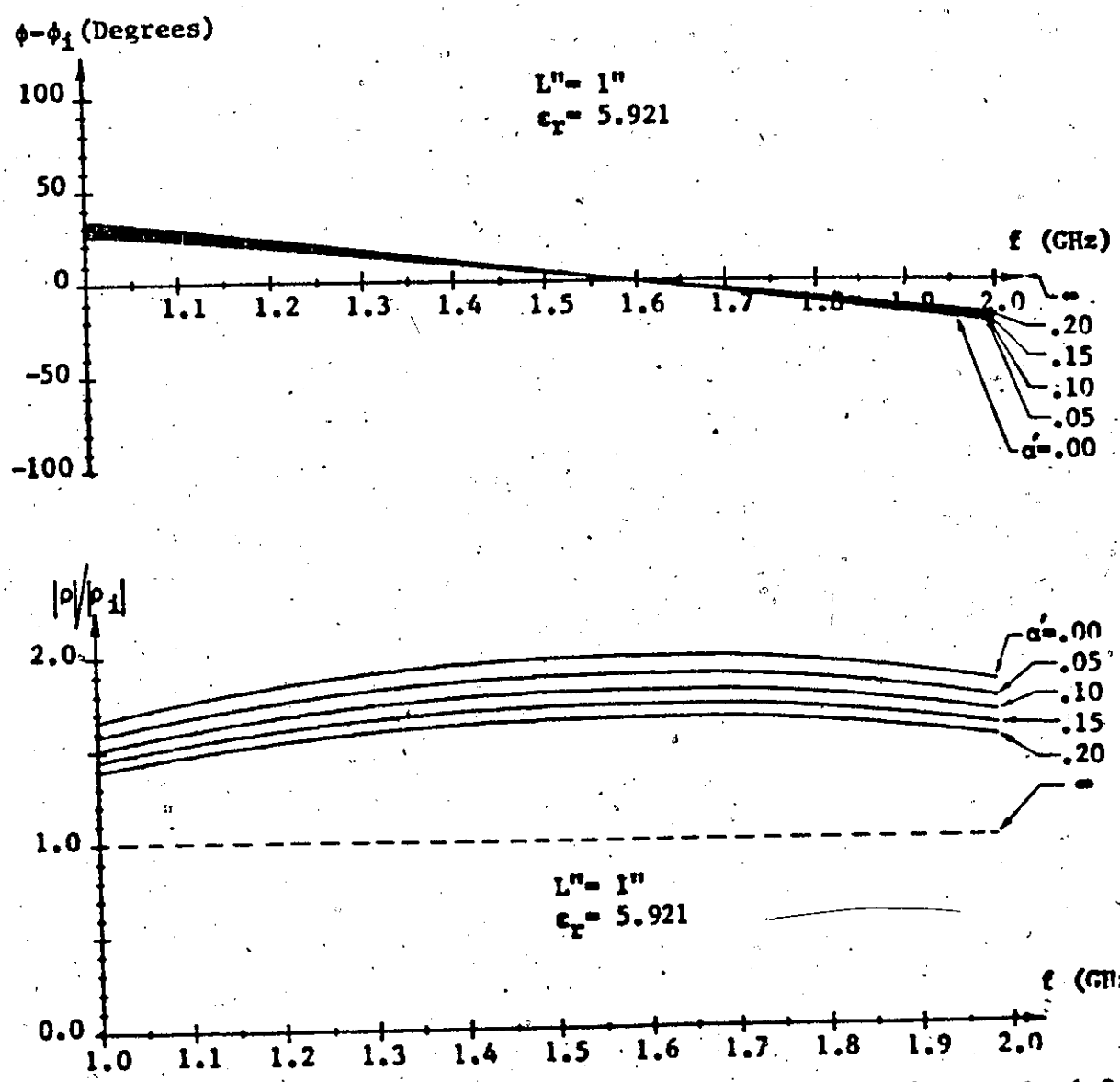

Figure E.3: Theoretical Frequency Response of the Ratio ρ/ρ_i in the 1-2 GHz Band with α' (Np/in) as Parameter, where ϵ_r=5.921 and the CPW is 1" Long.

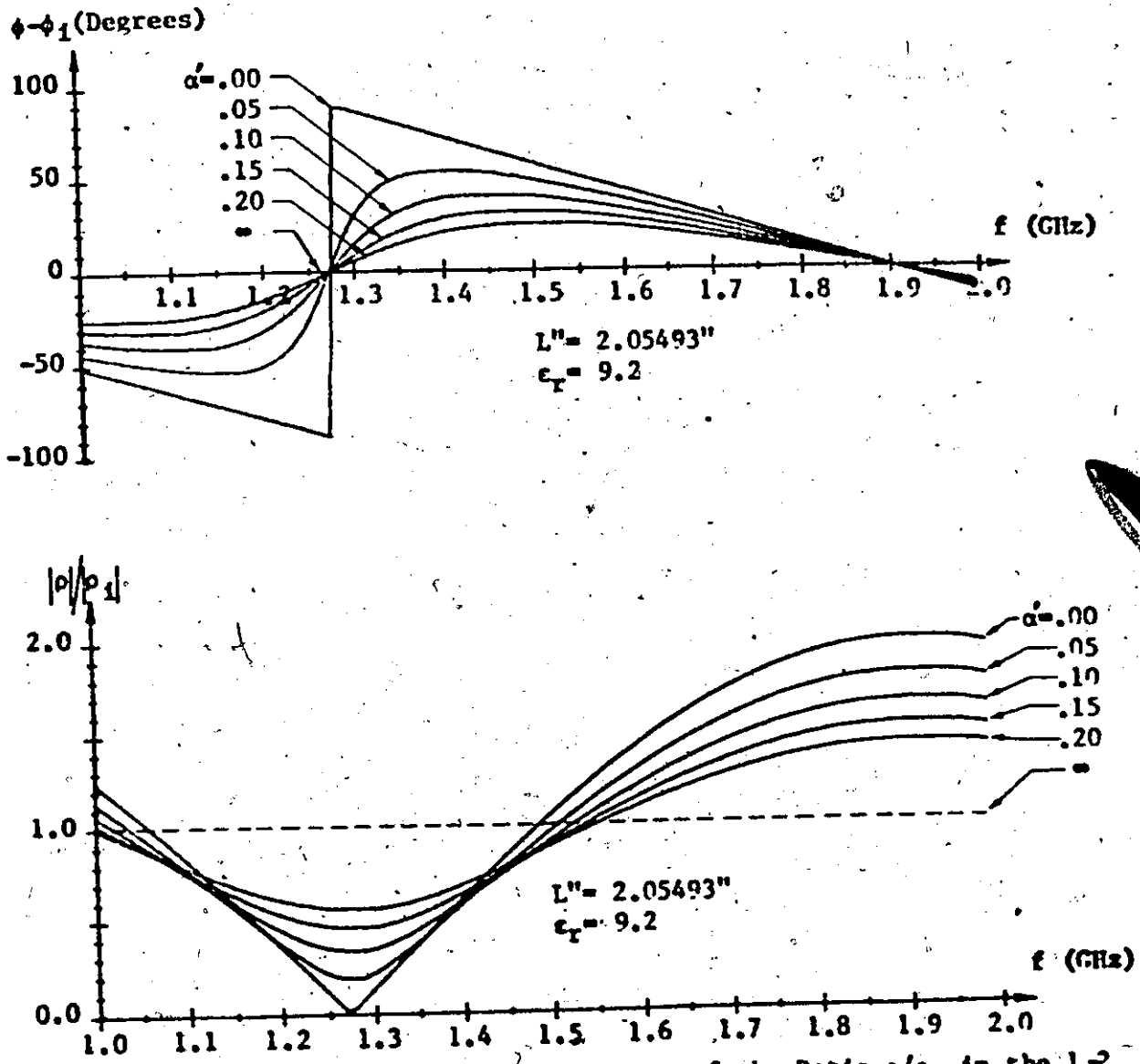

Figure E.4: Theoretical Frequency Response of the Ratio ρ/ρ_1 in the 1-2 GHz Band with α' (Np/in) as Parameter, where ϵ_r= 9.2 and the CPW is 2.05493" Long.

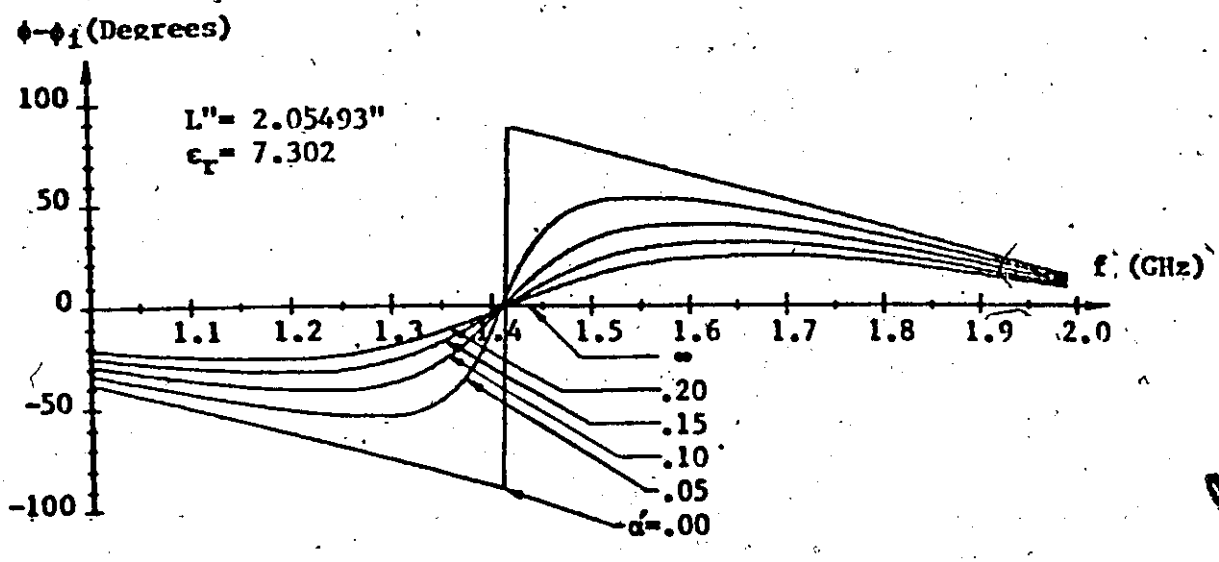

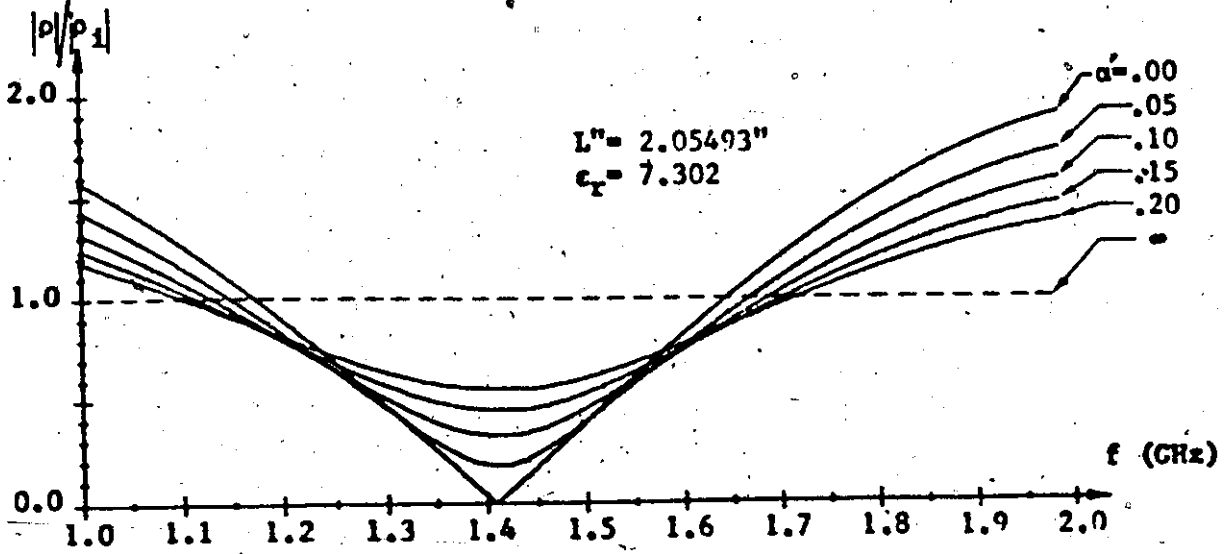

Figure E.5: Theoretical Frequency Response of the Ratio ρ/ρ_i in the 1-2 GHz Band with α' (Np/in) as Parameter, where ϵ_r= 7.302 and the CPW is 2.05493" Long.

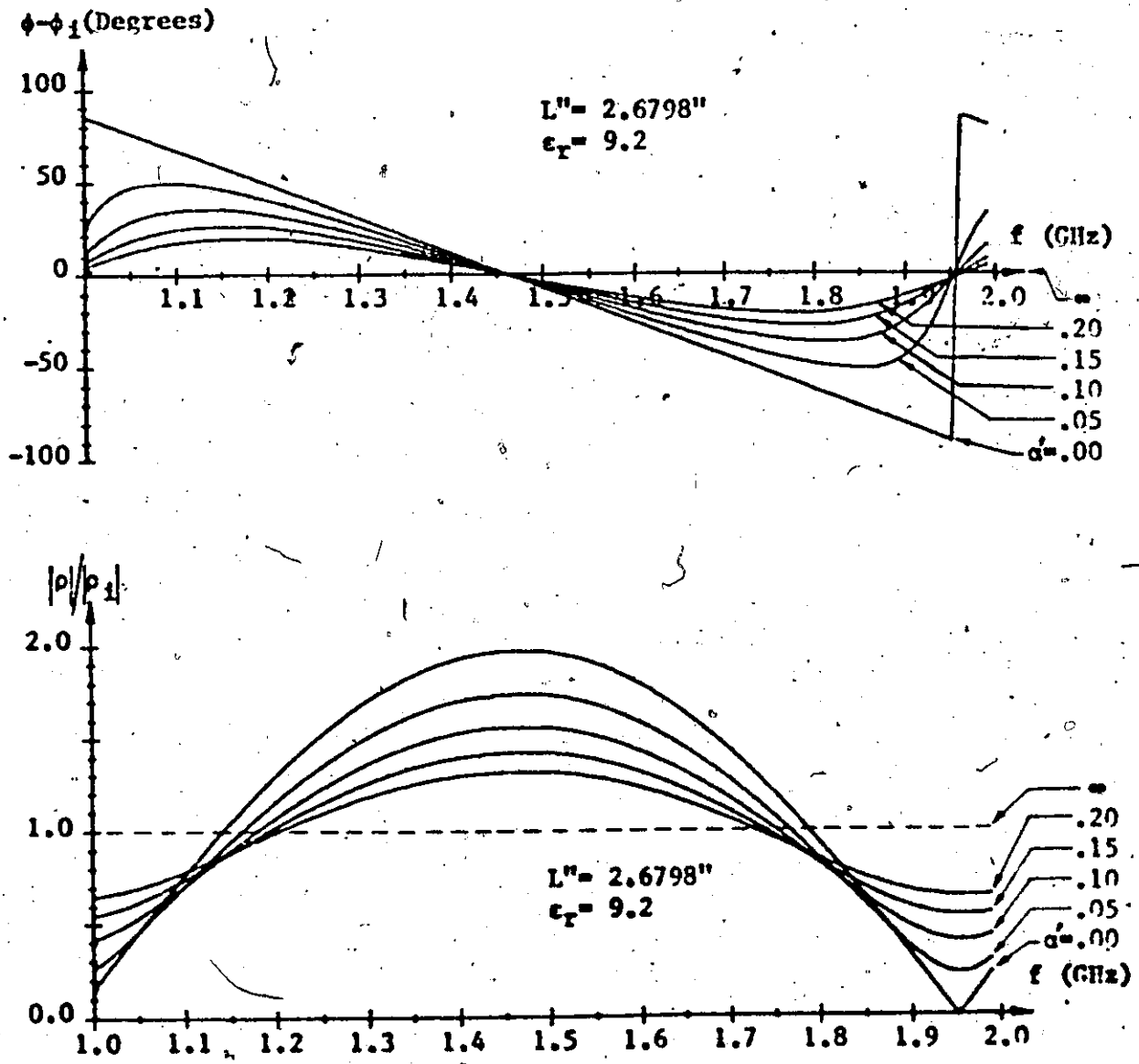

Figure E.6: Theoretical Frequency Response of the Ratio ρ/ρ_1 in the 1-2 GHz Band with α' (Np/in) as Parameter, where ϵ_r= 9.2 and the CPW is 2.6798" Long.

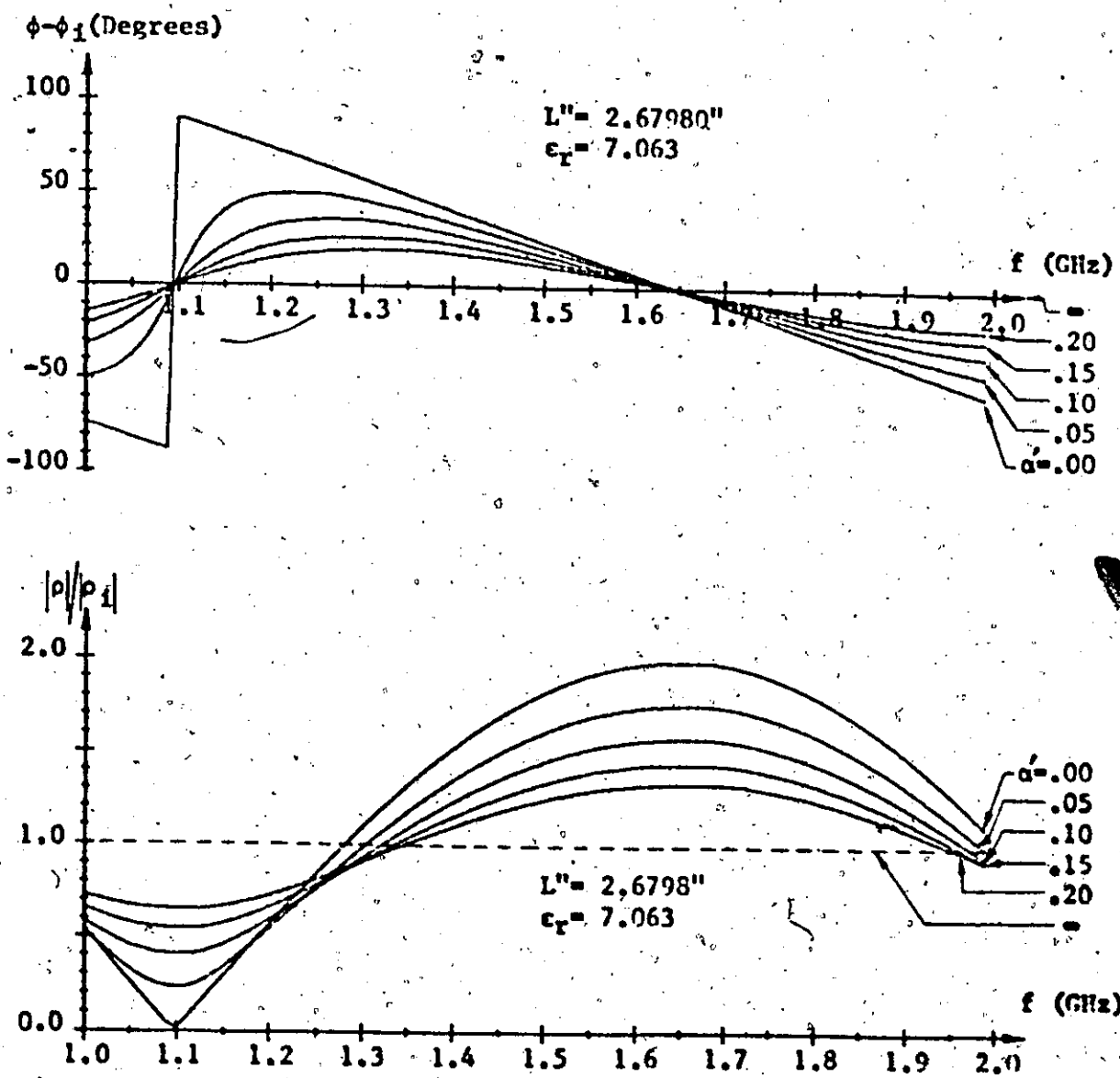

Figure E.7: Theoretical Frequency Response of the Ratio ρ/ρ_i in the 1-2 GHz Band with α' (Np/in) as Parameter, where ϵ_r= 7.063 and the CPW is 2.6798" Long.

Figures E.4 and E.5 are for comparison with meandered sample M1-2 since the same line length has been used in the calculation and the sample. Figure E.4 uses the nominal value of ϵ_r and Figure E.5 uses the TDR measured value of 7.302.

Figures E.6 and E.7 are for comparison with meandered sample M2-3 since the same line length has been used in the calculation and the M2-3 sample. Figure E.6 uses the nominal value of ϵ_r and Figure E.7 uses the TDR measured value of 7.063.

Figures E.8 to E.11 each represent plots of ρ_1 in the frequency band of interest for fixed values of α' with Z_{LC} as parameter. These plots were derived from equations (4.1-13) (4.1-15) and (4.1-16) of section 4.1 in Chapter IV. In these calculations the capacitance per unit length C was kept constant at the nominal design value of 150.66 pf/m. According to (2.1-12) and (2.1-2), maintaining a constant value of C and increasing Z_{LC} is equivalent to increasing ϵ_r since Z_{LC} then varies directly with $(\epsilon_r+1)^{\frac{1}{2}}$.

The relationship of thin film thickness t_f in kÅ to attenuation α' Np/m and R Ω/m is given in Table E.0-1. This will enable the results of the reflection theory from Chapter IV to be compared to the measured $|\rho|$ values in Appendix D for different thin film thicknesses. The value of t_f in Table E.0-1 has been scaled appropriately to account for the average aluminum thin film resistivity measured from the series A- and ECD- samples. This measurement is described in section 5.1.3, Chapter V. The average measured resistivity was found to be 2.68 times larger than

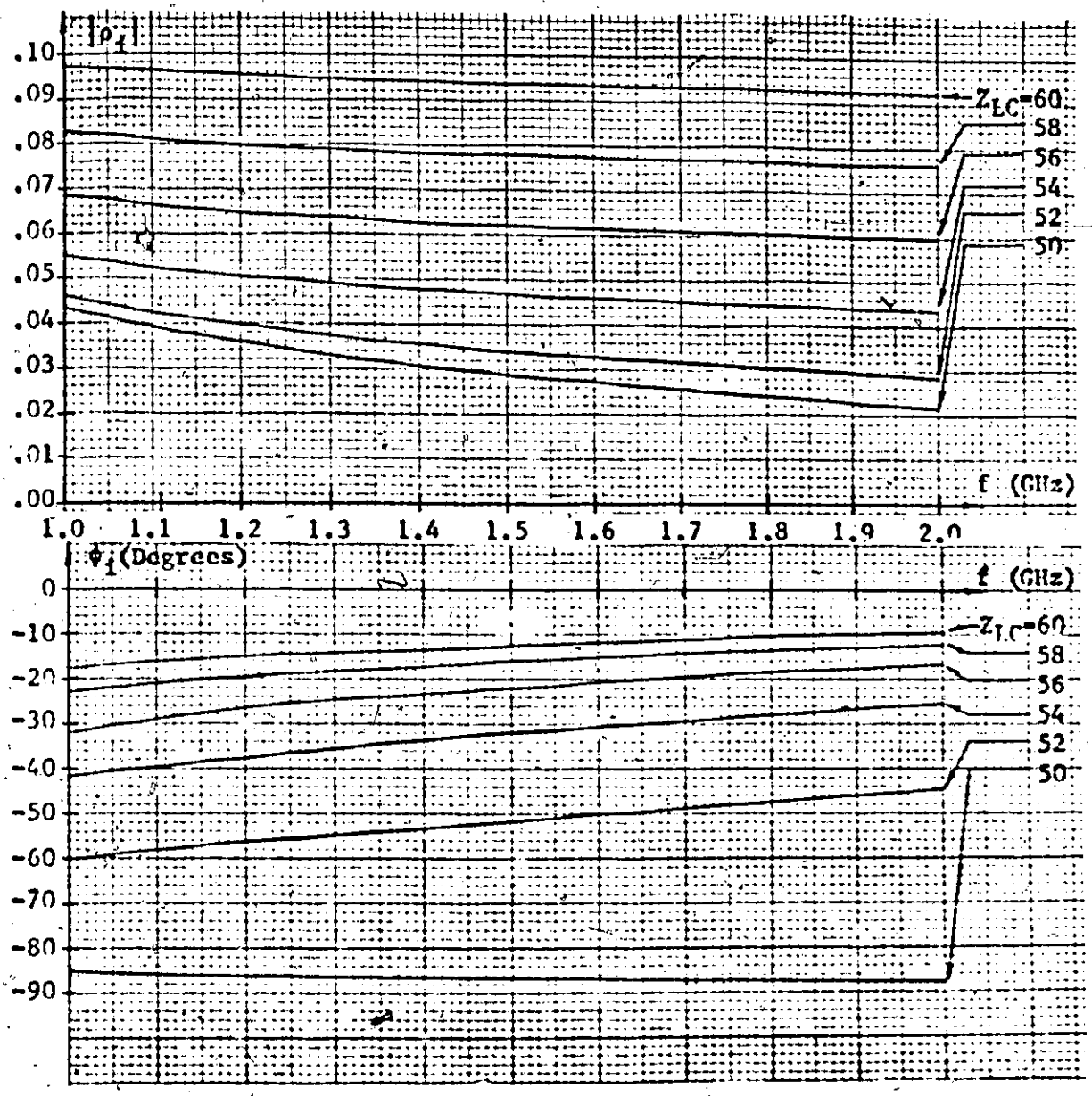

Figure E.8: Theoretical Frequency Response of the Input Reflection Coefficient ρ_i in the 1-2 GHz Band with Z_{LC} as Parameter where R=412 Ω/m and α'= .1047 Np/in.

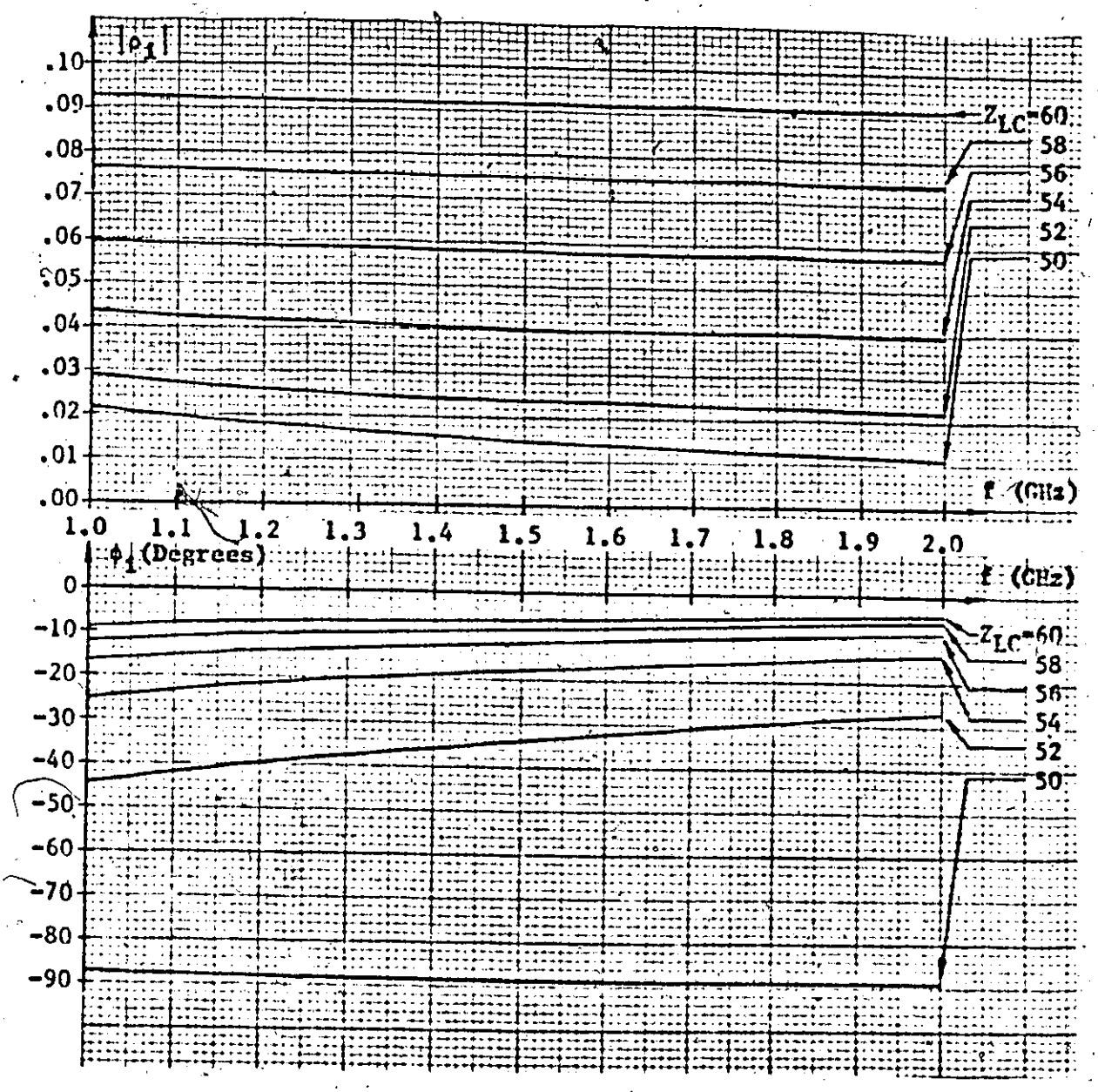

Figure E.9: Theoretical Frequency Response of the Input Reflection Coefficient ρ_1 in the 1-2 GHz Band with Z_{LC} as Parameter where R=206 Ω/n and α' = .0523 Np/in.

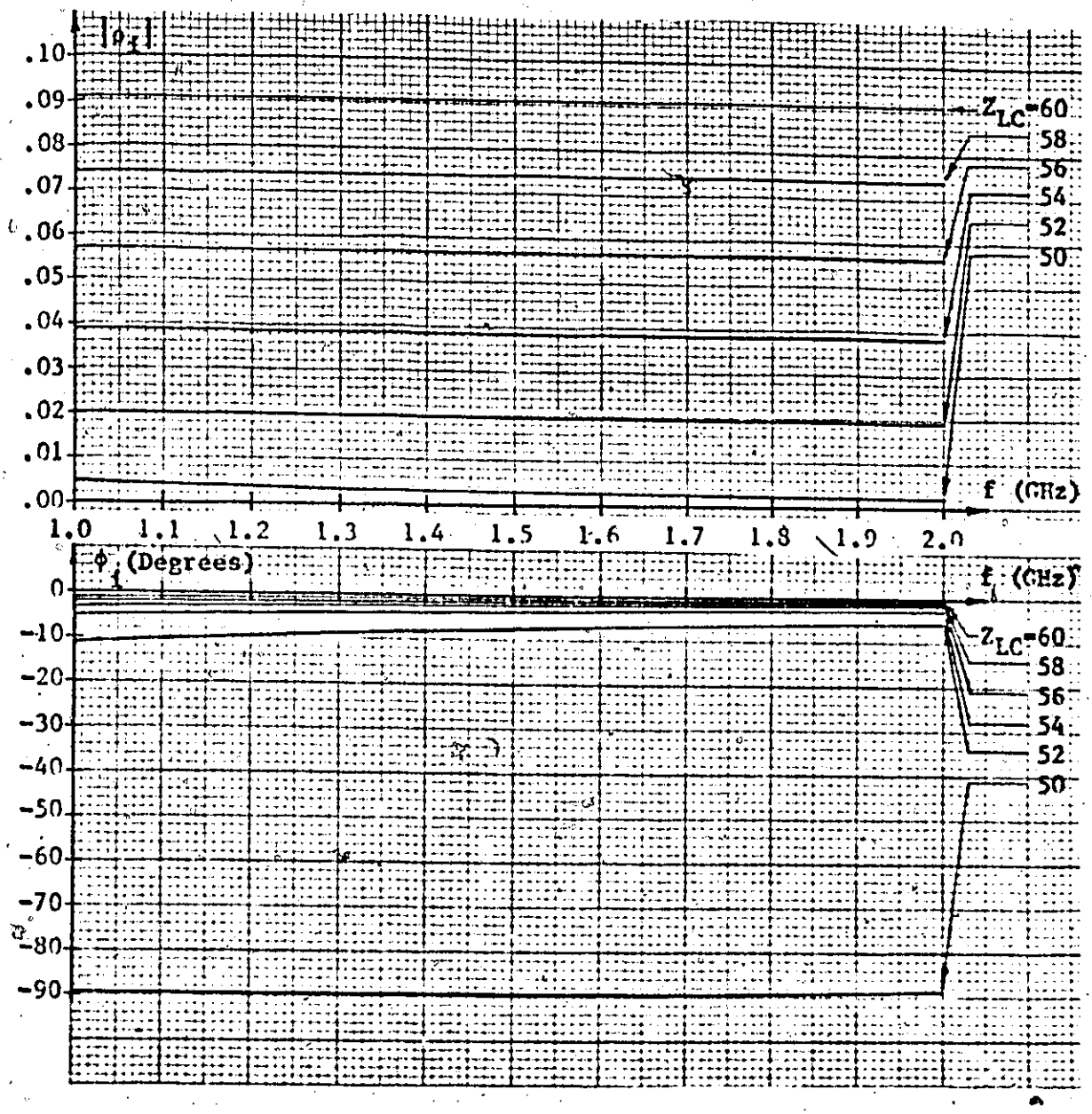

Figure E.10: Theoretical Frequency Response of the Input Reflection Coefficient ρ_i in the 1-2 GHz Band with Z_{LC} as Parameter where R= 41.2 Ω/n and α'= .01047 Np/in.

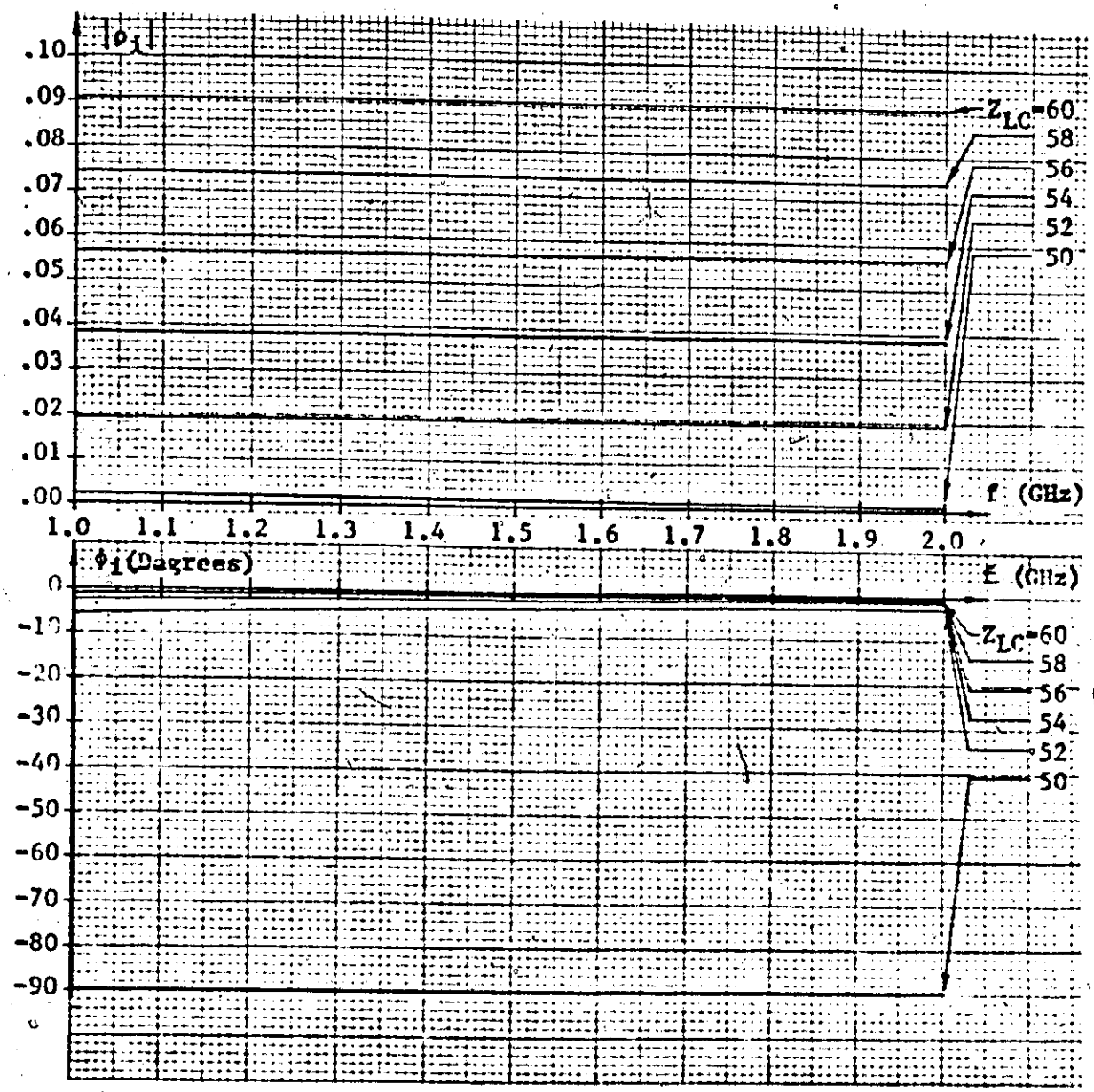

Figure E.11: Theoretical Frequency Response of the Input Reflection Coefficient ρ_i in the 1-2 GHz Band with Z_{LC} as Parameter where R=20.6 Ω/n and α'= .00523 Np/in.

R	α'	t_f (Å)	
(Ω/n)	(Np/in)	50 Mil Wide Center Strip	100 Mil Wide Center Strip
412	.1047	1.34	0.67
206	.0523	2.68	1.34
41.2	.01047	13.4	6.7
20.6	.00523	26.8	13.4

Table E.0-1 : Relationship of R and α' to t_f in CPW's having 50 mil and 100 mil Center Strip Widths, Assuming the Losses in the Ground Planes to be Negligeable and Using the Average Measured Thin Film Resistivity of 2.68 x (2.62×10^{-6}) Ω-cm for Aluminum at 20 °C.

the bulk value of 2.62×10^{-6} Ω-cm at 20° C.

E.1 Resonance In Mismatched CPW Samples

A $|\rho|/|\rho_i|$ plot in the frequency band of interest, and not $|\rho_i|$, determines the basic shape of the $|\rho|$ vs frequency plots since ρ/ρ_i describes the resonance phenomena associated with input and output reflections, and ρ_i is in comparison much less frequency dependent. A general mathematical description of ρ/ρ_i as a function of frequency

is given in section 4.1 of Chapter IV where attenuation in each CPW is also taken into account. Herein, resonance will be described by simpler mathematical expressions which at the same time give physical insight into the problem of resonance.

The ideal linear phase of ρ/ρ_i is also distorted significantly at and near the resonance frequencies by small values of α'. This is apparent from Figures E.4, E.5, E.6, and E.7 at frequencies where $\phi-\phi_i$ makes an immediate transition from -90^o to $+90^o$. The shorter 1" long CPW samples do not exhibit resonance in the 1-2 GHz band of frequencies because these samples are too short. As a result, Figures E.1, E.2, and E.3 do not show severe phase distortion for various values of α'. The first resonance frequency for the 1" samples occurs above 2 GHz.

For a simple physical explanation of this phenomena one only has to realize that resonance between input and output reflections of a mismatched CPW can occur only when the total phase difference between input and output reflections is an odd multiple of π radians. This means that $2\theta = $ equals $(2n+1) \cdot \pi$ where θ is the electrical length of the mismatched CPW and n is any positive integer including zero. Hence resonance occurs when the length of a mismatched CPW

$$L' = (n+1) \cdot \frac{\lambda}{2} \qquad n=0,1,2,... \qquad (E.1-1)$$

where λ represents one wavelength at a given frequency f_o. In other words, resonance occurs when the length L' is a multiple of half wave-

lengths at f_o. A similar argument applies to the reinforcement of input and output reflections. When $2\theta - \pi$ equals $2n\pi$, reinforcement of these reflections should occur. This is equivalent to saying that when the length of a mismatched CPW is

$$L' = (2n + 1) \cdot \frac{\lambda}{4} \qquad n=0,1,2,... \qquad (F.1\text{-}2)$$

reinforcement of input and output reflections will occur: ie when the length of the CPW is an odd multiple of quarter wavelengths at a given reinforcement frequency f_o'.

Figures F.1 to F.7 show that as ϵ_r is decreased for a fixed length of coplanar line L', resonance or reinforcement frequencies take on higher values. This is easily explained from (F.1-1) and (F.1-2) since these equations imply that for a fixed length L', resonance and reinforcement are determined by a specific choice of n and λ. The wavelength λ is in turn inversely proportional to frequency f and also inversely proportional to $(\epsilon_r + 1)^{\frac{1}{2}}$. Hence, as ϵ_r decreases, f_o and f_o' must increase to maintain the specific value of λ required by a fixed length of coplanar line. For $\epsilon_r = 9.2$ at 1.5 GHz the CPW wavelength has been calculated to be 3.4867". At 2.0 GHz with the same value of ϵ_r the CPW wavelength is 2.615". These wavelengths ensure that 1" CPW samples will not exhibit resonance in the 1-2 GHz range since 1" is less that $\lambda/2$ across the entire 1-2 GHz band. If ϵ_r decreases because of a finite substrate thickness, the resonance frequency moves to an even higher value, again ensuring that 1" mismatched CPW samples

will not have resonance frequencies in the 1-2 GHz Band. They do however exhibit the first reinforcement effect at some specific frequency f_o' in this band. For this case n=o.

E.2 Effect of Thin Film Thickness on Input and Output Reflections

As mentioned briefly in Section E.1, the ρ_1 plots show only a slight frequency dependence. In fact, this only becomes noticable for very thin films which correspond approximately to $a' > .01047$ Np/in and for values of Z_{LC} close to 50 Ω. Figures E.8 and E.9 apply to such thin films. As the films are allowed to become thinner, the functional dependence of $|\rho_1|$ on $1/t_f$ $(\text{kÅ})^{-1}$ at any specific frequency with Z_{LC} as parameter becomes more and more significant. For example, at 1.0 GHz, with Z_{LC} = 50 Ω and $2a_1$ = 50 mils, $|\rho_1|$ increases linearly as a function of $1/t_f$ from .0043 to .043 if t_f is reduced from 13.4 kÅ to 1.34 kÅ. For values of Z_{LC} > 50 Ω the increase of $|\rho_1|$ with decreasing film thickness is less severe and becomes a nonlinear function of $1/t_f$. In fact, for thicker films $1/t_f$ approaches a very small value and $|\rho_1|$ approaches the lossless case value. This is due to the mismatch of the CPW with respect to a 50 Ω line becoming more dependent on the distributed L and C properties of the CPW as thin film thickness increases rather than on the distributed R value.

Figures E.8 and E.9 also show that ρ_1 has a significant phase ϕ_1 when $a' > .01047$ Np/in. This phase has a slight functional dependence on frequency in the 1-2 GHz range and this functional dependence is practically a linear one. Hence the total phase ϕ will be changed in

magnitude by ϕ_i in the 1-2 GHz band but in a linear sense and ϕ_i will not cause significant phase distortion; even for very thin films. Most of the phase distortion will come from the ϕ-ϕ_i characteristic previously described. It was shown to be strongly dependent on α' in the neighbourhood of the resonance frequency f_o.

In comparison, Figures E.10 and E.11 exhibit the behavior of ρ_i in the 1-2 GHz band for α' = .01047 Np/in and α' = .00523 Np/in respectively. For α' = .01047 Np/in $|\rho_i|$ shows only a very small frequency dependence and ϕ_i is very small. In Figure E.11, where α' = .00523 Np/in, the dependence of ρ_i on frequency is barely detectable. Figure E.11 applies to a 50 mil wide center strip of 26.8 $k\mathring{A}$ thickness or a 100 mil wide center strip half as thick as shown in Table E.1. The film thickness of 26.8 $k\mathring{A}$ is approximately equal to one skin depth at 1.0 GHz for bulk aluminum if a resistivity of 2.62×10^{-6} $k\mathring{A}$ Ω - cm is used in the skin depth calculation; see Figure 2.4-1.

All of the discussion for ρ_i above applies to ρ_o at the output of each CPW as well since ρ_i and ρ_o are equal in magnitude and differ in phase by only the constant π radians. One should also note that the theory of section 4.1 in Chapter IV neglected the effect of contact resistance. The curves in this appendix also neglect this effect which intuitively should increase the modulus of ρ_i and alter its phase as well. The theoretical aspect of contact resistance with regard to its effect on the total reflection coefficient ρ and on phase distortion has not been studied in this thesis, though an average empirical value for contact loss has been extracted from the loss measurements

in section 5.1 of Chapter V. In section 5.2 of the same chapter, TDR measurements on CPW samples terminated with S/C loads are discussed. These indicated a significant contact resistance with the d.c resistance of each sample added to it. Though contact resistance was detectable by these two measuring instruments, the foregoing theory for ρ/ρ_i and ρ_1, neglecting contact resistance, proved to be quite valid empirically.

REFERENCES

1. E. G. Cristal, A. F. Podel, D. Parker, "Microguide: A New Microwave Integrated Circuit Transmission Line," 1972 IEEE-GMTT International Microwave Symposium, IEEE Cat. No. 72 CHO 612-2-MTT, May 22-24, 1972.

2. M. Caulton, P. Sobel, "Microwave Integrated-Circuit Technology -A Survey" IEEE Journal of Solid-State Circuits, Vol. SC-5, No. 6, Dec. 1970.

3. M. Caulton, "Film Technology in Microwave Integrated Circuits" Proceedings of the IEEE, Vol. 59, No. 10, October 1971.

4. F. E. Meister, "An Evaluation of Materials and Processes for Integrated Microwave Circuits," IEEE Transactions on Microwave Theory and Techniques, Vol. MTT-14, No. 7, July 1966.

5. Cheng P. Wen, "Coplanar Waveguide: A Surface Strip Transmission Line Suitable for Nonreciprocal Gyromagnetic Device Applications," IEEE Transactions on Microwave Theory and Techniques, Vol. MTT-17, No. 12, pp.1087-1090, Dec. 1969.

6. M. A. Wheeler, "Transmission Line Properties of Parallel Wide Strips by a Conformal Mapping Approximation, IEEE Transactions on Microwave Theory and Techniques, Vol. MTT-12, pp. 280-289, May 1964.

7. H. A. Wheeler, "Transmission Line Properties of Parallel Strips Separated by a Dielectric Sheet," IEEE Trans. on Microwave Theory and Techniques, Vol. MTT-13, No.2, pp. 172-185, March 1965.

8. S. B. Cohn, "Thickness Corrections for Capacitive Obstacles and Strip Conductors," IEEE Transactions on Microwave Theory and Techniques, Vol. MTT-8, No. 6, pp. 638-644, November 1960.

9. R. A. Pucel, D. J. Masse, C. P. Hartwig, "Losses in Microstrip," IEEE Transactions on Microwave Theory and Techniques, Vol. MTT-16, No. 6, June 1968, pp 342-350

10. W. R. Smythe, "Two Dimensional Potential Distributions." Static and Dynamic Electricity, 3rd ed., New York: McGraw Hill, 1950.

11. E. Weber, "Two Dimensional Analytic Solutions," Electromagnetic Fields-Theory and Applications-Mapping of Fields, New York: John Wiley and Sons, Inc., Volume 1, 1950.

12. E. Jahnke, F. Emde, "Tables of Functions with Formulae and Curves," New York: Dover, 1945.

13. Jahnke-Emde-Losch, "Tables of Higher Functions," New York: McGraw-Hill, 1960.

14. H. Kober, "Higher Transcendental Functions," Dictionary of Conformal Representations, Dover Publications, Inc., 1957.

15. W. J. Troop and E. Peskin, "The Transfer Function and Sensitivity of a Network with n Variable Elements," IEEE Transactions on Circuit Theory, pp. 242-244, May 1969.

16. E. Kehel, "Sensitivity Relationships in Linear Networks and Some Observations on Hybrid Networks," IEEE Transactions on Circuit Theory, pp. 430-432, August 1970.

17. I. Shiraishva, T. Terra, and H. Ozaki, "Synthesis of Minimum-Sensitivity Networks Through Some Classes of Equivalent Transformations," IEEE Transactions on Circuit Theory, Vol. CT-17, No. 1, pp. 3-4, Feb. 1970.

18. R. De Buda, "About Sensitivity Invariants of Equivalent Networks," IEEE Transactions on Circuit Theory, pp. 248, May 1970.

19. G. F. Moschytz, "Second-Order Pole-Zero Pair Selection for nth-Order Minimum Sensitivity Networks," IEEE Transactions on Circuit Theory, Vol. CT-17, No. 4, pp. 527-534, Nov. 1970.

20. W. J. Kerwin, L. P. Huelsman, and R. W. Newcomb, "State-Variable Synthesis for Insensitive Integrated Circuit Transfer Functions," IEEE Journal of Solid-State Circuits, Vol. SC-2, No. 3, pp. 87, Sept. 1967.

21. E. Lueder, "Decomposition of a Transfer Function Minimizing Sensitivity," IEEE Transactions on Circuit Theory, pp. 426-427, Aug. 1970.

22. K. Hirano, I. Unami, and M. Hashimoto, "Sensitivity of Active Two-ports," IEEE Transactions on Circuit Theory, Vol. CT-16, No. 4, pp. 489-495, Nov. 1969.

23. K. E. Daggett, and J. Valach, "Sensitivity-Compensated Active Networks," IEEE Transactions on Circuit Theory, Vol. CT-16, No. 4, pp. 416-422, Nov. 1969.

24. A. G. J. Holt, and P. Tourron, "Sensitivity of Active RC Distributed Networks," IEEE Transactions on Circuit Theory, pp. 99-101, Feb. 1969.

25. G. W. Zobrist, "Signal-Flow Graphs as an Aid in the Design of Linear Circuits by Computer," Computer-Aided Integrated Circuit Design, Gerald J. Herskowitz, Ed., McGraw-Hill, 1968.

26. W. J. Butler, and S. S. Haykin, "Multiparameter Sensitivity Indexes of Performance for Linear Time-Invariant Networks," Proc. IEEE, Vol. 117, July 1970.

27. J. W. Bandler, and R. E. Seviora, "Computation of Sensitivities for Noncommensurate Networks," IEEE Transactions on Circuit Theory, Jan. 1971.

28. S. W. Director, and R. A. Rohrer, "The Generalized Adjoint Network and Network Sensitivities" IEEE Transactions on Circuit Theory, Vol. CT-16, No. 3, Aug. 1969.

29. S. R. Parker, "Sensitivity Analysis and Models of Nonlinear Circuits" IEEE Transactions on Circuit Theory, Vol. CT-16, No. 4, pp.440-447, Nov. 1969.

30. S. R. Parker, "Sensitivity: Old Questions, Some New Answers," IEEE Transactions on Circuit Theory, pp. 25-35, Vol. CT-18, No. 1, Jan. 1971.

31. D. A. Pierre, "Optimization Theory with Applications," John Wiley and Sons Inc., New York, London, Sydney, Toronto: 1969.

32. E. M. Butler, "Realistic Design Using Large Change Sensitivities and Performance Contours," IEEE Transactions on Circuit Theory, Jan. 1971.

33. J. W. Bandler, R. E. Seviora, M. Sallatash, "Least Pth and Minimax Objectives for Automated Network Design" Electronics Letters, Vol. 6, No. 1, 8th Jan. 1970.

34. J. W. Bandler, "Conditions for a Minimax Optimum," Allerton Conference, 1970.

35. J. W. Bandler, "Optimization Methods for Computer-Aided Design," IEEE Transactions on Microwave Theory and Techniques, Aug. 1969.

36. "ITT Reference Data for Radio Engineers", 5th ed., Howard W. SAMS and Co., Inc., 5th ed., 1969.

37. Smithell, "Metals Reference Book", Volume 2, Butterworths, London, 1962.

38. R. E. Collin, "Foundations For Microwave Engineering", McGraw Hill, Inc., pg. 224-226, 1966.